UNIVERSIDADE FEDERAL DE SANTA CATARINA
CENTRO TECNOLÓGICO
PROGRAMA DE PÓS-GRADUAÇÃO EM ENGENHARIA MECÂNICA

Bernardo Peressoni Vieira

MODELING AND OPTIMIZATION OF ACTIVE MAGNETIC REGENERATORS USING LA-FE-SI BASED ALLOYS

FLORIANÓPOLIS
2020

Bernardo Peressoni Vieira

MODELING AND OPTIMIZATION OF ACTIVE MAGNETIC REGENERATORS USING LA-FE-SI BASED ALLOYS

Dissertação submetida ao Programa de Pós-Graduação em Engenharia Mecânica da Universidade Federal de Santa Catarina para a obtenção do título de Mestre em Engenharia Mecânica.

Supervisor:	Prof. Jader Riso Barbosa Jr., Ph.D.
Co-supervisor:	Dr. Jaime Andrés Lozano Cadena
Co-supervisor:	Henrique Neves Bez, Ph.D.

FLORIANÓPOLIS
2020

Ficha de identificação da obra elaborada pelo autor,
através do Programa de Geração Automática da Biblioteca Universitária da UFSC.

Vieira, Bernardo Peressoni
Modeling and optimization of active magnetic regenerators using La-Fe-Si based alloys / Bernardo Peressoni Vieira ; orientador, Jader Riso Barbosa Jr., coorientador, Jaime Andrés Lozano Cadena, coorientador, Henrique Neves Bez, 2020.
280 p.

Dissertação (mestrado) - Universidade Federal de Santa Catarina, Centro Tecnológico, Programa de Pós-Graduação em Engenharia Mecânica, Florianópolis, 2020.

Inclui referências.

1. Engenharia Mecânica. 2. Engenharia Mecânica. 3. Refrigeração Magnética. 4. Regenerador Magnético Ativo. 5. Modelagem Computacional. I. Barbosa Jr., Jader Riso. II. Cadena, Jaime Andrés Lozano. III. Bez, Henrique Neves IV. Universidade Federal de Santa Catarina. Programa de Pós Graduação em Engenharia Mecânica. V. Título.

Bernardo Peressoni Vieira

MODELING AND OPTIMIZATION OF ACTIVE MAGNETIC REGENERATORS USING LA-FE-SI BASED ALLOYS

O presente trabalho em nível de mestrado foi avaliado e aprovado por banca examinadora composta pelos seguintes membros:

Prof. Jader Riso Barbosa Jr., Ph.D.
Universidade Federal de Santa Catarina

Prof. Amir Antônio Martins de Oliveira Jr., Ph.D.
Universidade Federal de Santa Catarina

Prof. Kurt Engelbrecht, Ph.D.
Universidade Técnica da Dinamarca

Certificamos que esta é a **versão original e final** do trabalho de conclusão que foi julgado adequado para obtenção do título de Mestre em Engenharia Mecânica.

Documento assinado digitalmente
Paulo de Tarso Rocha de Mendonca
Data: 09/02/2021 16:36:36-0300
CPF: 149.822.691-49

Prof. Dr. Paulo de Tarso Rocha de Mendonça
Coordenador do Programa

Documento assinado digitalmente
Jader Riso Barbosa Junior
Data: 09/02/2021 15:53:38-0300
CPF: 010.026.207-40

Prof. Jader Riso Barbosa Jr., Ph.D.
Orientador

Dr. Jaime Andrés Lozano Cadena
Coorientador

Henrique Neves Bez, Ph.D.
Coorientador

Florianópolis, 15 de dezembro de 2020.

To my parents Elianne Maria and Paulo Afonso
to my siblings Carolina, Eduardo, Daniela and Felipe
to my nephews and nieces Letícia, Helena, Miguel, Guenther and Henrique
and to my dear friend Henrique Neves Bez (in memoriam).
You always give me the strength to keep moving forward and I will cherish you always.

Agradecimentos

Agradeço inicialmente ao Prof. Jader Riso Barbosa Jr. pela contínua orientação não só neste trabalho, mas durante os últimos 6 anos iniciando ainda durante a graduação, resultando em inestimáveis contribuições e conhecimentos compartilhados. Agradeço também ao meu coorientador, Dr. Eng. Jaime Andrés Lozano Cadena pelas contribuições, sugestões e companheirismo durante os últimos anos.

Agradeço também ao meu coorientador, Henrique Neves Bez, Ph.D., não só pela valiosa orientação, mas pela incrível amizade que formamos, a qual precedia a relação orientador-orientando. Muito obrigado pelas conversas, lições, experiências e pelo carinho e consideração que você sempre mostrou a mim na nossa convivência diária no laboratório. Obrigado por dar valor e incentivar não só meus méritos acadêmicos, mas também outras atividades e aspirações que compartilhei com você. Você foi um amigo muito especial para mim e me considero uma pessoa de sorte incomparável por ter tido a oportunidade de lhe conhecer. Carregarei para sempre comigo nossas experiências e sempre terei você na minha memória.

Agradeço tambem à banca: Prof. Amir A. M. de Oliveira e Prof. Kurt Engelbrecht pelo tempo disponibilizado para avaliar este trabalho e pelas contribuições oferecidas.

Agradeço o suporte fornecido pelo CNPq, FEESC, CODEMGE, Instituto Nacional em Ciência e Tecnologia (INCT) e INRiM, e também pelo programa de Pós-Graduação em Engenharia Mecância.

Agradeço a todos os membros do time Polomag que tornaram possível a realização deste trabalho. Ao Higor, pela realização de experimentos e contínuo suporte fornecido durante a maior parte deste trabalho. À Natália, pela parceria dentro e fora do laboratório. À Gislaine pela constante ajuda em todos os aspectos referentes à bancada experimental e por ser uma incrível companheira de sala. Ao Luís Felipe, pelos resultados referentes ao circuito magnético e auxílio na solução dos mistérios mais interessantes e mágicos da física e da matemática. Ao Marcelo e a toda a equipe do MAGMA, pelos testes de materiais presentes neste trabalho. Agradeço também aos demais membros que contribuíram para este projeto, obrigado Alan, Guilherme, Fábio, Victor, Sergio, Gusttav, Diego, Gabriel, Joana, Maria, Luiza, Anderson, Larissa e Mayara. Agradeço também aos demais membros do POLO cujos conhecimentos auxiliaram no desenvolvimento deste trabalho.

Agradeço aos meus amigos fora do laboratório, Murilo, Alan, João, Otávio, Gabriel, Giovanni e Lucas pelo suporte ao longo dos últimos 7 anos de dedicação à engenharia mecânica.

Finalmente, agradeço aos meus pais, Elianne Maria e Paulo Afonso, por todo

amor e apoio que me deram ao longo da minha vida. Não há palavras que descrevam o quão importante vocês são na minha vida. Todo desafio que enfrento é mais fácil porque sei que tenho vocês ao meu lado. Agradeço também aos meus irmãos mais velhos, Carolina, Eduardo, Daniela e Felipe por me apoiarem constantemente desde o dia em que nasci. Vocês serão sempre grandes exemplos para mim. Aos meus sobrinhos Letícia, Helena, Miguel, Guenther e Henrique por, com sua alegria e inocência, trazerem felicidade ao seu tio mal-humorado que está sempre trabalhando. Agradeço também aos meus demais familiares, com uma menção especial ao meu primo Rafael, pelo apoio e confiança que depositaram em mim.

Muito obrigado a todos que tornaram possível a realização deste trabalho.

"The most important step a person can take is always the next one."
(Brandon Sanderson)

Resumo

Tecnologias alternativas de refrigeração buscam o desenvolvimento de sistemas que tenham um consumo de energia e impacto ambiental menores do que os sistemas convencionais. Recentemente, principalmente devido à questão ambiental, a busca por tais sistemas vem se intensificando cada vez mais. Neste contexto, a refrigeração magnética surge como uma das alternativas mais atrativas e promissoras, porém ainda sofre com limitações que impedem sua aplicação em larga escala como o custo de seus componentes, sua complexidade e seu tamanho. Esta dissertação consiste do desenvolvimento de um modelo numérico de simulação de regeneradores magnéticos ativos, os quais são um dos principais componentes de um sistema de refrigeração magnética, com o objetivo de projetar o regenerador de uma unidade de refrigeração magnética com capacidade de 9000 BTU/h para temperaturas das fontes fria e quente de 22ºC e 35ºC. Um sistema de refrigeração magnética é uma estrutura complexa, porém este trabalho tem como foco o regenerador e sua interação com dois outros subsistemas: o sistema hidráulico e o circuito magnético. O sistema hidráulico é responsável pelo escoamento dentro do regenerador, influenciando a vazão máxima, o perfil de escoamento e a frequência de operação. O circuito magnético fornece o perfil de campo magnético através de sua rotação e contém os regeneradores no seu interior, afetando não só o efeito magnetocalórico, mas também a frequência de operação e as dimensões do regenerador. Dessa forma, este trabalho pode ser dividido em duas partes: desenvolvimento e aprimoramento de um modelo de regeneradores magnéticos ativos capaz de simular características específicas de regeneradores à base de La-Fe-Si, e uso de tal modelo para analisar a influência de diversos parâmetros de operação na capacidade de refrigeração do sistema, visando o projeto do regenerador final. O modelo resultante da primeira parte é descrito de maneira aprofundada e inclui, além do modelo básico de um regenerador magnético ativo, perdas devido aos volumes mortos, à troca de calor através da carcaça, à influência do epóxi na troca de calor e perda de carga, à desmagnetização causada pelo material e outras perdas menores. A segunda parte consiste inicialmente da validação do modelo com resultados experimentais, os quais foram realizados para três tipos diferentes de materiais a base de La-Fe-Si. A validação mostrou resultados promissores, com o modelo demostrando um desvio menor do que 7% em relação à capacidade de refrigeração a *span* zero obtida experimentalmente em um regenerador ligado por epóxi. Em seguida, uma análise dos resultados obtidos pelo modelo é feita, descrevendo o desempenho do regenerador em função de diversos parâmetros de projeto. A maior parte dessas análises é feita dentro do contexto de uma unidade de refrigeração magnética, ou seja, de maneira integrada com os outros subsistemas, principalmente o magnético, os quais foram modelados por outros membros da equipe do projeto. Ao final, o processo de decisão aplicado para definir o regenerador final e o seu material é descrito, e as especificações resultantes deste processo são expostas, incluindo as dimensões do circuito magnético. O regenerador escolhido é equivalente a um regenerador prismático de base retangular com altura de 45 mm, largura de 59 mm e comprimento de 130 mm. A massa final de cada regenerador foi estimada em 1.5 kg, com 16 regeneradores sendo utilizados no sistema, resultando em 24 kg de material. Cada regenerador é composto por 12 camadas de material com temperaturas de Curie variando entre 288.15 K e 314.15 K. O sistema hidráulico precisará fornecer uma vazão média por blow de 800 kg h^{-1} com uma frequência de 2.5 Hz. Nessas condições, a capacidade de refrigeração esperada é de 2638 W (9000 BTU/h).

Palavras-chave: Refrigeração magnética. Regenerador magnético ativo. Modelagem e otimização.

Resumo Expandido

Introdução

O desenvolvimento de sistemas com menores consumo de energia e impactos ambientais é um dos principais objetivos das tecnologias alternativas de refrigeração, as quais ganharam proeminência nos últimos anos principalmente devido a questões ambientais. Dentre tais tecnologias, destaca-se a refrigeração magnética como uma das alternativas mais promissoras, porém esta ainda sofre com limitações que impedem sua aplicação em larga escala principalmente no que se refere ao seu custo, complexidade e tamanho. A refrigeração magnética se baseia no efeito magnetocalórico, o qual é uma resposta térmica que um material apresenta quando submetido a uma variação de campo magnético, podendo ser descrito por uma variação de temperatura adiabática ou uma variação de entropia isotérmica. Uma das características mais importantes deste fenômeno é sua reversibilidade, a qual é observada em diversos materiais magnetocalóricos e cria o potencial para o desenvolvimento de tecnologias com maior eficiência do que alternativas convencionais como compressão de vapor. Apesar desse fator e dos resultados promissores de trabalhos recentes no que se refere à solução de desafios e limitações da tecnologia, a literatura disponível ainda apresenta poucos trabalhos que se referem ao desenvolvimento de sistemas de refrigeração magnética para uso comercial. No momento, a maior parte dos trabalhos se limita ao desenvolvimento de protótipos não comerciais e à otimização de componentes e subsistemas específicos, cada um proporcionando o próximo passo para uma eventual comercialização da tecnologia.

Objetivos

Os principais componentes de um sistema de refrigeração magnética são o regenerador magnético ativo, o circuito magnético, os trocadores de calor e o sistema hidráulico. O regenerador, o qual é composto de material magnetocalórico, é submetido a um campo magnético variável produzido pelo circuito magnético e sofre o efeito magnetocalórico. Enquanto isso, o sistema hidráulico é responsável pelo escoamento de fluido através do regenerador de maneira sincronizada com o perfil de campo magnético. Tal fluido é então direcionado aos trocadores de calor, os quais trocam calor com os reservatórios quente e frio. Um dos principais motivos para o número limitado de trabalhos contemplando o projeto de um sistema de refrigeração magnética para aplicação comercial é a complexidade inerente à integração destes componentes e subsistemas, a qual ocorre principalmente no regenerador. Neste contexto, um projeto está sendo desenvolvido no POLO/UFSC que tem como objetivo desenvolver um ar condicionado magnético capaz de atingir uma capacidade de refrigeração de 9000 BTU/h quando operando entre ambientes a 22ºC e 35ºC, similarmente a sistemas encontrados no mercado. A primeira parte deste projeto consiste do desenvolvimento de uma unidade de refrigeração magnética capaz de atingir as condições especificadas neste projeto utilizando ímãs permanentes e materiais magnetocalóricos de primeira-ordem. Desta forma, o objetivo deste trabalho é projetar um regenerador magnético ativo de primeira-ordem para ser aplicado a uma unidade de refrigeração magnética capaz de atingir 9000 BTU/h quando operando entre ambientes a 22ºC e 35ºC.

Metodologia

O desenvolvimento de um sistema de refrigeração magnética é uma atividade complexa, porém este trabalho tem como foco principal o regenerador e sua interação com dois subsistemas: o circuito magnético e o sistema hidráulico. O circuito magnético é responsável por gerar o perfil de campo magnético através da sua rotação e contém os regeneradores no seu interior, afetando não só o efeito magnetocalórico, mas também a frequência de operação e as dimensões do regenerador. O sistema hidráulico é responsável pelo escoamento dentro do regenerador, influenciando a vazão máxima, o perfil de escoamento e a frequência de operação. Para simular esta integração, um modelo de regeneradores magnéticos ativos capaz de simular características específicas de regeneradores à base de La-Fe-Si (primeira ordem) foi desenvolvido de forma a permitir analisar a influência de diversos parâmetros de operação na capacidade de refrigeração do sistema, visando o projeto do regenerador final. O modelo consiste da solução das equações de conservação nas fases sólida e líquida, além de seções descrevendo as perdas devido aos volumes mortos, à troca de calor através da carcaça, à influência do epóxi na troca de calor e perda de carga, à desmagnetização causada pelo material e outras perdas menores. A validação do modelo foi realizada através de resultados experimentais obtidos numa bancada de testes de regeneradores. No total, três materiais a base de La-Fe-Si foram analisados em tais testes.

Resultados e Discussão

A validação do modelo apresentou resultados positivos, com uma diferença inferior a 7% entre a capacidade de refrigeração *span* zero obtida pelo modelo e experimentalmente em um regenerador ligado por epóxi. No que se refere ao projeto do regenerador para uso na unidade de refrigeração magnética, parâmetros como diâmetro de partícula, porosidade e quantidade de epóxi não puderam ser alterados, portanto a influência destes parâmetros no desempenho do sistema foi analisada separadamente. No contexto do projeto, foram definidas as dimensões do regenerador bem como suas condições de operação, baseado na sua integração com o sistema hidráulico e o circuito magnético. O regenerador selecionado possui geometria equivalente a um regenerador prismático de base retangular com altura de 45 mm, largura de 59 mm e comprimento de 130 mm. A massa final de cada regenerador foi estimada em 1.5 kg, com 16 regeneradores sendo utilizados no sistema, resultando em 24 kg de material. Cada regenerador é composto por 12 camadas de material com temperaturas de Curie variando entre 288.15 K e 314.15 K. O sistema hidráulico precisará fornecer uma vazão média por blow de 800 kg h^{-1} com uma frequência de 2.5 Hz. Nessas condições, a capacidade de refrigeração esperada é de 2638 W (9000 BTU/h).

Considerações Finais

Esta dissertação é parte de uma série de diferentes trabalhos que em conjunto têm como objetivo projetar uma unidade de refrigeração magnética que atinja uma capacidade de refrigeração de 9000 BTU/h quando operando entre 22ºC e 35ºC. Este trabalho teve foco no desenvolvimento do regenerador e sua integração em especial com o sistema hidráulico e o circuito magnético. Para tanto, um modelo numérico foi desenvolvido que permitia a simulação de regeneradores magnéticos ativos bem como

a sua integração com os demais subsistemas. A validação experimental incluiu testes de regeneradores de três diferentes materiais, com ou sem a adição de epóxi. A influência de parâmetros não analisados no projeto foi analisada separadamente, e parâmetros relevantes para o projeto como as dimensões do regenerador e as condições de operação foram analisados visando encontrar os valores ótimos de acordo com a integração com os demais subsistemas. A versão selecionada do regenerador contém 1.5 kg de material com dimensões de 45 mm x 59 mm x 130 mm. Um total de 16 regeneradores será utilizado no sistema com capacidade resultante prevista de 2638 W (9000 BTU/h).

Palavras-chave: Refrigeração magnética. Regenerador magnético ativo. Modelagem e otimização.

Abstract

Alternative refrigeration technologies aim for the development of systems that have a lower energy consumption and environmental impact than conventional systems. Recently, mainly due to environmental issues, the search for such systems has been increasingly intensifying. In this context, magnetic refrigeration emerges as one of the most attractive and promising alternatives, but it still suffers from limitations that prevent its large-scale application such as the cost of its components, its complexity and its size. This dissertation consists of the development of a numerical model of active magnetic regenerators, which are one of the main components of a magnetic refrigeration system, with the objective of designing the regenerator of a magnetic refrigeration unit with a cooling capacity of 9000 BTU/h between cold and hot environments with temperatures of 22ºC and 35ºC. A magnetic cooling system is a complex structure, but this work focuses on the regenerator and its interaction with two other sub-systems: the hydraulic system and the magnetic circuit. The hydraulic system is responsible for the flow within the regenerator, influencing the maximum mass flow rate, the flow profile and the frequency of operation. The magnetic circuit provides the magnetic field profile through its rotation and contains the regenerators inside it, affecting not only the magnetocaloric effect, but also the frequency of operation and the dimensions of the regenerator. Thus, this work can be divided into two parts: development and improvement of a model of active magnetic regenerators capable of simulating specific characteristics of La-Fe-Si-based regenerators, and use of this model to analyse the influence of different operating parameters on the cooling capacity of the system, aiming for the design of the final regenerator. The model resulting from the first part is described in depth and includes, in addition to the basic model of an active magnetic regenerator, losses due to void volumes, heat exchange through the casing, the influence of epoxy bonding on the heat exchange and the pressure drop, demagnetization caused by the material and other minor losses. The second part initially consists of validating the model with experimental results, which were performed with three different types of La-Fe-Si based materials. The validation showed promising results, with the model showing a deviation of less than 7% in relation to the cooling capacity at zero-span obtained experimentally in an epoxy-bonded regenerator. Then, an analysis of the results obtained by the model is made, describing the performance of the regenerator according to several design parameters. Most of these analyses are made within the context of the magnetic refrigeration unit, that is, in an integrated manner with the other sub-systems, mainly the magnetic circuit, which were modeled by other members of the project team. In the end, the decision process applied to define the final regenerator and its material is described, and the specifications resulting from this process are exposed, including the dimensions of the magnetic circuit. The chosen regenerator is equivalent to a prismatic regenerator with a rectangular base 45 mm high, 59 mm wide and 130 mm long. The final mass of each regenerator was estimated at 1.5 kg, with 16 regenerators being used in the system, resulting in 24 kg of material. Each regenerator consists of 12 layers of material with Curie temperatures ranging from 288.15 K to 314.15 K. The hydraulic system will need to provide an average mass flow rate per blow of 800 kg h^{-1} with a frequency of 2.5 Hz. Under these conditions, the expected cooling capacity is 2638 W (9000 BTU / h).

Keywords: Magnetic refrigeration. Active magnetic regenerator. Modelling and opti-

mization.

List of Figures

List of Tables

Nomenclature

Roman

A	Area	m^2
A_{dp}	Particle surface area	m^2
A_{reg}	Regenerator cross-sectional area	m^2
B	Magnetic flux density	T
Bi	Biot number	-
c	Specific heat capacity	$\mathrm{J\,kg^{-1}\,K^{-1}}$
c_{E}	Ergun constant	-
c_{H}	Isofield specific heat capacity	$\mathrm{J\,kg^{-1}\,K^{-1}}$
c_{p}	Isobaric specific heat capacity	$\mathrm{J\,kg^{-1}\,K^{-1}}$
$D_{\parallel}$	Longitudinal thermal dispersion	$\mathrm{m^2\,s^{-1}}$
d_{h}	Hydraulic diameter	m
d_{P}	Particle diameter	m
D_{reg}	Regenerator diameter	m
e_{air}	Air gap thickness	m
f	Frequency	Hz
$\vec{f}$	Body forces	N
Fo	Fourier number	-
H	Magnetic field	$\mathrm{A\,m^{-1}}$
h	Interstitial heat transfer coefficient	$\mathrm{W\,m^{-2}\,K^{-1}}$
H_{reg}	Regenerator height	m
K	Permeability of the porous medium	m^2
k	Thermal conductivity	$\mathrm{W/(m\,K)}$
k_{K}	Kozeny constant	-

L_c	Characteristic length	m
L_{ep}	Epoxy layer length	m
L_{reg}	Regenerator length	m
L_{vv}	Void volume length	m
M	Magnetization	$A\,m^{-1}$
$\dot{m}$	Mass flow rate	$kg\,s^{-1}$
m	Mass	kg
$\overline{\overline{N}}_D$	Demagnetization tensor	-
NTU	Number of transfer units	-
Nu_{dp}	Nusselt number based on the particle diameter	-
P	Pressure	Pa
Pe_{dp}	Peclet number based on the particle diameter	-
Pr	Prandtl number	-
p_{reg}	Regenerator perimeter	m
$\dot{Q}_c$	Cooling capacity	W
$\dot{Q}$	Energy rate	W
$\dot{q}$	Energy rate per unit volume	$W\,m^{-3}$
$\dot{Q}_h$	Rejected heat rate	W
R	Radius	m
Re_{dp}	Reynolds number based on the particle diameter	-
s	Specific entropy	$J\,kg^{-1}\,K^{-1}$
T	Temperature	K
T_{Curie}	Curie Temperature	K
t	Time	s
u	Darcy velocity	$m\,s^{-1}$
$\vec{v}$	Velocity	$m\,s^{-1}$

V	Volume	m^3
$\dot{W}_m$	Magnetic power	W
$\dot{W}_p$	Pumping power	W
W_{reg}	Regenerator width	m
y	Position perpendicular to the regenerator length	m
z	Position along the regenerator length	m

Greek

α	Thermal diffusivity,	$m^2\,s^{-1}$
β	Surface area density of the porous medium	$m^2\,m^{-3}$
ε	Porosity	-
ϵ	Thermal effectiveness	-
μ	Dynamic viscosity	Pa s
ω	Angular velocity	rad/s
ϕ	Utilization factor	-
ρ	Density	$kg\,m^{-3}$
σ	Specific magnetization	$A\,m^2\,kg^{-1}$
τ	Period	s
φ	Weight fraction	-

Sub and Super-Scripts

ad	Adiabatic
air	Air
apl	Applied
CB	Cold blow
C	Cold side
cond	Conduction
conv	Convection

csg	Casing
dem	Demagnetization
E	Electronic
eff	Effective
ep	Epoxy
eq	Equivalent
f	Fluid phase
geo	Geometry
HB	Hot blow
H	Hot side
HT	Heat transfer
int	Interstitial
L	Lattice
mag	Magnetization
MCE	Magnetocaloric effect
MCM	Magnetocaloric material
M	Magnetic
pm	Porous medium
reg	Regenerator
s	Solid phase
vv	Void volume
wall	Wall

Abbreviations

CTDF	Curie temperature distribution factor
MAC	Magnetic air conditioner
MCE	Magnetocaloric effect

MCM	Magnetocaloric material	
MRU	Magnetic refrigeration unit	
TBD	To be determined	
VAC	Vacuumschmelze	
WUDS	Weighted upstream differencing scheme	

Constants

μ_0	Magnetic permeability of vacuum	$4\pi \times 10^{-7}\ \mathrm{N\,A^{-2}}$

Contents

1 Introduction

Refrigeration is defined as the process of cooling a body or a fluid to a lower temperature than the ambient in which it is located. It is a fundamental part of modern society with applications ranging from food conservation to cryogenics. Therefore, the development and optimization of refrigeration systems is an extremely important topic in mechanical engineering, which has been consistently studied for more than a century.

The second law of thermodynamics, as stated by Clausius, says that it is impossible to transfer heat from a cold source to a hot sink without changing the surroundings by means of work input. The most widespread refrigeration technology, especially for near room-temperature applications, is based on vapor compression. In this cycle, a volatile fluid (refrigerant) is compressed (external work input), condensed, expanded and evaporated, allowing the heat to flow from the cold to the hot environment.

This system, despite centuries of evolution, still has limitations and issues even after continuous research and improvement (MONFARED, 2018). Namely, the use of refrigerants which are inflammable (R600a), dangerous for the environment (CFCs and HCFCs, which harm the ozone layer) or even toxic (amonia) depending on the application. The environmental damage caused by refrigerants has become such an important issue that it has been addressed by the Montreal Protocol, which proposes a complete phase out of HCFC use in developed countries by 2020 and in developing countries by 2030 (UNITED NATIONS, 2020). Additionally, the efficiencies reached by these systems are usually considerably below the Carnot's maximum theoretical efficiency. This becomes even more important when one considers that refrigeration and air conditioning account for about 17% of the global electricity consumption (KITANOVSKI, 2020).

Due to these and other limitations, there has been an increasing search for alternative refrigeration technologies to reduce or eliminate these problems. Some of those not-in-kind technologies are based on solid-state, field change-induced phase transitions, which are characterized by the potential to develop high thermodynamic efficiencies (QIAN; YU; YAN, 2017). Amongst said technologies is magnetic refrigeration, which is based on the magnetocaloric effect (MCE). This effect can be defined as the thermal response of certain magnetic materials when submitted to a variation of magnetic field. Like the other so-called caloric technologies (electrocaloric, barocaloric, elastocaloric), it is characterized by an adiabatic temperature change and an isothermal entropy change.

One of the most interesting characteristics of the magnetocaloric effect is the reversibility observed in most known magnetocaloric materials (MCMs), which potentially enables the development of efficiencies higher than vapor compression

(PECHARSKY; GSCHNEIDER, 2006). Besides that, the use of a solid refrigerant removes the risk of leakages and problems associated with the handling of high-pressure fluids. Moreover, both the magnet, which is the component of the system responsible for generating the magnetic field variation, and the solid-state refrigerant, if handled properly, can be recycled at the end of the system life cycle. For those advantages, research on magnetic refrigeration systems has been increasing considerably during the last decades, aiming, among other things, to show its possible applications and to make it economically viable for more widespread use, especially at room temperature refrigeration (SMITH et al., 2012; KITANOVSKI et al., 2015).

1.1 Magnetic Refrigeration History

The discovery of the magnetocaloric effect is usually attributed to Weiss and Piccard in 1918, when they observed a reversible temperature change of around 0.7 K in a field of 1.5 T on nickel in the vicinity of its Curie temperature (around 627 K) (SMITH, 2013). The Curie temperature is defined as the temperature where the material transitions from the ferromagnetic to the paramagnetic state and, for the materials discussed in this work, is the point where, at low applied fields, the magnetocaloric effect reaches its maximum. Applications of the MCE, however, were initially restricted to cryogenics and temperature ranges below 20 K (PECHARSKY; GSCHNEIDER, 1999). Room temperature magnetic refrigeration only began to be explored after the pioneering work of Brown (1976) that gave rise to the development of other devices, like the one due to Steyert (1978) (SMITH et al., 2012). Such applications were made possible with the use of gadolinium (Gd) as the solid-state refrigerant. This rare-earth element is the only pure substance to exhibit a Curie temperature near room-temperature, with values ranging from 290 to 297 K (BAHL; NIELSE, 2009). As mentioned above, this is the point where the magnetocaloric effect reaches a maximum, which, for Gd is of the order of 3 K/T (SMITH et al., 2012; KITANOVSKI et al., 2015). Gd is classified as having a second-order magnetic phase transition, meaning that the behaviour of the transition is continuous (i.e., the variation of the intrinsic spontaneous magnetization of the material is continuous). Other materials, such as the La-Fe-Si alloys that will be analysed in this work, have so-called first-order magnetic phase transitions, which are discontinuous. The implications of these classifications will be briefly mentioned in this chapter and discussed in detail in Chapter 2. Using gadolinium, Brown (1976) was able to achieve a no-load temperature span of 47 K in his device, which used a superconducting coil to generate a 7 T magnetic flux density, prompting interest in the technology for near room-temperature applications.

A few years later, Barclay & Steyert (1982) proposed a configuration that became known as the Active Magnetic Regenerator (AMR), in which the solid refrigerant

(magnetocaloric material) is also used as a regenerative matrix. Virtually all devices developed after the work of Barclay and Steyert applied some variation to the AMR principle, with this trend continuing to this day. The AMR is subjected to alternating axial fluid flows (called hot and cold blows) which are responsible for transporting the heat between the ends of the porous medium, which are thermodynamically connected to the hot and cold thermal reservoirs. This allows for much higher temperature spans to be achieved, increasing the range of applications of the technology. The next major breakthrough in the area of magnetic refrigeration occurred with the discovery of the giant magnetocaloric effect observed in $Gd_5Si_2Ge_2$ alloys by Pecharsky & Gschneider (1997), which triggered an increase in interest from both the scientific community and industry in the study of this technology (SMITH et al., 2012). Figure 1 presents the evolution of the number of yearly publications in the areas of materials science, engineering and energy related to the previously mentioned caloric technologies between 1990 and 2020 obtained from the Scopus database. The increase in interest in magnetocaloric technologies caused by the work of Pecharsky & Gschneider (1997) can clearly be seen, with the number of publications in the area increasing from less than 10 in 1996 to a peak of over 500 in 2018.

Figure 1 also shows that while the growing interest in caloric energies started with magnetocaloric refrigeration, the interest in other caloric technologies has also increased during the last years (GRECO et al., 2019). A recent elastocaloric device was declared to be able to reach a temperature span of 20 K according to Engelbrecht et al. (2017). This technology, however, is held back mainly due to the fatigue-life of the elastocaloric materials, which does not allow the construction of long-lasting devices. Electrocaloric devices have yet to show more promising results, with the high losses related to the electric-field generation preventing them from reaching satisfactory energy performances, and barocaloric technologies are still laying the bases for the development of cooling devices, but have been showing promising results (GRECO et al., 2019). Regarding magnetocaloric technologies, despite the achievements and results of the recent works in regards to overcoming the challenges and limitations of the technology, the available literature has yet to present works related to the commercial development of a magnetic refrigeration system. Currently, most works are limited to the development of non-commercial prototypes and consist mostly of analysis and optimization of specific components and sub-systems, instead of the system as a whole. According to Kamran, Ahmad & Wang (2020) the technology still requires research breakthroughs in the field of system design, higher magnetic fields and advanced magnetocaloric materials to conquer space in the market. It is clear, however, that steps are constantly being taken towards this direction of marketization, with recent devices being able to reach cooling capacities of 3042 W (JACOBS et al., 2014) and spans as high as 40 K (GRECO et al., 2019).

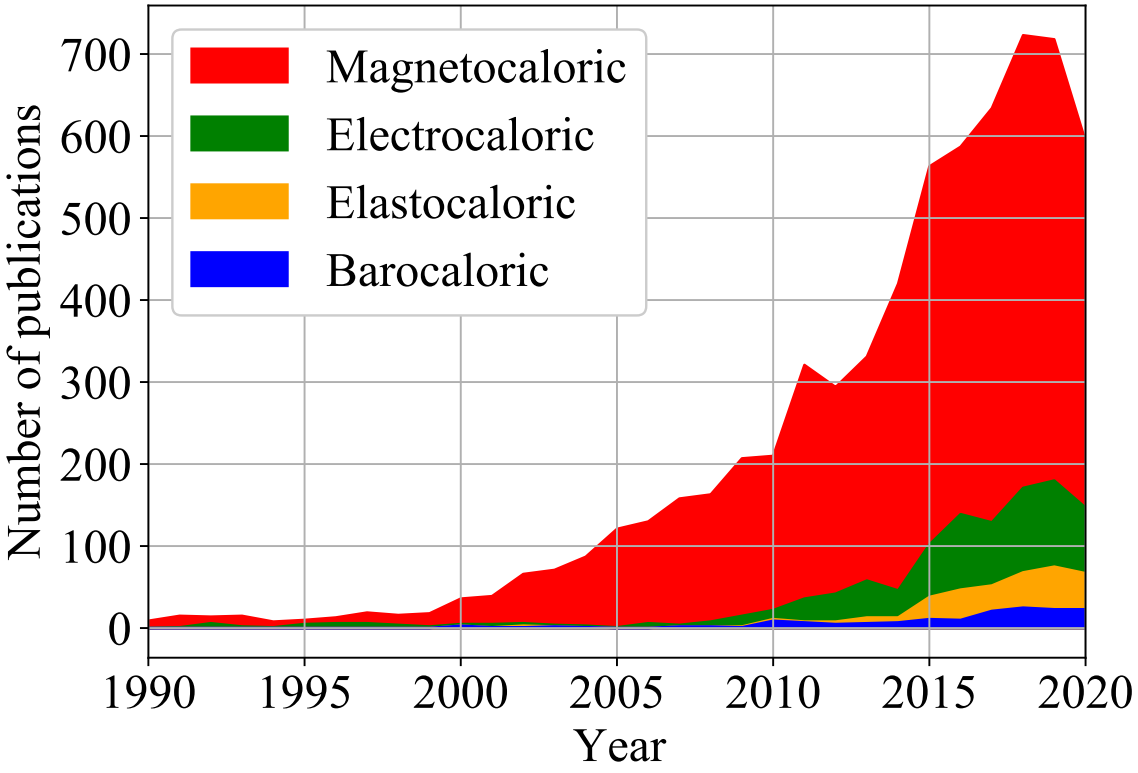

Figure 1 – Number of papers related to magnetocaloric, electrocaloric, elastocaloric and barocaloric technologies published yearly between 1990 and 2020.

1.2 Active Magnetic Regenerators

The main components (or sub-systems) of a magnetic refrigerator are the AMR, the magnetic circuit (MC), the cold and hot heat exchangers (CHEx and HHEx) and the hydraulic (fluid) management system, which are shown in Figure 2. The AMR, which is composed of the magnetocaloric material, is subjected to a varying magnetic applied field produced by the MC, inducing the magnetocaloric effect in the solid refrigerant. Meanwhile, the hydraulic system is responsible for generating the flow of the heat transfer fluid through the AMR in synchronization with the magnetic field profile. The fluid exchanges heat with the MCM in the regenerator and transports it to the heat exchangers, which exchange heat with the cold and hot reservoirs.

Based on this configuration, the AMR is considered the heart of the system since it connects all the other relevant components. The MCM in the regenerator can be composed of first- or second-order magnetic phase transition materials. Although the implications of solid-state refrigerant selection will be dealt with and further explained in Chapter 2, from a design point of view, first-order materials present a higher MCE within a narrower range of temperatures while second-order materials present a lower MCE over a wider range of temperatures. This gives the potential for first-order ma-

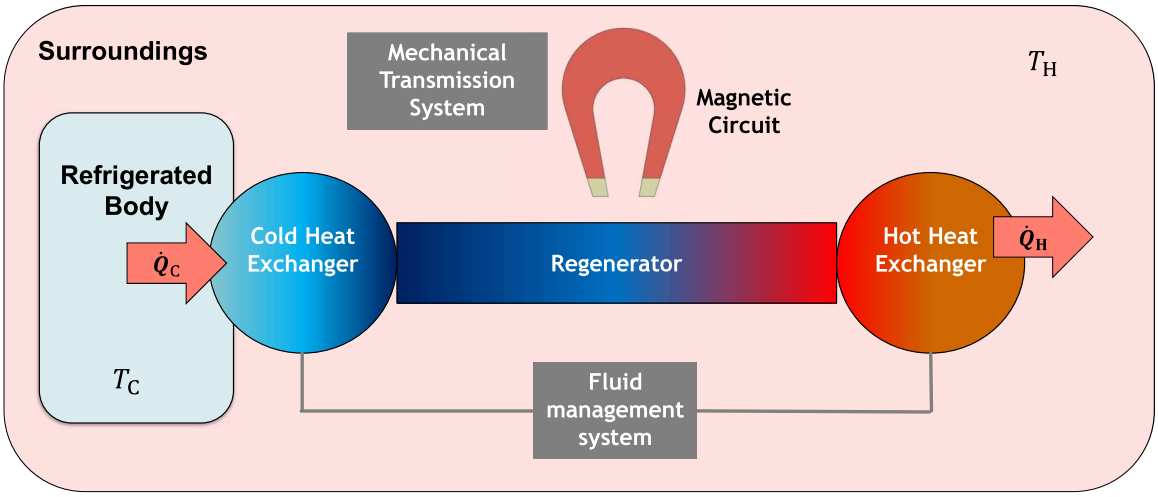

Figure 2 – Schematic representation of a magnetocaloric refrigeration system and its main sub-systems. Adapted from Lozano et al. (2018).

terials to reach higher cooling capacities, at the expense of requiring a more complex design to guarantee that the magnetocaloric effect is exploited in full. Because of this special condition of the regenerator, its design and operation involve the application of concepts from Thermodynamics, Fluid Mechanics, Heat Transfer, Materials Science, Hydraulics, Magnetism and Mechanical Design.

1.3 Motivation and Main Objective

As mentioned in the previous sections, there is a limited number of works in the current literature that describe the design of a magnetic refrigerator considering the integration between its sub-systems. This is in part because a large number of interconnected design variables is involved in the design of said systems, which greatly increases the complexity. In this context, a research project is being carried out at POLO/UFSC which aims to develop a magnetic air conditioner which produces a cooling capacity of 9000 BTU/h operating between cold and hot environments at 22ºC and 35ºC, similarly to conventional air conditioners found in the market. The first part of this project consists on the development of a magnetic refrigeration unit (MRU), which is a prototype that aims to reach the specified conditions using permanent magnets and first-order materials as solid refrigerants. This MRU will serve as a proof of concept and starting point for the development of the final magnetic air conditioner (MAC) which is intended to be much closer to a final product than a prototype. If successful, this project would be an important step towards the commercialization of the technology, proving that it is comparable to some conventional air conditioners, at least from an operating point (cooling capacity and temperature span) point of view. For a project with this scope, the integration between the sub-systems is fundamental

for the requirements to be met, and the regenerator, as previously mentioned, is the sub-system that interconnects all the other main components. With this in mind, the main objective of this dissertation is:

> *To design a first-order active magnetic regenerator to be applied in a 9000-BTU/h magnetic refrigeration unit operating between 22ºC and 35ºC.*

To achieve this objective, a 1-D mathematical model of an AMR has been developed based on the methods put forward by Trevizoli (2015) and Lang (2018). Thermophysical properties of the first-order La-based MCMs were measured and correlated prior to their implementation in the model. Factors such as the influence of binding polymers and void (dead) volumes on the cooling capacity were analysed. Experimental tests were performed on first-order material regenerators to ascertain their thermal and mechanical performance and to validate the model. In total, three different $La(Fe,Mn,Si)_{13}H_z$ alloys were tested, showing varying degrees of mechanical stability and magnetocaloric effect intensity. Uncertainties associated with the manufacturing process of the functional material were evaluated and procedures to incorporate them in the analysis of the performance of the AMR have been proposed in the course of this study. Experimental results and numerical models for the other sub-systems were integrated with the AMR model to more closely represent the final operating condition, including their design limitations. Finally, at the end of this work, a final design and operating condition of the AMR which considers the influence of all other systems has been determined and numerically tested to guarantee it delivers the desired cooling capacity of 9000 BTU/h while operating between 22ºC and 35ºC. Between the three $La(Fe,Mn,Si)_{13}H_z$ alloys that were analysed, only one showed the mechanical integrity required to operate under the AMR cycle and was thus selected to be used in the final design.

1.4 Outline of the Dissertation

This dissertation is divided into 6 different chapters. This chapter aims to contextualize this dissertation within the current literature while also describing the motivation, challenges and objectives pertaining to this work. Chapter 2 presents a literature review of magnetic refrigeration, starting with the basic thermodynamics of the magnetocaloric effects followed by a description of magnetocaloric materials and ending with a description of state-of-the-art magnetic refrigerator prototypes. While the chapter describes magnetic refrigeration as a whole, a special focus is given to the regenerators (particularly first-order regenerators) and their integration within the system. Chapter 3 presents a detailed description of the mathematical model used in this work to describe and predict the performance of a regenerator, including the main

equations of the model, the closure relationships, the implementation of the physical properties of the material and the solution method. Chapter 4 presents a description of all regenerators that were tested for this work alongside a description of the experimental apparatus used for said tests. Chapter 5 contains the results obtained using the model described in Chapter 3, including the validation using the tests presented in Chapter 4. It also includes a description of the basic operating parameters of a regenerator and the process through which the final regenerator was designed, including its integration within the system. Chapter 6 presents an overview of the work and provides suggestions for future works based on this overview.

Four appendices are also included in this document. Appendix A presents an additional description of the implementation of the epoxy within the model. Appendix B presents further validation results that were not added to the main text. Appendix C contains the routine used to optimize the lengths of the regenerator layers. Appendix D presents a description of the physical properties interpolation process and the property profiles of all materials used in this work.

2 Literature Review

This chapter presents a literature review of all areas relevant to the development of a first-order active magnetic regenerator. It starts with the thermodynamics of the magnetocaloric effect, a review of some of the most important magnetocaloric materials and an analysis of the operating and performance parameters of a regenerator. These are then combined in a section describing AMRs and the AMR cycle, with a focus on AMRs that use first-order phase transition materials, including the challenges inherent to these regenerators. Next, a review of AMR and magnetic circuit models is presented to analyse the integration of these systems. Lastly, the state-of-the-art of magnetic refrigerators prototypes is briefly discussed, leading to the specific objectives of this dissertation.

2.1 The Magnetocaloric Effect

The Magnetocaloric Effect (MCE) is the thermal response from a magnetic material when subjected to a changing magnetic field ($\vec{H}$). This response manifests itself as a variation of the material's entropy due to the coupling of the magnetic sublattice with the magnetic field (PECHARSKY; GSCHNEIDER, 1999). In order to describe this phenomenon, the entropy of a magnetic solid at constant pressure is described as the combined contributions of the magnetic, s_M, lattice, s_L and electronic, s_E, entropies (TISHIN, 1997; PECHARSKY; GSCHNEIDER, 1999), as follows:

$$s(T, \vec{H}) = s_M(T, \vec{H}) + s_L(T) + s_E(T) \tag{2.1}$$

As shown in Equation 2.1, the magnetic entropy is a function of the magnetic field and the absolute temperature, while the other two are only a function of the absolute temperature. Therefore, when the applied magnetic field is changed, the magnetic entropy will be affected and the material will show a thermal response, characterizing the MCE. This response will depend on the conditions under which the material is subjected to a magnetic field change, but the MCE can be fully described by the two thermodynamic processes shown in Figure 3.

In the first process, the change in magnetic field occurs isothermally, therefore both the lattice and electronic entropies remain constant, and the total entropy variation is equal to the magnetic entropy change:

$$\Delta s = \Delta s_M \tag{2.2}$$

Due to the isothermal conditions, the substance will experience a heat flow to the surroundings corresponding to the change in entropy. For most magnetocaloric materials, Δs is negative during magnetization and the substance will reject heat to its surroundings. Reversibly, the substance will absorb heat during demagnetization. The process of isothermal magnetization is illustrated by the vertical line in Figure 3, with the MCE being represented by the isothermal entropy change.

In the second process, the change in magnetic field occurs adiabatically, causing the total entropy to remain constant:

$$\Delta s = \Delta s_{\mathrm{M}} + \Delta s_{\mathrm{L}} + \Delta s_{\mathrm{E}} = 0 \tag{2.3}$$

Thus, the variation of magnetic entropy due to the changing field needs to be compensated by the lattice and electronic entropies:

$$\Delta s_{\mathrm{M}} = -\Delta s_{\mathrm{L}} - \Delta s_{\mathrm{E}} \tag{2.4}$$

During magnetization, this results in an increase of the lattice and electronic entropies, i.e., an increase in temperature. Reversibly, during demagnetization, the lattice and electronic entropies decrease and, consequently, the temperature also decreases. The process of adiabatic magnetization is illustrated by the horizontal line in Figure 3, and the MCE is represented by the adiabatic temperature change, ΔT_{ad} (TISHIN, 1997; PECHARSKY; GSCHNEIDER, 1999; SMITH et al., 2012; TREVIZOLI, 2015).

An important characteristic of the MCE, already mentioned above, is its reversibility in magnetocaloric materials (MCMs) exhibiting a continuous magnetic phase transition at the Curie temperature (NIELSEN, 2010). This reversibility has been experimentally shown by Trevizoli et al. (2012), who measured the temperature of a gadolinium sample submitted to successive magnetization and demagnetization steps, as shown in Figure 4. The temperature variation in both processes was virtually the same, with the solid returning to its original equilibrium temperature after the demagnetization.

2.1.1 *Thermodynamics of the MCE*

This section will focus in describing the thermodynamics of solid magnetocaloric materials, assuming conditions of constant pressure and volume. Under such conditions, the entropy is a function of temperature and magnetic field as follows:

$$ds = \left(\frac{\partial s}{\partial T}\right)_{\mathrm{H}} dT + \left(\frac{\partial s}{\partial H}\right)_{\mathrm{T}} dH \tag{2.5}$$

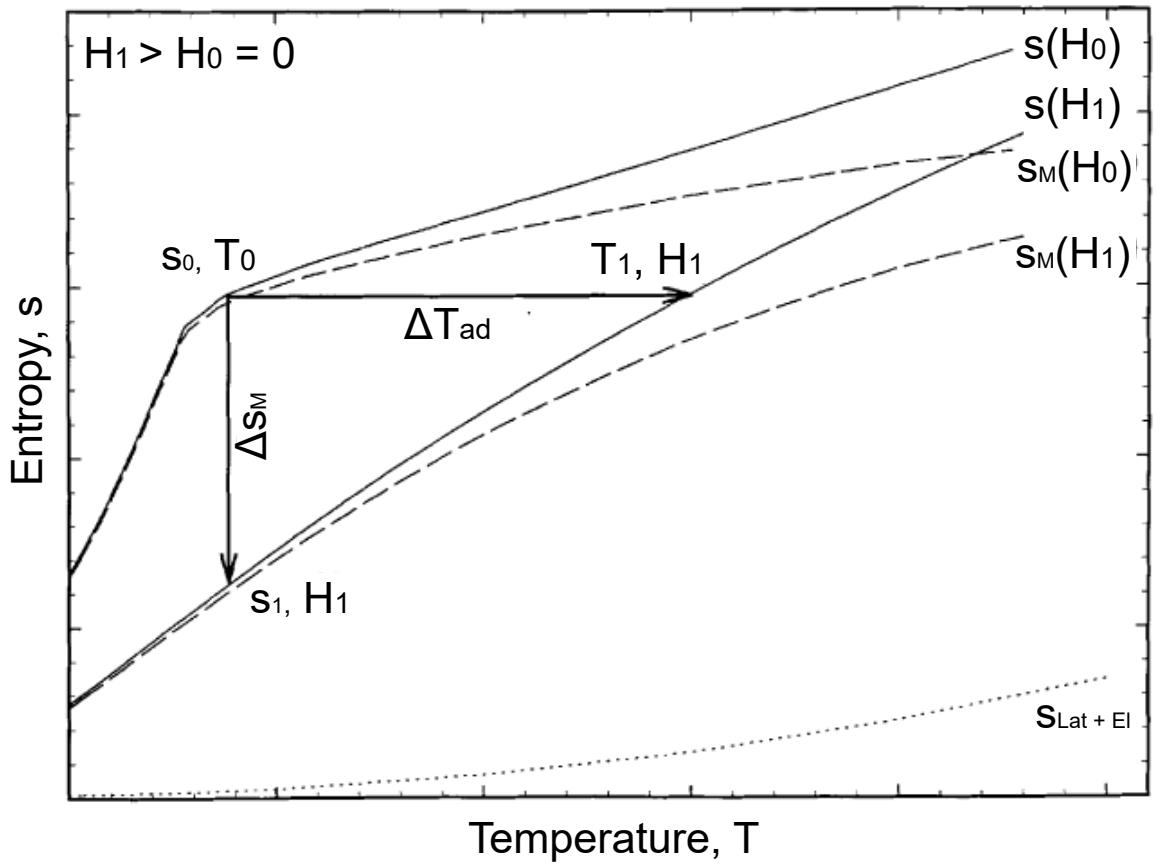

Figure 3 – $s - T$ diagram illustrating the adiabatic and isothermal magnetization processes. Adapted from Pecharsky & Gschneider (1999).

where the following Maxwell relation can be used to relate the entropy with the specific magnetization, σ:

$$\left(\frac{\partial s}{\partial H}\right)_{\mathrm{T}} = \mu_0 \left(\frac{\partial \sigma}{\partial T}\right)_{\mathrm{H}} \tag{2.6}$$

where μ_0 is the magnetic permeability of vacuum ($4\pi \times 10^{-7}$ N A^{-2}). Therefore, during isothermal magnetization (see vertical line in Figure 3), the specific entropy change, Δs, is given by:

$$\Delta s = \int_{H_0}^{H_1} \mu_0 \left(\frac{\partial \sigma(T,H)}{\partial T}\right)_{\mathrm{H}} dH \tag{2.7}$$

This expression allows the MCE to be determined using magnetization data as a function of temperature and magnetic field. Similarly, the isofield specific heat capacity (c_{H}), defined below, can also be used to determine the MCE.

$$\frac{c_{\mathrm{H}}}{T} = \left(\frac{\partial s}{\partial T}\right)_{\mathrm{H}} \tag{2.8}$$

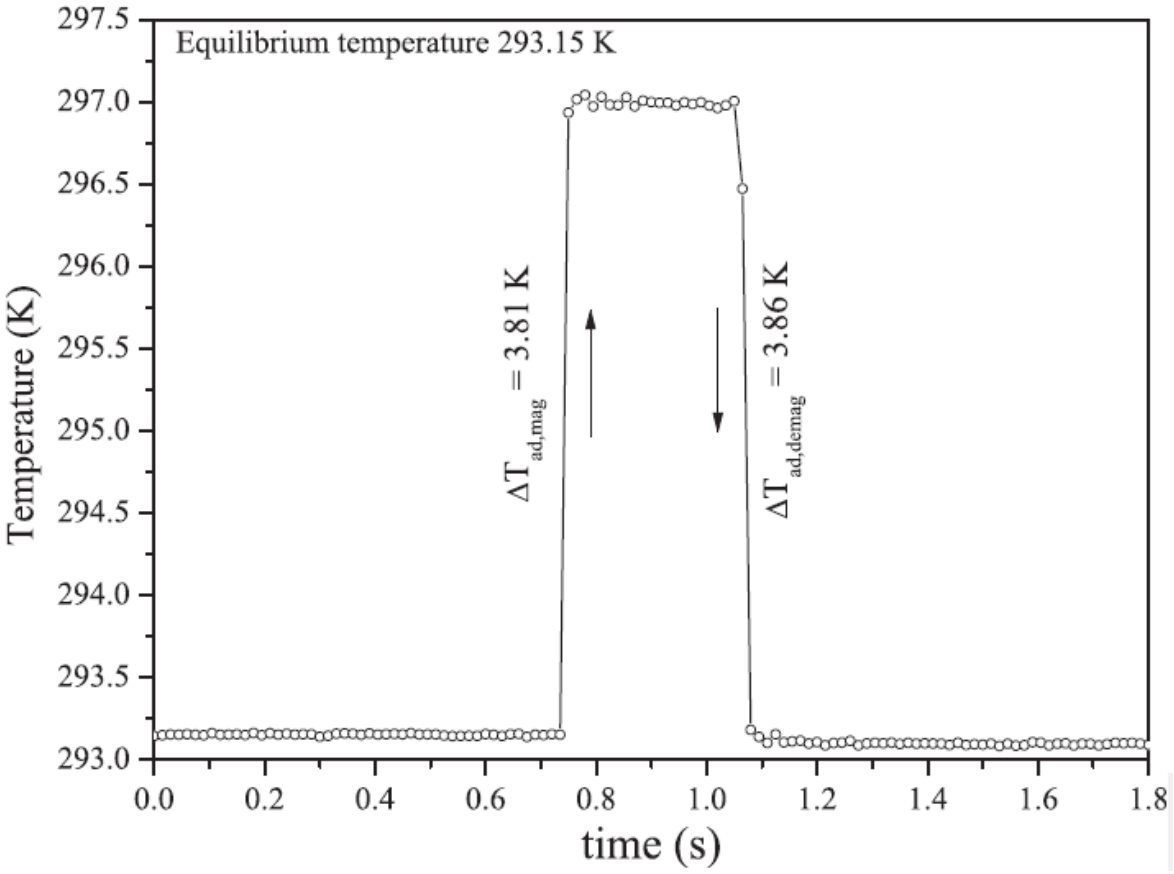

Figure 4 – Experimental results for the reversibility of the magnetocaloric effect. Adapted from Trevizoli et al. (2012).

To achieve this, Equation 2.8 can be integrated, resulting in the following expression for Δs:

$$\Delta s = \int_0^T \frac{c_{\mathrm{H}}(T, H_1) - c_{\mathrm{H}}(T, H_0)}{T} dT \tag{2.9}$$

allowing for the MCE to also be determined using isofield specific heat capacity data as a function of temperature and magnetic field. However, specific heat capacity data near 0 K is particularly hard to obtain and thus Equation 2.9 is usually limited to theoretical analysis.

For an adiabatic magnetization process (see horizontal line in Figure 3), Equation 2.5 becomes:

$$\left(\frac{\partial s}{\partial T}\right)_{\mathrm{H}} dT = -\left(\frac{\partial s}{\partial H}\right)_{\mathrm{T}} dH \tag{2.10}$$

which, after applying Equations 2.6 and 2.8 results in:

$$dT = -\mu_0 \frac{T}{c_{\mathrm{H}}} \left(\frac{\partial \sigma}{\partial T}\right)_{\mathrm{H}} dH \tag{2.11}$$

Equation 2.11 can then be integrated to determine the adiabatic temperature change, ΔT_{ad}, for a magnetization process:

$$\Delta T_{ad}(T; H_1, H_0) = -\mu_0 \int_{H_0}^{H_1} \frac{T}{c_H(T,H)} \left(\frac{\partial \sigma(T,H)}{\partial T}\right)_H dH \tag{2.12}$$

Note that, while these results were obtained considering a magnetization process ($H_1 > H_0$), they are also valid for a demagnetization process ($H_1 < H_0$).

The above results show that the MCE depends on both the temperature and the intensity of the magnetic field variation. This results in a peak value for the MCE around the temperature where the absolute value of $\left(\frac{\partial \sigma}{\partial T}\right)_H$ reaches a maximum. This peak occurs around the temperature where the material transitions from the ferromagnetic to the paramagnetic state, called the Curie temperature (SMITH et al., 2012; KITANOVSKI et al., 2015). The value of this temperature and the material's behaviour during this transition is very important to determine if and how it can be used in a magnetic refrigeration system.

2.2 Magnetocaloric Materials

The MCE is present in all magnetic materials, differing between them mostly in magnitude and in the value of the Curie temperature, as shown in Figure 5. This section will focus only on materials which are considered promising in the field of magnetic refrigeration at near room temperature. These materials present most or all of the following characteristics (GSCHNEIDNER; PECHARSKY, 2008; KITANOVSKI et al., 2015; TREVIZOLI, 2015):

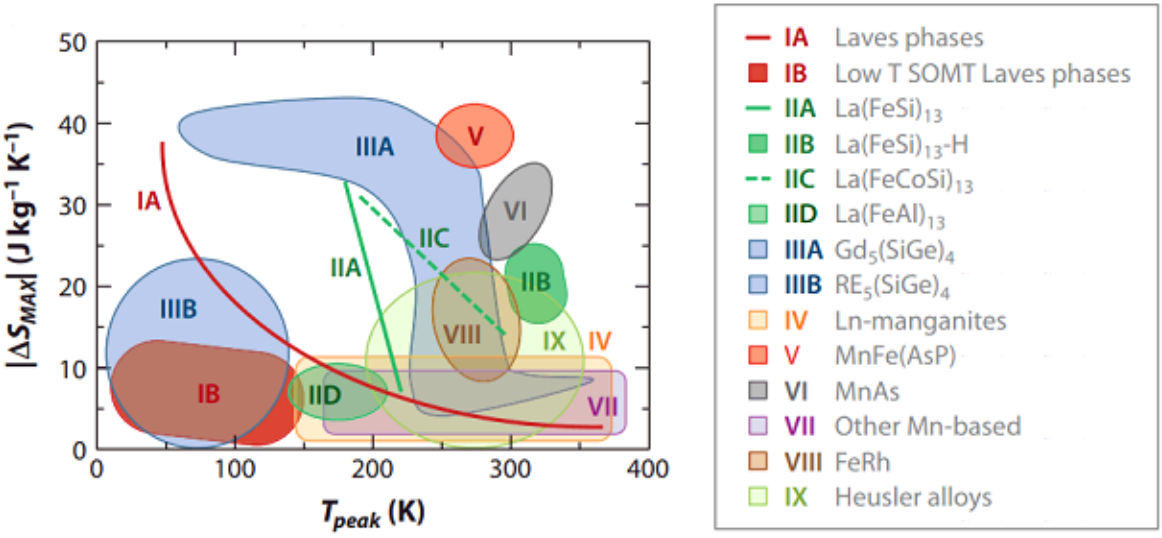

Figure 5 – Maximum entropy change for a magnetic flux density variation from 0 to 5 T as a function of the peak temperature for different magnetocaloric materials. Adapted from Franco et al. (2012).

- Suitable Curie temperature, ensuring the MCE occurs in the desired temperature range (in this case, near room temperature);
- Large magnetocaloric effect in order to be applicable for near room temperature refrigeration, which requires an adiabatic temperature change of at least 2 K/T (ROWE et al., 2005);
- Small thermal and magnetic hysteresis, whose presence results in energy loss and therefore an increase in the input work of the cycle;
- Chemical stability, to avoid corrosion;
- High thermal conductivity, increasing the regenerator's effectiveness;
- Large electrical resistance, avoiding eddy currents;
- Good manufacturing properties;
- Low cost.

Furthermore, magnetocaloric materials are also classified according to their magnetic phase transition: second-order materials exhibit a continuous magnetic phase transition, characterized by a continuous variation of the intrinsic spontaneous magnetization. First-order materials exhibit a discontinuous phase transition, in which the magnetization discontinuously changes at a given temperature and a latent heat associated with the phase transition is present. However, in real first-order materials, impurities and spatial variations spread out the transition, making it more continuous (SMITH et al., 2012; BEZ, 2016). The behaviour of the magnetization for both types of phase transitions is schematically shown in Figure 6.

As shown by Equations 2.7 and 2.11, the intensity of the magnetocaloric effect is proportional to the absolute value of the magnetization derivative. Therefore, an analysis of Figure 6 shows that second-order materials are expected to have a smaller MCE (smaller absolute derivative) within a relatively large temperature range. Conversely, first-order materials have a larger MCE (larger absolute derivative) within a considerably smaller temperature range. An example of this difference is shown in the experimental results of isothermal entropy variation obtained by Lei et al. (2015) for Gd (second-order) and $La(Fe,Mn,Si)_{13}H_y$ (first-order), shown in Figure 7.

While there are many different MCMs which could be, in theory, exploited in magnetic cooling at near room temperature, this dissertation will only describe gadolinium and its alloys (second-order) and La-Fe-Si based MCMs (first-order), with the latter being the main focus and proposed material of the regenerator being designed here.

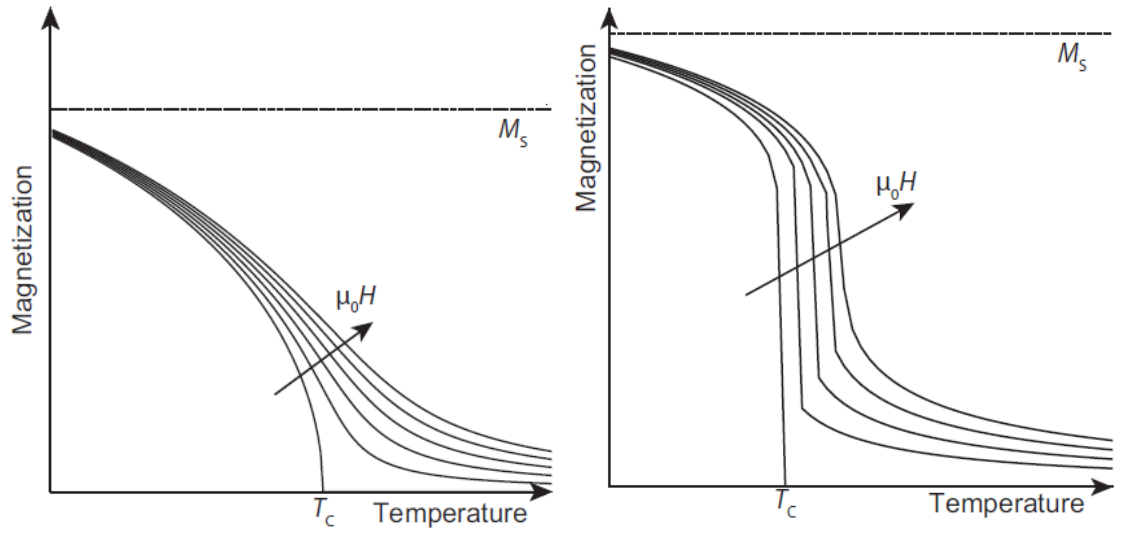

Figure 6 – Magnetization as a function of temperature for (a) second and (b) first-order phase transitions. Adapted from Bez (2016).

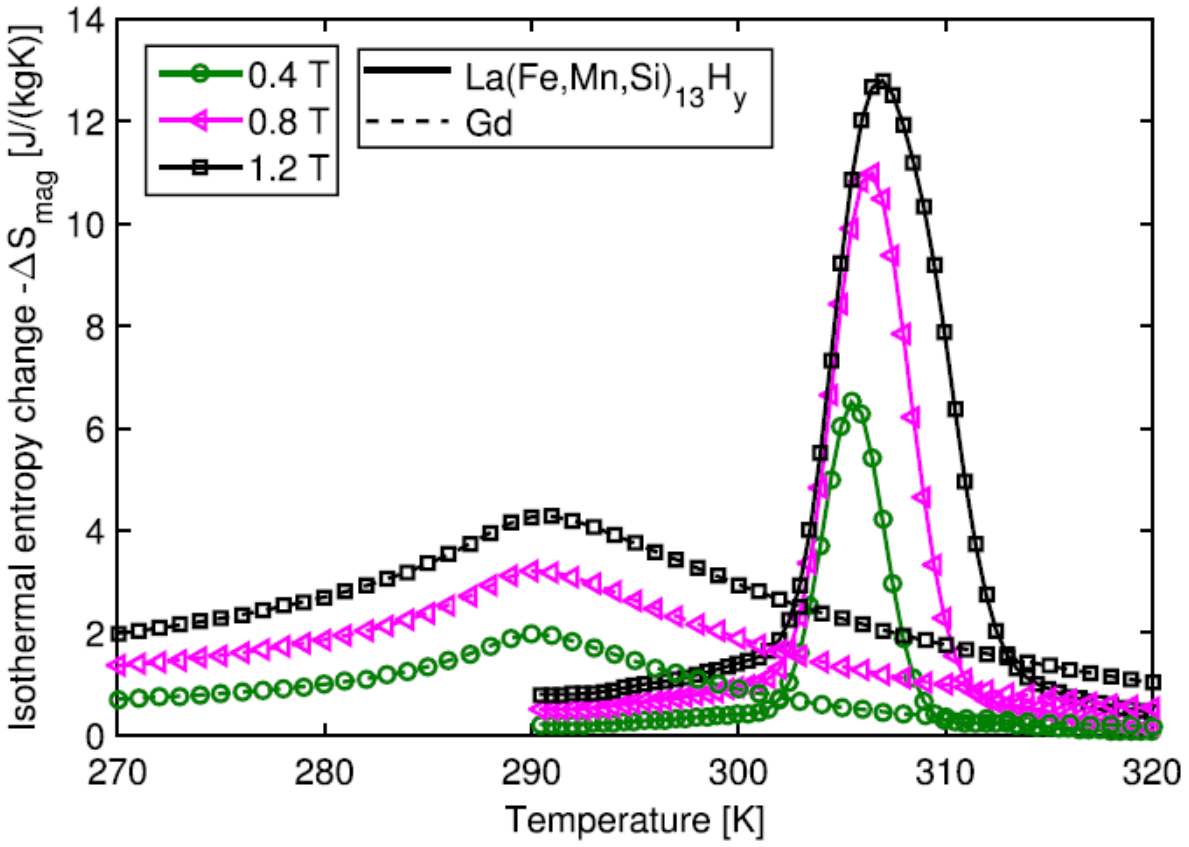

Figure 7 – Isothermal entropy change in Gd (second-order) and La(Fe,Mn,Si)$_{13}$H$_y$ (first-order). Adapted from Lei et al. (2015).

2.2.1 Gadolinium Alloys

Gadolinium (Gd) and its alloys are the most common materials for near room temperature magnetic refrigeration and, therefore, the most relevant second-order MCMs. Gd is the only pure element with a near room temperature Curie point (approximately 293 K) and good magnetocaloric properties (ΔT_{ad} = 3.3 K and Δs_M = 3.1 J kg^{-1} K^{-1} for a magnetic field change of 1 T) (BJøRK; BAHL; KATTER, 2010; KITANOVSKI et al., 2015). As a result, it is usually the reference material of the area, and many magnetic refrigeration devices and prototypes have been developed using gadolinium, as will be shown in Section 2.6.

Gadolinium can also be alloyed with different elements to obtain positive effects. For example, the Curie temperature can be reduced without affecting the magnetocaloric effect by alloying Gd with manganese (Mn), with the resulting Curie temperature depending on the ratio between these elements. Alloying gadolinium with other rare-earth elements, such as Tb, Dy, Ho and Er, can also shift the Curie temperature to lower values (ENGELBRECHT, 2008; JAYARAMAN; BOONE; SHIELD, 2011; JAYARAMAN; BOONE; SHIELD, 2013; KITANOVSKI et al., 2015; BEZ, 2016).

There also are Gd alloys with first-order phase transitions, such as the Gd-Si-Ge alloys, which present the so-called giant magnetocaloric effect. This effect was discovered by Pecharsky & Gschneider (1997) in $Gd_5Si_2Ge_2$ and was characterized by adiabatic temperature changes up to 30% higher than the peak value of gadolinium. However, these materials also presented high thermal and magnetic hysteresis, which are detrimental to the efficiency of the magnetic refrigeration system (KITANOVSKI et al., 2015).

Regular, second-order gadolinium alloys, however, present low or zero hysteresis, can be relatively easily manufactured in different shapes and forms, and present most of the desired characteristics of a magnetocaloric material described above. Their main drawback is their high price, which limits application. Hence, larger devices, which would require more material, may become prohibitively expensive if designed using gadolinium (KITANOVSKI et al., 2015; BEZ, 2016).

2.2.2 La-Fe-Si Alloys

La-Fe-Si alloys are one of the most important first-order materials for magnetic refrigeration at near room temperature and are considered one of the possible alternatives to Gd alloys. These materials are based in a hypothetical compound $LaFe_{13}$, which does not exist, but stable compounds can be made by substituting part of the Fe by Si or Al. The Curie temperature of these alloys can be tuned by adding H to their structures or by substituting Fe with Al, Co or Mn. This gives La-Fe-Si alloys a great potential to be used in layered regenerators, which will be discussed in Section 2.4.2 (BJøRK; BAHL; KATTER, 2010; KITANOVSKI et al., 2015; BEZ, 2016).

Due to their first-order phase transition, La-Fe-Si alloys reach higher MCE peaks than Gd alloys, with Basso et al. (2015) obtaining Δs_M values of around 9 J kg^{-1} K^{-1} for a magnetic field change of 1 T and Lei et al. (2015) obtaining a Δs_M of around 11 J kg^{-1} K^{-1} for a magnetic field change of 0.8 T. The main advantages of these alloys are their low cost compared to Gd (with La being one of the cheapest rare-earth elements), availability, and capacity to be produced in large-scale industrial quantities (APREA et al., 2015; BASSO et al., 2015; KITANOVSKI et al., 2015; BEZ, 2016).

Basso et al. (2015) also showed that the addition of Mn to the La-Fe-Si alloys considerably reduced the thermal and magnetic hysteresis, one of the main problems with first-order materials. This, however, reduced the refrigerating effect of the material, requiring a compromise between hysteresis and MCE, which was proposed to be at values of hysteresis smaller than 1 K. It also changed the Curie temperature of the material, which is a factor to be dealt with during manufacturing. The effect of adding Mn to a La-Fe-Si alloy is shown in Figure 8, with the number above each plot relating to the value of y in $LaFe_xMn_ySi_z$-$H_{1.65}$ ($x + y + z = 13$).

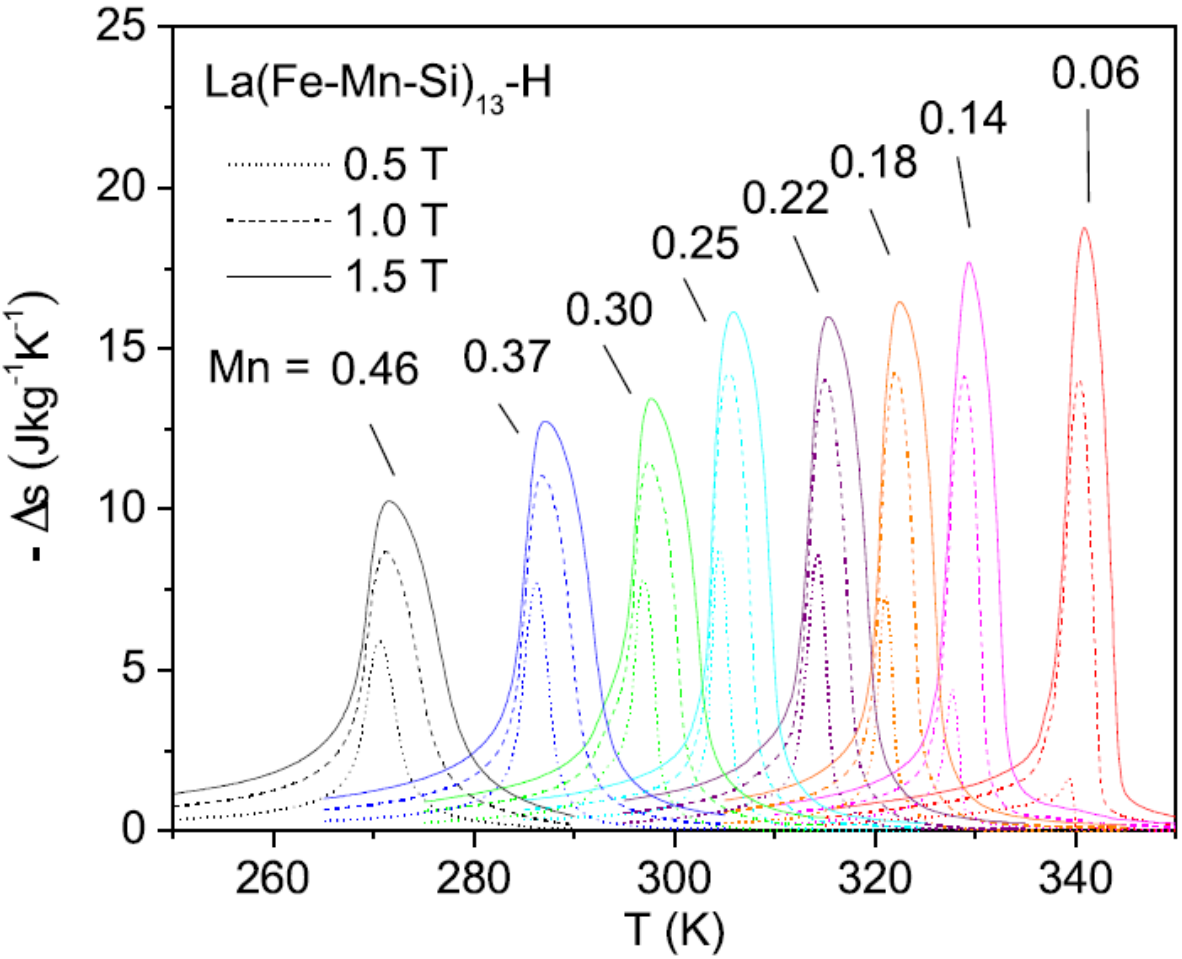

Figure 8 – Isothermal entropy change in La-Fe-Si alloys with different Mn contents. The number above each plot represents the value of y in $LaFe_xMn_ySi_z$-$H_{1.65}$ ($x + y + z = 13$). Adapted from Basso et al. (2015).

Another limitation of La-Fe-Si alloys is their relatively low mechanical integrity, which causes them to break easily if submitted to the stresses caused by the alternating fluid flow of an AMR cycle (see Section 2.4.1). This limitation can be reduced by the use of treatments such as thermally induced decomposition and recombination (TDR), which increases the amount of α-Fe in the alloy, increasing its mechanical integrity. This, however, reduces the MCE of the material, since the α-Fe in the alloy does not undergo magnetic phase transitions during operation, requiring another compromise when designing the material (ZHUKOV, 2016).

2.3 Thermal Regenerators

Regenerators or regenerative heat exchangers are storage type heat exchangers in which the flow channels are alternatively occupied by hot and cold fluid flows, resulting in intermittent heat transfer between the solid and the fluid. In other words, the heat exchange between the hot fluid and cold fluid does not occur directly, but indirectly through the solid matrix. The cycle of a regenerator can be divided in two parts: the hot blow, which is the period where the high temperature fluid flows through the matrix rejecting heat to the solid phase, and the cold blow, which is the period where the low temperature fluid flows through the matrix absorbing heat from the solid phase (KUPPAN, 2000; NELLIS; KLEIN, 2009; TREVIZOLI, 2015; LOZANO, 2015).

Because of the transient nature of a regenerator's operation, the temperature, pressure and properties of both phases are time and space dependent. However, a condition of cyclic equilibrium is reached after a number of cycles in which the variations of temperature with time are the same during successive cycles for both phases (NELLIS; KLEIN, 2009).

There are two basic types of regenerator: the stationary regenerator and the rotary regenerator. The stationary regenerator, as the name suggests, has a fixed bed in which the hot and cold fluids alternately flow through, resulting in the hot and cold blows. This kind of regenerator requires valves to properly direct the fluid flows during operation, resulting in greater complexity and cost. However, it has the advantage of making the matrix materials easier to remove, clean and replace (KUPPAN, 2000; LOZANO, 2015). A rotary regenerator, on the other hand, has the fluids flowing continuously in one direction while the regenerator itself rotates (NELLIS; KLEIN, 2009). These regenerators do not require a valve system to direct the flows, but do require additional work input to rotate the matrix (SHAH; SEKULIĊ, 2003). A schematic representation of both types of regenerator is shown in Figure 9.

Due to their general operating conditions, a few characteristics are considered desirable in a regenerator (KUPPAN, 2000; NELLIS; KLEIN, 2009; TREVIZOLI, 2015):

- Compactness;

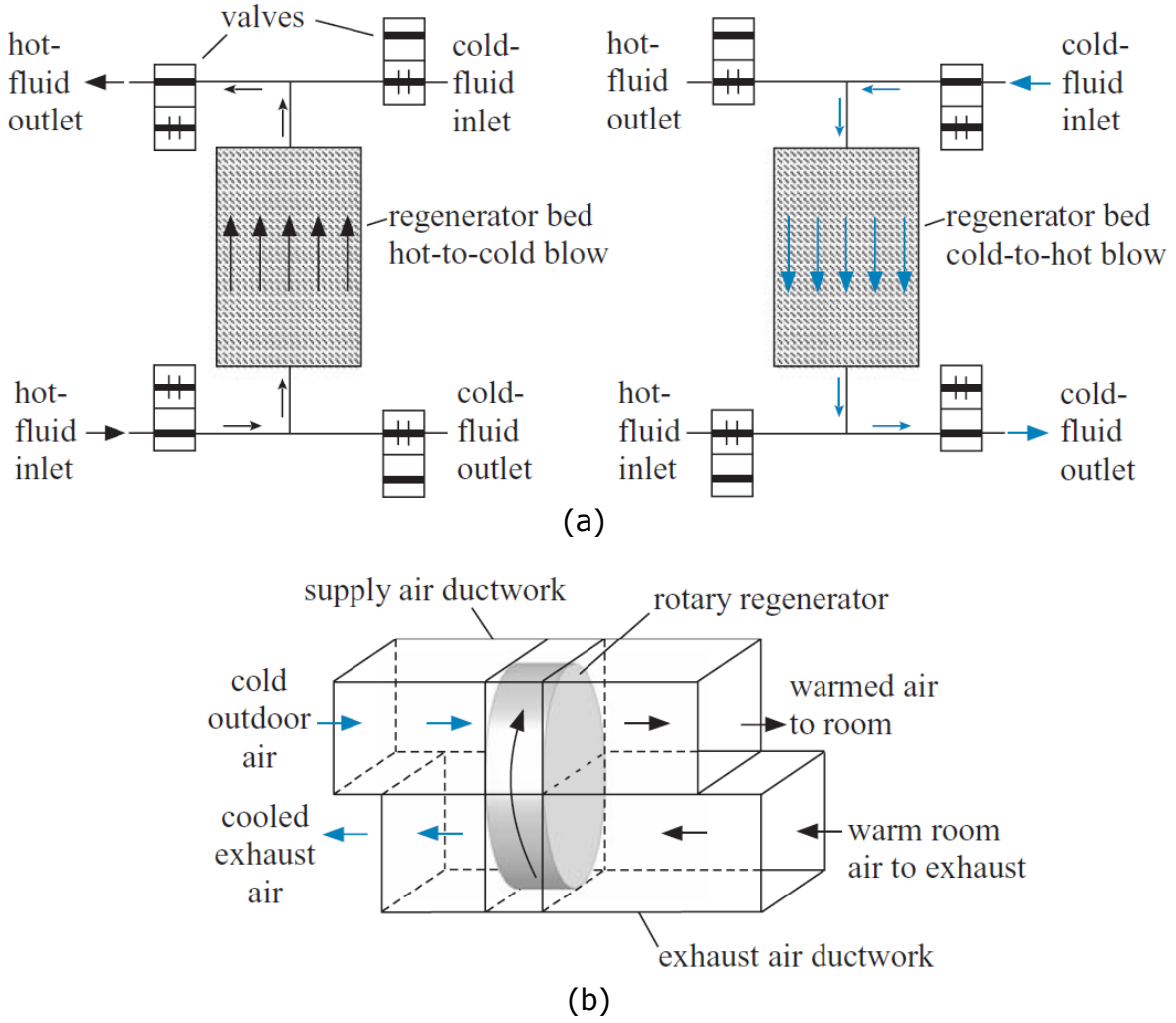

Figure 9 – Schematic representation of (a) stationary and (b) rotary regenerators. Adapted from Nellis & Klein (2009)

- A highly permeable and non-obstructed porous medium;
- High axial thermal resistance, minimizing axial heat conduction;
- Large heat transfer rate, achieved thorough a high heat transfer area per unit of volume and/or through a high interstitial heat transfer coefficient;
- Large thermal capacity.

2.3.1 *Regenerator Operating and Performance Parameters*

The usual parameters analysed when designing a regenerator are (SCHMIDT; WILMOOT, 1981; HAUSEN, 1983):

- Cold and hot flows inlet temperatures, T_C and T_H;
- Overall thermal conductance, UA;

- Operating frequency;
- Thermal capacity of the matrix, mc_s;
- Thermal capacity rates of the fluid in both blows, $\dot{m}c_{p,C}$ and $\dot{m}c_{p,H}$.

These parameters will directly influence the outlet temperature of the fluid during each blow, which can be used to evaluate the performance of a regenerator. However, it is often more convenient to analyze the performance of regenerators in terms of non-dimensional parameters (SCHMIDT; WILMOOT, 1981; HAUSEN, 1983; TREVIZOLI, 2015). The first of these parameters is the thermal effectiveness, ϵ, which is defined as the ratio between the real heat transfer between the fluid and the matrix during one of the blows and the maximum (ideal) heat transfer:

$$\epsilon = \frac{\dot{Q}_{\text{blow}}}{\dot{Q}_{\text{max}}} \tag{2.13}$$

which,for the cold blow, can be written as:

$$\epsilon_{\text{CB}} = \frac{\dot{m}c_{\text{p,C}}(\overline{T}_{\text{H,out}} - T_{\text{C,in}})}{(\dot{m}c_{\text{p}})_{\text{min}}(T_{\text{H,in}} - T_{\text{C,in}})} \tag{2.14}$$

and, for the hot blow:

$$\epsilon_{\text{HB}} = \frac{\dot{m}c_{\text{p,H}}(T_{\text{H,in}} - \overline{T}_{\text{C,out}})}{(\dot{m}c_{\text{p}})_{\text{min}}(T_{\text{H,in}} - T_{\text{C,in}})} \tag{2.15}$$

However, under balanced flow conditions, which means identical thermal capacity rates in both blows, these expressions can be simplified to:

$$\epsilon_{\text{CB}} = \frac{\overline{T}_{\text{H,out}} - T_{\text{C,in}}}{T_{\text{H,in}} - T_{\text{C,in}}} \tag{2.16}$$

$$\epsilon_{\text{HB}} = \frac{T_{\text{H,in}} - \overline{T}_{\text{C,out}}}{T_{\text{H,in}} - T_{\text{C,in}}} \tag{2.17}$$

A counterflow arrangement is preferred in regenerators since it yields a higher thermal effectiveness than any other configuration. Equations 2.16 and 2.17 show that the effectiveness can be directly calculated by measuring the average temperature at the outlet during each blow, however, the effectiveness relationship can be cast using two other non-dimensional parameters, the utilization factor (ϕ) and the number of transfer units (NTU) (NELLIS; KLEIN, 2009; LOZANO, 2015; TREVIZOLI et al., 2016).

The utilization factor (or simply utilization) is the ratio between the thermal capacity of the fluid phase during a given blow and the thermal capacity of the solid matrix:

$$\phi = \frac{\dot{m}c_{\text{p}}\tau}{mc_{\text{s}}} \tag{2.18}$$

where τ is the blow time period. As mentioned in the beginning of the section, the regenerator solid matrix must have a large thermal capacity in order to store the energy of the fluid without altering its temperature substantially (NELLIS; KLEIN, 2009).

The number of transfer units, which is equivalent to the thermal size of the heat exchanger, is given by (NELLIS; KLEIN, 2009; TREVIZOLI, 2015; LOZANO, 2015):

$$NTU = \frac{\bar{h} A_{\mathrm{HT}}}{\dot{m} c_{\mathrm{p}}} \tag{2.19}$$

Increasing the value of NTU will increase the effectiveness, which will result in an increase of the overall efficiency of the thermodynamic system in which the regenerator operates.

Figure 10 shows the effectiveness as a function of NTU and utilization for a balanced, symmetric regenerator. These results are based on the solution of the energy equations for the solid and fluid media in an ideal regenerator (DRAGUTINOVIC; BACLIC, 1998). Only regenerators with an utilization smaller than 1 can reach 100% effectiveness, and this limit is reached at smaller values of NTU for smaller utilizations. Regenerators with utilizations larger than 1 (thermal capacity of the blow exceeds that of the matrix) cannot reach 100% effectiveness, but the maximum value of effectiveness is reached at smaller NTUs for larger utilizations (ACKERMAN, 1997; NELLIS; KLEIN, 2009).

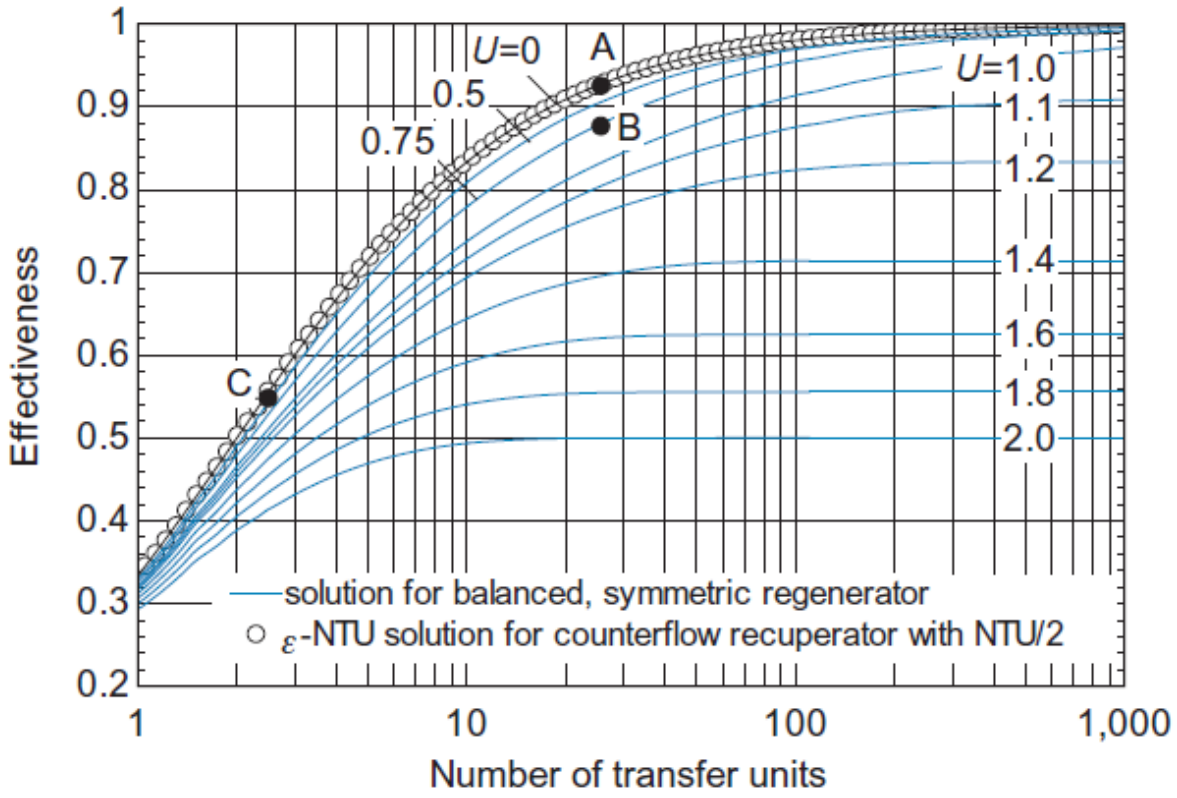

Figure 10 – Effectiveness of a balanced, symmetric regenerator as a function of NTU and ϕ. Adapted from Nellis & Klein (2009).

These results are useful to determine the influence of certain operating parameters on the regenerator performance, however, when designing a real regenerator, non-ideal effects and losses have to be incorporated. For magnetic refrigeration applications, the following phenomena need to be considered when designing a regenerator (TREVIZOLI, 2015):

- Axial heat conduction in the fluid and solid phases;
- Non-negligible thermal capacity of the fluid phase to deal with regenerators that use aqueous solutions;
- Viscous dissipation, which can be considerably significant in regenerators with low porosity and high mass flow rates;
- Use of effective properties of the porous medium, such as dispersion, as a function of the flow regime;
- Variable thermophysical properties of the solid and fluid phases with respect to temperature, pressure and magnetic field.

2.4 Active Magnetic Regenerators (AMRs)

A regenerator can also be classified as an active or passive regenerator. Passive regenerators function only as a storage media of the energy associated with the temperature differences between the blows. In this case, the temperature difference is not generated by the regenerator, but by other components of the system. Passive regenerators are widely applied in thermodynamic systems, with applications including power plants, cryogenic separation processes, noncatalytic chemical reactors and refrigerators (KUPPAN, 2000).

Active regenerators, on the other hand, have a solid matrix that directly generates a temperature difference, acting as an energy storage, heat sink and heat source at the same time. Perhaps the most common type of active regenerator is the *active magnetic regenerator*, which is the main focus of this work and an integral part of magnetic refrigerators. The regenerative beds of these regenerators are made of a magnetocaloric material, which is exposed to magnetic field variations while fluid flows through the matrix, creating a temperature difference. Despite the usually small values of MCE currently obtainable for relatively low magnetic field variations, thermal regeneration allows for larger temperature spans and cooling capacities to be obtained (LOZANO, 2015; TREVIZOLI, 2015).

2.4.1 AMR Cycle

Magnetic refrigerators can be based on many idealized thermodynamic cycles, such as the Ericsson, Brayton and Carnot cycles. Among these, the Brayton cycle is the basis of the AMR cycle and the most used in practical applications of magnetic refrigeration. The idealized thermo-magnetic Brayton cycle is composed of two isofield and two isentropic processes, as follows (ROWE et al., 2005; YU et al., 2010; KITANOVSKI et al., 2014; KITANOVSKI et al., 2015; LOZANO, 2015; TREVIZOLI, 2015):

1. **Adiabatic magnetization**: the magnetic field applied to the regenerative matrix is increased adiabatically, therefore, the entropy of the material remains constant. This results in an increase of the temperature of the solid, as described in Section 2.1.

2. **Isofield cold blow**: after the adiabatic magnetization, fluid from the cold reservoir flows through the matrix, absorbing heat from the solid phase and cooling it. The fluid then exits the matrix and rejects heat to the hot reservoir.

3. **Adiabatic demagnetization**: the magnetic field applied to the regenerative matrix is decreased adiabatically, which reduces the temperature of the solid phase.

4. **Isofield hot blow**: fluid from the hot reservoir flows through the matrix, rejecting heat to the solid phase and heating it. The fluid then exits the matrix and absorbs heat from the cold reservoir.

Figure 11 shows a schematic representation of each step of the Brayton cycle, the temperature profile along the regenerator after each step of the cycle and the *T-s* diagram of the ideal Brayton cycle. Each volume of magnetocaloric material in the matrix experiences a specific Brayton cycle, which has a temperature difference corresponding to the ΔT_{ad} of the material at the local temperature and magnetic field. In a regenerator, these are combined and result in one single extending Brayton cycle between a larger temperature span, as shown in Figure 11.

The efficiency of the cooling system depends on both the intensity of the MCE and the effectiveness of the matrix. The intensity of the MCE in the cycle depends on the properties of the magnetocaloric material, the initial magnetic field and the final magnetic field. This is so because, for second-order materials, the MCM increases with increasing field to a power n which is close to $\frac{2}{3}$. For first-order materials the increase with field is also sublinear. Therefore, the MCM is not just a function of the field variation and ensuring a small initial field can be more important than increasing the final field. The effectiveness of the regenerator, in turn, depends on the thermophysical properties of the matrix, its thermal capacity, porosity and operating parameters (ROWE et al., 2005; NIELSEN et al., 2012; SMITH et al., 2012; TREVIZOLI, 2015).

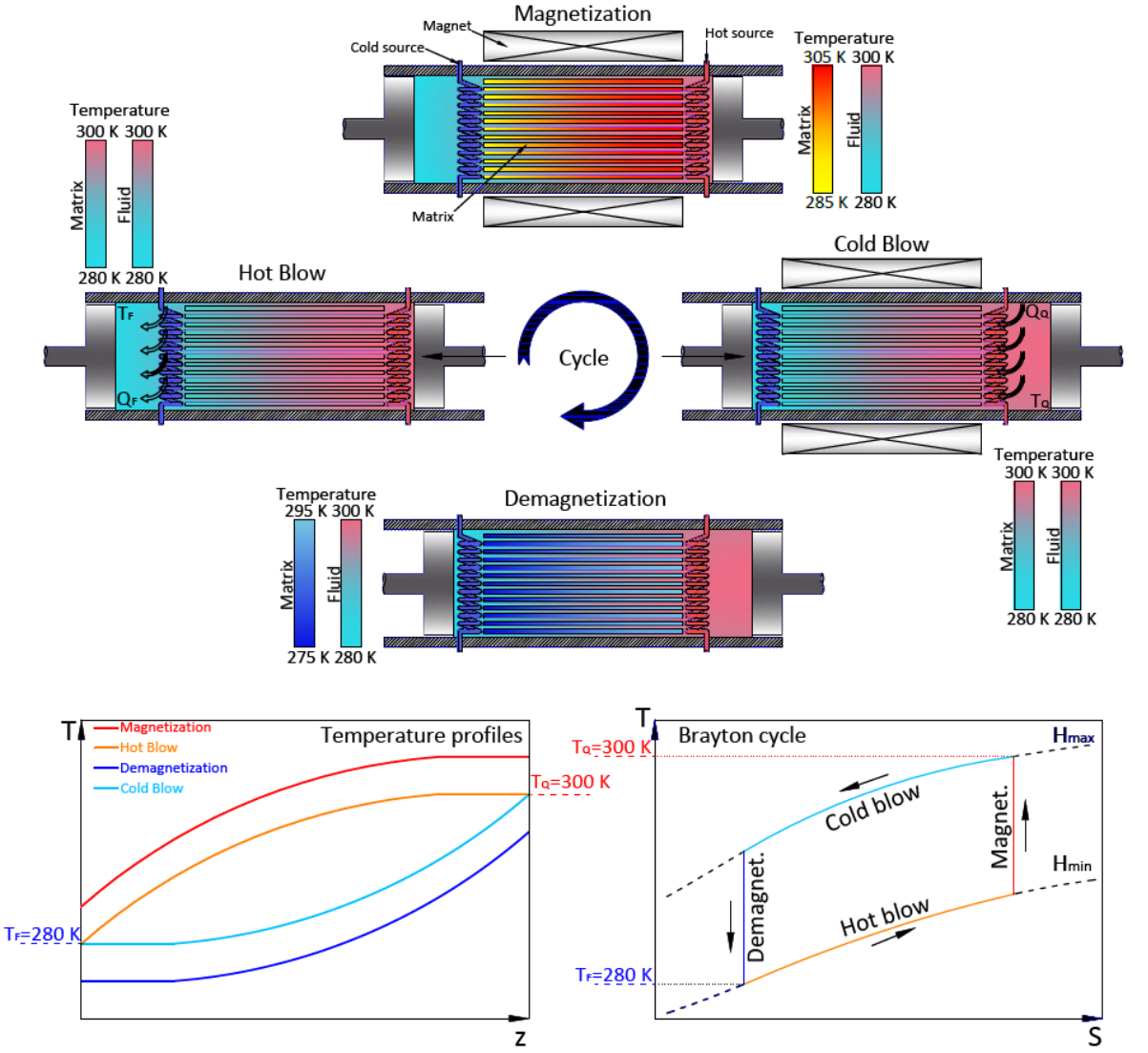

Figure 11 – Representation of the four steps that compose the Brayton cycle. The left plot shows the temperature profile along the regenerator after each of the steps and the plot on the right show the *T*-*s* diagram of an ideal Brayton cycle. Adapted from Barbosa Jr., Lozano & Trevizoli (2014)

2.4.2 *La-Fe-Si Based Regenerators*

La-Fe-Si alloys have several important aspects that must be considered when being applied to a regenerator. The first one is their first-order phase transition. As already stated, although this transition has a considerably high MCE, it is limited to a very narrow temperature range. Therefore, a regenerator made with a single type of material would not be able to operate over a large temperature span. The solution to this problem is the use of layered (graded) regenerators, i.e. regenerators whose composition varies spatially along their length, such that the Curie temperature profile follows the local average temperature during operation. These layers guarantee that most of the material will be active during operation, as shown in Figure 12. La-Fe-Si

MCMs are especially advantageous regarding their use in layered AMRs because their Curie temperature can be tuned in a temperature range from 200 to 340 K using the methods described in Section 2.2.2 (SMITH et al., 2012; TREVIZOLI, 2015; LEI et al., 2015; KITANOVSKI et al., 2015; NAVICKAITĖ et al., 2018).

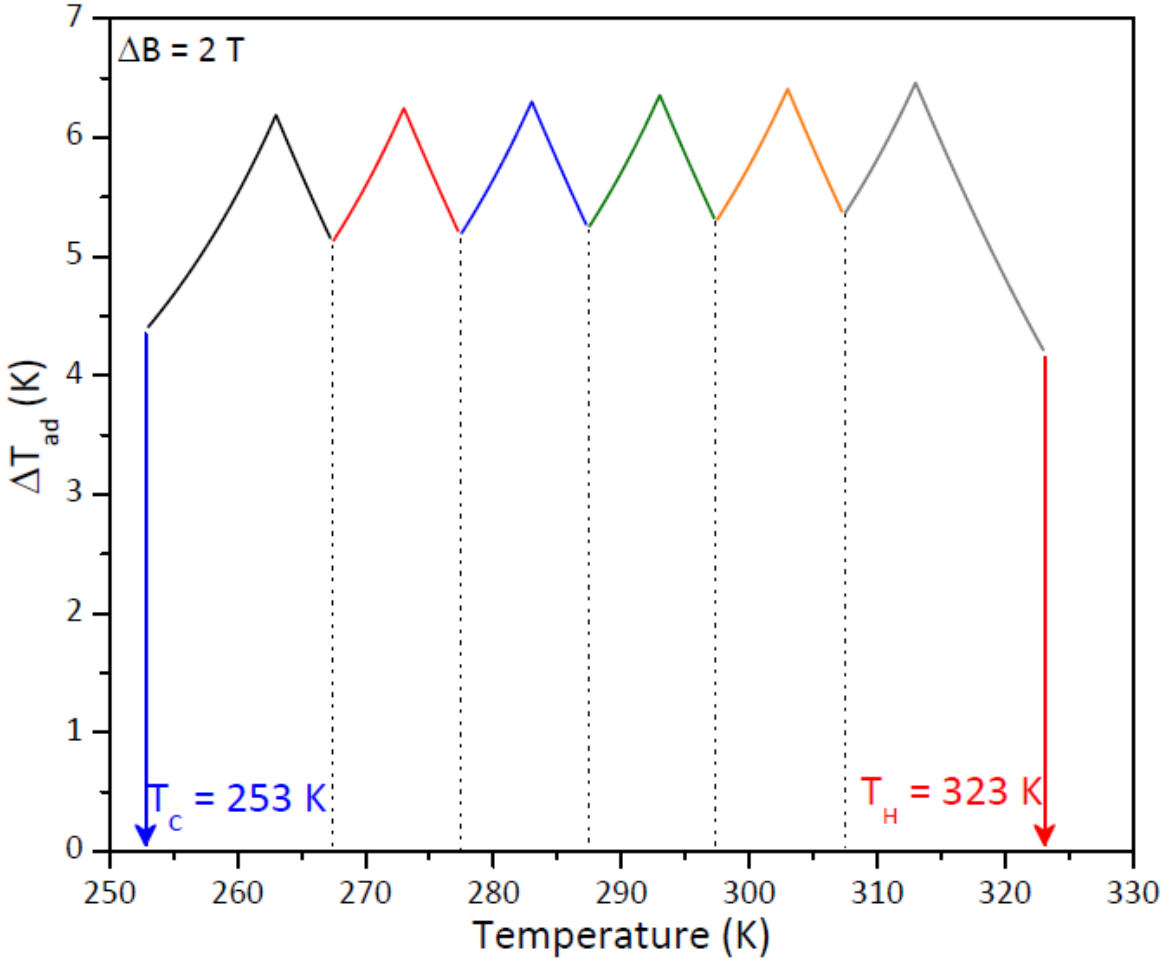

Figure 12 – Magnetocaloric effect along a hypothetical multi-layered regenerator. Adapted from Trevizoli (2015).

Two parameters need to be determined when designing a layered regerenerator: the number of layers and the values of the Curie temperatures. Theoretically, the regenerator cooling capacity continuously increases as more layers are added, tending to an ideal regenerator with an infinite number of layers, each with a Curie temperature equal to the local time average temperature of its position. In practice, increasing the number of layers is expensive and may not be worth the increase in cooling capacity. Lei et al. (2015) modelled a multi-layered La-Fe-Si based regenerator with a temperature span of 30 K and tested it with different numbers of layers, as shown in Figure 13. The Curie temperature of the last layer was kept constant at 305 K, and the Curie temperature of the other layers decreased with fixed steps matching the number of layers with the span of 30 K. These results show that while increasing the number

of layers does increase the cooling capacity, after a certain value this trend becomes almost unnoticeable, making increasing the number of layers less interesting. The ideal number will depend on many factors, including the operating conditions of the cooling system and the cost of the regenerator.

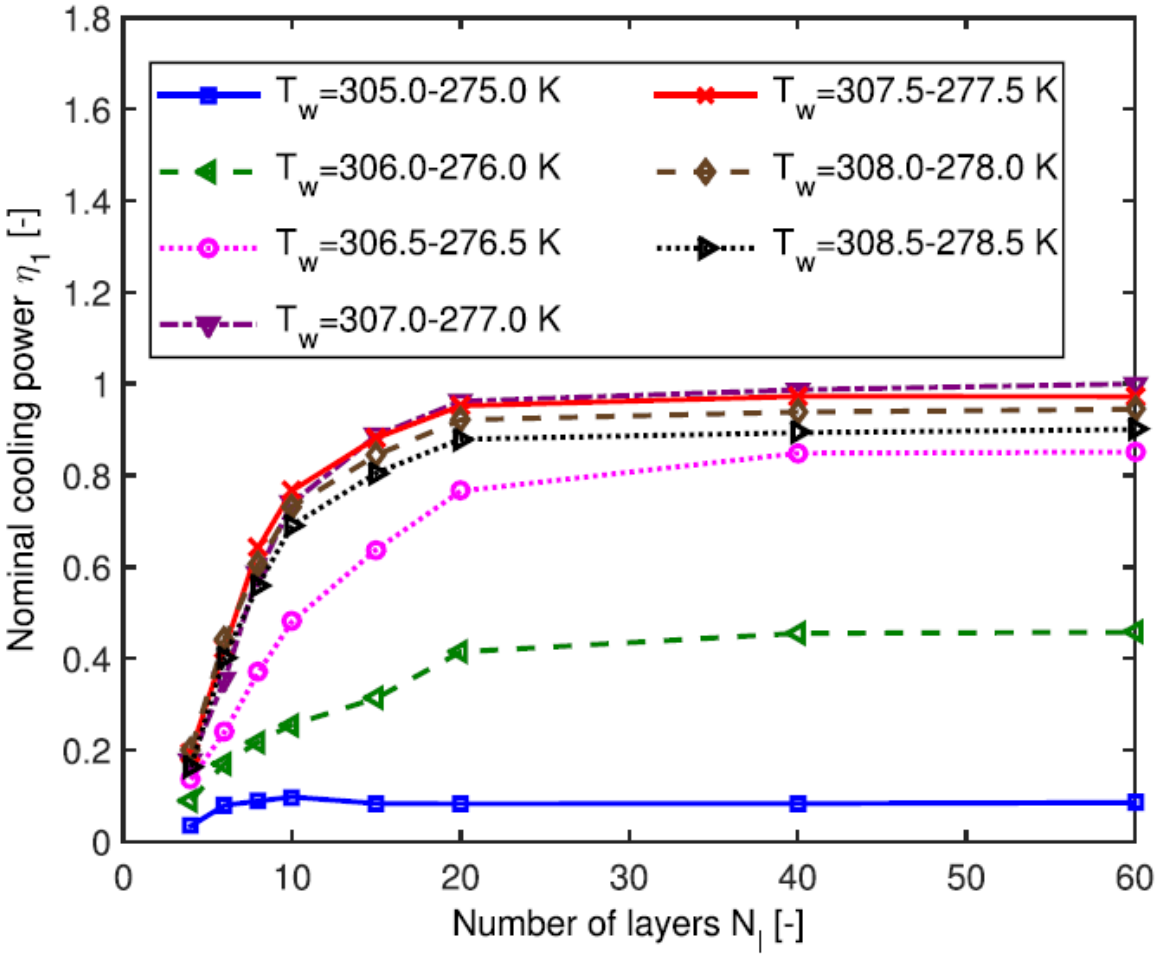

Figure 13 – Effect of the number of layers and hot reservoir temperature in a La-Fe-Si regenerator cooling capacity. Adapted from Lei et al. (2015).

Another important result shown in Figure 13 is the influence of the hot and cold reservoirs temperatures on the cooling capacity. At first glance, one would expect that these temperatures should match the highest and lowest Curie temperatures in the regenerator in order to achieve the highest cooling power, however, the results show that the maximum cooling power is obtained with a hot reservoir temperature 2 K higher than the highest Curie temperature (and consequently a cold source temperature 2 K higher than the lowest Curie temperature). Lei et al. (2015) states that this is explained by the increase of the temperature that corresponds to the MCE peak with the magnetic field, as can be seen in Figure 7.

From a mechanical point of view, La-Fe-Si alloys show performance issues due to their low mechanical stability. One solution to this problem is to increase the

concentration of α-Fe in the alloy, which was already discussed in Section 2.2.2. This, however, is usually not enough to guarantee the integrity of the regenerator during operation while maintaining a significant MCE. In order to solve this, some binding agent, for example, epoxy resin, is added to the porous medium, increasing its stability. While this is vital to the long-term stability and operation of the regenerator, it may significantly reduce the heat transfer between the solid and fluid phases while also increasing the chances of obstructing flow passages (clogging) in the porous medium, which greatly increases the pressure drop (BEZ et al., 2016; NAVICKAITĖ et al., 2018).

Bez et al. (2016) showed that for irregular particles of La-Fe-Si, values of 2 wt.% of epoxy yielded the best performance while still maintaining mechanical integrity. A similar conclusion was reached by Navickaitė et al. (2018), however, two regenerators in their study with an epoxy fraction of 2 wt.% showed some mechanical degradation. Therefore, in order to guarantee the mechanical stability, concentrations between 2 wt% and 3 wt% are required. The temperature span results obtained by Navickaitė et al. (2018) for a 2-layer La-Fe-Si regenerator are presented in Figure 14, showing that the maximum span was indeed reached with a regenerator with 2 wt% epoxy. Regenerators with higher epoxy concentrations had worse performances, probably due to the negative impacts of the epoxy mentioned above. The regenerator with 1 wt% epoxy broke, but was also showing worse results than the 2 wt% regenerator, however, as stated by Navickaitė et al. (2018), adequate results for this regenerator could not be obtained due to its disintegration.

2.5 Magnetic Refrigeration Systems

A magnetic cooling device can be divided in multiple subsystems, including the regenerators. One of these systems is the magnetic circuit (MC), which is responsible for generating the magnetic profile, i.e., an oscillating (time-dependent) magnetic field applied over the air gap that houses the regenerator beds.

While the literature regarding the individual design of each of those subsystems (AMR and MC) is abundant, in general, works focusing on the design of the magnetic circuit do not take the AMR performance into account, and works focusing on regenerator design only use the magnetic field profile as an input, not considering how it is generated or how it could be adapted to improve the system performance (FORTKAMP et al., 2020).

2.5.1 Magnetic Circuit Models

Three different kinds of magnetic field generators have been applied to magnetic refrigeration systems: superconducting coils (BROWN, 1976; ROWE et al., 2005), electromagnetic coils (YU et al., 2006), and permanent magnet arrays (TUŠEK et al.,

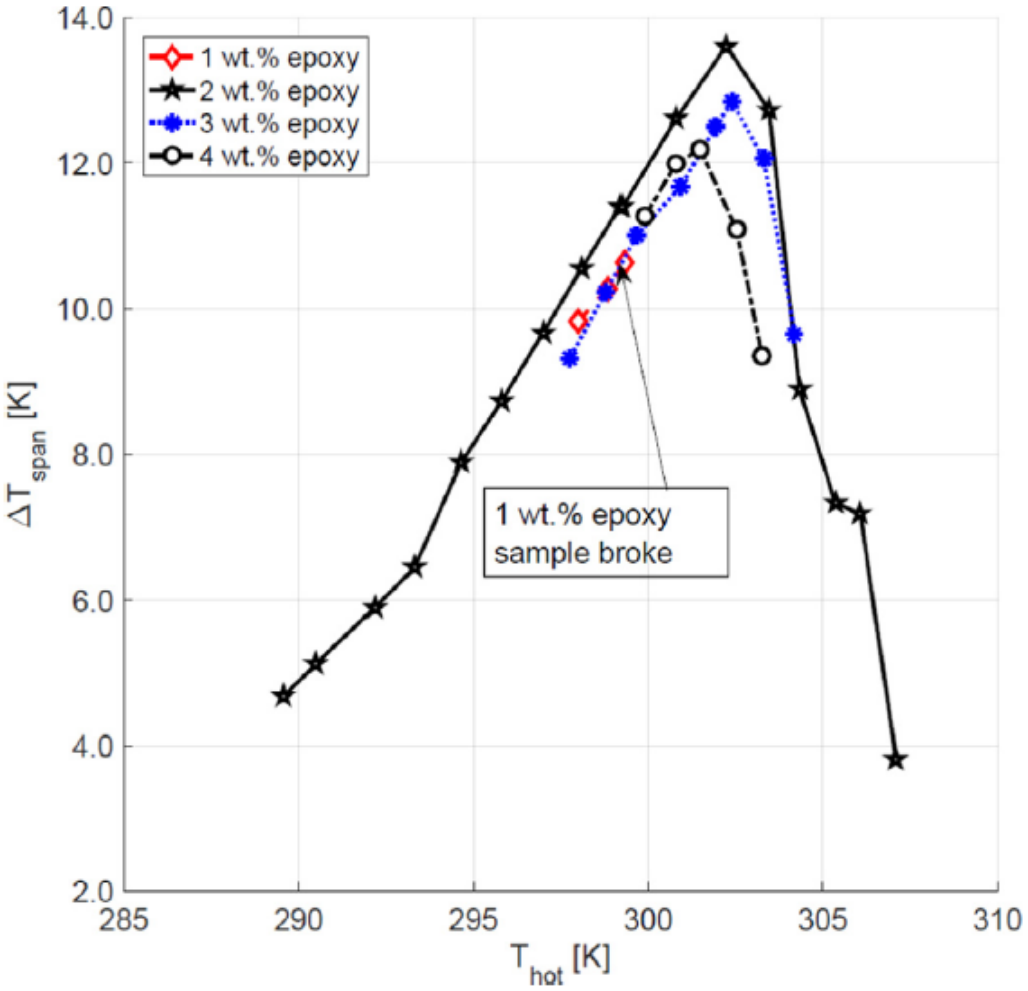

Figure 14 – Effect of the epoxy concentration on the performance of a 2-layer La-Fe-Si regenerator. Adapted from Navickaitė et al. (2018).

2010; BJøRK et al., 2010). Since superconducting coils require cryogenic cooling by either liquid helium or nitrogen, they are unfeasible for low and medium cooling capacity applications near room-temperature. Similarly, electromagnetic coils require high electric power, thus being subjected to Joule heating, which deteriorates the system performance. Therefore, this section will focus on permanent magnet arrays, which do not present the above mentioned issues, and have the advantage of not requiring electrical energy input.

Design studies of magnetic circuits using permanent magnets for magnetic refrigeration systems are abundant in the available literature. While there are several ways to generate a magnetic field, nested Halbach cylinders have been used in several AMR apparatuses (ARNOLD et al., 2014; TREVIZOLI, 2015). This configuration consists of two concentric Halbach cylinders, with each magnet array generating a magnetic field in its core, and an air gap between them, as shown in Figure 15. This allows for the creation of a variable magnetic field by rotating the cylinders, enabling higher operating frequencies. It also has the advantage of containing the regenerator in a high

magnetic field region, the air gap (TURA; ROWE, 2011; TREVIZOLI, 2015).

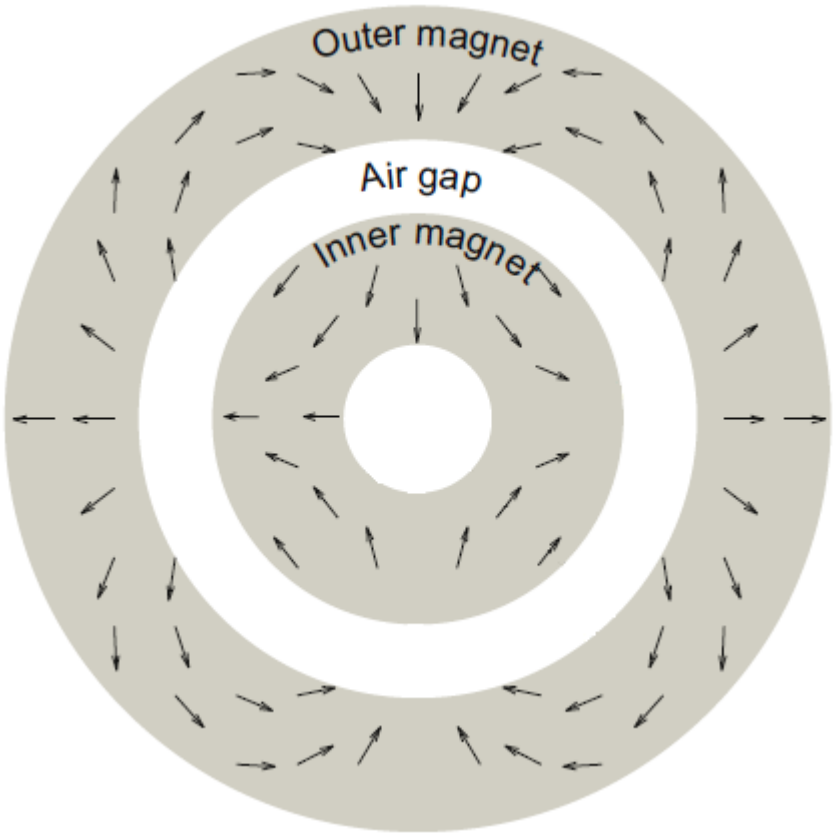

Figure 15 – Nested Halbach cylinder design with the magnetization direction shown as arrows. Adapted from Bjørk et al. (2010)

Bjørk et al. (2010) optimized a magnetic circuit with this configuration and obtained a magnetic flux density peak value of 1.24 T, with an average flux density of 0.9 T in a volume of 2 L (air gap) using only 7.3 L of magnet. This design was then used in the prototype developed by Engelbrecth et al. (2012). Lorenz & Kevlishvili (2017) presented a design procedure to optimize a Halbach circuit, which amplifies the magnetic profile and reduces the mass of permanent magnet. Fortkamp, Lozano & Barbosa Jr. (2017) developed an analytical model of a magnet with the nested Halbach cylinder configuration which estimates the magnetic field and magnetic flux density in the air gap and presented a parametric analysis of its performance. Their study showed that there are optimal values for the air gap height which maximize the magnet efficiency parameter (as defined by Bjørk et al. (2008)). It also showed that the inner magnet contributes poorly to the magnitude of the magnetic field, which suggests it can be replaced by soft ferromagnetic materials, reducing the cost. Other studies regarding optimization of Halbach cylinders were made by Trevizoli et al. (2015), Lee, Nomura & Dede (2017) and Bjørk, Bahl & Insinga (2017).

2.5.2 AMR Models

Similarly to the magnetic circuit, many AMR models for near room temperature applications have been developed, with a comprehensive review being found in Nielsen et al. (2011). In this work, Nielsen et al. (2011) proposed that the models be classified into two types: (i) steady-state and (ii) time dependent AMR models. As suggested by their name, steady-state AMR models (also called zero-period AMR models) are time independent. These models start from an ideal AMR cycle and reduce the performance by individually adding losses such as axial conduction and heat transfer losses. These models have a greater computational efficiency than their counterpart and are useful for qualitative analysis of an AMR performance, but are unable to capture interactions between the many mechanisms of an AMR operation. Amongst the models that fit this category are the ones developed by Yan & Chen (1992), Zhang et al. (1993), Zhang et al. (2000) and He, Chen & Wu (2003). Time dependent models, on the other hand, do not take such a macroscopic approach and usually solve the transient equations for the solid and fluid phases present in the regenerator. This allows not only for a more detailed description of the phenomena happening in the porous medium, but also captures the interactions between the many aspects and losses of the regenerator. Because of this complexity, these models are generally less computationally efficient. The models developed by Kirol & Mills (1984), Hu & Xiao (1995), Smailli & Chahine (1998), Engelbrecht (2008) and Petersen et al. (2008) fit in this category (NIELSEN et al., 2011).

The time dependent models can further be categorized by their dimensionality (one-dimensional to three-dimensional) and by how the magnetocaloric effect is implemented. There are two main ways of including the MCE in the model: (i) to directly apply the adiabatic temperature change to the solid during the magnetization and demagnetization processes and (ii) to add a source term to the solid phase energy equation to represent the MCE, the so-called built-in method, which will be further described in Chapter 3. Regarding heat transfer, one-dimensional models are generally required to assume a Nusselt number correlation to describe the interstitial heat transfer between the phases. More advanced models may account for temperature gradients within the solid phase such as the ones developed by Engelbrecht (2008) and Sarlah (2008). Two and three-dimensional models can describe the heat transfer between the phases through an internal boundary condition, which for a 2D model can be expressed as (NIELSEN et al., 2011):

$$k_s \frac{\partial T_s}{\partial y} = k_f \frac{\partial T_f}{\partial y} \tag{2.20}$$

however, these models are expected to have a much greater computational complexity than one-dimensional models.

Tušek et al. (2011) developed a 1D AMR model which solved the energy equa-

tions for the magnetocaloric material and heat-transfer fluid simultaneously using MATLAB. The magnetocaloric effect was implemented using the adiabatic temperature change, and the MCM was gadolinium (arranged as a packed bed of spheres). The magnetic field was assumed to have a discrete "on-off" change from 0.0001 T to 1 T. This model was used to optimize a packed-bed regenerator, mainly focusing on the influence of the mass flow rate, frequency and sphere diameter. This process showed, among other things, that:

1. Each frequency has one mass flow rate that leads to the best performance of the AMR;

2. The value of the optimal mass flow rate increases with the frequency;

3. The maximum cooling load is obtained at a higher frequency compared to the maximum COP;

4. Smaller sphere diameters lead to a large cooling load due to better heat transfer properties.

Trevizoli (2015) developed a similar 1D model, which was also based on solving the energy equations for both phases and the momentum equation for the fluid phase. The model allowed for different matrix geometries (parallel plates, pin arrays and packed beds of spheres) and included several losses: the heat transfer through the casing, the effect of the void volumes, the demagnetizing effect, the axial conduction, and the viscous dissipation. The time-dependent applied magnetic field profile was an input parameter and could have the shape of a square wave, a rectified cosine or a trapezoidal wave. For the wave-shaped profiles, the maximum and minimum field values along with the relevant periods of the profiles could be changed at will. The magnetocaloric effect was implemented using both the adiabatic temperature change and the built-in method, with the magnetocaloric material being gadolinium. The model originally only allowed for a single layer of material, but was later updated to allow for up to three layers (LANG, 2018). Trevizoli & Barbosa Jr. (2015) used this model to optimize regenerators through an entropy minimization analysis. The simulations in this study were carried out based on the performance evaluation criteria of Webb & Kim (2005): (i) variable geometry, which allowed for the cross sectional area of the regenerator to be changed, with the length being changed accordingly to keep the volume constant and (ii) fixed face area, which kept the cross sectional area constant and varied the regenerator length, thus changing the volume. This study focused in the passive part of the regenerator, namely the effectiveness results, and showed that:

1. For a fixed frequency, variable geometry, the optimal configuration for low mass flow rates had a long regenerator with a small diameter and large particles to

increase the particle Reynolds number. For high mass flow rates, the optimal regenerator had a large housing diameter, small particle diameter and small aspect ratio;

2. For a fixed frequency, fixed face area, the optimal regenerator for low mass flow rates was short and had small particles. High mass flow rates required larger particle sizes and longer regenerators;

3. For a fixed mass flow rate, variable geometry, the optimal regenerator for small frequencies had a short length and large diameter with small particles. For higher frequencies, long regenerators with large particle diameters were sufficient to reach high effectivenesses;

4. For a fixed mass flow rate, fixed face area, smaller frequencies required a regenerator with a large aspect ratio and large particle diameters while higher frequencies required smaller particles diameters.

Another 1D model was developed by Lei et al. (2017) which allowed for the simulation of different regenerator geometries, including packed beds of spheres, parallel plates, packed screen beds, and rectangular and circular micro-channels. This model was also used to optimize regenerators, and did so by calculating the entropy production rates for different processes during the operation, namely the axial conduction, viscous dissipation and insufficient heat transfer, in a similar matter to that of Trevizoli & Barbosa Jr. (2015). The magnetocaloric effect was calculated using the built-in method and the time-dependent applied magnetic filed was an input parameter, as shown in Figure 16. Most of the conclusions drawn from that study related to maximizing the COP of an AMR with a given specific cooling capacity instead of maximizing the cooling capacity itself. For a packed bed of spheres, some of the conclusions were:

1. The maximum COP varies with the hydraulic diameter (which is proportional to the sphere diameter);

2. The optimal frequency decreases and the optimal aspect ratio increases as the hydraulic diameter increases;

3. For a small hydraulic diameter, the COP changes significantly with the aspect ratio while it is less sensitive to the frequency.

The first 2D model of a parallel plate regenerator was developed by Petersen et al. (2008) and used gadolinium as the MCM. The 2D energy equations for both phases were solved, and the magnetocaloric effect was implemented via the adiabatic temperature change. The time-dependent magnetic field profile had the shape of a square wave, with the applied magnetic flux density ranging from 0 to 1 T. The x

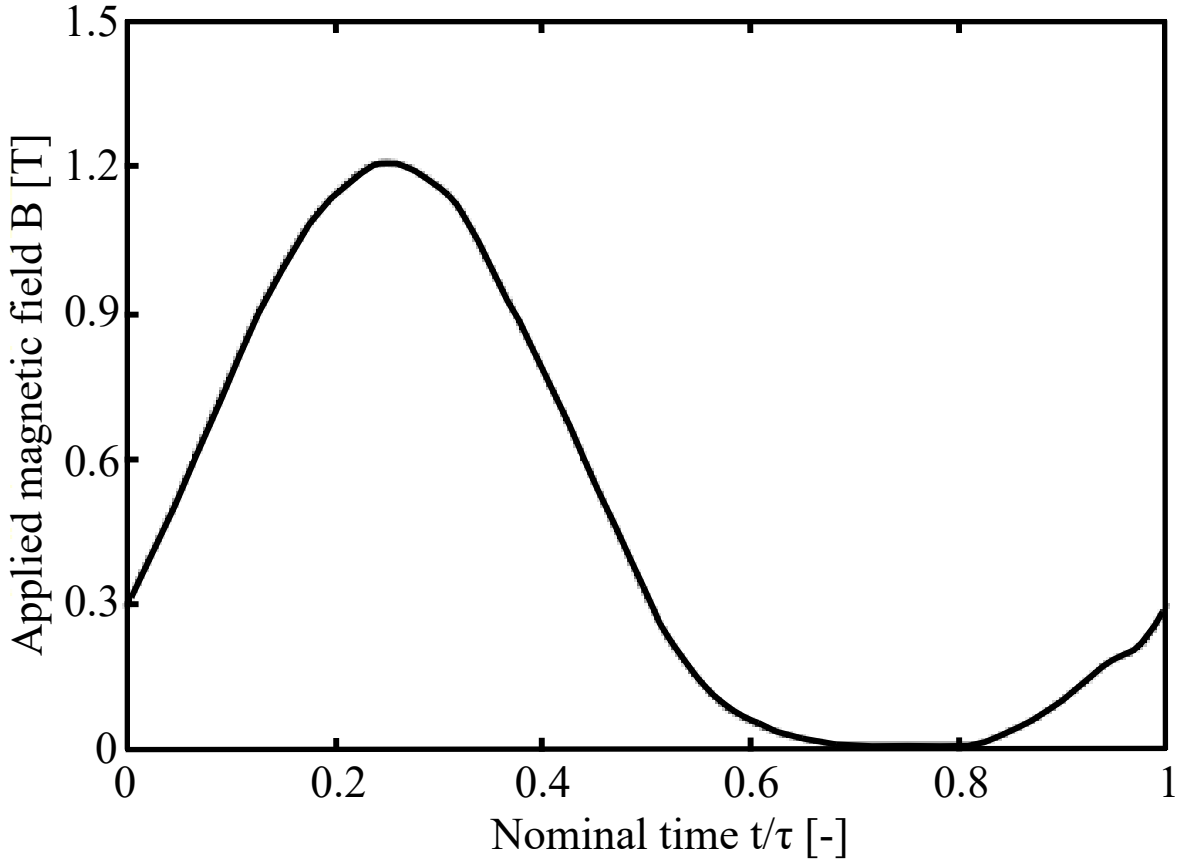

Figure 16 – Applied magnetic field in the model used by Lei et al. (2017). Adapted from Lei et al. (2017).

and y-directions represented the positions along the regenerator and perpendicular to it, respectively. The heat exchange between the phases was determined through the derivative of the temperature profiles at the boundaries in the y-direction, using Equation 2.20 as the boundary condition in said position. Preliminary results showed that the model was able to correctly predict the temperature profiles in the regenerator and indicated the presence of large temperature differences between the fluid and the paralleled plate regenerator, which was interpreted as an indication of the necessity to use 2D models to simulate regenerators with configurations that are not packed beds of spheres.

Oliveira et al. (2012) developed a similar 2D model of a parallel plate magnetic regenerator. This model contained a hybrid calculation which consisted of an analytical solution for the flow and a numerical solution for the thermal field. The regenerator consisted of 28 evenly spaced thin plates of Gd forming 26 0.1mm-wide channels. The heat exchange fluid was water, which flowed through said channels. The heat transfer model was very similar to that of Petersen et al. (2008), but instead used non-dimensional variables. The magnetic field had the shape of a square wave and was assumed to be evenly distributed along the length of the regenerator. The magnetocaloric effect was implemented using the adiabatic temperature change. The

main conclusion of the study was that the performance of the regenerator was significantly influenced by the volume of fluid displaced inside the regenerator during the isofield periods and that the matrix temperature profiles were strongly dependent on the specific heat of the MCM.

Lionte, Vasile & Siroux (2015) developed a 2D model for a parallel plate regenerator which used Gd as the MCM and water as the heat transfer fluid. The 2D configuration allowed the authors to determine the velocity profiles within the flow channels of the regenerator. However, the fluid displacement function was still idealized as a ramp profile, with the same being done to the magnetic field profile. The model solved the 2D energy equations for both phases, with the MCE being determined using the adiabatic temperature change. Figure 17 shows the results for temperature span at no-cooling load obtained using this model for different operating frequencies. The temperature difference increases with the frequency from 0.3 to 1.5 Hz, but decreases when the frequency reaches 2 Hz, as the residence time of the fluid within the matrix becomes too short for an effective heat exchange with the solid phase, a phenomenon which can be quantified in terms of the utilization factor and Fourier number.

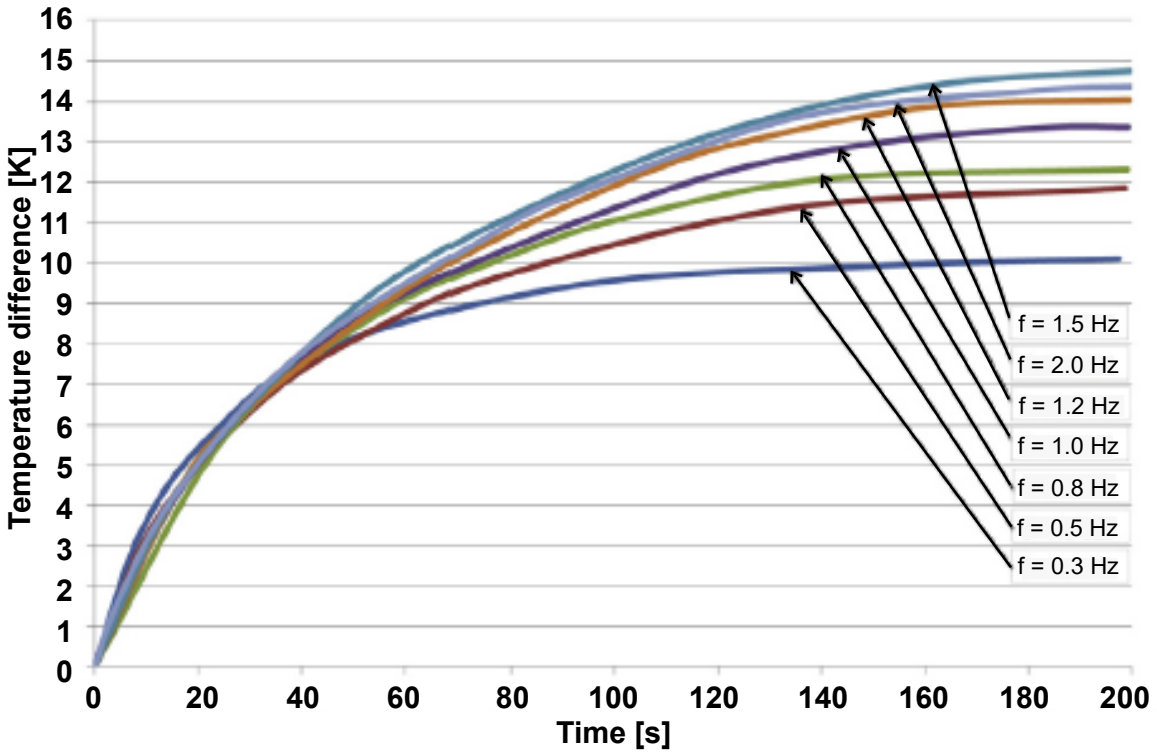

Figure 17 – Maximum temperature span obtained at no-cooling load by Lionte, Vasile & Siroux (2015). Adapted from Lionte, Vasile & Siroux (2015).

Bouchard, Nesreddine & Galanis (2009) developed a transient, 3D AMR model which was the first of its kind to ever be published (NIELSEN et al., 2011). The model solved the incompressible Navier-Stokes equations and the coupled 3D energy equa-

tions of both phases. The magnetocaloric effect was implemented using the built-in method and magneto-static theory was used to determine the field intensity within the ferromagnetic material, resulting in different magnetic flux densities along the regenerator. The porous medium was composed of spherical and elliptical particles of gadolinium. Analysis of the resulting velocity and temperature profiles were shown to be fairly realistic, but the model required the use of a subdivision of the computation domain to reduce the required memory and CPU time to run simulations.

2.5.3 *Integrated Design of an AMR with the MC through the Air Gap*

In general, most studies that focus on the MC do not take the AMR performance into consideration, and studies that focus on regenerators use the magnetic profile as an input, without considering the MC needed to generate it (FORTKAMP et al., 2020). Regarding this integration between the AMR and MC, Fortkamp et al. (2020) proposed classifying published AMR performance optimization works into three categories: (i) *segregated*, (ii) *semi-segregated* and (iii) *integrated* designs. Segregated AMR designs are characterized for having a constant magnetic field waveform, i.e, with a fixed shape and amplitude. Examples of segregated AMR designs can be found in Petersen et al. (2008), Tušek et al. (2011), Momen et al. (2014) and Zhang et al. (2017). Semi-segregated designs allow parameters associated to the waveform to change, but do not consider the configuration of the magnetic circuit needed to generate such waveforms. Example of semi-segregated AMR designs can be found in Bouchekara et al. (2014), Ganjehsarabi, Dincer & Gungor (2016) and Roy, Poncet & Sorin (2017). Lastly, integrated designs incorporate the magnetic circuit that generates the waveform in the analysis through conservation equations and appropriate closure relationships involving the magnetic field, requiring the formulation of objective functions involving the mass, size, geometry or cost of the magnetic circuit. An example of integrated design can be found in Teyber et al. (2017), who aimed to minimize the cost of the magnetic circuit by employing a topology-based optimization using genetic algorithms.

Geometrically, the AMR and MC are interrelated through the air gap, as illustrated in Figure 18. Considering the MC, a smaller air gap height (h_{gap}) results in a higher magnetic field strength and a better magnetic field profile. On the other hand, increasing the height of the air gap increases the mass of refrigerant through an increase in the AMR height. Not only that, the pressure drop is reduced due to the increase in the cross section area of the porous medium (assuming a constant mass flow rate). Therefore, while separately an AMR model would always aim to increase the air gap height and a MC model would aim to decrease it, when coupled together these models would reach an optimal air gap height, as shown in Figure 19.

Similarly, increasing the inner and outer air gap radii (without necessarily increasing the air gap height) would result in regenerators with a larger width or in a

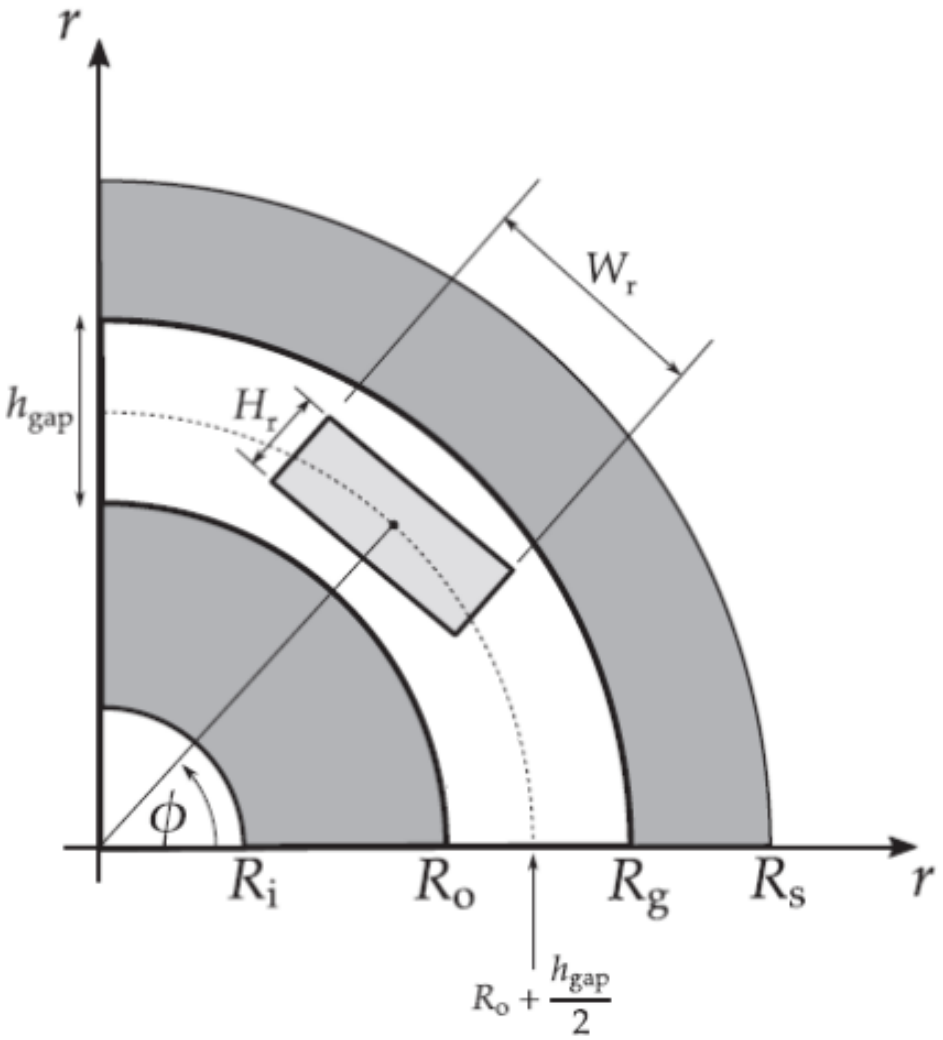

Figure 18 – Nested Halbach cylinder with regenerator in the air gap. Adapted from Fortkamp et al. (2020).

larger number of regenerators along the air gap. However, in order to keep the same magnetic field strength, more magnet material would be required due to the radii increase, affecting the cost of the system (FORTKAMP et al., 2020). Lastly, the ratio between the length of the regenerator and the length of the magnet also needs to be considered. Generally, the magnetic field strength is considerably weaker at the edges of the magnet, therefore, the magnet length needs to be larger than the AMR length in order to have a sizeable MCE along the whole length of the regenerator.

2.6 State-of-the-art Magnetic Refrigerator Prototypes

The first magnetic heat pump to work at room-temperature was developed by Brown (1976). It used Gadolinium with a Curie temperature of 293 K as a refrigerant and reached a magnetic flux density of 7 T using superconducting coils, allowing the

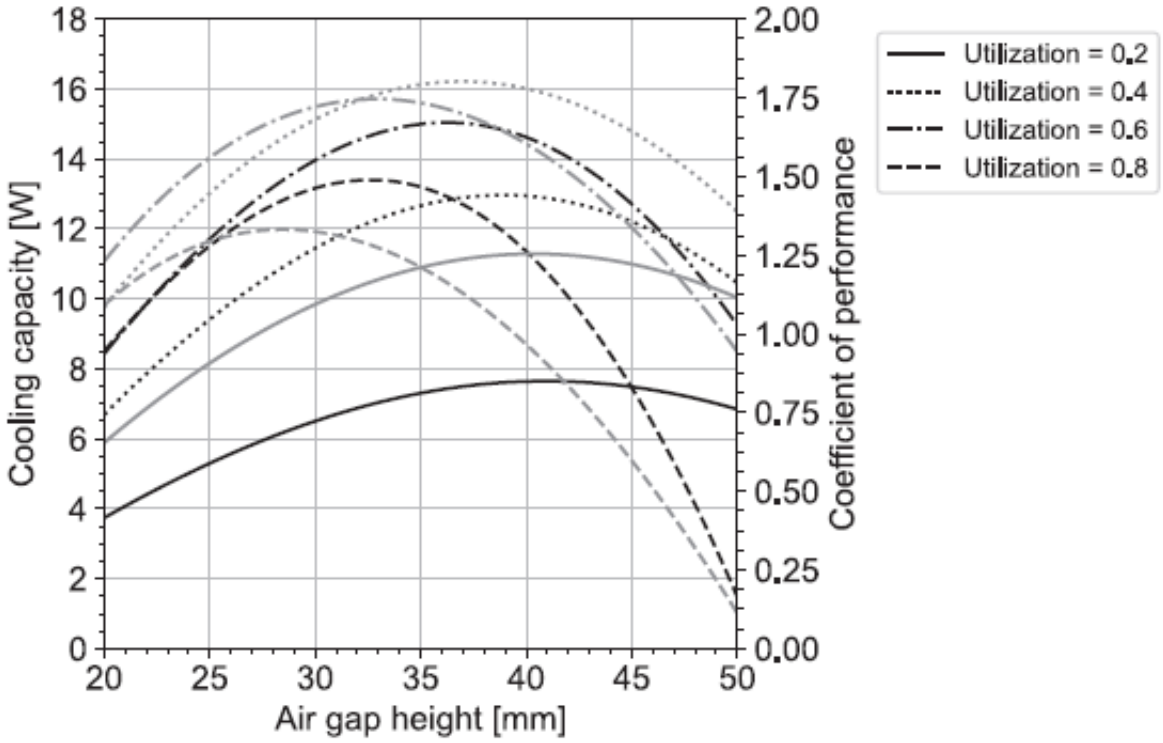

Figure 19 – Fortkamp et al. (2020) results for cooling capacity and COP as a function of the air gap height for a regenerator operating at a frequency of 1 Hz. Adapted from Fortkamp et al. (2020).

system to reach a temperature span of 47 K. Few prototypes were made during the two decades that followed, until developments in magnetocaloric materials allowed the area to become more active (TREVIZOLI, 2015). This can be seen in Figure 20, which shows the number of prototypes built each year between 1976 and 2018.

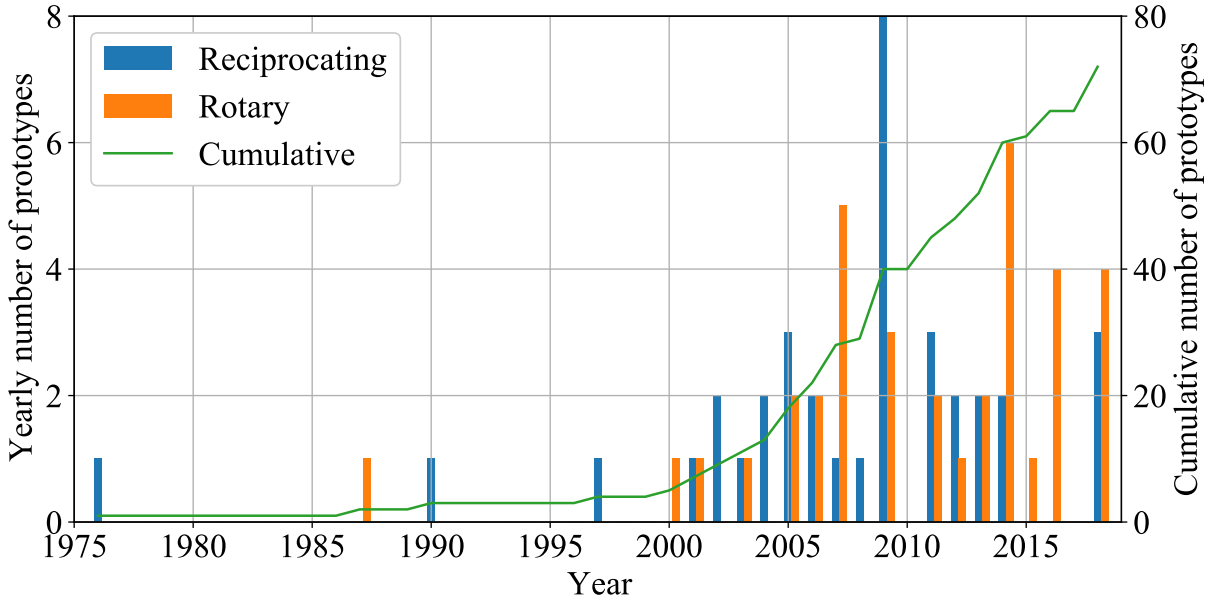

Figure 20 – Number of prototypes built yearly between 1976 and 2018. Based on information found in Yu et al. (2010) and Greco et al. (2019).

Figure 20 also makes the distinction between reciprocating and rotary systems. This definition relates to the method through which the application and removal of the magnetic field is achieved. Reciprocating systems are characterized by a linear, back and forth method. This can be achieved by moving the regenerator in and out of the stationary field generated by the magnet or by keeping the regenerator stationary and moving the magnet linearly to apply and remove the field. The latter case usually operates at lower frequencies due to the considerable mass of the magnetic circuit (TREVIZOLI; BARBOSA JR.; FERREIRA, 2011). Rotary systems magnetize and demagnetize the MCM through a rotating motion. Once again, this can be done to both the regenerator and the magnet. Rotating the regenerator has the advantage of allowing higher operating frequencies, but adds complexities to the hydraulic system due to the flow distribution and leakages (ENGELBRECTH et al., 2012; TREVIZOLI, 2015). Rotating the magnets simplifies the hydraulic system, but limits the operating frequency due to the high torque required to rotate the magnet (TURA; ROWE, 2011; TREVIZOLI, 2015). A few selected prototypes will be briefly described ahead, while a more detailed review of these and other prototypes can be found in Yu et al. (2010), Kitanovski et al. (2015), Greco et al. (2019) and Kitanovski (2020).

2.6.1 *Technical University of Denmark Rotary Prototype*

Engelbrecth et al. (2012) presented a rotary magnetic refrigeration prototype built in the Technical University of Denmark. This prototype had an AMR ring rotating in the gap between two Nd-Fe-B Halbach magnets, which allowed it to reach high operating frequencies. The main characteristics of this prototype are shown in Table 1 and a picture is shown in Figure 21 (ENGELBRECTH et al., 2012; KITANOVSKI et al., 2015).

Table 1 – Rotary prototype from the Technical University of Denmark (ENGELBRECTH et al., 2012; KITANOVSKI et al., 2015).

Name of the institute	Department of Energy Conversion and Storage, Technical University of Denmark
Year of production	2010
Maximum frequency	10 Hz
Maximum cooling power	1012 W
Maximum temperature span	25.4 K
AMR	Packed bed of Gd (2800 g)
Magnet	Modified concentric double Halbach cylinder

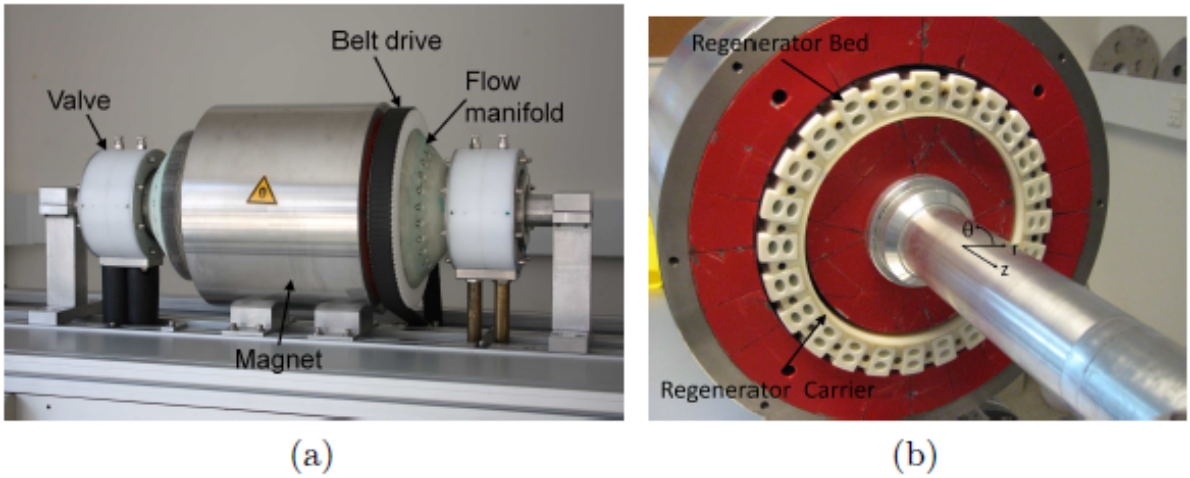

Figure 21 – AMR system developed at the Technical University of Denmark. (a) Device showing the magnet assembly, the flow manifold and the rotary valves; (b) The 24-bed regenerator assembly installed in the magnetized gap (ENGELBRECTH et al., 2012).

2.6.2 *Astronautics Corporation of America Prototype*

One of the devices presented by the Astronautics Corporation of America aimed to deliver 2000 W of cooling power over a temperature span of 12 K. The system used a rotary magnet circuit which reached a peak field of 1.44 T and had twelve AMR beds arranged in a circumference. Each AMR had six layers of La-Fe-Si-H, each with a specific Curie temperature. This system reached a cooling power of 3042 W at zero span, and 2502 W at a span of 11 K, which was claimed to be the largest cooling power observed for a magnetic refrigeration system. Further details can be found in Table 2 and a picture is shown in Figure 22 (JACOBS et al., 2014; KITANOVSKI et al., 2015).

Table 2 – Rotary prototype from the Astronautics Corporation of America (JACOBS et al., 2014; KITANOVSKI et al., 2015).

Name of the institute	Department of Energy Conversion and Storage, Astronautics Corporation of America
Year of production	2013
Maximum frequency	4 Hz
Maximum cooling power	3042 W
Maximum temperature span	18 K
AMR	Packed bed of La-Fe-Si-H
Magnet	Modified Halbach array

2.6.3 *POLO Prototypes*

Lozano (2015) developed magnetic refrigerator prototype which was built using a 2-pole rotor-stator magnetic circuit and stationary packed regenerator beds,

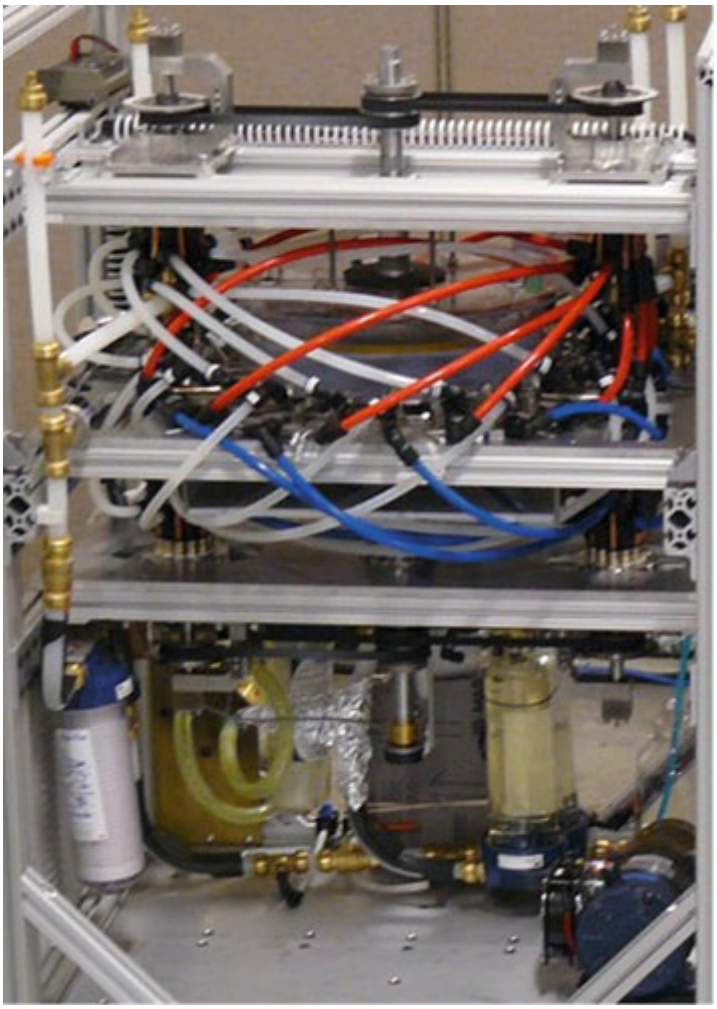

Figure 22 – AMR system developed at the Astronautics Corporation of America (JACOBS et al., 2014; KITANOVSKI et al., 2015).

shown in Figure 23. The rotor-stator configuration for the magnetic circuit was chosen because of its ability to easily perform magnetic field changes within the magnetic gap. 8 pairs of ring shaped regenerators were used, containing amongst themselves 1.7 kg of Gd spheres with diameters between 425 and 600 μm. The heat transfer fluid was a mixture of distilled water and commercial ethylene-glycol with corrosion inhibitors. Experimental analysis resulted in a maximum cooling capacity of 150 W at zero-span and a maximum no-load temperature span of 12 K. At a frequency of 0.8 Hz and flow rate of 200 Lh^{-1}, the prototype was able to deliver a cooling capacity of 80.4 W while maintaining a temperature span of 7.1 K. The maximum torque was 7.2 Nm for an operating frequency of 0.4 Hz and the maximum motor power was of 159.2 W at 1.6 Hz. A summary of the main characteristics of the prototype can be found in Table 3 and further details can be found in Lozano (2015) and Lozano et al. (2016).

More recently, the group developed a magnetic wine cooler prototype (Figure 24), which aimed to control the temperature of a 31-bottle wine cooler cabinet between 5 ºC and 20 ºC in a controlled environment. This device included eight multi-layered

Table 3 – Rotary prototype from POLO (LOZANO, 2015; LOZANO et al., 2016).

Name of the institute	POLO — Research Laboratories for Emerging Technologies in Cooling and Thermophysics
Year of production	2015
Maximum torque	7.2 Nm
AMR	Packed bed of Gd
Maximum cooling power	150 W
Maximum temperature span	12 K
Magnet material	Nd-Fe-B

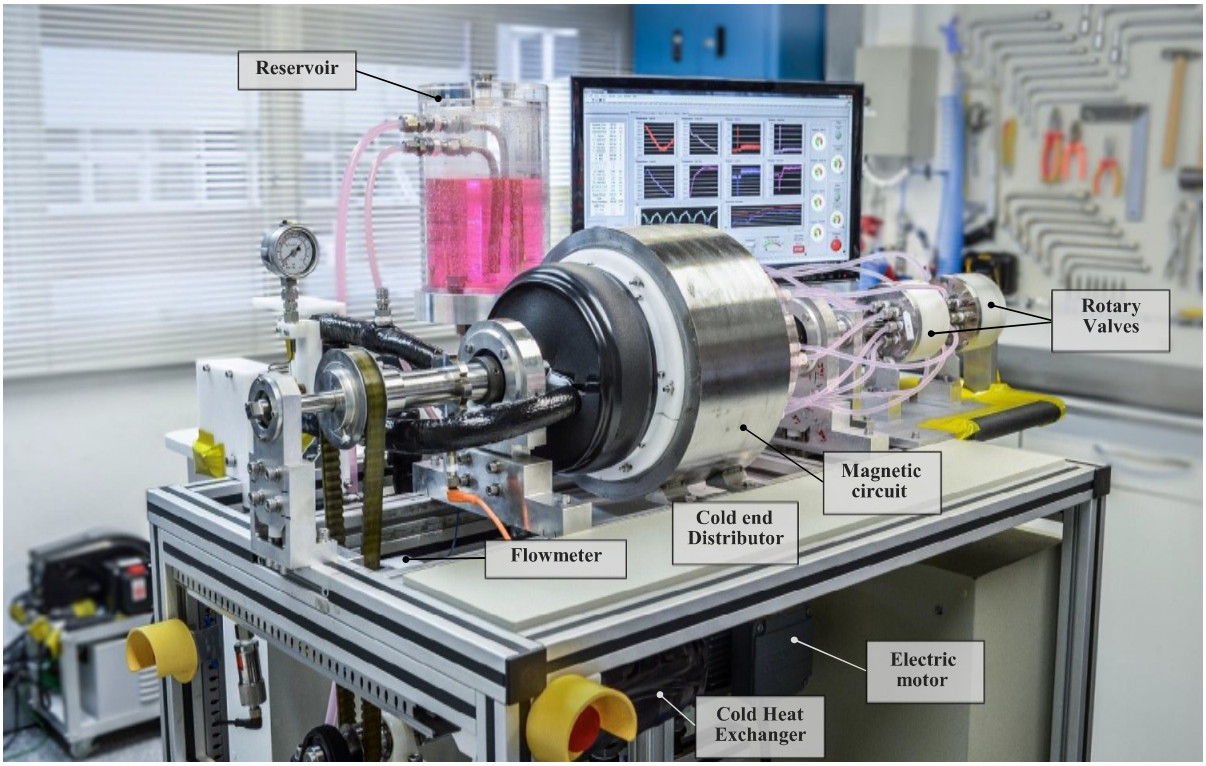

Figure 23 – AMR system developed at POLO (LOZANO, 2015; LOZANO et al., 2016).

AMRs composed of Gd and Gd-Y alloys, a two-pole Halbach cylinder as the magnetic circuit (reaching a maximum field of 1 T), eight solenoid valves to control the flow and two tube-fin heat exchangers (NAKASHIMA et al., 2020a).

2.7 Summary and Specific Objectives

This section presented a review of the available literature regarding AMR design for near room-temperature magnetic refrigeration. This review focused mainly in AMRs using first-order phase transition materials and the modeling and integration of said AMRs with the rest of the system, aiming to apply that knowledge in developing a magnetic refrigeration unit. Considering this, the following specific objectives for this

Figure 24 – Wine cooler developed at POLO (NAKASHIMA et al., 2020b).

work can be proposed:

1. Develop an AMR model to be applied in designing an AMR to be used in a magnetic refrigeration unit by revising and improving the models developed by Trevizoli (2015) and Fortkamp et al. (2020).
2. Validate the model by comparing the results obtained by it with experimental results;
3. Analyse the influence of the epoxy on the performance of an AMR;
4. Analyse the influence of the losses related to first-order phase transition materials on the performance of an AMR;
5. Analyse and predict the impact that uncertainties in the MCM production might have in the system performance;

6. Develop methods to optimize the performance of multilayered regenerators;
7. Develop methods that integrate the design of the regenerator with the design of the magnetic circuit and other relevant sub-systems;
8. Use the results of the previous objectives to determine the regenerator to be used in the magnetic refrigeration unit and its operating conditions.

3 Model Description and Solution Method

This chapter presents the mathematical model developed to describe the behaviour of the regenerator and its interaction with the heat transfer fluid and the environment. The simplifying assumptions will be discussed and the closure relationships will be described. The method used to determine the material properties for any given Curie temperature will be discussed along with the solution method used to solve the equations, the boundary conditions and all other relevant calculations needed. Finally, a brief analysis of the convergence criteria and mesh refinement will be made.

3.1 System Layout

The AMR is treated as a porous medium (packed bed of spheres) inside a stainless steel casing which is inserted in the magnetic circuit, forming an air gap between the casing and the permanent magnet. The porous medium is made of layers of magnetocaloric material with different Curie temperatures and, in principle, different lengths. The regenerator is connected via ideal heat exchangers (i.e., no thermal resistance) to two thermal reservoirs, representing the hot and cold environments. Between the regenerator and the reservoirs there exist void (dead) volumes, representing the connections and fittings necessary to connect the regenerator to the thermal reservoirs. A schematic representation of the system with a three-layered regenerator is shown in Figure 25.

3.2 Porosity Estimation

The first aspect of the porous medium to be analysed is the porosity, which represents the volume occupied by the fluid phase. This analysis should be fairly straightforward when the porous medium is comprised of a single material, but due to mechanical integrity issues typical of first-order magnetocaloric materials, some kind of binding agent, such as epoxy resin, needs to be added to the medium to bond the particles and prevent them from breaking during the alternating blows. The epoxy resin not only reduces the porosity due to an increase of solid material, but also increases the pressure drop due to clogging of the porous medium and reduces the regenerator heat transfer effectiveness due to an additional thermal resistance. In order to appropriately describe all these factors, three different porosities are proposed in the present calculation method:

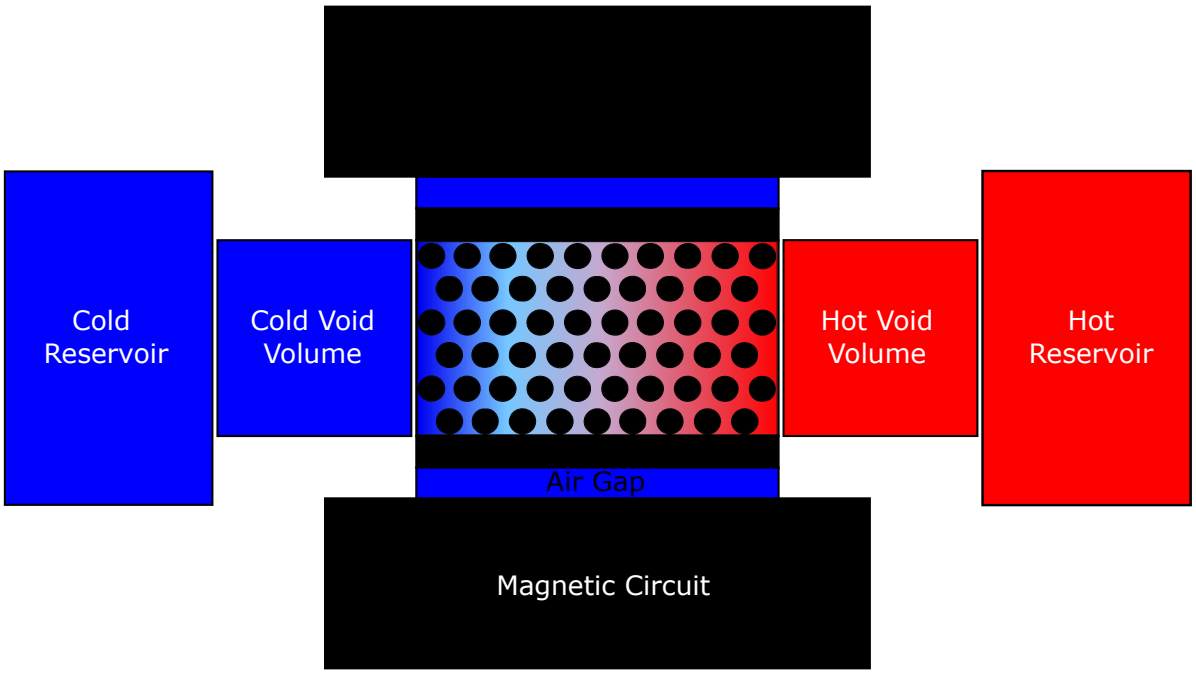

Figure 25 – Schematic representation of the magnet-regenerator assembly.

- MCM relative porosity (ε) → Porosity calculated using the volume that the fluid would occupy if only the magnetocaloric material was present in the porous medium. This porosity is used mainly to determine the source term related to the magnetocaloric effect (to be defined below), and to solve the energy equation for the solid;

- Real porosity (ε_f) → Porosity calculated using the volume occupied by the fluid considering both the magnetocaloric material and the epoxy, but without considering any clogging. This porosity is mainly used to determine the total contact area between the fluid and the solid;

- Effective porosity (ε_{eff}) → Porosity considering both materials, the clogging caused by the epoxy and other not accounted phenomena that might affect the pressure drop. This porosity aims to determine the volume of open pores through which the fluid actually flows in the regenerator. This porosity is used in the solution of the momentum and energy equations for the fluid.

The relative and real porosities can be calculated directly from the mass and dimensions of the porous medium, together with the weight fraction of epoxy in the regenerative matrix (φ_e) provided by the regenerator manufacturer (VACUUMSCHMELZE GmbH). With these parameters, the porosities are given by Equations 3.1 and 3.2 as follows:

$$\varepsilon = 1 - \frac{m_{pm}(1 - \varphi_{ep})}{\rho_{MCM} V_{pm}} \tag{3.1}$$

$$\varepsilon_f = \varepsilon - \frac{m_{pm}\varphi_{ep}}{\rho_{ep}V_{pm}} \tag{3.2}$$

The effective porosity cannot be obtained analytically, since the clogging cannot be predicted or measured directly. Therefore, it can only be estimated empirically via direct measurements of pressure drop in a real regenerator, as will be described in Section 3.5.4. It is important to distinguish between the above mentioned porosities, since each one plays a different role in the mathematical model.

3.3 Active Magnetic Regenerator Modeling

The regenerator mathematical model consists of conservation equations for both the fluid and solid phases, namely the energy equation for the solid and the momentum and energy equations for the fluid (two-temperature or non-equilibrium approach). A volume-average formulation is used, allowing the conservation equations to be solved without the need to model the transfer processes at the pore scale level. Besides that, five simplifying assumptions are made:

- One-dimensional flow;
- Low porosity medium ($\varepsilon < 0.6$);
- Absence of body forces;
- Incompressible, laminar flow;
- The fluid never flows through a clogged channel.

Solving the equations using these assumptions yields the temperature profile and the pressure drop along the regenerator, which are used to determine the performance parameters of the system, such as the cooling capacity, rejected heat and total pumping and magnetic power.

3.3.1 Fluid Phase Momentum Equation

The macroscopic fluid phase momentum equation also known as Brinkman-Forcheimer equation is given by (KAVIANY, 1995):

$$\frac{\rho_f}{\varepsilon_f}\left(\frac{\partial\vec{v}}{\partial t} + \vec{v}.\nabla\vec{v}\right) = -\nabla P + \rho_f\vec{f} + \frac{\mu_f}{\varepsilon_f}\nabla^2\vec{v} - \frac{\mu_f}{K}\vec{v} - \frac{c_E\rho_f}{K^{1/2}}|\vec{v}|\vec{v} \tag{3.3}$$

where the terms of this equation, from left to right, represent the macroscopic inertial force, the pore pressure gradient, the body forces, the macroscopic shear stress diffusion, also known as Brinkman viscous term, the microscopic viscous shear stress, also

known as Darcy term and the microscopic inertial force, also called the Ergun inertial term. As suggested by Trevizoli (2015), in the momentum equation, the fluid properties are evaluated at a mean fluid temperature, allowing the momentum and energy equations to be solved uncoupled. Applying the previously stated simplifying assumptions reduces Equation 3.3 to:

$$\frac{\rho_{\mathrm{f}}}{\varepsilon_{\mathrm{eff}}}\left(\frac{\partial u}{\partial t}\right) = -\frac{\partial P}{\partial z} - \frac{\mu_{\mathrm{f}}}{K}u - \frac{c_{\mathrm{E}}\rho_{\mathrm{f}}}{K^{1/2}}|u|u \tag{3.4}$$

where u is the superficial flow velocity (also known as Darcy velocity), z is the position along the regenerator length, K is the permeability and c_{E} is the Ergun constant. The term $\vec{v}.\nabla\vec{v}$ disappears for an incompressible flow, while the Brinkman viscous term disappeared due to the low porosity. The body forces were neglected and the real porosity was replaced by the effective porosity, which represents the actual volume occupied by the fluid.

In order to provide closure to the governing equation, the permeability and the Ergun constant still need to be analysed. The permeability, according to Darcy's law, is a measure of the flow conductance of the matrix (KAVIANY, 1995) and does not depend on the fluid (if the fluid does not affect or change the porous medium). A common expression for the permeability has the following form:

$$K = \frac{\varepsilon_{\mathrm{eff}} d_{\mathrm{h}}^2}{16 k_{\mathrm{K}}} \tag{3.5}$$

where k_{K} is the Kozeny constant and d_{h} is the hydraulic diameter, which can be calculated for a packed bed of spheres using the following expression (TREVIZOLI, 2015):

$$d_{\mathrm{h}} = \frac{2}{3}\frac{\varepsilon_{\mathrm{eff}}}{1-\varepsilon_{\mathrm{eff}}} d_{\mathrm{P}} \tag{3.6}$$

where d_{P} is the particle diameter. There have been many proposed values of the Kozeny constant for a packed bed of spheres and other media, for which a comprehensive list can be found in Ozgumus, Mobedi & Ozkol (2014). In this work, the selected value of $k_{\mathrm{K}} = 9.375$ was originally proposed by Ergun (1952). The expression for the Ergun constant was also the one proposed by Ergun (1952) for a packed bed of spheres, which is given by Equation 3.7.

$$c_{\mathrm{E}} = \frac{1.75}{\sqrt{16 k_{\mathrm{K}} \varepsilon_{\mathrm{eff}}^3}} \tag{3.7}$$

With expressions for both the permeability and the Ergun constant, and having the mass flow rate (and therefore the velocity) as an input (independent) parameter while using averaged properties, Equation 3.4 can be used directly to determine the pressure drop along the regenerator.

3.3.2 Fluid Phase Energy Equation

The one-dimensional macroscopic energy conservation equation for the fluid phase is given by:

$$\rho_f c_{p,f}\left(\varepsilon_{eff}\frac{\partial T_f}{\partial t} + u\frac{\partial T_f}{\partial z}\right) = h\beta(T_s - T_f) + \left|u\frac{\partial P}{\partial z}\right| + \varepsilon_{eff}[k_f^{eff} + \rho_f c_{p,f} D_{\parallel}]\frac{\partial^2 T_f}{\partial z^2} + \dot{q}_{csg} \tag{3.8}$$

where the terms on the left side of the equation are the thermal capacity and longitudinal advection, and the ones on the right are due to interstitial heat transfer, viscous dissipation, axial conduction in the porous medium (KAVIANY, 1995) and heat transfer between the porous medium and the regenerator casing, respectively. Obtaining the value of the last term requires solving the energy equations in the casing and air gap, which is the subject of Section 3.5.2.

In the axial conduction therm, k_f^{eff} is the effective thermal conductivity of the fluid, which is the volume averaged thermal conductivity that describes the macroscopic heat transfer along the porous medium. For a packed bed of spheres, it is given by (KAVIANY, 1995):

$$\frac{k_f^{eff}}{k_f} = \varepsilon_{eff} \tag{3.9}$$

and $D_{\parallel}$ is the longitudinal thermal dispersion, which represents the dispersion that occurs in the porous medium due to non uniform effects of velocity and volume averaging of the temperature field (OZGUMUS et al., 2011). In this case, the dispersion occurs due to fluid mixing along the direction of the flow (TREVIZOLI, 2015). For a packed bed of spheres, the longitudinal dispersion is given by (KOCH; BRADY, 1985):

$$\frac{D_{\parallel}}{\alpha_f} = \left(\frac{Pe_{dp}}{2}\right)^2 \frac{\sqrt{2}}{60(\sqrt{1-\varepsilon_{eff}})} \quad \text{for} \quad \left(\frac{Pe_{dp}}{2}\right)^2 << 1 \tag{3.10}$$

$$\frac{D_{\parallel}}{\alpha_f} = 0.75\frac{Pe_{dp}}{2} \quad \text{for} \quad \frac{Pe_{dp}}{2} > 1 \tag{3.11}$$

where the Peclet number is based on the particle diameter ($Pe_{dp} = ud_P/\alpha_f$).

The interstitial heat transfer coefficient (h) and the surface area density of the porous medium (β) in the heat transfer term will be discussed further ahead. Since this equation is solved uncoupled from the momentum equation, both u and $\frac{\partial P}{\partial z}$ are the input parameters. Solving Equation 3.8 will yield the fluid temperature profile along the regenerator during each instant of the AMR cycle.

3.3.3 Solid Phase Energy Equation

The macroscopic energy conservation equation for the solid phase is given by:

$$\rho_s c_H(1-\varepsilon)\frac{\partial T_s}{\partial t} = h\beta(T_f - T_s) + (1-\varepsilon)k_s^{eff}\frac{\partial^2 T_s}{\partial z^2} + \dot{q}_{MCE} \tag{3.12}$$

where the term on the left represents the heat capacity of the solid, while the terms on the right represent the interstitial heat transfer, axial conduction in the porous medium and the magnetocaloric effect (source term). This equation only considers the magnetocaloric material without the epoxy, so ε is used as the porosity. Constant values of density and thermal conductivity are used for the solid phase ($7000\,\mathrm{kg\,m^{-3}}$ and $8\,\mathrm{W\,m^{-1}\,K^{-1}}$ respectively), while the specific heat capacity is dependent on both temperature and applied field (magnetic flux density).

As in the fluid energy equation, an effective thermal conductivity ($k_\mathrm{s}^\mathrm{eff}$) is used in the axial conduction term. In order to calculate it, the correlation proposed by Hadley (1986) is used:

$$\frac{k_\mathrm{s}^\mathrm{eff}}{k_\mathrm{f}} = (1-\alpha_0)\frac{\varepsilon_\mathrm{f} f_0 + (1-\varepsilon_\mathrm{f} f_0)\frac{k_\mathrm{s}^\mathrm{eq}}{k_\mathrm{f}}}{1-\varepsilon_\mathrm{f}(1-f_0)+\frac{k_\mathrm{s}^\mathrm{eq}}{k_\mathrm{f}}\varepsilon_\mathrm{f}(1-f_0)} + \alpha_0\frac{2(\frac{k_\mathrm{s}^\mathrm{eq}}{k_\mathrm{f}})^2(1-\varepsilon_\mathrm{f})+(1+2\varepsilon_\mathrm{f})\frac{k_\mathrm{s}^\mathrm{eq}}{k_\mathrm{f}}}{(2+\varepsilon_\mathrm{f})\frac{k_\mathrm{s}^\mathrm{eq}}{k_\mathrm{f}}+(1-\varepsilon_\mathrm{f})} \tag{3.13}$$

where $f_0 = 0.8$ and $log\ \alpha_0 = -1.084 - 6.778(\varepsilon_f - 0.298)$ for $0.298 < \varepsilon_f < 0.58$. k_s^eq is the equivalent conductivity of the solid phase considering both the MCM and the epoxy, which will be described in Sections 3.5.4 and 3.6.3.

The magnetocaloric effect is implemented as a heat source term in the energy equation, using the so-called built-in approach. This method best describes situations where the magnetic field changes continuously, but requires detailed and numerically differentiable data sets for the magnetization and specific heat as a function of temperature and magnetic field (NIELSEN et al., 2011). In this method, the source term is given by (ENGELBRECHT, 2008; NIELSEN et al., 2011):

$$\dot{q}_\mathrm{MCE}(t,z) = -\rho_\mathrm{s}(1-\varepsilon)T_\mathrm{s}\frac{\partial s(B,T_\mathrm{s})}{\partial B}\frac{\partial B}{\partial t} \tag{3.14}$$

where s is the solid phase specific entropy and B is the magnetic flux density ($B = \mu_0 H$). In the solid phase energy equation, porous medium properties and the interstitial heat transfer coefficient are the input parameters, therefore Equation 3.12 will yield the instantaneous solid phase temperature profile along the regenerator in the AMR cycle.

3.4 Fluid and Solid Phase Properties Modeling

In this section, the methods used to determine the physical properties of both phases will be discussed. The method used to determine the fluid properties is simple and uses values obtained from a database. The solid-phase properties, however, require more steps and need to be handled carefully, since mistakes in their calculation can lead to internal inconsistencies that could generate wrong results, such as a a rejected heat rate lower than the cooling capacity of the thermodynamic cycle.

3.4.1 Fluid Phase Properties

The fluid used in the model, which is the same heat transfer fluid used in the most experiments is a 2.0 wt% solution of ENTEK FNE in deionized water to avoid degradation of the MCM. Due to the low mass fraction of ENTEK FNE (an organic anti-corrosion fluid), the properties are assumed identical to those of water, and are obtained from the Engineering Equation Solver (EES) software database (KLEIN, 2013).

3.4.2 Solid Phase Properties

The properties of the magnetocaloric material depend on both the temperature and the applied field. Being a first-order phase transition material, the MCM investigated here may present hysteresis effects, which makes their implementation in the model considerably harder. Furthermore, the properties of the material change considerably with the Curie temperature and the manufacturing process. Due to the above mentioned factors and the relatively recent development of first-order phase transition magnetocaloric materials, there are no established databases or correlations for these properties.

Therefore, the properties had to be measured using samples of the material supplied by VACUUMSCHMELZE GmbH — VAC. These samples were sent to the Istituto Nazionale di Ricerca Metrologica (INRiM) where their properties were measured using the method described in detail by Basso, Sasso & Küpferling (2010), which returned results of isofield specific heat capacity and entropy as a function of temperature for four different applied magnetic flux densities (0, 0.5, 1.0 and 1.5 T). The magnetization was measured at LABCAM-UFSC using a Physical Properties Measurement System's magnetometer (PPMS EverCool-II™ P935). Three types of $La(Fe,Mn,Si)_{13}H_z$ alloys manufactured by VAC were used henceforth termed CV-H, CV-HS and CV-HS-2, with CV standing for CALORIVAC [1], which is the name given by VAC to these materials. During manufacturing, CV-HS and CV-HS-2 were expected to have a higher concentration of α-Fe, which increases mechanical stability, but reduces the magnetocaloric properties and consequently the MCE. However, later tests showed that the concentration of α-Fe in CV-HS-2 was very similar to that of CV-H (11 - 13 wt.%) and that the concentration of α-Fe in CV-HS was much lower (around 2.5 wt.%), as will be discussed in Section 4.1. The isofield specific heat capacity results obtained by INRiM then need to be fitted into a curve in order to be interpolated to intermediate values of applied magnetic flux density for use in the model. For CV-H and CV-HS, the results were fitted into an asymmetric Lorentzian distribution using the method described in detail in Bez (2016) and briefly in Appendix D. This method proved incapable of fitting the results for CV-HS-2 and thus a different equation, which was derived from the shape of the entropy curves

[1] The CALORIVAC catalogue can be found in https://vacuumschmelze.com/products/Further-Technologies/Magnetocaloric-Material–CALORIVAC

and is also shown in Appendix D, was used. The measured values of isofield specific heat capacity for samples with different Curie temperatures of CV-H and CV-HS after the fitting are shown in Figure 26.

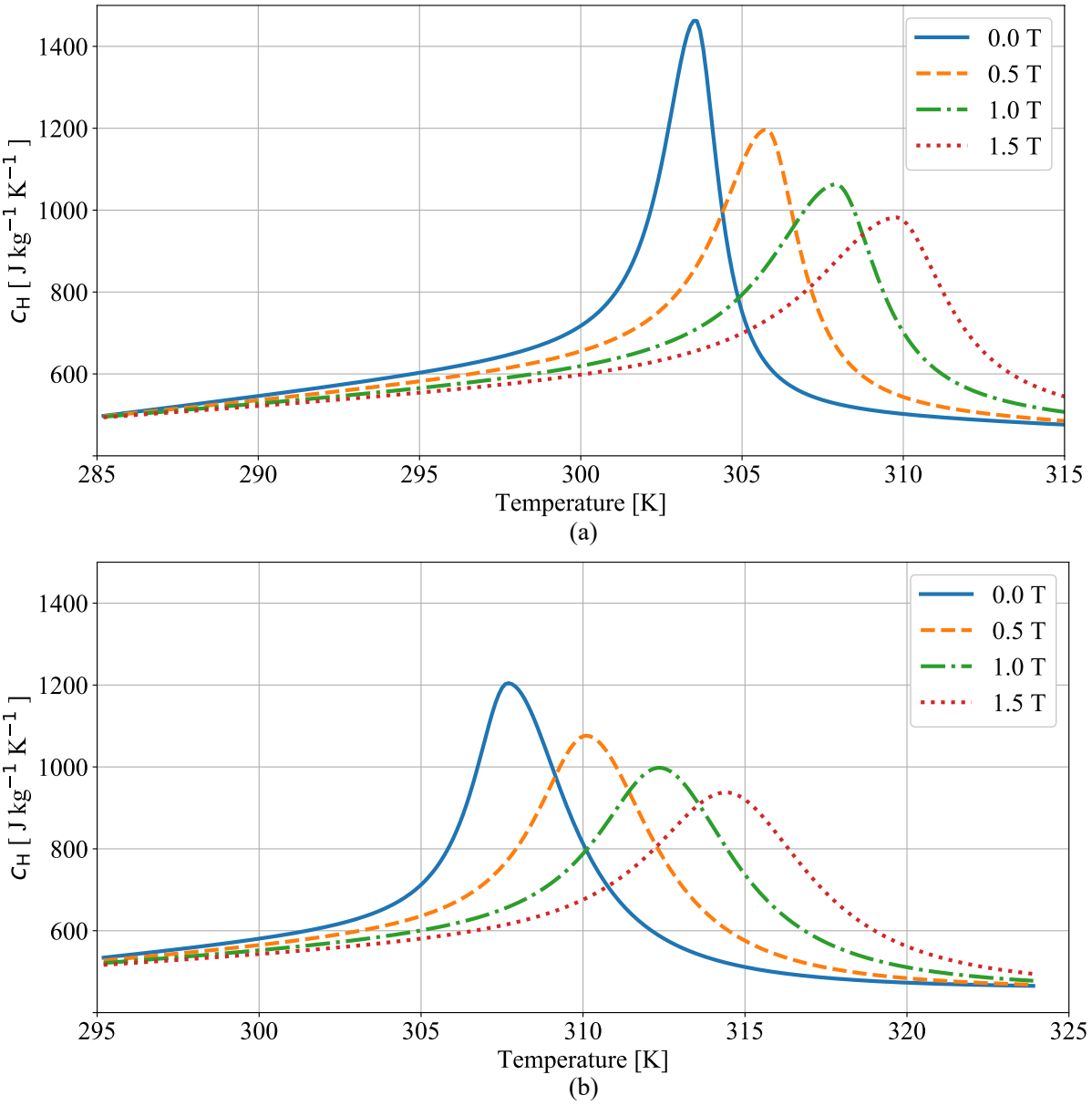

Figure 26 – Specific heat capacity of (a) CV-H and (b) CV-HS measured in four different applied magnetic flux densities.

For all three materials, the resulting coefficients of the fitting are then interpolated to generate the specific heat capacity curves for fields between 0 T and 1.5 T with a step of 0.01 T. The results for CV-HS-2 along with detailed descriptions of the interpolation process and of the physical properties can be found in Appendix D. A property which can be derived from the INRiM results is the adiabatic temperature change (ΔT_{ad}), which is used to calculate the value of $\frac{\partial s}{\partial H}$ using the following thermodynamic

relationship:

$$\frac{c_{\mathrm{H}}}{T_{\mathrm{s}}}\, dT_{ad} = -\frac{\partial s}{\partial H} dH \tag{3.15}$$

where the adiabatic temperature change resulting from the change in magnetic field is calculated as an equivalent change in entropy. While the value of $\frac{\partial s}{\partial H}$ could be calculated directly from the interpolated entropy profiles, the use of Equation 3.15 was observed to better guarantee the internal consistency of the properties and the overall energy balance. For CV-HS-2, which went through a different fitting process, $\frac{\partial s}{\partial H}$ was calculated directly from the entropy profiles and the internal consistency of the properties did not seem to be affected. The values of $\frac{\partial s}{\partial H}$ for CV-H and CV-HS are shown in Figure 27. Note that, as originally expected, CV-H has a considerably larger MCE (larger $\frac{\partial s}{\partial H}$) than CV-HS, especially at low fields, which makes it more desirable from the thermal point of view.

3.4.3 Property Shift

One of the major requirements of the mathematical model is that it must be able to simulate regenerators with multiple layers and, therefore, multiple Curie temperatures (T_{Curie}). Ideally, the number and values of these T_{Curie} should also be easily modifiable between simulations. In practice, this would require measurements of many materials with different values of T_{Curie}, which would be impossible.

In order to circumvent this problem, a procedure called shifting is used. This procedure involves using the properties of one specific alloy composition (one specific T_{Curie}) as a reference for all layers of the regenerator. This means that all layers are assumed to have the same properties as the reference, but shifted along the temperature axis to match their respective T_{Curie}. An example of this procedure is shown in Figure 28 where the values of $\frac{c_{\mathrm{H}}}{T}$ of the reference material (T_{Curie} = 307.7 K) is shifted to represent a real material with a Curie temperature of 297.7 K. Note that apart from the position along the temperature axis, both property profiles are exactly the same.

This shift is also used to determine all of the other physical properties already mentioned for each T_{Curie}. However, care must be taken to keep the properties internally consistent during the procedure. This becomes clear when shifting the specific heat capacity since, by definition, it depends on the temperature. A direct shift of both entropy and specific heat would create an inconsistency between the value of $(\frac{\partial s}{\partial T})_{\mathrm{H}}$ calculated directly from the entropy and from the definition of c_{H}. Therefore, the shift needs to be applied to the value of $\frac{c_{\mathrm{H}}}{T}$ as shown in Figure 28, which is effectively the same as shifting $(\frac{\partial s}{\partial T})_{\mathrm{H}}$ directly, so all the properties remain internally consistent. Correctly shifting the properties guarantees that the conservation of energy is compatible when considering either the specific heat or the entropy when the field is constant, i.e., that

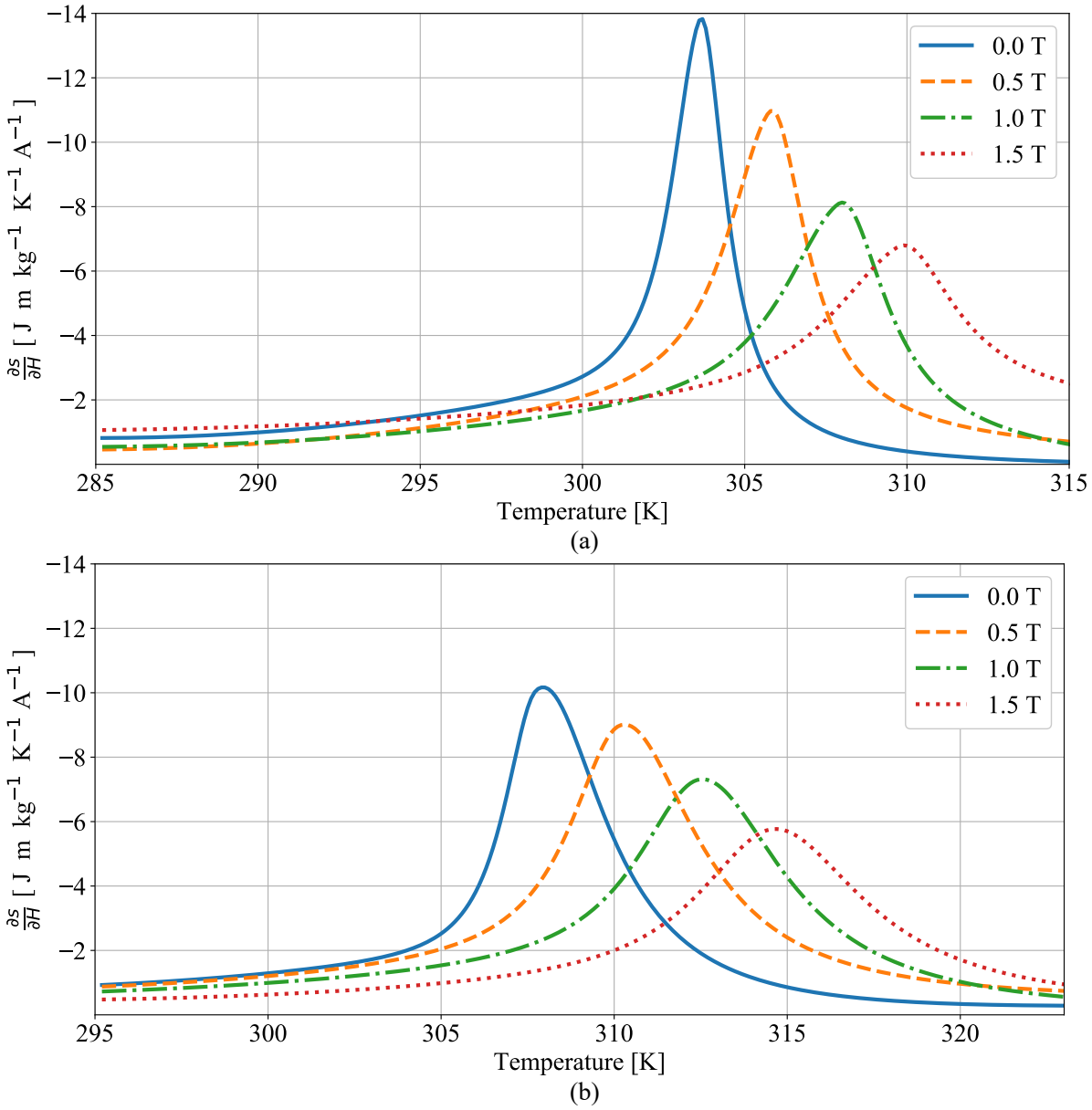

Figure 27 – Values of $\frac{\partial s}{\partial H}$ for (a) CV-H and (b) CV-HS for four different values of the applied magnetic flux density.

the following equation holds for constant applied magnetic fields:

$$c_{\mathrm{H}} dT = T_{\mathrm{s}} ds \tag{3.16}$$

Thus, if the value of c_{H} is shifted incorrectly, the left and right sides of this equation would not be equal, which would make the model internally inconsistent.

3.5 Losses Modeling

There are four main sources of losses in the system that need to be modeled in order to appropriately describe and compare the theoretical results and the experi-

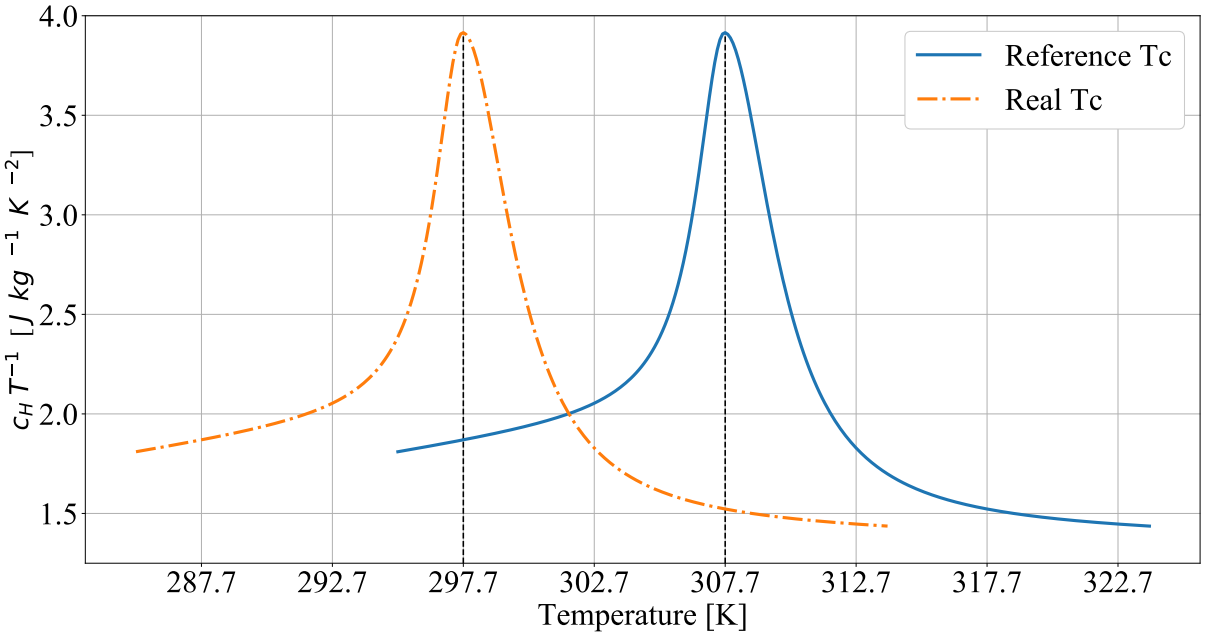

Figure 28 – Example of the $\frac{c_H}{T}$ shift used in the model to determine the properties of any given T_{Curie}.

mental data. The first one is due to the void (dead) volumes shown in Figure 25, which are the volumes located between the ends of the regenerator and the reservoirs. During one blow, a portion of fluid goes through the regenerator but does not reach the heat exchangers and remains in these volumes. Not only does this fluid fail to exchange heat with the reservoirs, but it also returns to the regenerator during the next blow, reducing its performance.

Another loss, which is ignored in many AMR models (NIELSEN et al., 2011), is due to heat transfer between the regenerator and the surroundings which, depending on the thermal insulation used and the temperature gradients involved, can become very significant.

The third loss occurs due to demagnetizing effects, which result in an effective (or internal) magnetic field vector which is different from the magnetic field applied on the material. In order to calculate the effective magnetic field, the so-called internal demagnetizing field, which is proportional to the magnetization and the demagnetizing tensor, needs to be determined.

Finally, the last loss that will be considered is due to the epoxy resin used to bond the regenerator. The epoxy has two negative effects on the performance of an AMR: it clogs some of the channels in the porous medium, increasing the pressure drop, and it adds an extra resistance to the heat exchange between the fluid and solid phases.

3.5.1 Void Volumes

As described before, there are two void volumes attached to the regenerator, located between their ends and the reservoirs, as shown in Figure 29. During a given blow, fluid that comes from the regenerators will go through these volumes to the heat exchangers, but when the blow ends some of the fluid will remain inside them. Since this fluid does not interact with the heat exchangers, it does not contribute to the heat exchange with the reservoirs and will return to the regenerator in the next blow. Thus, the temperature of the fluid in the void volume will be the temperature of the fluid entering the regenerator during each blow, which is time dependent. In order to determine these temperatures, the energy equations in both void volumes need to be solved coupled with the energy equations in the regenerator.

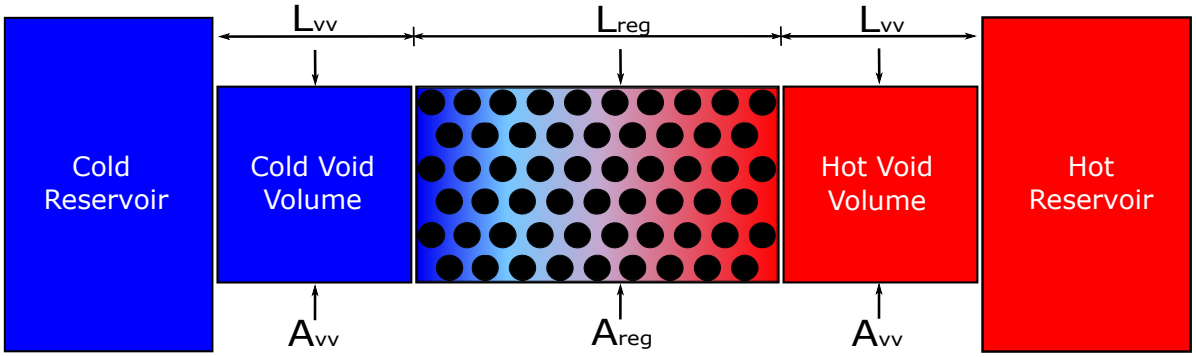

Figure 29 – Representation of the basic geometry of the regenerator including the void volumes.

The assumptions made to derive the energy equation for the void volumes were:

- The heat transfer between the fluid and the walls in the void volumes is negligible;
- Both void volumes are identical and have the same cross-sectional area as the regenerator ($A_{vv} = A_{reg}$);
- The flow is one dimensional, laminar and incompressible.

The assumption that A_{vv} is equal to A_{reg} requires L_{vv} to be adjusted to match the volume of the actual void volume. This will guarantee that the volume of fluid that does not reach the reservoirs and returns to the regenerator is the same as in the real system. With these assumptions, the void volume energy equation becomes:

$$\frac{\partial T_f^{vv}}{\partial t} = -u\frac{\partial T_f^{vv}}{\partial z} + \alpha_f \frac{\partial^2 T_f^{vv}}{\partial z^2} \tag{3.17}$$

where the term on the left side of the equation is related to the thermal capacity and the terms on the right are the longitudinal advection and axial conduction, respectively.

Solving this equation yields the temperature profile along both void volumes during each instant along the AMR cycle.

3.5.2 Casing Losses

During regular operation, a regenerator will gain heat from the outside environment though the casing, which will negatively impact its performance. This loss can be reduced by insulating the regenerator, but due to the little room available inside the magnetic gap, properly insulating the AMR is not practical (TREVIZOLI, 2015).

In order to determine the casing losses, the heat transfer rate per unit volume through the casing wall ($\dot{q}_{csg}$) needs to be calculated. It is then used as a source term in the fluid energy equation (Equation 3.8). To determine the value of $\dot{q}_{csg}$, the energy equations in both the casing and the air gap between the casing and the magnetic circuit need to be solved. A representation of these adjacent domains is shown in Figure 30.

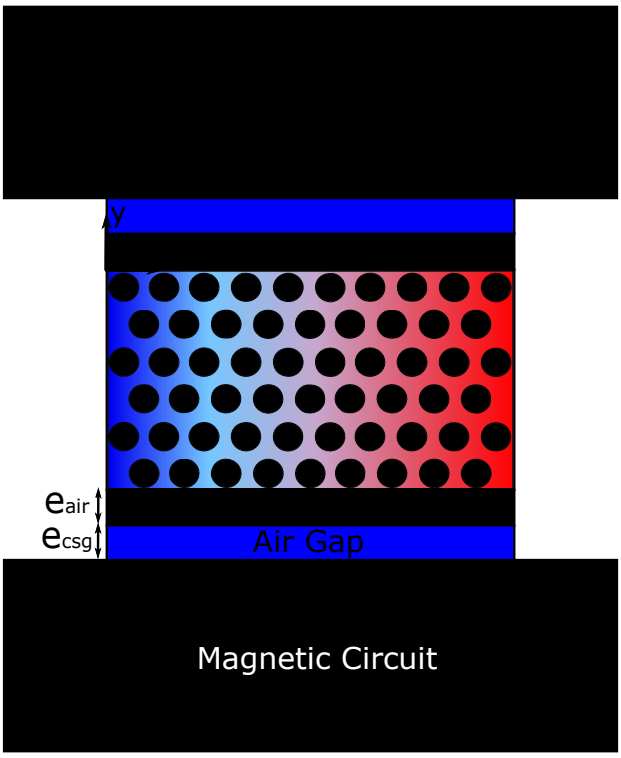

Figure 30 – Representation of the basic geometry of the regenerator including the casing, air gap and magnetic circuit.

The simplifying assumptions associated with the heat transfer modeling in the casing are:

- The air properties are only a function of temperature;
- The curvature of the regenerator is negligible, allowing the use of a cartesian coordinate system;

- The magnetic circuit has a constant temperature due to its large thermal capacity;
- The heat transfer is two-dimensional (radial and longitudinal);
- The physical properties of the wall are constant and the thermal conductivity is isotropic (for stainless steel).

With these assumptions, the energy balance in the air gap can be written as:

$$\rho_{\text{air}} c_{\text{p,air}} \frac{\partial T_{\text{air}}}{\partial t} = k_{\text{air}} \frac{\partial^2 T_{\text{air}}}{\partial y^2} + k_{\text{air}} \frac{\partial^2 T_{\text{air}}}{\partial z^2} + \dot{q}_{\text{air}} \tag{3.18}$$

where $\dot{q}_{air}$ is the viscous dissipation rate per unit volume which, assuming laminar Couette flow in the gap, is given by:

$$\dot{q}_{\text{air}} = \mu_{\text{air}} \left(\frac{\omega R}{e_{\text{air}}} \right)^2 \tag{3.19}$$

where ω is the angular speed and R is the internal radius of the magnetic circuit. Similarly, the energy balance for the casing wall is given by:

$$\rho_{\text{wall}} c_{\text{wall}} \frac{\partial T_{\text{wall}}}{\partial t} = k_{\text{wall}} \frac{\partial^2 T_{\text{wall}}}{\partial y^2} + k_{\text{wall}} \frac{\partial^2 T_{\text{wall}}}{\partial z^2} \tag{3.20}$$

which is the 2-D heat equation for a solid without internal generation. Solving Equations 3.18 through 3.20 yields the temperature profile along the casing wall and air gap. This profile can then be used to calculate $\dot{q}_{csg}$:

$$\dot{q}_{\text{csg}} = -h_{\text{wall}} \frac{p_{\text{reg}}}{A_{\text{reg}}} (T_{\text{f}} - T_{\text{wall}}|_{\text{y=0}}) \tag{3.21}$$

where p_{reg} is the inner perimeter of the regenerator and h_{wall} is the heat transfer coefficient between the casing wall and the fluid which, for packed beds of spheres, is given by the relation proposed by Li & Finlayson (1977):

$$Nu_{\text{dp}}^{\text{wall}} = \frac{h_{\text{wall}} d_{\text{P}}}{k_{\text{f}}} = 0.17 Re_{\text{dp}}^{0.79} \quad \text{for} \quad 20 \leq Re_{\text{dp}} \leq 7600 \tag{3.22}$$

where Re_{dp} is the Reynolds number based on the particle diameter:

$$Re_{\text{dp}} = \frac{\rho_{\text{f}} u d_{\text{P}}}{\mu_{\text{f}}} \tag{3.23}$$

This correlation was chosen because it was based on h_{wall} data for a spherical particle system and because of its applicability to a wide range of Reynolds numbers (WAKAO; KAGUEI, 1982).

3.5.3 Demagnetizing Effects

As mentioned before, subjecting a magnetic material to a magnetic flux density creates an internal demagnetizing field which will cause the effective magnetic field to be lower than the applied magnetic field:

$$\vec{H}_{\text{eff}} = \vec{H}_{\text{apl}} - \vec{H}_{\text{dem}}(\vec{H}_{\text{eff}}, T) \tag{3.24}$$

where the demagnetizing field can be obtained from the product between the magnetization and the demagnetization tensor:

$$\vec{H}_{\text{dem}}(\vec{H}_{\text{apl}}, T) = \overline{\overline{N}}_{\text{D}}\vec{M}(\vec{H}_{\text{eff}}, T) \tag{3.25}$$

However, for a homogeneous temperature solid, the demagnetization tensor becomes a scalar (TREVIZOLI, 2015) and Equation 3.24 can be simplified to:

$$H_{\text{eff}} = H_{\text{apl}} - N_{\text{D}}M(H_{\text{eff}}, T) \tag{3.26}$$

When designing a regenerator, one should bear in mind that having a small effective magnetic field reduces the magnetocaloric effect, which in turn reduces the cooling capacity and the regenerator temperature span. Because of that, it is necessary to aim for a small product between the demagnetization factor and the magnetization. The magnetization is a property of the material and is particularly high when it is in the ferromagnetic phase ($T < T_{\text{C}}$). On the other hand, the demagnetization factor is dependent on the regenerator geometry and its orientation in relation to the applied field.

The demagnetization factor can be divided in two parts: the demagnetization factor due to the casing geometry ($N_{\text{D,csg}}$) and the demagnetization factor due to the matrix geometry ($N_{\text{D,geo}}$). For a packed bed of spheres, $N_{\text{D,geo}} = 1/3$ (TREVIZOLI, 2015). The casing demagnetization factor for a cylindrical regenerator is estimated with the relation proposed by Sato & Ishii (1989):

$$N_{\text{D,x}} = N_{\text{D,y}} = \frac{\frac{L_{\text{reg}}}{D_{\text{reg}}}}{2\frac{L_{\text{reg}}}{D_{\text{reg}}} + 1} \tag{3.27}$$

The demagnetization factor for a prismatic regenerator is estimated with the relation proposed by (AHARONI, 1998). For a packed bed of spheres, the total demagnetization factor is then given by (COEY, 2010):

$$N_{\text{D}} = N_{\text{D,geo}} + (1 - \varepsilon)(N_{\text{D,csg}} - N_{\text{D,geo}}) \tag{3.28}$$

Trevizoli et al. (2012) showed that, for an isothermal parallel-plate regenerator, $H_{\text{eff}}/H_{\text{apl}}$ agrees well with a more complex model that assumes a linear temperature profile along the plates. With this in mind, the present model calculates the effective

magnetic field assuming a linear temperature profile along the regenerator with values ranging from the hot and cold reservoirs temperatures. This gives an average temperature for every finite volume in the regenerator, which is used along with the applied field to obtain the magnetization of each volume. Then, Equations 3.26 to 3.28 are solved to obtain the effective magnetic field in each volume, which is used to estimate new values of magnetization, restarting the process. The process is repeated until convergence and results in the effective magnetic field profile along the regenerator during the cycle, $H_{\text{eff}}(t, z)$, which is kept constant during the remainder of the simulation.

3.5.4 Epoxy Losses

Navickaitė et al. (2018) tested regenerators made from $La(Fe,Mn,Si)_{13}H_z$ with different amounts of epoxy (from 1 wt.% to 4 wt.%) and analysed their mechanical integrity while in operation. The regenerator with 1 wt.% of epoxy broke during operation and two regenerators with 2 wt.% showed mechanical degradation. Because of that, most regenerators analysed in this work had at least 2.7 wt% of epoxy in order to guarantee their mechanical integrity. The epoxy, however, while good for the mechanical performance of the regenerator, also causes the previously mentioned problems of clogging channels and reducing the heat exchange between the fluid and porous medium, which need to be considered in the model.

In order to determine the thermal resistance of the epoxy within the regenerator bed, the following assumptions were made:

- The bed is formed by perfect, mono-disperse spheres;
- The epoxy completely covers the spheres forming a layer with a thickness L_{ep};
- The epoxy is homogeneously distributed along the regenerator, so all spheres are covered with the same amount of epoxy;
- The epoxy layer is thin, so the surface area of the layer can be approximated by the surface area of the sphere;
- The heat conduction through the epoxy layer can be calculated as if through a plane wall.

These assumptions are further illustrated in Figure 31, which also shows the new thermal resistance associated with the conduction through the epoxy layer around the sphere. Based on the last assumption, the conduction resistance is given by:

$$R_{\text{cond}} = \frac{L_{\text{ep}}}{k_{\text{ep}} A_{\text{dp}}} \tag{3.29}$$

where, as shown in Appendix A:

$$L_{ep} = \frac{1}{2}\left[d_P\left(\frac{\varepsilon - \varepsilon_f}{1-\varepsilon} + 1\right)^{\frac{1}{3}} - 1\right] \tag{3.30}$$

where ε and ε_f are, respectively, the porosity considering only the MCM and considering both the MCM and epoxy, as detailed in Section 3.2. The effective porosity, ε_{eff}, which is also discussed in that section, is used to determine the other loss caused by the epoxy: clogging. This porosity will always be smaller or equal to ε_f, depending on the degree of clogging, and will result in higher pressure drops in the regenerator. However, differently from the other porosities and the epoxy layer thickness, there is no analytical way to determine the value of ε_{eff}, thus requiring an empirical estimation for each regenerator.

To do that, the regenerator is subjected to independent steady flow isothermal experiments in order to measure the pressure drop as a function of the mass flow rate. This result then needs to be fitted to the steady-state version of Equation 3.4, which is a function of the particle diameter, d_P, and the effective porosity, ε_{eff}. The particle diameter, however, is independently obtained from dynamic laser scattering (DLS) results, leaving only the effective porosity as an independent variable. An example of a fitting done on a 3-layered, 50-mm long regenerator is shown in Figure 32. In this case, the fitting ($R^2 = 0.994$) yielded a value for ε_{eff} of approximately 0.29, in contrast with $\varepsilon_f \approx 0.37$. More details about this process will be presented in Chapter 5.

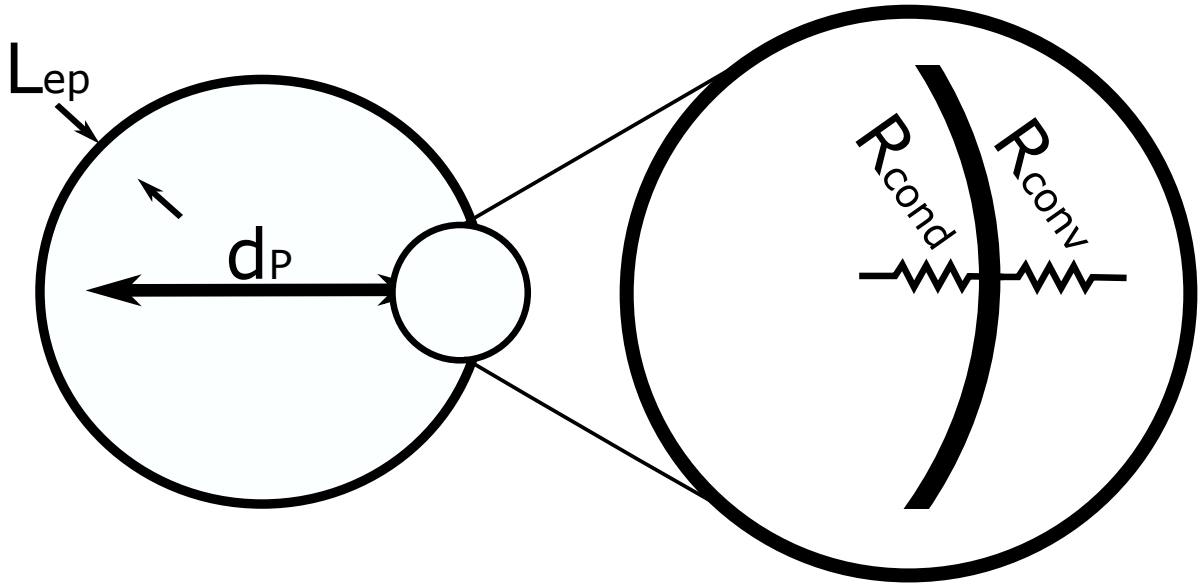

Figure 31 – Representation of a sphere of MCM covered by epoxy and the thermal resistances associated with them.

Lastly, a secondary effect of the clogging needs to be considered: the reduction of the heat transfer area. This is so because the interstitial area of the porous medium in the clogged channels is not available for thermal exchange with the fluid, and this

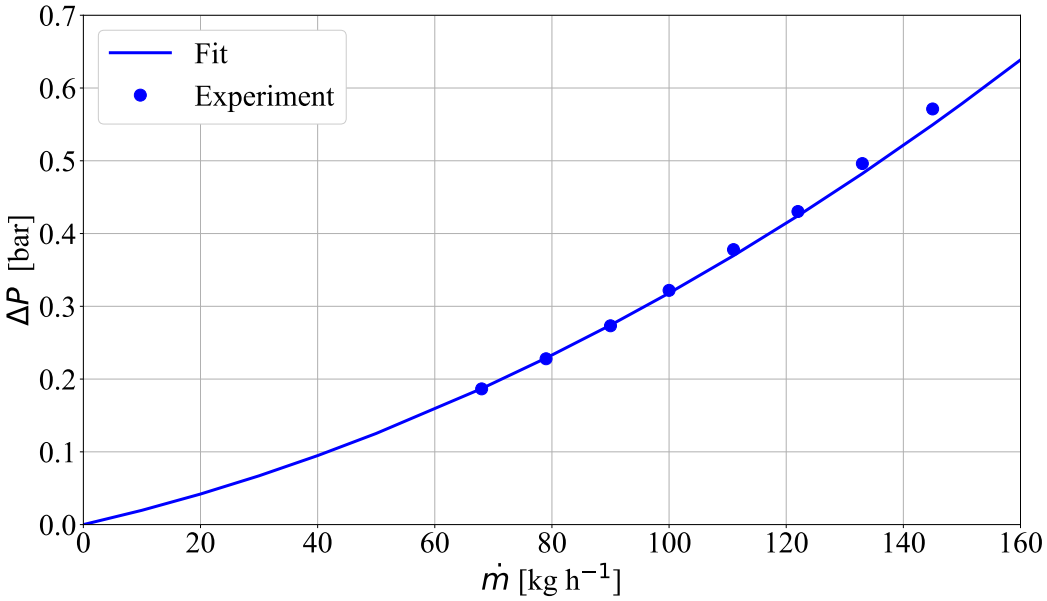

Figure 32 – Fitting of the pressure drop as a function of the mass flow rate for the steady flow isothermal experiments.

needs to be taken into account in the model. Assuming that the heat transfer area is homogeneously distributed along the regenerator, the fraction of area that effectively exchanges heat is given by the ratio between the effective and real porosities, $\varepsilon_{\text{eff}}/\varepsilon_{\text{f}}$. This term will appear when estimating the surface area density of the porous medium, β.

3.6 Heat Transfer Modeling

In order to model the heat transfer between the solid and fluid phases in the porous medium, two parameters need to be determined: the surface area density of the porous medium, β, and the interstitial heat transfer coefficient, h. The value of β for a packed bed of spheres can be obtained geometrically, but the value of h needs to be estimated from appropriate Nusselt number relationships found in the literature.

3.6.1 *Surface Area Density*

The surface area density of a porous medium is defined as the ratio between the interstitial area and the total volume of the porous medium as follows (KAVIANY, 1995):

$$\beta = (1 - \varepsilon_{\text{f}})\frac{A_{\text{int}}}{V_{\text{s}}} \tag{3.31}$$

where the term $\frac{A_{\text{int}}}{V_{\text{s}}}$ is the interstitial area per unit of solid volume which, for a packed bed of spheres is given by:

$$\frac{A_{\text{int}}}{V_{\text{s}}} = \frac{6}{d_{\text{P}}} \tag{3.32}$$

This, combined with Equation 3.31 gives the expression for β in an open pore (unclogged) porous medium:

$$\beta = (1 - \varepsilon_{\text{f}})\frac{6}{d_{\text{P}}} \tag{3.33}$$

However, to take into account the clogging discussed in Section 3.5.4, the value of β needs to be adjusted considering the effective porosity:

$$\beta = \frac{\varepsilon_{\text{eff}}}{\varepsilon_{\text{f}}}(1 - \varepsilon_{\text{f}})\frac{6}{d_{\text{P}}} \tag{3.34}$$

which will return values ranging from the open pore area density of Equation 3.33 to zero, if the medium is completely clogged.

3.6.2 Interstitial Heat Transfer Coefficient

In the open literature, there are several Nusselt number correlations for packed beds of spheres, such as the ones proposed by Gunn (1978), Wakao & Kaguei (1982), Kuwahara, Shirota & Nakayama (2001) and Pallares & Grau (2010), which is presented in Equation 3.35. In this work, the latter correlation was chosen because of its validity over a wide range of Prandtl numbers, porosities between 0.2 and 0.9 and low Reynolds numbers ($Re_{\text{dp}} < 100$), and for its good agreement with experimental data (TREVIZOLI, 2015). The effective porosity is used in Equation 3.35 to be consistent with the definition of the corrected surface area density in Equation 3.34. Not coincidentally, this led to a very good agreement with the experimental results generated in the present work. These results and a further discussion about the process leading to the selection of this correlation will be shown in Chapter 5.

$$Nu_{\text{dp}} = \frac{hd_{\text{P}}}{k_f} = 2\left(1 + \frac{4(1 - \varepsilon_{\text{eff}})}{\varepsilon_{\text{eff}}}\right) + (1 - \varepsilon_{\text{eff}})^{1/2} Re_{\text{dp}}^{0.6} Pr^{1/3} \tag{3.35}$$

3.6.3 Solid Phase Thermal Resistance

A thermal resistance not considered thus far is the total resistance within the solid material (including the epoxy layer). If this thermal resistance is much smaller than the interstitial convection resistance, then the matrix can be assumed to have a homogeneous temperature. However, if the solid thermal resistance is larger than the one in the fluid, the uniform solid-phase temperature assumption needs to be corrected. The dimensionless parameter used to determine if the assumption is valid is the Biot

number, Bi, defined in terms of the heat transfer coefficient between the fluid and the matrix obtained with Equation 3.35, $Bi = \frac{hL_c}{k}$, where L_c is the characteristic length of the solid given by the ratio of its volume to the exposed surface area, $L_c \equiv V/A_s$ (BERGMAN et al., 2011). Therefore, for a sphere of MCM, one has $L_c = d_P/6$ and, for the epoxy layer, $L_c \approx L_{ep}$ (for a small L_{ep}).

In order to calculate the Biot number using the above assumptions, the sphere of MCM and epoxy is treated as a composite material with a characteristic length $L_c = d_P/6 + L_{ep}$, and an equivalent thermal resistance given by:

$$k_{eq} = \left(\frac{d_P}{6} + L_{ep}\right)\left(\frac{d_P}{6k_s} + \frac{L_{ep}}{k_{ep}}\right)^{-1} \tag{3.36}$$

these values can then be used to calculate the Biot number which, as shown by Engelbrecht (2004), affects the convection heat transfer coefficient according to the following expression:

$$h_{eff} = \frac{h}{1 + \frac{Bi}{5}} \tag{3.37}$$

The final factor to be analysed is the Fourier number, $Fo = \frac{\alpha\tau}{L_c^2}$, which can be interpreted as the ratio between the cycle period and the time required for a thermal wave to reach the center of the sphere. A large Fourier number implies that the thermal wave reaches far into the sphere, allowing most of the sphere to participate in the energy storage process. If the Fourier number is small, the thermal wave does not properly penetrate the sphere, allowing only the outer surface to participate in the energy storage process. The Fourier number is also calculated considering a composite solid, and its influence in the heat exchange process is calculated used the correlation proposed by Engelbrecht (2008):

$$h_{eff} = \frac{h}{1 + \frac{Bi}{5}\chi(Fo)} \tag{3.38}$$

where:

$$\chi(Fo) = Fo\,\exp\left[0.246196 - 0.84878\,\ln(Fo) - 0.05639(\ln(Fo))^2\right] \tag{3.39}$$

A further discussion on the influence of the Biot and Fourier numbers can be found in Appendix A.

3.7 Solution Method

Of all governing equations, Equations 3.4, 3.8, 3.12, 3.17, 3.18 and 3.20, only the fluid momentum equation, Equation 3.4, was not solved using the finite volume method (PATANKAR, 1980; MALISKA, 2004). In order to use this method, the domains had to

be divided in control volumes in which each equation was integrated and discretized. The momentum equation, on the other hand, can be solved directly due to the variables involved only being time-dependent and the properties assumed constant, therefore uncoupling the momentum and energy equations.

3.7.1 Momentum Equation

The momentum equation, Equation 3.4, is solved differently from all other equations. This is because both the Darcy velocity, u, and the pressure drop, $\frac{\partial P}{\partial z}$, depend only on the time and not the position along the regenerator. This, together with the profile of $u(t)$ being used as an input parameter in the model, allows for the pressure drop to be directly calculated from Equation 3.4 with the derivative of the velocity being calculated using the finite difference method:

$$\frac{\partial P}{\partial z}(t) = \frac{\rho_f}{\varepsilon_{eff}}\left[\frac{u(t+\Delta t) - u(t)}{\Delta t}\right] - \frac{\mu_f}{K}u(t) - \frac{c_E \rho_f}{K^{1/2}}|u(t)|u(t) \tag{3.40}$$

Since this equation does not require any iterative solution, it is solved at the beginning of the routine before the energy equations, which require iterative solution processes, are solved.

The model allows for two different $u(t)$ analytical profiles to be set: (i) an instantaneous (step) profile, which has the shape of a square wave and (ii) a ramped profile, which has the shape of a trapezoidal wave. These profiles are shown in Figure 33, along with the relevant periods which are used to define them. The step profile is given by the following equations:

$$u(t) = \begin{cases} 0, & \text{if} \quad 0 \le t < \frac{1}{2}(\frac{\tau}{2} - \tau_{CB}) \\ |u_{max,CB}|, & \text{if} \quad \frac{1}{2}(\frac{\tau}{2} - \tau_{CB}) \le t < \frac{1}{2}(\frac{\tau}{2} - \tau_{CB}) + \tau_{CB} \\ 0, & \text{if} \quad \frac{1}{2}(\frac{\tau}{2} - \tau_{CB}) + \tau_{CB} \le t < \frac{1}{2}(\frac{\tau}{2} - \tau_{HB}) + \frac{\tau}{2} \\ -|u_{max,HB}|, & \text{if} \quad \frac{1}{2}(\frac{\tau}{2} - \tau_{HB}) + \frac{\tau}{2} \le t < \frac{1}{2}(\frac{\tau}{2} - \tau_{HB}) + \frac{\tau}{2} + \tau_{HB} \\ 0, & \text{if} \quad \frac{1}{2}(\frac{\tau}{2} - \tau_{HB}) + \frac{\tau}{2} + \tau_{HB} \le t \le \tau \end{cases} \tag{3.41}$$

which generate the square wave form with the cold and hot blows centralized at $\frac{\tau}{4}$ and $\frac{3\tau}{4}$, respectively. To change the synchronization, the resulting vector $u(t)$ can be shifted backwards or forwards as required. The values of $u_{max,CB}$ and $u_{max,HB}$ are calculated from the imposed mass flow rate according to the following expression:

$$u_{max,CB,HB} = \frac{\dot{m}_{CB,HB}}{\rho_f A_{reg}} \tag{3.42}$$

The ramped profile is more complex than the step profile and allows for different opening and closing times, and therefore its equations are considerably longer. A

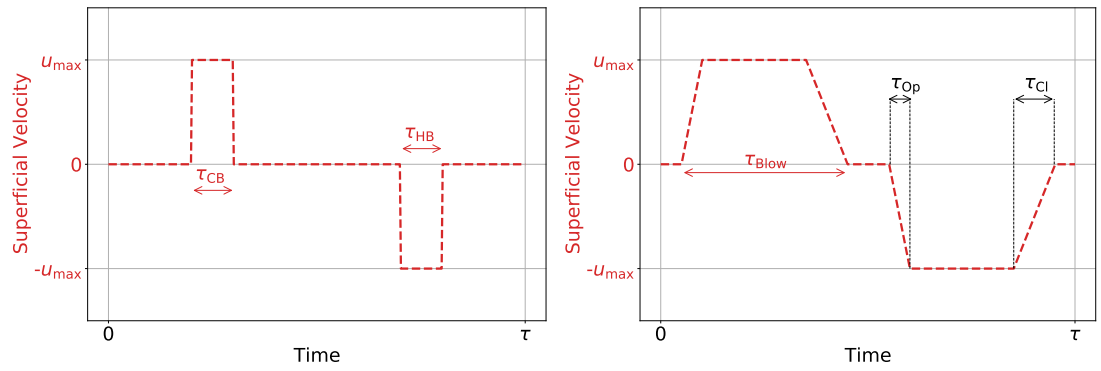

(a) (b)

Figure 33 – (a) Square and (b) trapezoidal waveforms of the superficial velocity profile.

simpler version of the equations, which allows only for blows with the same profile (but different maximum mass flow rates) is given by:

$$u(t) = \begin{cases} 0, \quad \text{if} \quad 0 \leq t < \frac{1}{2}(\frac{\tau}{2} - \tau_{\text{Blow}}) \\ |u_{\text{max,CB}}|\frac{1}{\tau_{\text{Op}}}[t - \frac{1}{2}(\frac{\tau}{2} - \tau_{\text{Blow}})], \quad \text{if} \quad \frac{1}{2}(\frac{\tau}{2} - \tau_{\text{Blow}}) \leq t < \frac{1}{2}(\frac{\tau}{2} - \tau_{\text{Blow}}) + \tau_{\text{Op}} \\ |u_{\text{max,CB}}|, \quad \text{if} \quad \frac{1}{2}(\frac{\tau}{2} - \tau_{\text{Blow}}) + \tau_{\text{Op}} \leq t < \frac{1}{2}(\frac{\tau}{2} - \tau_{\text{Blow}}) + \tau_{\text{Blow}} - \tau_{\text{Cl}} \\ |u_{\text{max,CB}}|\frac{1}{\tau_{\text{Cl}}}(\frac{\tau}{4} + \frac{\tau_{\text{Blow}}}{2} - t), \quad \text{if} \quad \frac{1}{2}(\frac{\tau}{2} - \tau_{\text{Blow}}) + \tau_{\text{Blow}} - \tau_{\text{Cl}} \leq t < \frac{1}{2}(\frac{\tau}{2} - \tau_{\text{Blow}}) + \tau_{\text{Blow}} \\ 0, \quad \text{if} \quad \frac{1}{2}(\frac{\tau}{2} - \tau_{\text{Blow}}) + \tau_{\text{Blow}} \leq t < \frac{\tau}{2} \\ -|u(t - \frac{\tau}{2})|\frac{u_{\text{max,HB}}}{u_{\text{max,CB}}}, \quad \text{if} \quad \frac{\tau}{2} \leq t \leq \tau \end{cases} \tag{3.43}$$

where τ_{Op} and τ_{Cl} are the opening and closing periods shown in Figure 33. Once again, the resulting vector can be shifted backwards or forwards to change synchronization. A more detailed analysis of these profiles can be found in Section 5.6.1.

3.7.2 *Energy Equations*

Both the fluid and solid energy equations, Equations 3.8 and 3.12, are one-dimensional and can be written in the same generic form:

$$\frac{\partial}{\partial t}(\Psi T) = -\frac{\partial}{\partial z}(\Lambda u T) + \frac{\partial^2}{\partial z^2}(\Gamma T) + S \tag{3.44}$$

where Ψ, Λ and Γ are the generic parameters of the transient, advective and diffusion terms, respectively, and S is the source term. In order to be discretized, Equation 3.44 is integrated in both time and space in the control volume for the 1-D domain shown

in Figure 34 (a) using the fully implicit scheme:

$$\int_t^{t+\Delta t}\int_w^e \frac{\partial}{\partial t}(\Psi T)\,dz\,dt = -\int_t^{t+\Delta t}\int_w^e \frac{\partial}{\partial z}(\Lambda u T)\,dz\,dt + \int_t^{t+\Delta t}\int_w^e \frac{\partial^2}{\partial z^2}(\Gamma T)\,dz\,dt + \int_t^{t+\Delta t}\int_w^e S\,dz\,dt \tag{3.45}$$

Maliska (2004) recommends linearizing the source term, S, to avoid divergence of the solution. This, however, has not been done here because the model did not show any divergence problems. The term is therefore assumed to be constant during the integration. Solving Equation 3.45 yields:

$$(\Psi_P T_P - \Psi_P^o T_P^o)\frac{\Delta z}{\Delta t} = -[(\Lambda u T)_e - (\Lambda u T)_w] + \left(\Gamma_e \frac{\partial T}{\partial z}\bigg|_e - \Gamma_w \frac{\partial T}{\partial z}\bigg|_w\right) + S\Delta z \tag{3.46}$$

which is the general discretization of the 1-D energy equations that will be used to solve Equations 3.8, 3.12 and 3.17. The values of the generic parameters for each of these equations is show in Table 4.

Table 4 – Variables in the 1-D energy equations.

Equation	Ψ	Λ	Γ	**S**
Fluid	$\rho_f \varepsilon_{eff}$	ρ_f	$\varepsilon_{eff}\left(\frac{k_f^{eff}}{c_{p,f}} + \rho_f D_{\parallel}\right)$	$\frac{h\beta}{c_{p,f}}(T_s - T_f) + \left\lvert \frac{u}{c_{p,f}}\frac{\partial P}{\partial z}\right\rvert + \frac{\dot{q}_{csg}}{c_{p,f}}$
Solid	$\rho_s c_H(1-\varepsilon)$	0	$(1-\varepsilon)k_s^{eff}$	$h\beta(T_f - T_s) + \dot{q}_{MCE}$
Void Volume	1	1	α_f	0

The generic form of the 2-D energy equations in this problem is:

$$\frac{\partial}{\partial t}(\Psi T) = \frac{\partial^2}{\partial y^2}(\Gamma_y T) + \frac{\partial^2}{\partial z^2}(\Gamma_z T) + S \tag{3.47}$$

where Ψ is the generic parameter of the transient term and Γ_y and Γ_z are the generic parameters of the diffusion terms in directions y and z, respectively. Following the discretization process, Equation 3.47 is integrated in both time and space in the control volume for the 2-D domain shown in Figure 34 (b) using the fully implicit scheme:

$$\int_t^{t+\Delta t}\int_w^e\int_s^n \frac{\partial}{\partial t}(\Psi T)\,dy\,dz\,dt = \int_t^{t+\Delta t}\int_w^e\int_s^n \frac{\partial^2}{\partial y^2}(\Gamma_y T)\,dy\,dz\,dt + \int_t^{t+\Delta t}\int_w^e\int_s^n \frac{\partial^2}{\partial z^2}(\Gamma_z T)\,dy\,dz\,dt + \int_t^{t+\Delta t}\int_w^e\int_s^n S\,dy\,dz\,dt \tag{3.48}$$

where the source term is once again assumed to be constant and $\Gamma_y = \Gamma_z$. Solving Equation 3.47 gives:

$$(\Psi_P T_P - \Psi_P^o T_P^o)\frac{\Delta y \Delta z}{\Delta t} = \left(\Gamma_{y,n}\frac{\partial T}{\partial y}\bigg|_n - \Gamma_{y,s}\frac{\partial T}{\partial y}\bigg|_s\right)\Delta z + \left(\Gamma_{z,e}\frac{\partial T}{\partial z}\bigg|_e - \Gamma_{z,n}\frac{\partial T}{\partial z}\bigg|_w\right)\Delta y + S\Delta z\Delta y \tag{3.49}$$

which is the general discretization of the 2-D energy equations used to solve Equations 3.18 and 3.20. The values of the generic parameters for these equations are shown in Table 5.

Table 5 – Variables in the 2-D energy equations.

Equation	Ψ	Γ	**S**
Air	$\rho_{air}c_{p,air}$	k_{air}	$\dot{q}_{air}$
Wall	$\rho_{wall}c_{wall}$	k_{wall}	0

3.7.3 Fluid Phase Energy Equation

The first step needed to solve the energy equation for the fluid is to determine a method to calculate the values of Λ and Γ at the eastern and western interfaces of the finite volume. This requires a method to calculate the fluid properties at those interfaces. It is important that the method is applied in such a manner that the properties at a given interface will be the same regardless of the finite volume in contact with it that is being analysed. Therefore, a generic property ϕ at an interface will be calculated as the average value of this property between the adjacent volumes forming the interface:

$$\phi_e = \frac{\phi_P + \phi_E}{2} \tag{3.50}$$

$$\phi_w = \frac{\phi_P + \phi_W}{2} \tag{3.51}$$

This applies to all fluid properties evaluated at the interface, with the only exception being the density, which is evaluated at the mean temperature and assumed constant in order to guarantee the conservation of mass (LANG, 2018). The values of the properties at the interfaces of the western and eastern boundaries of the regenerator are assumed to be equal to those of their respective adjacent finite volume.

The interpolation of the temperature values at the interfaces was made using the Weighted Upstream Differencing Scheme (WUDS). This method uses α^{WUDS} and β^{WUDS} as weight coefficients for the advective and diffusion terms, respectively. Both weights are a function of the Peclet number as follows (MALISKA, 2004):

$$\alpha_{e,w}^{WUDS} = 0.5 - \frac{\exp(Pe_{e,w}/2) - 1}{\exp(Pe_{e,w}) - 1} \tag{3.52}$$

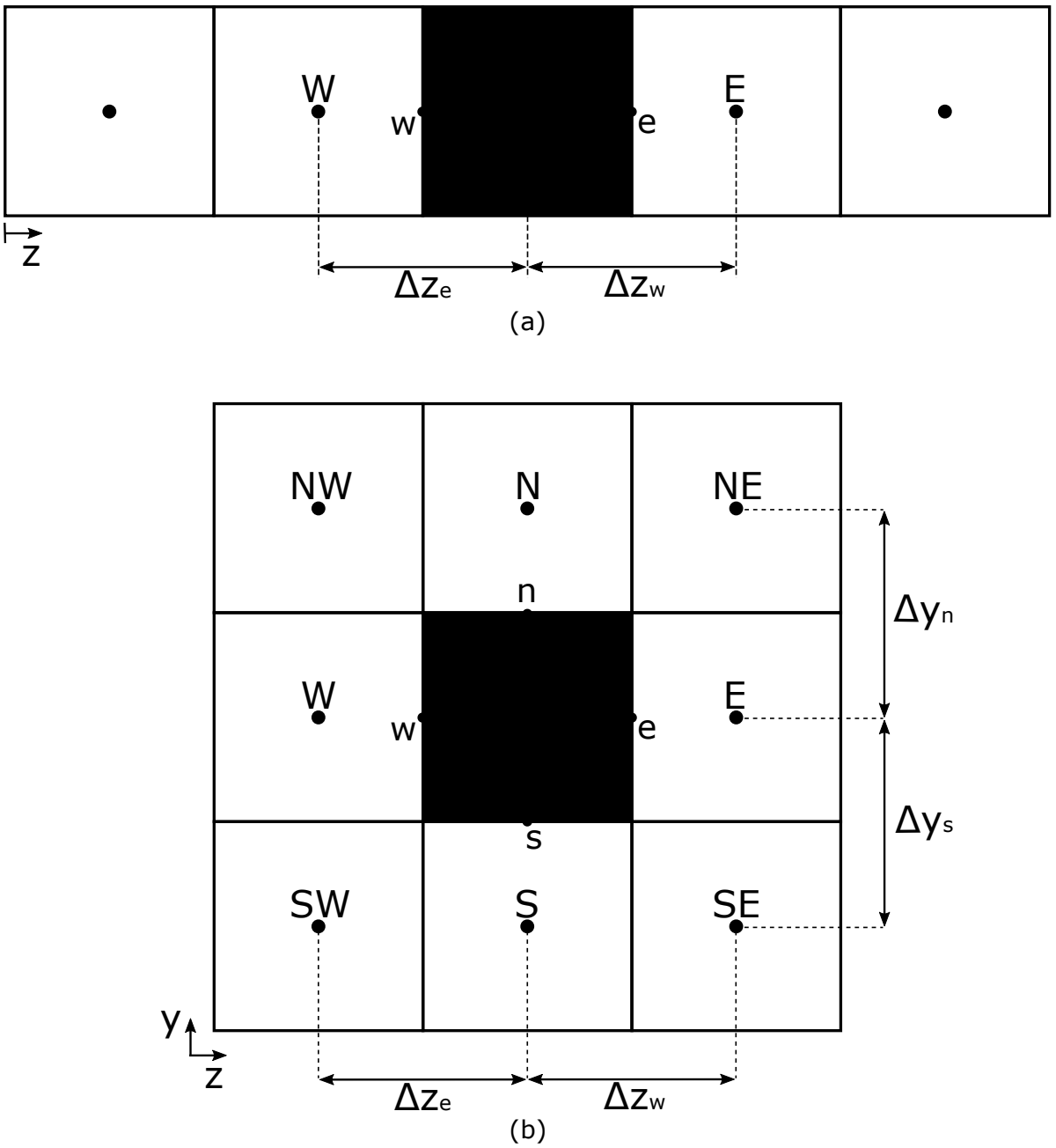

Figure 34 – Grids of control volumes for the (a) 1-D domain and (b) 2-D domain. Adapted from Trevizoli (2015).

$$\beta_{e,w}^{WUDS} = Pe_{e,w}\frac{\exp(Pe_{e,w}/2)}{\exp(Pe_{e,w}) - 1} \tag{3.53}$$

and the temperatures and their derivatives in the interface are given by:

$$T_{f,e} = (0.5 + \alpha_e^{WUDS})T_{f,P} + (0.5 - \alpha_e^{WUDS})T_{f,E} \tag{3.54}$$

$$T_{f,w} = (0.5 + \alpha_w^{WUDS})T_{f,W} + (0.5 - \alpha_w^{WUDS})T_{f,P} \tag{3.55}$$

$$\left.\frac{\partial T_\mathrm{f}}{\partial z}\right|_\mathrm{e} = \beta_\mathrm{e}^{\mathrm{WUDS}}\left(\frac{T_{\mathrm{f,E}} - T_{\mathrm{f,P}}}{\Delta z_\mathrm{e}}\right) \tag{3.56}$$

$$\left.\frac{\partial T_\mathrm{f}}{\partial z}\right|_\mathrm{w} = \beta_\mathrm{w}^{\mathrm{WUDS}}\left(\frac{T_{\mathrm{f,P}} - T_{\mathrm{f,W}}}{\Delta z_\mathrm{w}}\right) \tag{3.57}$$

Applying Equations 3.50 to 3.57 to Equation 3.46 results in an equation with the form:

$$a_\mathrm{p} T_\mathrm{P} = a_\mathrm{e} T_\mathrm{E} + a_\mathrm{w} T_\mathrm{W} + b \tag{3.58}$$

where:

$$a_\mathrm{e} = \rho_\mathrm{f} u(\alpha_\mathrm{e}^{\mathrm{WUDS}} - 0.5) + \frac{\beta_\mathrm{e}^{\mathrm{WUDS}}}{(\delta z)_\mathrm{e}} \varepsilon_{\mathrm{eff}}\left(\frac{k_\mathrm{f}^{\mathrm{eff}}}{c_{\mathrm{p,f}}} + \rho_\mathrm{f} D_{\parallel}\right)_\mathrm{e} \tag{3.59}$$

$$a_\mathrm{w} = \rho_\mathrm{f} u(\alpha_\mathrm{w}^{\mathrm{WUDS}} + 0.5) + \frac{\beta_\mathrm{w}^{\mathrm{WUDS}}}{(\delta z)_\mathrm{w}} \varepsilon_{\mathrm{eff}}\left(\frac{k_\mathrm{f}^{\mathrm{eff}}}{c_{\mathrm{p,f}}} + \rho_\mathrm{f} D_{\parallel}\right)_\mathrm{w} \tag{3.60}$$

$$a_\mathrm{p}^\mathrm{o} = \rho_\mathrm{f} \varepsilon_{\mathrm{eff}} \frac{\Delta z}{\Delta t} \tag{3.61}$$

$$a_\mathrm{p} = a_\mathrm{e} + a_\mathrm{w} + a_\mathrm{p}^\mathrm{o} + \frac{h\beta}{c_{\mathrm{p,f}_\mathrm{P}}} \Delta z \tag{3.62}$$

$$b = \frac{h\beta}{c_{\mathrm{p,f}_\mathrm{P}}} \Delta z T_{\mathrm{s,P}} + \frac{\Delta z}{c_{\mathrm{p,f}_\mathrm{P}}} \left| u \frac{\partial P}{\partial z} \right| + a_\mathrm{p}^\mathrm{o} T_\mathrm{p}^\mathrm{o} + \dot{q}_{\mathrm{csg}} \frac{\Delta z}{c_{\mathrm{p,f}_\mathrm{P}}} \tag{3.63}$$

which can be used to solve the energy equation for the fluid in all volumes except the right and left boundaries, where the values of T_E and T_W are not defined, respectively.

For these volumes, it is necessary to determine the boundary conditions of the fluid phase energy equation. In the case of the fluid, the boundary conditions depend on the type of blow: Cold Blow ($u > 0$), Hot Blow ($u < 0$) and No Blow ($u = 0$). When $u > 0$, the boundary condition consists of a prescribed temperature at the western inlet ($T_\mathrm{f}(z = 0) = T_\mathrm{C}$) and an adiabatic eastern outflow ($\frac{\partial T_\mathrm{f}}{\partial z}(z = L) = 0$). When $u < 0$, the boundary conditions are inverted, having a prescribed temperature at the eastern inlet ($T_\mathrm{f}(z = L) = T_H$) and an adiabatic western outflow ($\frac{\partial T_\mathrm{f}}{\partial z}(z = 0) = 0$). Finally, if $u = 0$ both boundaries are assumed to be adiabatic ($\frac{\partial T_\mathrm{f}}{\partial z}(z = 0) = \frac{\partial T_\mathrm{f}}{\partial z}(z = L) = 0$). When void (dead) volumes are considered, those boundary conditions are applied at the ends of the void volumes instead of the ends of the regenerator. The appropriate coefficients of Equation 3.58 for the boundary volumes considering the boundary conditions without void volumes are shown in Tables 6 and 7. Note that $a_{\mathrm{w,f}}$ and $a_{\mathrm{e,f}}$ are auxiliary variables and should not be mistaken with a_w and a_e.

Table 6 – Coefficients of Equation 3.58 in the western volume for the fluid phase.

	Cold (Western) Volume
$u > 0$	$a_e = \rho_f u(\alpha_e^{WUDS} - 0.5) + \frac{\beta_e^{WUDS}}{(\delta z)_e}\varepsilon_{eff}\left(\frac{k_f^{eff}}{c_{p,f}} + \rho_f D_{\parallel}\right)_e$
	$a_w = 0$
	$a_{w,f} = \rho_f u + \frac{2}{(\delta z)_w}\varepsilon_{eff}\left(\frac{k_f^{eff}}{c_{p,f}} + \rho_f D_{\parallel}\right)_w$
	$a_p^o = \rho_f \varepsilon_{eff}\frac{\Delta z}{\Delta t}$
	$a_p = a_e + a_{w,f} + a_p^o + \frac{h\beta}{c_{p,f\,P}}\Delta z$
	$b = \frac{h\beta}{c_{p,f\,P}}\Delta z T_{s,P} + \frac{\Delta z}{c_{p,f\,P}}\left\lvert u\frac{\partial P}{\partial z}\right\rvert + a_p^o T_p^o + \dot{q}_{csg}\frac{\Delta z}{c_{p,f\,P}} + a_{w,f}T_C$
$u < 0$	$a_e = \rho_f u(\alpha_e^{WUDS} - 0.5) + \frac{\beta_e^{WUDS}}{(\delta z)_e}\varepsilon_{eff}\left(\frac{k_f^{eff}}{c_{p,f}} + \rho_f D_{\parallel}\right)_e$
	$a_w = 0$
	$a_p^o = \rho_f \varepsilon_{eff}\frac{\Delta z}{\Delta t}$
	$a_p = a_e + a_w + a_p^o + \frac{h\beta}{c_{p,f\,P}}\Delta z$
	$b = \frac{h\beta}{c_{p,f\,P}}\Delta z T_{s,P} + \frac{\Delta z}{c_{p,f\,P}}\left\lvert u\frac{\partial P}{\partial z}\right\rvert + a_p^o T_p^o + \dot{q}_{csg}\frac{\Delta z}{c_{p,f\,P}}$
$u = 0$	$a_e = \rho_f u(\alpha_e^{WUDS} - 0.5) + \frac{\beta_e^{WUDS}}{(\delta z)_e}\varepsilon_{eff}\left(\frac{k_f^{eff}}{c_{p,f}} + \rho_f D_{\parallel}\right)_e$
	$a_w = 0$
	$a_p^o = \rho_f \varepsilon_{eff}\frac{\Delta z}{\Delta t}$
	$a_p = a_e + a_w + a_p^o + \frac{h\beta}{c_{p,f\,P}}\Delta z$
	$b = \frac{h\beta}{c_{p,f\,P}}\Delta z T_{s,P} + \frac{\Delta z}{c_{p,f\,P}}\left\lvert u\frac{\partial P}{\partial z}\right\rvert + a_p^o T_p^o + \dot{q}_{csg}\frac{\Delta z}{c_{p,f\,P}}$

3.7.4 Solid Phase Energy Equation

Similarly to the fluid energy equation, the first step needed to solve the solid phase energy equation is to determine a method to calculate the values of Λ and Γ at the eastern and western interfaces of the finite volume. This is, once again, done using Equations 3.50 and 3.51 to interpolate the solid properties in the interfaces. The treatment for the properties at the boundary interfaces is also the same.

For the diffusion terms, the derivative of the temperature is needed at the interfaces. In this case, the Central Difference Scheme (CDS) is used to interpolate this

Table 7 – Coefficients of Equation 3.58 in the eastern volume for the fluid phase.

	Hot (Eastern) Volume
$u > 0$	$a_e = 0$
	$a_w = \rho_f u(\alpha_w^{WUDS} + 0.5) + \frac{\beta_w^{WUDS}}{(\delta z)_w}\varepsilon_{eff}\left(\frac{k_f^{eff}}{c_{p,f}} + \rho_f D_{\parallel}\right)_w$
	$a_p^o = \rho_f \varepsilon_{eff}\frac{\Delta z}{\Delta t}$
	$a_P = a_e + a_w + a_p^o + \frac{h\beta}{c_{p,f_P}}\Delta z$
	$b = \frac{h\beta}{c_{p,f_P}}\Delta z T_{s,P} + \frac{\Delta z}{c_{p,f_P}}\left\lvert u\frac{\partial P}{\partial z}\right\rvert + a_p^o T_p^o + \dot{q}_{csg}\frac{\Delta z}{c_{p,f_P}}$
$u < 0$	$a_e = 0$
	$a_{e,f} = -\rho_f u + \frac{2}{(\delta z)_e}\varepsilon_{eff}\left(\frac{k_f^{eff}}{c_{p,f}} + \rho_f D_{\parallel}\right)_e$
	$a_w = \rho_f u(\alpha_w^{WUDS} + 0.5) + \frac{\beta_w^{WUDS}}{(\delta z)_w}\varepsilon_{eff}\left(\frac{k_f^{eff}}{c_{p,f}} + \rho_f D_{\parallel}\right)_w$
	$a_p^o = \rho_f \varepsilon_{eff}\frac{\Delta z}{\Delta t}$
	$a_P = a_{e,f} + a_w + a_p^o + \frac{h\beta}{c_{p,f_P}}\Delta z$
	$b = \frac{h\beta}{c_{p,f_P}}\Delta z T_{s,P} + \frac{\Delta z}{c_{p,f_P}}\left\lvert u\frac{\partial P}{\partial z}\right\rvert + a_p^o T_p^o + \dot{q}_{csg}\frac{\Delta z}{c_{p,f_P}} + a_{e,f}T_H$
$u = 0$	$a_e = 0$
	$a_w = \rho_f u(\alpha_w^{WUDS} + 0.5) + \frac{\beta_w^{WUDS}}{(\delta z)_w}\varepsilon_{eff}\left(\frac{k_f^{eff}}{c_{p,f}} + \rho_f D_{\parallel}\right)_w$
	$a_p^o = \rho_f \varepsilon_{eff}\frac{\Delta z}{\Delta t}$
	$a_P = a_e + a_w + a_p^o + \frac{h\beta}{c_{p,f_P}}\Delta z$
	$b = \frac{h\beta}{c_{p,f_P}}\Delta z T_{s,P} + \frac{\Delta z}{c_{p,f_P}}\left\lvert u\frac{\partial P}{\partial z}\right\rvert + a_p^o T_p^o + \dot{q}_{csg}\frac{\Delta z}{c_{p,f_P}}$

term, resulting in:

$$\left.\frac{\partial T_s}{\partial z}\right|_e = \left(\frac{T_{s,E} - T_{s,P}}{\Delta z_e}\right) \tag{3.64}$$

$$\left.\frac{\partial T_s}{\partial z}\right|_w = \left(\frac{T_{s,P} - T_{s,W}}{\Delta z_w}\right) \tag{3.65}$$

which, when applied to Equation 3.46, will once again result in an equation in the form:

$$a_P T_P = a_e T_E + a_w T_W + b \tag{3.66}$$

where:

$$a_{\mathrm{e}} = \frac{(1-\varepsilon)k_{\mathrm{s,e}}^{\mathrm{eff}}}{(\delta x_{\mathrm{e}})} \tag{3.67}$$

$$a_{\mathrm{w}} = \frac{(1-\varepsilon)k_{\mathrm{s,w}}^{\mathrm{eff}}}{(\delta x_{\mathrm{w}})} \tag{3.68}$$

$$a_{\mathrm{p}}^{\mathrm{o}} = \rho_{\mathrm{s}}(1-\varepsilon)c_{\mathrm{H,P}}\frac{\Delta z}{\Delta t} \tag{3.69}$$

$$a_{\mathrm{p}} = a_{\mathrm{e}} + a_{\mathrm{w}} + a_{\mathrm{p}}^{\mathrm{o}} + h\beta\Delta z \tag{3.70}$$

$$b = h\beta\Delta z T_{\mathrm{f,P}} + \dot{q}_{\mathrm{MCE}}\Delta z + a_{\mathrm{p}}^{\mathrm{o}}T_{\mathrm{P}}^{\mathrm{o}} \tag{3.71}$$

The solid phase boundary conditions are independent of the type of blow and of the presence of void volumes. Both boundaries are considered adiabatic at all times ($\frac{\partial T_{\mathrm{s}}}{\partial z}(z=0) = \frac{\partial T_{\mathrm{s}}}{\partial z}(z=L) = 0$) resulting in $a_{\mathrm{w}} = 0$ in the cold (western) volume and $a_{\mathrm{e}} = 0$ in the hot (eastern) volume, as shown in Table 8.

Table 8 – Coefficients of Equation 3.66 at the boundaries of the solid phase.

Cold (Western) Volume	**Hot (Eastern) Volume**
$a_{\mathrm{e}} = \frac{(1-\varepsilon)k_{\mathrm{s,e}}^{\mathrm{eff}}}{(\delta x_{\mathrm{e}})}$	$a_{\mathrm{e}} = 0$
$a_{\mathrm{w}} = 0$	$a_{\mathrm{w}} = \frac{(1-\varepsilon)k_{\mathrm{s,w}}^{\mathrm{eff}}}{(\delta x_{\mathrm{w}})}$
$a_{\mathrm{p}}^{\mathrm{o}} = \rho_{\mathrm{s}}(1-\varepsilon)c_{\mathrm{H,P}}\frac{\Delta z}{\Delta t}$	$a_{\mathrm{p}}^{\mathrm{o}} = \rho_{\mathrm{s}}(1-\varepsilon)c_{\mathrm{H,P}}\frac{\Delta z}{\Delta t}$
$a_{\mathrm{p}} = a_{\mathrm{e}}+a_{\mathrm{w}} + a_{\mathrm{p}}^{\mathrm{o}} + h\beta\Delta z$	$a_{\mathrm{p}} = a_{\mathrm{e}}+a_{\mathrm{w}} + a_{\mathrm{p}}^{\mathrm{o}} + h\beta\Delta z$
$b = h\beta\Delta z T_{\mathrm{f,P}} + \dot{q}_{\mathrm{MCE}}\Delta z + a_{\mathrm{p}}^{\mathrm{o}}T_{\mathrm{P}}^{\mathrm{o}}$	$b = h\beta\Delta z T_{\mathrm{f,P}} + \dot{q}_{\mathrm{MCE}}\Delta z + a_{\mathrm{p}}^{\mathrm{o}}T_{\mathrm{P}}^{\mathrm{o}}$

The solver for both the solid and fluid energy equations is a line-by-line TDMA (Tri-Diagonal Matrix Algorithm). This is only possible because in both equations the resultant matrix of coefficients only has non-zero elements in the three main (central) diagonals. This method has the advantage of requiring computer storage and time proportional to N (number of volumes), instead of N^2 or N^3 (PATANKAR, 1980). Also, it does not require an iterative process. Both temperature profiles are initially assumed linear between the hot and cold reservoirs temperatures in order to accelerate convergence.

3.7.5 *Void Volume Energy Equation*

The void volume energy equation is very similar to that for the fluid, having its properties at the interfaces calculated with Equations 3.50 and 3.51 and using the

WUDS method to interpolate the temperature values at the interfaces. The weights are once again obtained using Equations 3.52 and 3.53, and the interpolation is done using Equations 3.54 to 3.57. With this, and using the values of Ψ, Λ, Γ and S shown in Table 4, the coefficients for the void volume equation become:

$$a_{\mathrm{e}} = u(\alpha_{\mathrm{e}}^{\mathrm{WUDS}} - 0.5) + \frac{\beta_{\mathrm{e}}^{\mathrm{WUDS}}}{(\delta z)_{\mathrm{e}}}\alpha_{\mathrm{f,e}} \tag{3.72}$$

$$a_{\mathrm{w}} = u(\alpha_{\mathrm{w}}^{\mathrm{WUDS}} + 0.5) + \frac{\beta_{\mathrm{w}}^{\mathrm{WUDS}}}{(\delta z)_{\mathrm{w}}}\alpha_{\mathrm{f,w}} \tag{3.73}$$

$$a_{\mathrm{p}}^{\mathrm{o}} = \frac{\Delta z}{\Delta t} \tag{3.74}$$

$$a_{\mathrm{p}} = a_{\mathrm{e}} + a_{\mathrm{w}} + a_{\mathrm{p}}^{\mathrm{o}} \tag{3.75}$$

$$b = a_{\mathrm{p}}^{\mathrm{o}} T_{\mathrm{p}}^{\mathrm{o}} \tag{3.76}$$

Considering the two void volumes, one at each end of the regenerator, four boundary conditions are needed, i.e., two for each void volume. These, like the fluid flow boundary conditions, also depend on the type of blow.

In the Cold Blow ($u > 0$), at the entrance of the cold void volume, an inlet boundary condition is applied, in which $T_{\mathrm{f}}^{\mathrm{vv}}(z = -L_{\mathrm{vv}}) = T_{\mathrm{C}}$ and the outflow is such that $\frac{\partial T_{\mathrm{f}}^{\mathrm{vv}}}{\partial z}(z = 0) = 0$. At the other side, the fluid leaving the regenerator enters the hot void volume, resulting in an inlet boundary condition of $T_{\mathrm{f}}^{\mathrm{vv}}(z = L) = T_{\mathrm{f}}(L)$ while the outlet is once again $\frac{\partial T_{\mathrm{f}}^{\mathrm{vv}}}{\partial z}(z = L + L_{\mathrm{vv}}) = 0$. In the Hot Blow ($u < 0$), the boundary conditions are simply inverted, with $\frac{\partial T_{\mathrm{f}}^{\mathrm{vv}}}{\partial z}(z = -L_{\mathrm{vv}}) = 0$, $T_{\mathrm{f}}^{\mathrm{vv}}(z = 0) = T_{\mathrm{f}}(0)$, $\frac{\partial T_{\mathrm{f}}^{\mathrm{vv}}}{\partial z}(z = L) = 0$ and $T_{\mathrm{f}}^{\mathrm{vv}}(z = L + L_{\mathrm{vv}}) = T_{\mathrm{H}}$. When there is no blow ($u = 0$), the ends of both void volumes are assumed adiabatic. The resulting coefficients for all boundary conditions are shown in Table 9. The TDMA method is also used to solve the energy equation for the void volumes. Note that when the void volumes are present the boundary conditions for the fluid phase inside the regenerator are affected, with the values of T_{C} and T_{H} in Tables 6 and 7 becoming $T_{\mathrm{f}}^{\mathrm{vv}}(z = 0)$ and $T_{\mathrm{f}}^{\mathrm{vv}}(z = L)$, respectively. Also, when void volumes are considered, the initial temperature profile of the fluid in both the void volumes and regenerator is assumed to be linear between the hot and cold reservoirs temperatures, slightly changing the initial estimation of the fluid temperature inside the regenerator.

3.7.6 Casing Energy Equation

The casing energy equation is the only 2-D equation solved in the model, and comprises two materials: the wall material (usually stainless steel) and air. The prop-

Table 9 – Coefficients of Equation 3.58 for the void volumes boundaries.

	Western Volume	**Eastern Volume**
$u > 0$ Cold VV: $T_{presc} = T_C$ Hot VV: $T_{presc} = T_f(L)$	$a_e = u(\alpha_e^{WUDS} - 0.5) + \frac{\beta_e^{WUDS}}{(\delta z)_e}\alpha_{f,e}$ $a_w = 0$ $a_{w,f} = u + \frac{2}{(\delta z)_w}\alpha_{f,w}$ $a_p^o = \frac{\Delta z}{\Delta t}$ $a_p = a_e + a_{w,f} + a_p^o$ $b = a_p^o T_p^o + a_{w,f} T_{presc}$	$a_e = 0$ $a_w = u(\alpha_e^{WUDS} + 0.5) + \frac{\beta_e^{WUDS}}{(\delta z)_e}\alpha_{f,e}$ $a_p^o = \frac{\Delta z}{\Delta t}$ $a_p = a_e + a_w + a_p^o$ $b = a_p^o T_p^o$
$u < 0$ Cold VV: $T_{presc} = T_f(0)$ Hot VV: $T_{presc} = T_H$	$a_e = u(\alpha_e^{WUDS} - 0.5) + \frac{\beta_e^{WUDS}}{(\delta z)_e}\alpha_{f,e}$ $a_w = 0$ $a_p^o = \frac{\Delta z}{\Delta t}$ $a_p = a_e + a_w + a_p^o$ $b = a_p^o T_p^o$	$a_e = 0$ $a_{e,f} = -u + \frac{2}{(\delta z)_e}\alpha_{f,e}$ $a_w = u(\alpha_w^{WUDS} + 0.5) + \frac{\beta_w^{WUDS}}{(\delta z)_w}\alpha_{f,w}$ $a_p^o = \frac{\Delta z}{\Delta t}$ $a_p = a_w + a_{e,f} + a_p^o$ $b = a_p^o T_p^o + a_{e,f} T_{presc}$
$u = 0$	$a_e = u(\alpha_e^{WUDS} - 0.5) + \frac{\beta_e^{WUDS}}{(\delta z)_e}\alpha_{f,e}$ $a_w = 0$ $a_p^o = \frac{\Delta z}{\Delta t}$ $a_p = a_e + a_w + a_p^o$ $b = a_p^o T_p^o$	$a_e = 0$ $a_w = u(\alpha_e^{WUDS} + 0.5) + \frac{\beta_e^{WUDS}}{(\delta z)_e}\alpha_{f,e}$ $a_p^o = \frac{\Delta z}{\Delta t}$ $a_p = a_e + a_w + a_p^o$ $b = a_p^o T_p^o$

erties of each material are considered constant and uniform, therefore an interpolation is only needed at the interface between materials. This interpolation is evaluated as:

$$k_{y,n} = \left(\frac{1-f}{k_{y,P}} + \frac{f}{k_{y,N}}\right) \tag{3.77}$$

where f is defined as the ratio between the segments shown in Figure 35:

$$f = \frac{\Delta y_{n+}}{\Delta y_n} \tag{3.78}$$

The temperatures are interpolated using the CDS scheme (linear interpolation), which

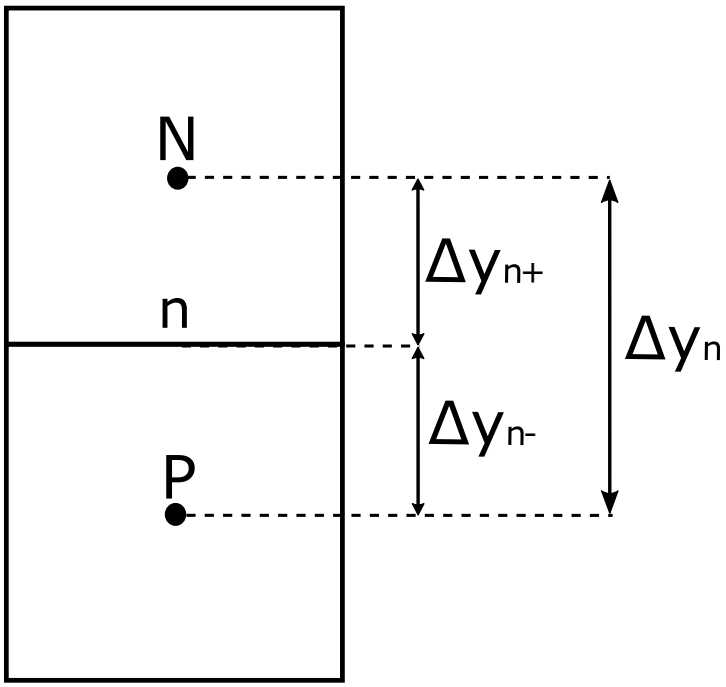

Figure 35 – Definition of the interpolation factor, f.

results in an equation with the format:

$$a_{\mathrm{p}} T_{\mathrm{P}} = a_{\mathrm{e}} T_{\mathrm{E}} + a_{\mathrm{w}} T_{\mathrm{W}} + a_{\mathrm{n}} T_{\mathrm{N}} + a_{\mathrm{s}} T_{\mathrm{S}} + b \tag{3.79}$$

where:

$$a_{\mathrm{e}} = \Gamma_{\mathrm{e}} \frac{\Delta y}{\delta z_{\mathrm{e}}} \tag{3.80}$$

$$a_{\mathrm{w}} = \Gamma_{\mathrm{w}} \frac{\Delta y}{\delta z_{\mathrm{w}}} \tag{3.81}$$

$$a_{\mathrm{n}} = \Gamma_{\mathrm{n}} \frac{\Delta z}{\delta y_{\mathrm{n}}} \tag{3.82}$$

$$a_{\mathrm{s}} = \Gamma_{\mathrm{s}} \frac{\Delta z}{\delta y_{\mathrm{s}}} \tag{3.83}$$

$$a_{\mathrm{p}}^{\mathrm{o}} = \Psi_{\mathrm{p}} \frac{\Delta z \Delta y}{\Delta t} \tag{3.84}$$

$$a_{\mathrm{p}} = a_{\mathrm{e}} + a_{\mathrm{w}} + a_{\mathrm{n}} + a_{\mathrm{s}} + a_{\mathrm{p}}^{\mathrm{o}} \tag{3.85}$$

$$b = a_{\mathrm{p}}^{\mathrm{o}} T_{\mathrm{p}}^{\mathrm{o}} + S \Delta z \Delta y \tag{3.86}$$

where the values of Γ, Ψ and S for each material can be found in Table 5.

For the boundary conditions, both the western and eastern boundaries of the casing are considered adiabatic, thus, $\frac{\partial T_{csg}(t,z=0,y)}{\partial z} = \frac{\partial T_{csg}(t,z=L,y)}{\partial z} = 0$. For the northern boundary, as mentioned in Section 3.5.2, the mass of the magnetic circuit is assumed to be large causing its temperature to remain constant. Therefore, the temperature at the northern border is prescribed as $T_{presc} = T_{amb}$, where T_{amb} is the ambient temperature. Finally, at the southern border, there is a prescribed flux condition which was also described in Section 3.5.2 and is calculated using Equations 3.21 and 3.22. Under no flow conditions, the prescribed flux is assumed to be zero. The resulting coefficients are shown in Table 10.

Table 10 – Coefficients of Equation 3.79 for the casing boundaries.

Western Volumes	**Eastern Volumes**
$a_e = \Gamma_e \frac{\Delta y}{\delta z_e}$	$a_e = 0$
$a_w = 0$	$a_w = \Gamma_w \frac{\Delta y}{\delta z_w}$
$a_n = \Gamma_n \frac{\Delta z}{\delta y_n}$	$a_n = \Gamma_n \frac{\Delta z}{\delta y_n}$
$a_s = \Gamma_s \frac{\Delta z}{\delta y_s}$	$a_s = \Gamma_s \frac{\Delta z}{\delta y_s}$
$a_p^o = \Psi_p \frac{\Delta z \Delta y}{\Delta t}$	$a_p^o = \Psi_p \frac{\Delta z \Delta y}{\Delta t}$
$a_p = a_e + a_w + a_n + a_s + a_p^o$	$a_p = a_e + a_w + a_n + a_s + a_p^o$
$b = a_p^o T_p^o + S \Delta z \Delta y$	$b = a_p^o T_p^o + S \Delta z \Delta y$
Southern Volumes	**Northern Volumes**
$a_e = \Gamma_e \frac{\Delta y}{\delta z_e}$	$a_e = \Gamma_e \frac{\Delta y}{\delta z_e}$
$a_w = \Gamma_w \frac{\Delta y}{\delta z_w}$	$a_w = \Gamma_w \frac{\Delta y}{\delta z_w}$
$a_n = \Gamma_n \frac{\Delta z}{\delta y_n}$	$a_n = 0$
$a_s = 0$	$a_{n,f} = \Gamma_n \frac{2\Delta z}{\delta y_n}$
$a_p^o = \Psi_p \frac{\Delta z \Delta y}{\Delta t}$	$a_s = \Gamma_s \frac{\Delta z}{\delta y_s}$
$a_p = a_e + a_w + a_n + a_s + a_p^o$	$a_p^o = \Psi_p \frac{\Delta z \Delta y}{\Delta t}$
$b = a_p^o T_p^o + S \Delta z \Delta y + q''_{presc} \Delta z$	$a_p = a_e + a_w + a_{n,f} + a_s + a_p^o$
	$b = a_p^o T_p^o + S \Delta z \Delta y + a_{n,f} T_{amb}$

Note that in the four volumes at the edges of the domain, the coefficients will be a combination of the two directions that form their specific edge. Numerically, the value of q''_{presc} needs to be calculated using the temperature of the casing at the center

of a finite volume, resulting in the expression:

$$q''_{\text{presc}} = \frac{h_{\text{csg}}}{1 + \frac{h_{\text{csg}}\Delta y}{2k_{\text{csg}}}}(T_{\text{f}}(t,z) - T_{\text{csg}}(t,z,y=\Delta y/2)) \tag{3.87}$$

To solve the casing energy equation, the TDMA method with an additional convergence loop for the y direction was used. The initial temperature profile is once again assumed to be linear between the hot and cold reservoirs temperatures in all layers of volumes in the casing.

3.7.7 Solver Routine

A flowchart of the routine is presented in Figure 36. The solving routine considering all losses starts by solving the momentum equation, which does not require any form of iteration. It then estimates the effective magnetic field, using the magnetic losses described in Section 3.5.3. Then, the value of $\dot{q}_{\text{MCE}}$ is obtained using Equation 3.14 and the casing energy equation is solved to obtain $\dot{q}_{\text{csg}}$ using Equation 3.21. Next, the solid, fluid and void volumes equations are solved together, yielding the temperature profiles in both phases. This process is repeated at each time step until convergence. This convergence is reached when the following expression is satisfied:

$$max\Big[\sigma\big|T_{\text{f}}(t,:)_{\text{i}} - T_{\text{f}}(t,:)_{\text{i-1}}\big|, \sigma\big|T_{\text{s}}(t,:)_{\text{i}} - T_{\text{s}}(t,:)_{\text{i-1}}\big|, \sigma\big|T_{\text{csg}}(t,:,:)_{\text{i}} - T_{\text{csg}}(t,:,:)_{\text{i-1}}\big|\Big] < \phi_{\text{conv}} \tag{3.88}$$

where i is the iteration number and σ is the standard deviation. When the end of the cycle is reached, an overall convergence of the cycle is evaluated and the process is repeated until the following condition is satisfied:

$$max\Big[\sigma\big|T_{\text{f}}|_{\text{i}} - T_{\text{f}}|_{\text{i-1}}\big|, \sigma\big|T_{\text{s}}|_{\text{i}} - T_{\text{s}}|_{\text{i-1}}\big|, \sigma\big|T_{\text{csg}}|_{\text{i}} - T_{\text{csg}}|_{\text{i-1}}\big|\Big] < \phi_{\text{conv, cycle}} \tag{3.89}$$

After the cycle converges, the values of the average cooling capacity ($\dot{Q}_{\text{c}}$), rejected heat rate ($\dot{Q}_{\text{h}}$), pumping power ($\dot{W}_{\text{p}}$), magnetic power ($\dot{W}_{\text{m}}$) and COP are calculated with the following expressions:

$$\dot{Q}_{\text{c}} = N_{\text{reg}}\frac{1}{\tau}\int_0^{\tau_{\text{HB}}} \dot{m}(t)c_{\text{p,f}}(t,-L_{\text{vv}})[T_{\text{C}} - T_f(t,-L_{\text{vv}})]dt \tag{3.90}$$

$$\dot{Q}_{\text{h}} = N_{\text{reg}}\frac{1}{\tau}\int_0^{\tau_{\text{CB}}} \dot{m}(t)c_{\text{p,f}}(t,L+L_{\text{vv}})[T_f(t,L+L_{\text{vv}}) - T_{\text{H}}]dt \tag{3.91}$$

$$\dot{W}_{\text{p}} = N_{\text{reg}}\frac{1}{\tau}\int_0^{\tau} \frac{\dot{m}(t)}{\rho_{\text{f}}}L\frac{\partial P}{\partial z}(t)dt \tag{3.92}$$

$$\dot{W}_{\text{m}} = \frac{1}{\tau}N_{\text{reg}}\sum_{\text{i=0}}^{\text{N-1}} m_{\text{s}}(i)\Big(\int_{T_{\text{s}(0,i)}}^{T_{\text{s}}(\tau,i)} c_{\text{H}}(t,i)dT_{\text{s}} + \int_{B_{\text{eff}}(0,i)}^{B_{\text{eff}}(\tau,i)} T_{\text{s}}(t,i)\frac{\partial s}{\partial B}(t,i)dB\Big) \tag{3.93}$$

$$COP = \frac{\dot{Q}_c}{\dot{W}_p + \dot{W}_m} \tag{3.94}$$

3.8 Convergence Criteria and Mesh Analysis

A discussion on the definition of the convergence criteria and mesh refinement is presented in this section. Reducing the convergence criteria and refining the mesh yield better converged and reliable results, however, this comes at a cost of computational time and memory. Therefore, when determining these parameters one needs to strive for a balance between good, converged results and acceptable computational demands. In order to achieve this balance, 16 test regenerators were chosen, with 2 extreme values for 4 operating parameters: mass flow rate, frequency, cross sectional area and maximum magnetic flux density (B). These are the most relevant controllable parameters of the regenerator and encompass two other great areas of the system design: hydraulics (frequency and mass flow rate) and the magnetic circuit (maximum magnetic flux density and size of the gap). The values of these properties for all 16 regenerators are shown in Table 11. Since the main focus of this project is to deliver the required cooling capacity, the values of this variable are the main focus of all of the analyses presented in this section, but other results, especially the overall energy balance, were also considered.

Table 11 – Test regenerators used in the convergence criteria assessment and mesh refinement tests.

Reg. Number	MFR [kg h^{-1}]	f [Hz]	A (HxW) [mm^2]	Maximum B [T]
0	1200	6	2400 (40x60)	1.8
1	1200	6	2400 (40x60)	1.0
2	1200	6	1125 (25x45)	1.8
3	1200	6	1125 (25x45)	1.0
4	1200	0.5	2400 (40x60)	1.8
5	1200	0.5	2400 (40x60)	1.0
6	1200	0.5	1125 (25x45)	1.8
7	1200	0.5	1125 (25x45)	1.0
8	400	6	2400 (40x60)	1.8
9	400	6	2400 (40x60)	1.0
10	400	6	1125 (25x45)	1.8
11	400	6	1125 (25x45)	1.0
12	400	0.5	2400 (40x60)	1.8
13	400	0.5	2400 (40x60)	1.0
14	400	0.5	1125 (25x45)	1.8
15	400	0.5	1125 (25x45)	1.0

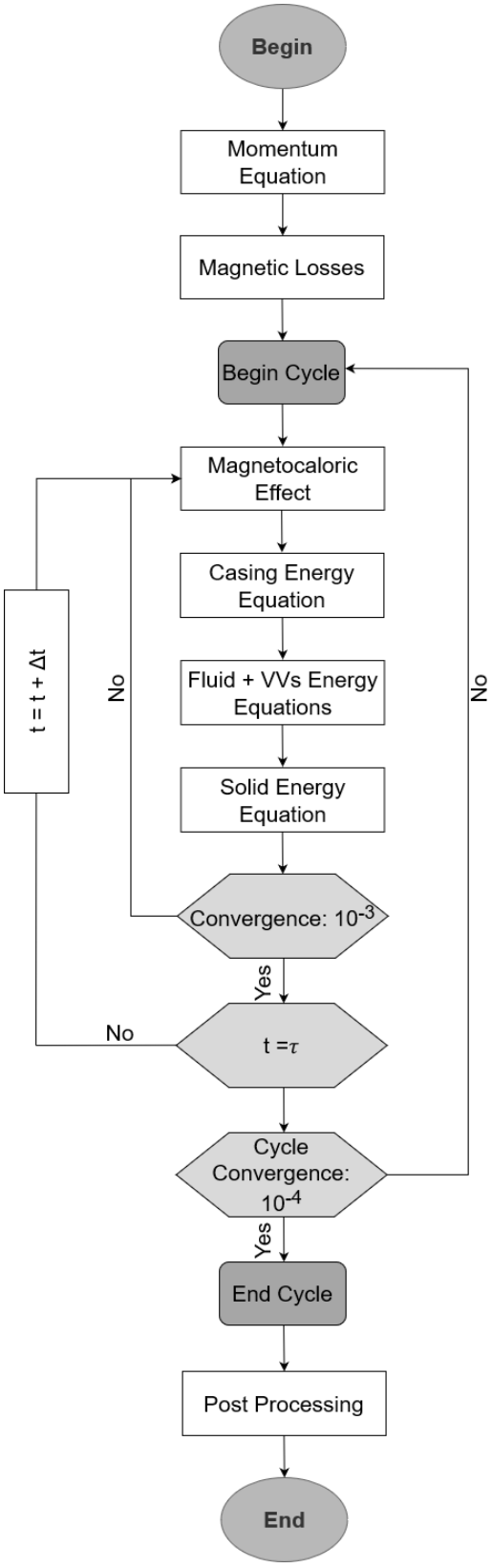

Figure 36 – Schmeatic representation of the solver routine.

3.8.1 Definition of the Convergence Criteria

In order to determine the appropriate convergence criteria of both cycles, all 16 regenerators were simulated with ϕ_{conv} and $\phi_{conv,cycle}$ varying from 10^{-1} to 10^{-6}. The values of $\dot{Q}_c$ and $\dot{Q}_h$ with both criteria set at 10^{-6} were considered as the reference results. Tighter convergence criteria required a great amount of computational time and were not considered. All regenerators were tested with different numbers of time steps and volumes and led to the following conclusions:

- The type of regenerator and mesh have a great influence on the absolute values of the simulation time, $\dot{Q}_c$ and $\dot{Q}_h$ but not on their dependence on the convergence criteria;
- The influence of $\phi_{conv,cycle}$ is much greater for the convergence than ϕ_{conv} when $\phi_{conv} \leq 10^{-3}$;
- The difference in $\dot{Q}_c$ and $\dot{Q}_h$ between the reference cases and the cases with $\phi_{conv} = 10^{-3}$ and $\phi_{conv,cycle} = 10^{-4}$ was always less than 5%, while the simulation time was up to 10 times smaller.

Therefore, the selected values of ϕ_{conv} and $\phi_{conv,cycle}$ were 10^{-3} and 10^{-4}, respectively. These values are already included in Figure 36.

3.8.2 Mesh Analysis

The same 16 regenerators were used to determine the appropriate number of volumes and time steps. The approach used was the same as the one for the convergence criteria, with both numbers starting at 20 and being doubled until reaching 2560, which is considered the reference. While there is no need for the number of time steps and volumes to be the same in any given simulation, this was done to reduce the number of tests and consequently the computational time required. $\dot{Q}_c$ and $\dot{Q}_h$ results for selected regenerators are shown in Figure 37.

Analysing the results, the following observations can be made:

- The type of regenerator does not have a great influence on the relation between the $\dot{Q}_c$ and $\dot{Q}_h$ results and the mesh;
- Using meshes that are not sufficiently refined will underestimate the values of both $\dot{Q}_c$ and $\dot{Q}_h$;
- The value of $\dot{Q}_c$ converges slightly faster than $\dot{Q}_h$;
- The results for a mesh with 640 time steps and volumes is considered converged since the average difference between their $\dot{Q}_c$ and that of the reference case is

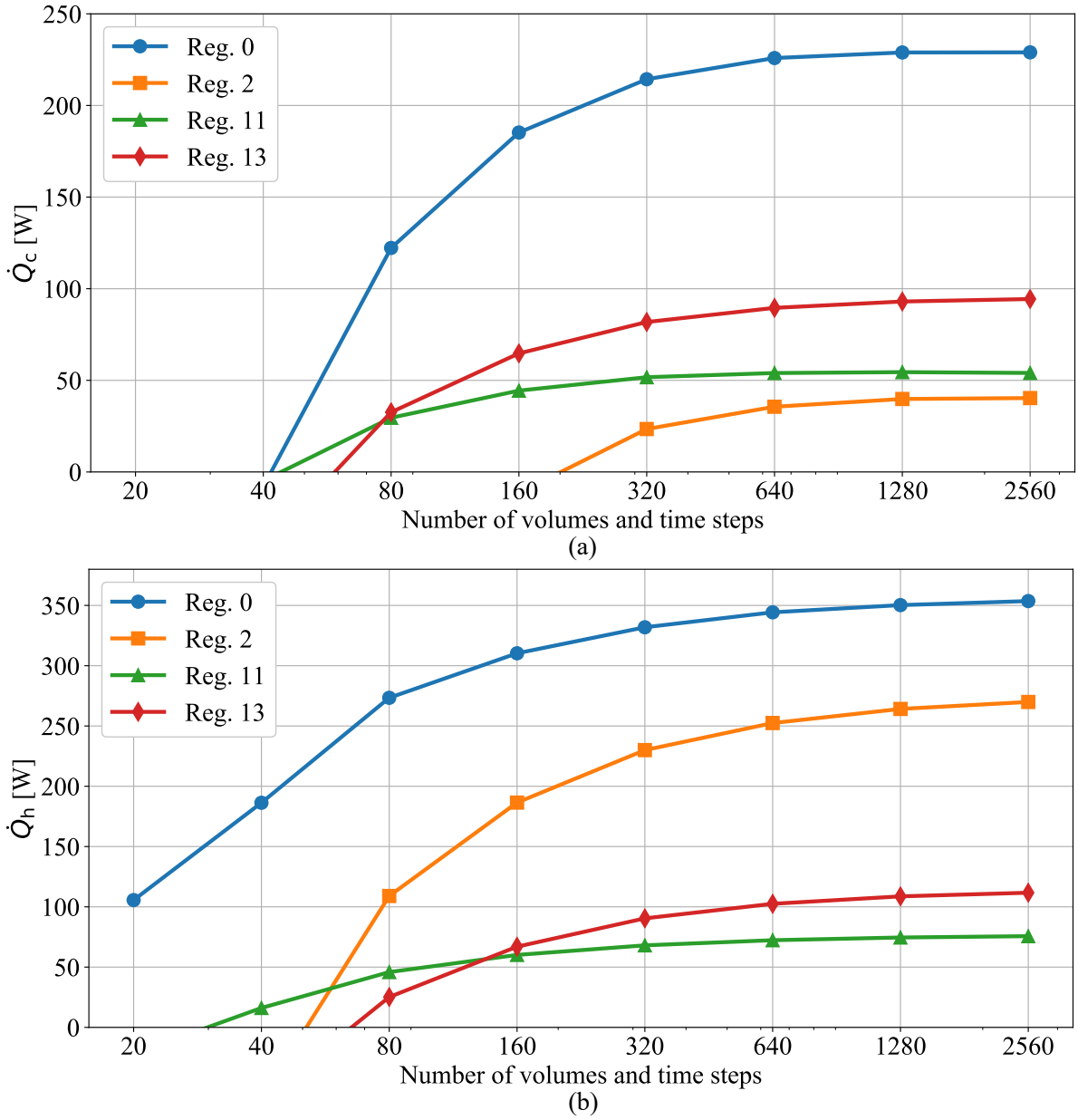

Figure 37 – Results for (a) $\dot{Q}_c$ and (b) $\dot{Q}_h$ for selected regenerators with different meshes.

2% and the maximum difference is 5.1%. For $\dot{Q}_h$, the average and maximum differences are 4% and 8.2%, respectively.

Therefore, when the focus of the simulation is the cooling capacity calculation, a mesh of 640 volumes and 640 time steps was used. However, after reaching the desired cooling capacity, it might be necessary to determine the COP and, consequently, the power input to the system. Therefore, the convergence of the magnetic power also needs to be determined. The pumping power convergence is not analysed because its result does not depend on the mesh. The results for the convergence of the magnetic power are shown in Figure 38.

These results show that, for some conditions, the magnetic work presents a

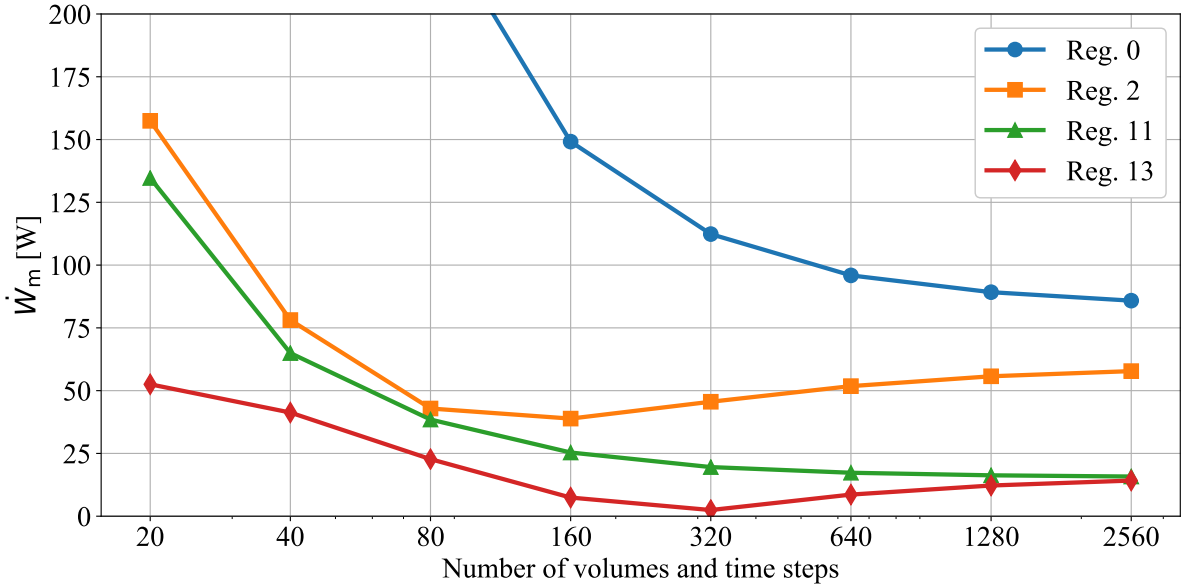

Figure 38 – Results for $\dot{W}_m$ for selected regenerators with different meshes.

minimum with respect to the number of mesh volumes and time steps before actually converging to a final value (a pattern which is not shared with the cooling capacity and the rejected heat rate). Because of that, a new criterion needed to be used to determine whether convergence was achieved or not. In this case, a suitable criterion seems to be the overall energy balance:

$$\dot{Q}_h - \dot{Q}_c - \dot{W}_m - \dot{W}_p = 0 \tag{3.95}$$

which was calculated for every regenerator as shown in Figure 39. The results show

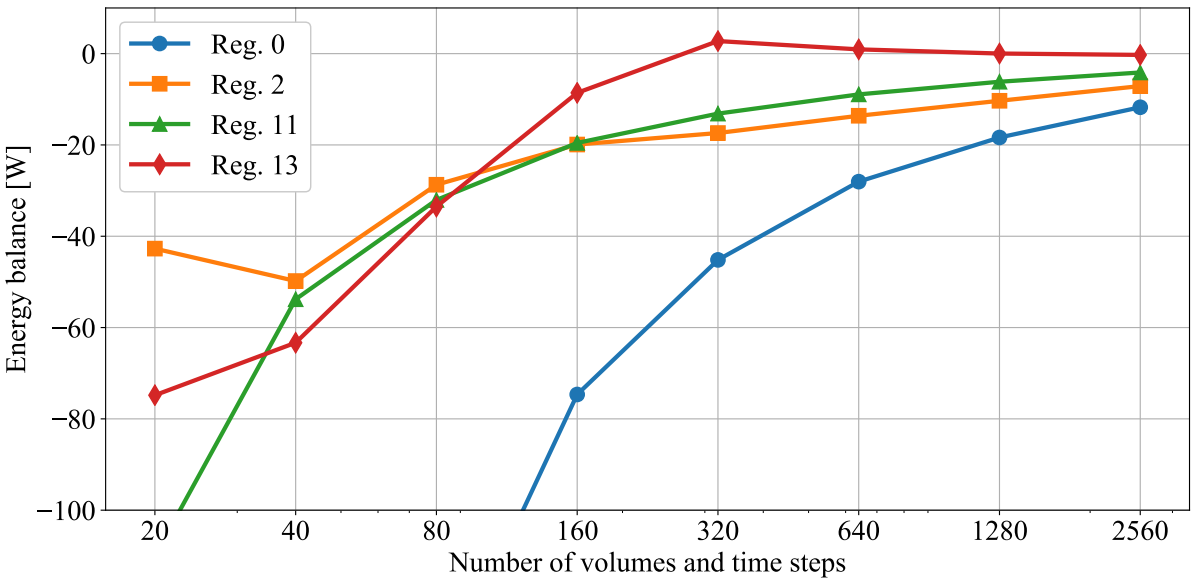

Figure 39 – Results for the energy balance for selected regenerators with different meshes.

that despite the more unusual behavior of the magnetic power, the energy balance slowly converges to 0, which is the desired result. This convergence is mainly due to changes in the magnetic power and in the rejected heat. Because of that behavior, once a regenerator with an appropriate cooling capacity is selected using the 640 mesh, it can then be analysed using increasingly refined meshes until Equation 3.96 is satisfied. When this happens, the COP and power input of the system can be determined.

$$\frac{\dot{Q}_h - \dot{Q}_c - \dot{W}_m - \dot{W}_p}{\dot{Q}_c} \leq 0.01 \tag{3.96}$$

4 Experimental Work

Experimental analysis is an efficient way to evaluate different operating parameters of passive and active regenerators. From a passive point of view, experimental tests help identify and evaluate the behavior of the heat exchange and the viscous losses, providing valuable information about the porous medium that could not be obtained otherwise. In the case of active regenerators, it has the added benefit of being the simplest way to determine their performance curves. Moreover, experimental results are necessary to validate the numerical model that will be used in this work. Thus, this chapter aims to describe the regenerators and the experimental apparatus used to obtain these results. The experimental apparatus that will be described in this work is the result of several updates made to the original apparatus developed by Trevizoli (2015), who provided the first detailed presentation of the original system. Detailed descriptions of the changes that were made can be found in Nakashima (2017), Dutra et al. (2017) and Nakashima et al. (2018).

4.1 Test AMRs

During the development of this work, 18 different first-order regenerators were tested. However, due to mechanical integrity issues, only two samples were able to withstand the multiple hours of operation required for proper testing without breaking. A third regenerator maintained its mechanical integrity only during the passive tests, but failed at the active tests. Thus, this section will focus on these three regenerators that managed to offer relevant information to this work (the two that did not break and the one that survived the passive tests), with the other regenerators being mentioned to contextualize the test history but not being described in detail.

The first regenerator (Regenerator-1) consisted of three layers assembled using different batches of spheroidal CV-H particles with an average diameter of 0.690 mm, measured using dynamic laser scattering (DLS). During manufacture, the average diameter target was 0.515 mm, with the particles being sieved between 0.400 and 0.630 mm. However, the extrusion process used to manufacture the particles is not able to create perfectly spherical particles, instead making them fairly elongated, i.e., with a length-to-diameter ratio larger than unity, which affects the particle size and allows larger particles to go through the sieve. The material used in this regenerator, CV-H, can be distinguished for having the best magnetocaloric properties amongst the three materials evaluated in this work (CV-H, CV-HS and CV-HS-2). This was originally attributed to a low $\alpha-$Fe concentration, but X-ray diffraction tests presented in Figure 40 showed that it instead had the highest $\alpha-$Fe of all three materials (13 wt.%). The

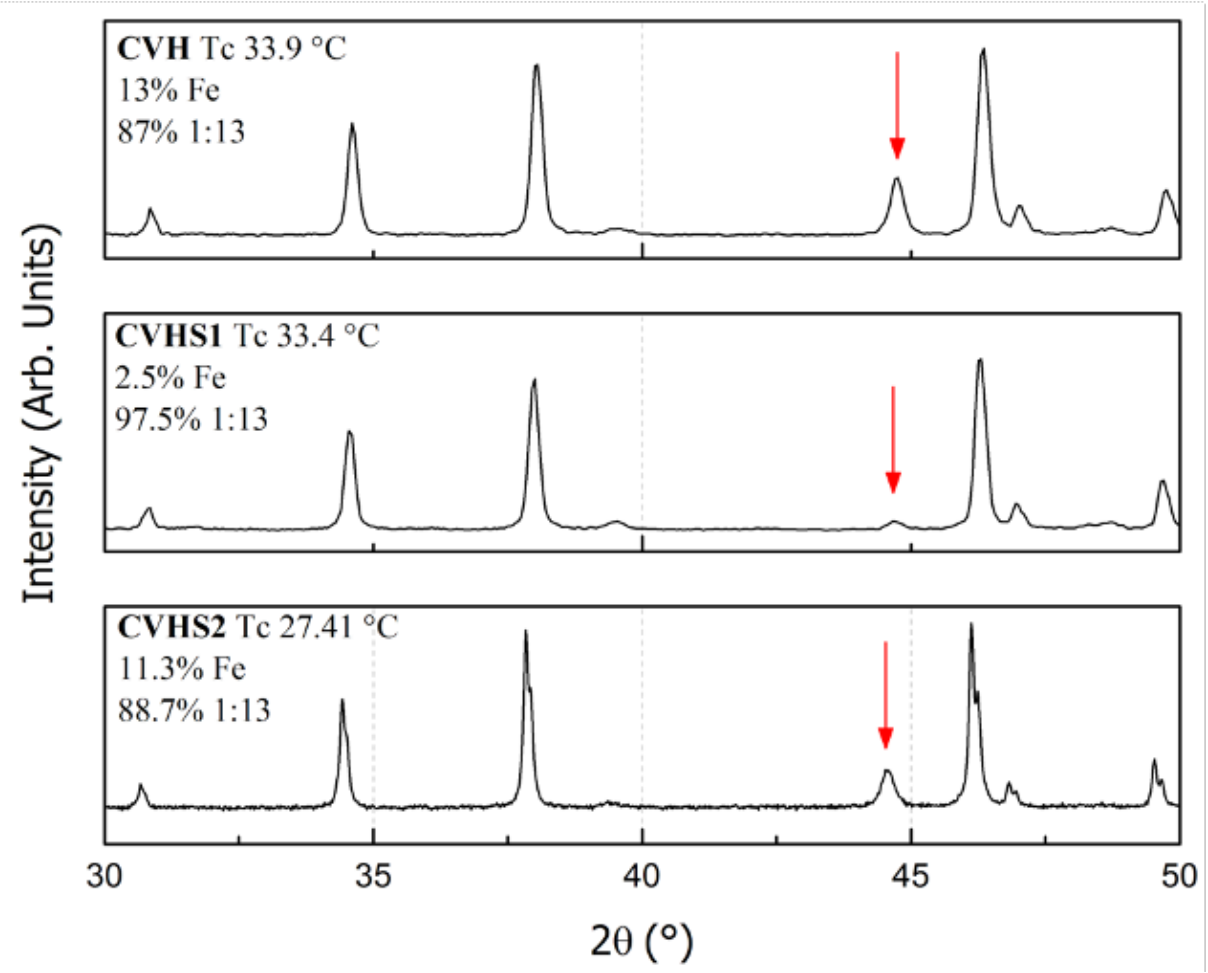

Figure 40 – $\alpha-$Fe concentration results for CV-H, CV-HS and CV-HS-2 obtained through X-ray diffraction tests.

better properties were then attributed to a better manufacturing process, which was later affected by equipment problems at the supplier, as will be discussed along this section.

Table 12 shows a summary of the regenerator's main parameters. The porous medium was cylindrical with length of 50 ± 0.05 mm and diameter of 24.3 ± 0.05 mm, resulting in a volume of approximately 23,200 mm^3. The regenerator housing consisted of a hollow cylinder of AISI 304 stainless steel with a wall thickness of 0.5 mm, which was selected based on numerical simulations that showed a trade-off between the amount of magnetocaloric material and the combined thermal insulation of the casing and air gap separating the porous medium from the magnetic circuit (PEIXER; LOZANO; BARBOSA JR., 2017). The conclusion of this work was that thinner casings result in higher cooling capacity values since the bulk of the thermal insulation is given by the air gap. A photograph of the regenerator assembly can be found in Figure 41.

The Curie temperature of the layers were 299.9, 303.5 and 307 K and all layers had approximately the same length fraction. The density of the material was estimated at 6150 kg m^{-3} through pycnometry tests. The particles of CV-H were bonded with

Table 12 – Properties of Regenerator-1.

Name	Regenerator-1
MCM relative porosity (ε)	0.45
Real porosity (ε_f)	0.376
Regenerator diameter	24.3 ± 0.05 mm
Porous medium length	50 ± 0.05 mm
Number of layers	3
Layer lengths	16.7 mm, 16.7 mm and 16.7 mm
Curie temperatures	299.9 K, 303.5 K and 307 K
Particle diameter	0.69 mm
Material	CV-H
Material density	6150 kg m^{-3}
Epoxy concentration	2.7 wt.%
Housing material	AISI 304 stainless steel
Housing thickness	0.5 mm
Heat transfer fluid	2 vol.% ENTEK-water solution

Figure 41 – Photograph of the bed of Regenerator-1 inside the AISI 304 stainless steel casing.

epoxy resin with a mass fraction of 2.7 wt.%, which aimed to increase the mechanical stability of the regenerator. During the manufacturing process, the MCM granules were mixed with epoxy powder prior to their insertion in the regenerator housing. The housing was then filled with the three desired layers which were then compacted to avoid displacements of the material. The resulting configuration was then submitted to a curing process which resulted in the final regenerator. This led to an estimated MCM porosity of 45%, with the real porosity (including epoxy) being 37.6%. Figure 42 shows back-scattered electrons (BSE) images of the resulting porous medium, with the MCM being shown in light gray and the epoxy being shown in white and dark gray. The images show that the epoxy seems to cover a large portion of the particles while also making bridges between them. Some loose epoxy can also be seen mixed with the other particles.

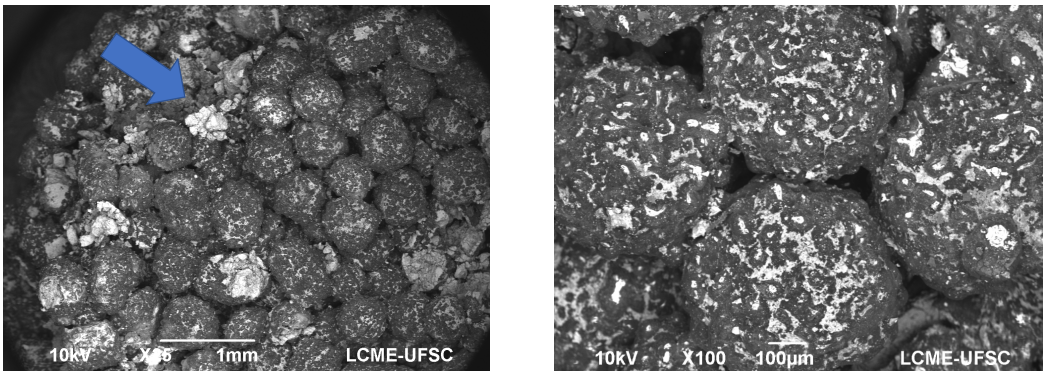

(a) (b)

Figure 42 – (a) BSE image of the regenerator bed (scanning electron microscope). The arrow indicates the presence of loose epoxy. (b) BSE zoomed-in image: The white regions show that the epoxy resin covers a large portion of the particles and makes some bridges between particles.

This was the first regenerator to be tested in this work, and it was able to withstand several hours of operation without any visible or measurable degradation of the porous medium. The AMR was submitted to both pressure drop and active tests which will be described in further sections. The results showed, however, one negative behaviour: the pressure drop obtained was considerably higher than expected for the regenerator. This phenomenon was not observed in gadolinium-based regenerators which had no epoxy, so it was suggested that the epoxy could be clogging the porous media channels and thus increasing the pressure drop.

After the promising results regarding the stability of the first regenerator, three other CV-H regenerators were ordered in order to analyze the influence of different assembly processes on their performance. These processes consisted of: (i) mounting the regenerator inside a square-U shaped stainless steel housing which was then closed by another square-U shaped housing, (ii) inserting each layer inside cylindrical polyacetal pellets which were then put inside the larger stainless steel housing, and (iii) inserting each layer inside square polyacetal pellets which were then put inside the larger stainless steel housing. A schematic of these assemblies is shown in Figure 43. The first regenerator broke during transportation and was not tested. The second and third regenerators did not break and went on to be tested. However, during the hydraulic measurements, a continuous increase in the pressure drop was observed. Furthermore, the cooling capacity results were far below what was initially expected, indicating that the regenerators were not performing correctly. These regenerators were split open and were found to be broken: the porous medium had lost its integrity and powder was found in the system filters, indicating that the particles were slowly being pulverized. Figure 44 shows the broken cylindrical-pellet regenerator, with a disintegrated porous medium.

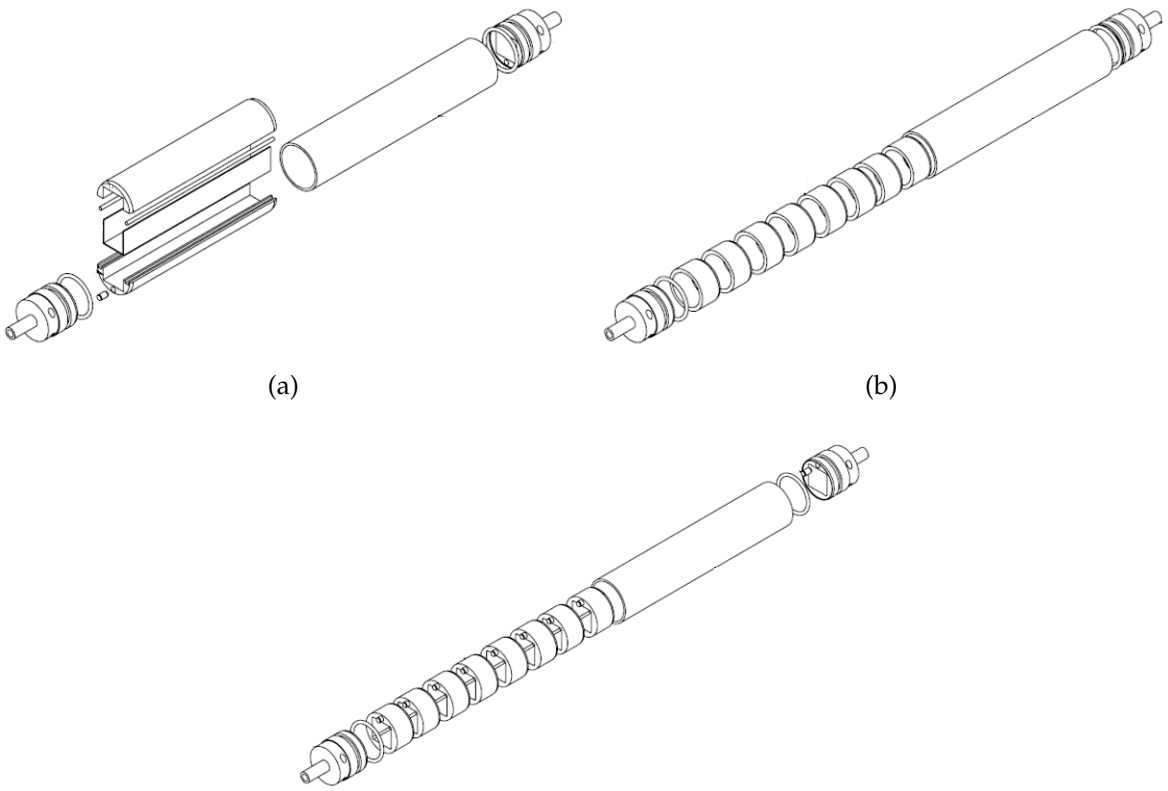

(a) (b)

(c)

Figure 43 – Schematics of the assemblies of the (a) U-shaped, (b) cylindrical-pellet and (c) square-pellet regenerators.

Figure 44 – Photograph of the opened cylindrical-pellet regenerator after being tested.

This posed a problem: despite the results of the first regenerator, the material seemed to no longer be able to withstand the stress to which it was submitted during operation. Many theories were proposed to explain why the porous medium was breaking, with most revolving around the epoxy and its curing. The most likely explanation was that during the filling the epoxy powder was falling and accumulating in the bottom of the layers, clogging some regions and reducing the integrity of others. Thus, six new regenerators were ordered to try to determine how to fix this issue, while reducing the epoxy clogging supposedly responsible for the increase in pressure drop. To try and achieve this, two modifications in the manufacturing process were proposed: using a device to fill the housing without dropping the material inside in order to prevent the epoxy powder from falling to the bottom of the layer and adding another sieving process between the addition of the epoxy powder and the filling and curing of the regenerator. Of the six regenerators, two were manufactured using only the sieving process, two were manufactured using only the device to prevent the epoxy from falling, one was manufactured using both processes and one was manufactured without any modifications in order to be used as a control regenerator.

The regenerators were then prepared for mechanical integrity tests. However, a possibility that had not yet been ruled out was that the regenerators were not breaking during operation, but during disassembly. Thus, a strategy to analyze the integrity of the regenerators without opening them had to be developed. As mentioned above, the regenerators that were breaking showed a continuous increase in pressure drop as they were tested. Thus, it was decided that pressure drop tests would be used to determine the integrity of the regenerator: if no major changes were observed, the regenerator would be considered mechanically stable, however, if the pressure drop showed a tendency to increase over time, the regenerator would be considered unstable. Figure 45 shows the pressure drop results over time for the regenerator which was submitted to both changes in the manufacturing process. The results show that the regenerator experienced a considerable increase in pressure drop within only 6 days of the first test even though all regenerators were tested during this time period, which means that the total operation time of this regenerator was actually much shorter than 6 days. All other regenerators exhibited the same phenomenon of increased pressure drop and thus were also considered unstable.

At the same time that the above results were being obtained, it was also observed that extra materials from the three original regenerators that had never been subjected to any type of test, stress or otherwise unfavorable conditions, had broken and turned to dust, especially materials with a Curie temperature close to room temperature. This result showed that while the stress caused by the AMR cycle could be accelerating the degradation process, the actual cause was the material itself and probably related to the magnetic phase transition. With this knowledge, it became clear that something had happened in the CV-H manufacturing process that impaired its

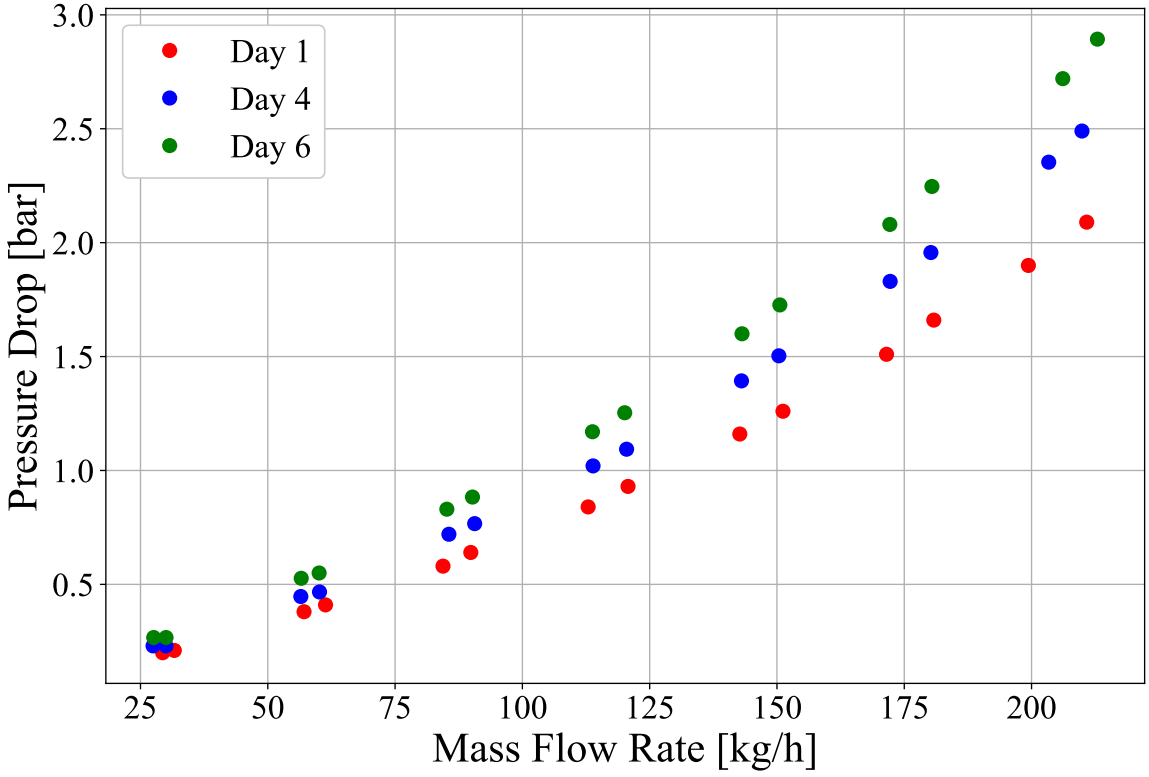

Figure 45 – Pressure drop results over time for the test regenerator in which the epoxy accumulation was prevented and an extra sieving was performed.

integrity since the original regenerator (Regenerator-1) material was still showing no signs of degradation.

Since it was not possible to clearly pinpoint and solve the issues in the manufacturing process of CV-H, a new material, called CV-HS, had to be tested. This material was expected to be almost identical to CV-H, but it supposedly had a higher concentration of $\alpha-$Fe, which was expected to increase the mechanical stability of the material but also reduce its magnetocaloric properties. However, as already shown in Figure 40, later tests showed that this material instead had the lowest concentration of $\alpha-$Fe of the three (2.5 wt.%). This concentration was much lower than expected and clearly indicated manufacturing problems, which would not only compromise the mechanical integrity, but the magnetocaloric properties as well. This can be seen in Figures 46 and 47 which show a comparison between the isothermal entropy change and the adiabatic temperature change in samples of CV-H and CV-HS. The results confirm that CV-H reaches higher values of MCE than CV-HS, but has a slightly narrower temperature range in which this happens. At the time, however, this was attributed to the supposedly higher concentration of $\alpha-$Fe and was considered acceptable provided that the material was able to withstand the stress of operation without breaking.

Three CV-HS regenerators were ordered, all similar to the original, stable, three-layered regenerator. One regenerator was broken during handling and could

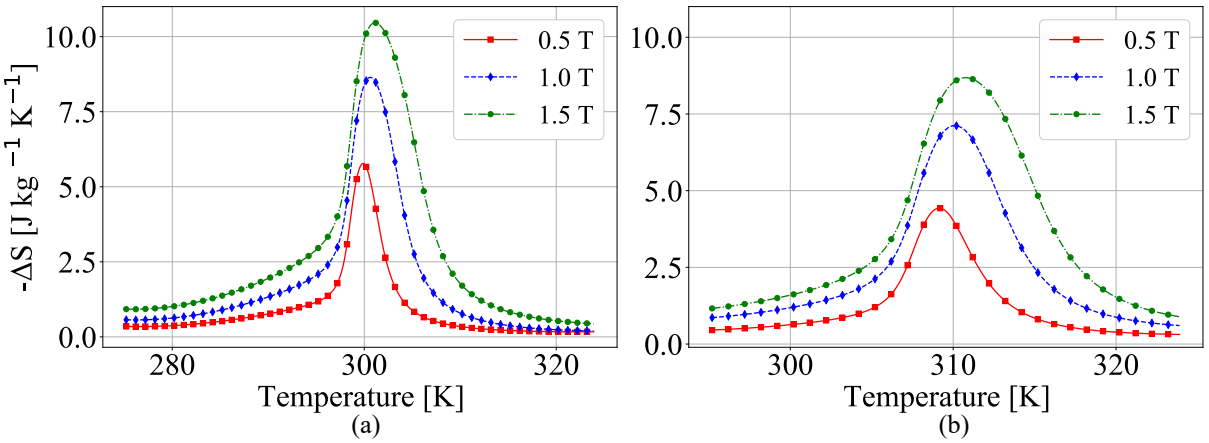

Figure 46 – Results for isothermal entropy change for samples of (a) CV-H and (b) CV-HS.

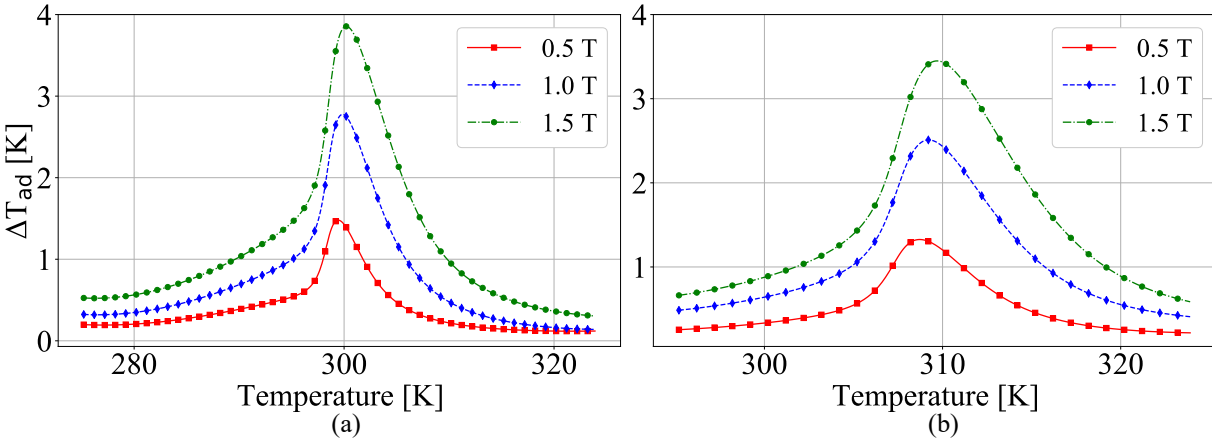

Figure 47 – Results for adiabatic temperature change for samples of (a) CV-H and (b) CV-HS.

not be tested. Another regenerator showed signs of increase in pressure drop during operation and broke after the pressure drop tests, so no active tests could be performed. The last regenerator, which will be referred to as Regenerator-2, showed much more stable results during the pressure drop tests, presenting only a small increase when compared to the previous regenerators. This regenerator was then subjected to passive and active tests with the pressure drop being consistently monitored. The pressure drop continued to increase throughout the tests, reaching a peak during the active tests. Thus, the results of the active tests were disregarded, but the results of the passive tests were considered usable.

Regenerator-2 consisted of three layers of spheroidal CV-HS particles with an average diameter of 0.65 mm. Similarly to Regenerator-1, the average target particle diameter was 0.515 mm, but this was not achieved due to the elongated shape of the particles. The porous medium was cylindrical with a length of 50 ± 0.05 mm and a diameter of 23 ± 0.05 mm, resulting in a volume of approximately 20,800 mm^3. The regenerator housing was identical to that of Regenerator-1, consisting of a hollow cylinder of AISI

Table 13 – Properties of Regenerator-2.

Name	Regenerator-2
MCM relative porosity (ε)	0.46
Real porosity (ε_f)	0.38
Regenerator diameter	23 mm
Porous medium length	50 mm
Number of layers	3
Layer lengths	13.82 mm, 18.27 mm and 17.91 mm
Curie temperatures	298.95 K, 299.6 K and 302.5 K
Particle diameter	0.65 mm
Material	CV-HS
Material density	7100 kg m^{-3}
Epoxy concentration	2.7 wt.%
Housing material	AISI 304 stainless steel
Housing thickness	0.5 mm
Heat transfer fluid	2 vol.% ENTEK-water solution

304 stainless steel with a wall thickness of 0.5 mm. The Curie temperature of the layers were 298.95, 299.6 and 302.5 K with lengths of 13.82, 18.27 and 17.91 mm, respectively. The density of the material was estimated at 7100 kg m^{-3} through pycnometry tests. The mass fraction of epoxy was kept at 2.7 % and, according to the manufacturer, no changes were made to the regenerator assembly process. The estimated MCM porosity was 46% and the real porosity was estimated at 38%. Table 13 shows a summary of the main parameters of Regenerator-2.

The above mentioned results demonstrated that the use of the new material CV-HS did not solve the regenerator integrity problems. However, as the new material was not turning to dust spontaneously, the attention was shifted to the AMR operation as a potential cause for the observed mechanical instability. An analysis of the working fluid used in all three regenerators showed solid residues that indicated deterioration of either the epoxy or the magnetocaloric material. To test this hypothesis, four new CV-HS regenerators were ordered and tested. Two of these regenerators had a higher concentration of epoxy (3.5%) while two of them had no epoxy at all. The epoxy in one of the regenerators was cured with it standing upright while the other was cured with it lying down along its axis. Two regenerators were tested with 1 vol% ENTEK-water solution as a working fluid instead of the usual 2 vol% ENTEK-water solution and two regenerators were tested with 20 vol% ethylene glycol-water solution. All four regenerators broke during operation, indicating that CV-HS would not be able to withstand long operation times without breaking.

With all the results showing that neither CV-H nor CV-HS would be able to operate in an AMR cycle without breaking, a third material was produced: CV-HS-2. This material supposedly had an even higher concentration of $\alpha-$Fe than CV-HS and thus should be more mechanically resistant at the expense of worse magnetocaloric

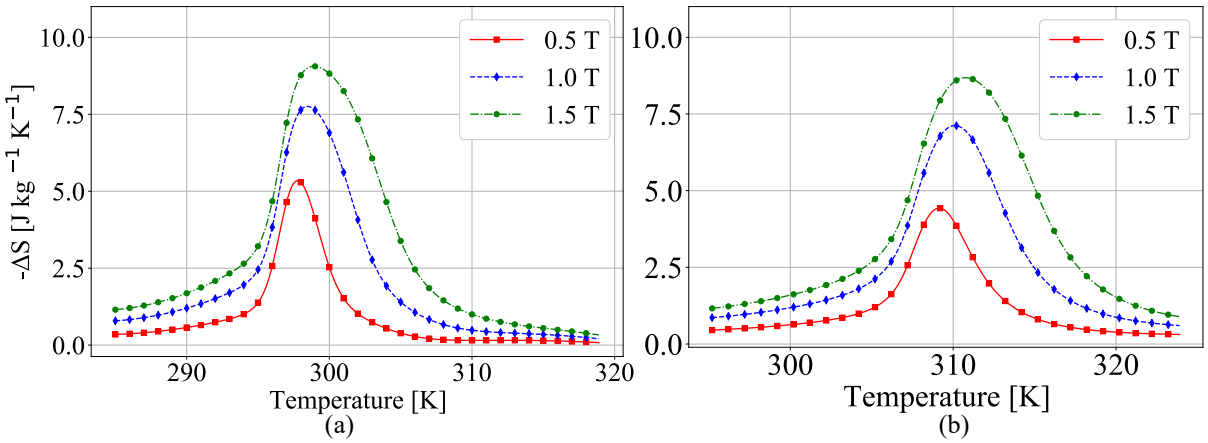

Figure 48 – Results for isothermal entropy change for samples of (a) CV-HS2 and (b) CV-HS.

properties. However, as shown in Figure 40, CV-HS-2 actually had an $\alpha-$Fe concentration close to that of CV-H, indicating that the real change between CV-HS and CV-HS-2 was an improvement in the manufacturing process. This is further corroborated by the results for the isothermal entropy change of CV-HS-2 presented in Figure 48 which show that the CV-HS-2 properties are actually better than those of CV-HS. This can be clearly seen at lower fields, where the entropy variation is much higher. In fact, the results showed that the properties of CV-HS-2 at lower applied magnetic flux densities were comparable to the ones of CV-H which is especially promising when considering that the effective magnetic flux density is not expected to surpass 1.1 T in the magnetic circuit developed for the MRU.

Only one CV-HS-2 regenerator was assembled for testing, which will be called Regenerator-3. It consisted of five layers of spheroidal particles with an average diameter of 0.75 mm. The porous medium was cylindrical with a length of 109 ± 0.05 mm and a diameter of 24.3 ± 0.05 mm, resulting in a volume of approximately 50,500 mm^3. The regenerator housing consisted of a hollow cylinder of AISI 304 stainless steel with a wall thickness of 0.5 mm. The Curie temperatures of the layers were 278.70, 284.06, 288.88, 294.05 and 300.56 K with lengths of 24.8, 24.8, 24.8, 24.8 and 9.8 mm respectively. The density of the material was estimated at 7150 kg m^{-3} through pycnometry tests. No epoxy was added to the regenerator, resulting in an estimated MCM porosity of 39.3% which is the same as the real porosity. Table 14 shows a summary of the main parameters of Regenerator-3.

This regenerator was submitted to multiple active, passive and pressure drop tests resulting in over 200 hours of operation and did not show signs of breaking. Figure 49 shows a comparison between the cumulative change in pressure drop for two CV-HS regenerators and the CV-HS-2 regenerator. As can be seen, the CV-HS regenerators showed great increases in pressure drop after very few tests, while the CV-HS-2 regenerator showed no consistent increase after a considerably larger number

Table 14 – Properties of Regenerator-3.

Name	Regenerator-3
MCM relative porosity (ε)	0.393
Real porosity (ε_f)	0.393
Regenerator diameter	24 mm
Porous medium length	109 mm
Number of layers	5
Layer lengths	24.8 mm, 24.8 mm, 24.8 mm, 24.8 mm and 9.8 mm
Curie temperatures	278.70 K, 284.06 K, 288.88 K, 294.05 K and 300.56 K
Particle diameter	0.746 mm
Material	CV-HS-2
Material density	7150 kg m^{-3}
Epoxy concentration	0 wt.%
Heat transfer fluid	2 vol.%. ENTEK-water solution

of tests. This allowed this regenerator to be submitted to more active and passive tests than any of the other 17 AMRs tested in the context of the present work. Between the passive and active tests, the regenerator was disassembled for further analysis of its integrity. Figure 50 (a) shows a picture of the regenerator before disassembly with no clear macroscopic signs of degradation, while Figures 50 (b) and (c) show pictures of the CV-HS-2 particles removed from the regenerator after disassembly with no microscopic signs of degradation, further confirming that the material did not break. The white and dark gray shades represent the epoxy, while the light gray shade represents the MCM. These combined results were considered strong indications that the material will be able to withstand operation during long periods of time, but further tests are still needed.

4.2 Experimental Apparatus

Figure 51 shows a photograph of the experimental facility used to test all regenerators described in Section 4.1 with some components highlighted. These components will be described further ahead, with special focus on the hydraulic and magnetic systems. A more in-depth description of the apparatus can be found in Trevizoli (2015), Nakashima (2017), Nakashima et al. (2018) and Bez et al. (2020). One important component that cannot be seen in the picture is the regenerator. The regenerator is located inside the magnetic circuit at the center of the apparatus, supported by two bearing units. Two auxiliary housings are added to guarantee that the AMR is properly centered in relation to the magnet. Figure 52 shows a photograph of the regenerator assembly outside the magnetic circuit.

A schematic representation which includes both the magnetic and hydraulic circuits of the experimental apparatus used to characterize the performance of the regenerators is shown in Figure 53. The magnetic circuit is composed of a stepper motor

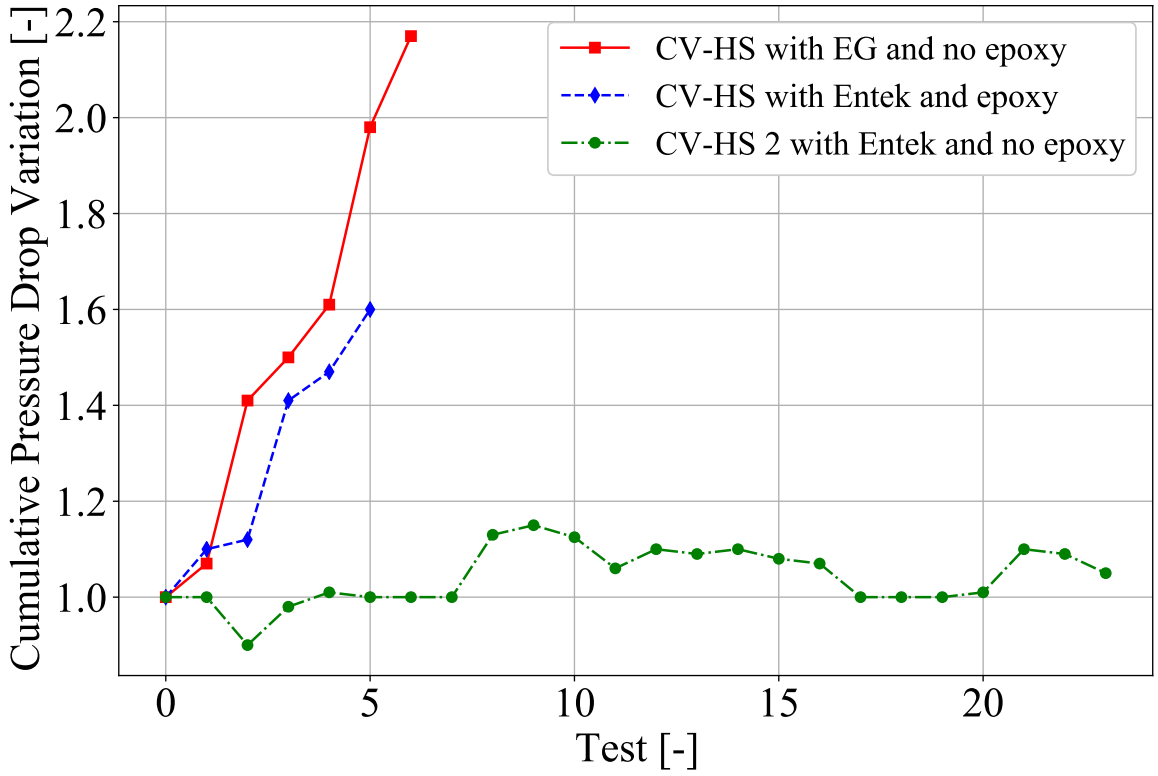

Figure 49 – Cumulative average variation of the pressure drop during tests for two CV-HS regenerators and one CV-HS-2 regenerator.

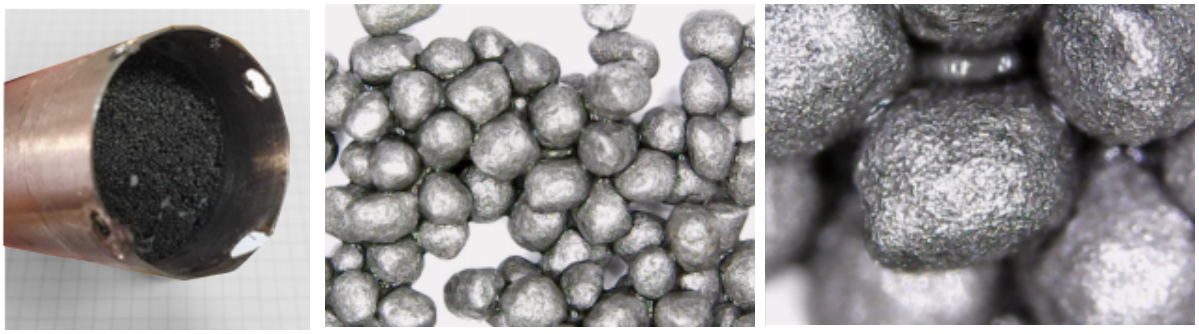

(a) (b) (c)

Figure 50 – (a) Regenerator-3 before disassembly after being submitted to passive tests. (b) Zoomed-out photograph of the CV-HS-2 particles of Regenerator-3 after the passive tests. (c) Zoomed-in photograph of the CV-HS-2 particles of Regenerator-3 after the passive tests.

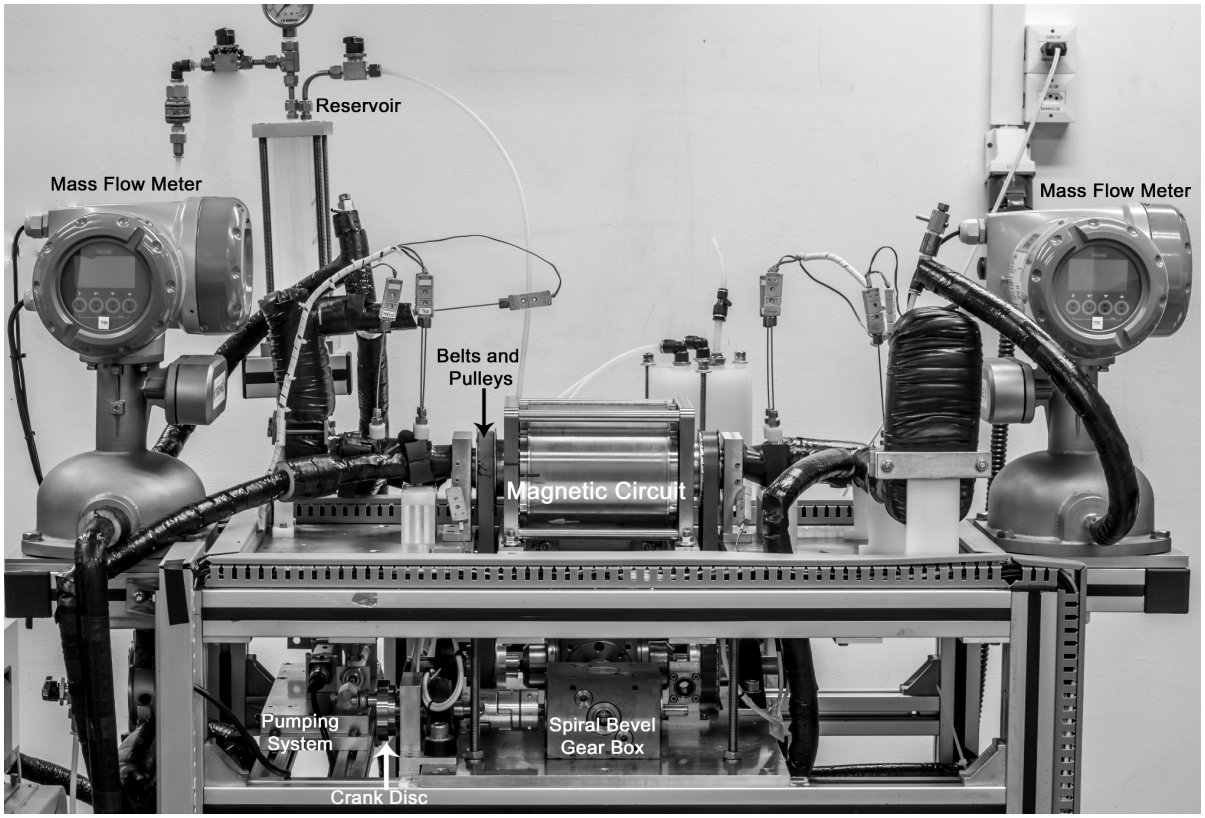

Figure 51 – Experimental apparatus used for testing. Adapted from Trevizoli (2015).

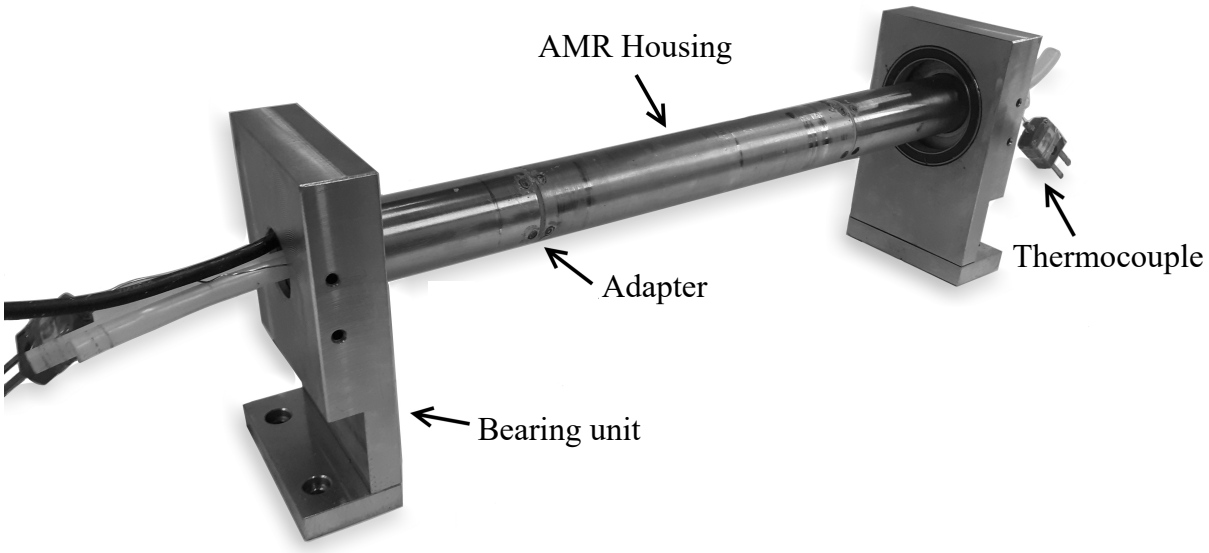

Figure 52 – Regenerator assembly. Adapted from Hoffmann (2020).

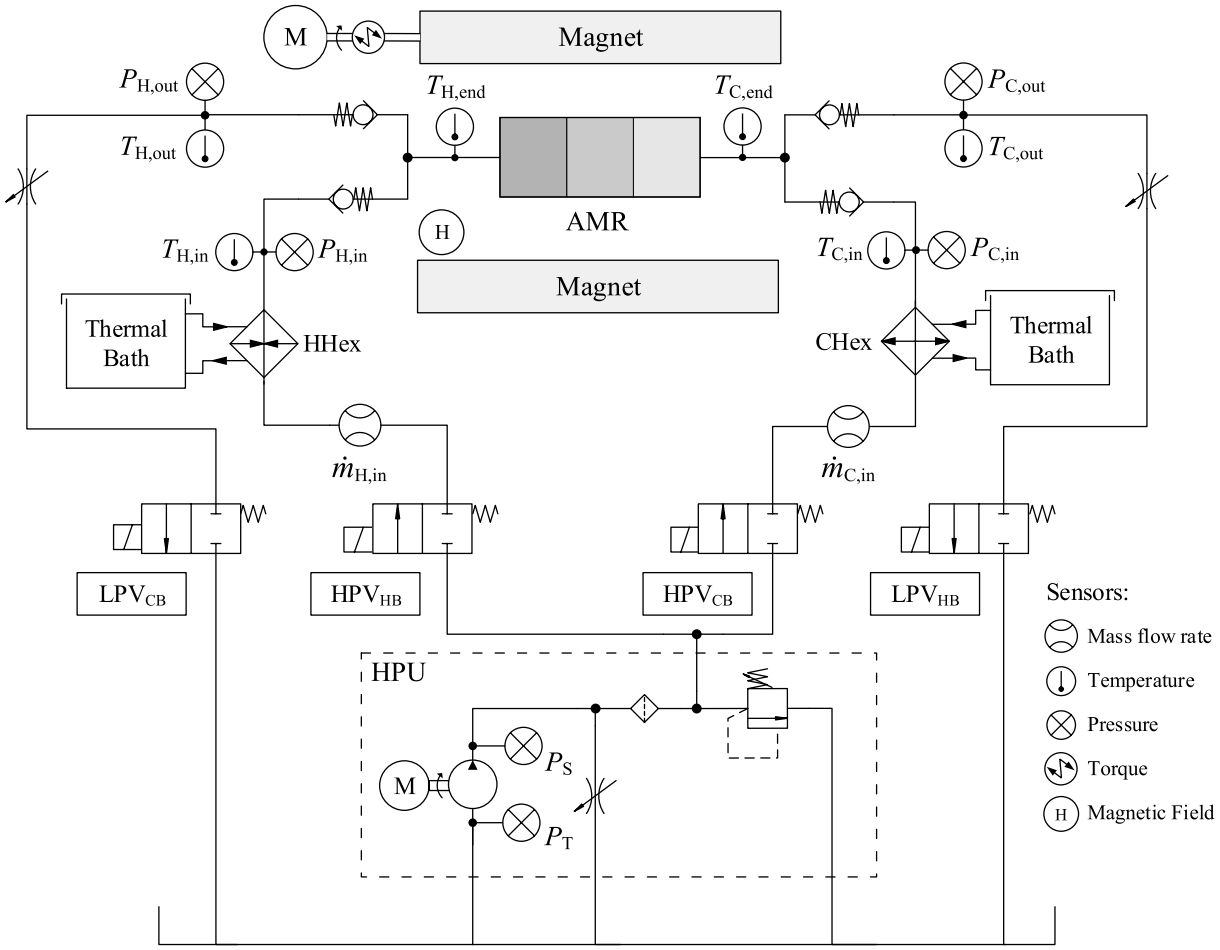

Figure 53 – Schematic diagram of the experimental apparatus used to characterize the thermal-hydraulic behavior of the AMR. Adapted from Vieira et al. (2021).

(M) which is responsible for rotating the two nested Halbach cylinders (NHC). The counter rotation of the concentric cylinders generates a rectified sinusoidal magnetic flux density profile which was measured by a Hall effect sensor (H). During one full counter rotation of the magnets, the maximum and minimum magnetic flux density are reached twice, allowing for the completion of two full AMR cycles during one rotation.

Figure 54 (a) shows the experimental measurements of the resultant magnetic flux density profiles at different positions along the z axis. At the center of the magnet (z = 0 mm) the measured values vary from 0.04 to 1.69 T, with the peak value becoming lower at positions further from the center. The magnet length was 115 mm, with detailed measurements of magnetic flux density being taken considering a 100 mm regenerator (-50 < z < 50 mm), meaning measurements where z > 50 mm were taken outside the regenerator. These outside measurements are indicated by the dotted and dashed lines. Figure 54 (b) further illustrates this by showing the maximum magnetic flux density profile along the z-axis with the magnetic circuit in the background for reference. It can be seen that the magnetic flux density decreases slowly within the regenerator going from 1.69 T at z = 0 mm to approximately 1.30 T at z = 50 mm while it decreases

sharply outside the regenerator, going from 1.30 T at z = 50 mm to 0.35 T at z = 75 mm (TREVIZOLI, 2015). During active regeneration tests, the center of the regenerator is aligned with the center of the magnet in order to impose the maximum applied magnetic field variation that could be attained along the porous medium with this magnetic circuit.

Regarding the hydraulic circuit, the hydraulic power unit (HPU) is formed by the gear pump and flow limiting valves. The gear pump is powered by an electric motor and is responsible for pumping the fluid from the reservoir through the lines. The flow limiting valves establish both the supply and reservoir pressures. Two pairs of solenoid valves, each comprising a low-pressure valve (LPV) and a high-pressure valve (HPV) are responsible for the synchronization between the fluid flow and magnetic field waveforms. One pair is responsible for the hot blow (HB) and the other is responsible for the cold blow (CB) (DUTRA et al., 2017). The high pressure valves are responsible for directing the fluid coming from the pump to the appropriate end of the regenerator while the low pressure valves direct the fluid coming from the regenerator to the reservoir. The control of the solenoid valves is activated using the output signal from the Hall effect sensor to guarantee proper synchronization between the hydraulic and magnetic profiles (HOFFMANN et al., 2017). This signal is also used to determine the operating frequency through a waveform analysis tool. The sensor is located at a distance of 128.5 mm from the center of the magnet on the hot side and is perpendicular to the applied magnetic field. The synchronization process consists of normalizing the signal from the sensor into a rectified sinusoidal curve varying from 0 to 1. When the curve reaches 0 the instant of maximum demagnetization is reached and a countdown to the activation of the valves starts. The logic that determines the countdown considers the desired blow fraction, the valve response time and the fluid flow waveform (NAKASHIMA et al., 2018). Figure 55 shows the resulting synchronization between the hydraulic, electric and magnetic waveforms for two different blow fractions. B is the magnetic flux density profile, ΔP is the regenerator pressure drop, which is proportional to the mass flow rate, and i is the current of the valves.

Two Coriolis effect mass flow meters with an expanded uncertainty of 1% determine the displaced fluid mass during each blow. These values are also included in the synchronization logic and are used to adjust the blow periods in order to correct mass imbalances between the blows. The hydraulic resistance is adjusted using needle valves. Care needs to be taken when applying the Coriolis mass flow meters to transient regimes such as the AMR cycles, since its operation will be influenced by its time constant. However, Nakashima (2017) showed that its results are accurate for low frequencies and mass flow rates. The pressure drop in the regenerator during both blows is obtained from four pressure transducers located in the suction and discharge lines, which have an uncertainty of 0.5 kPa, by integrating the pressure drop during each blow and dividing it by the blow period. The average pressure drop is then

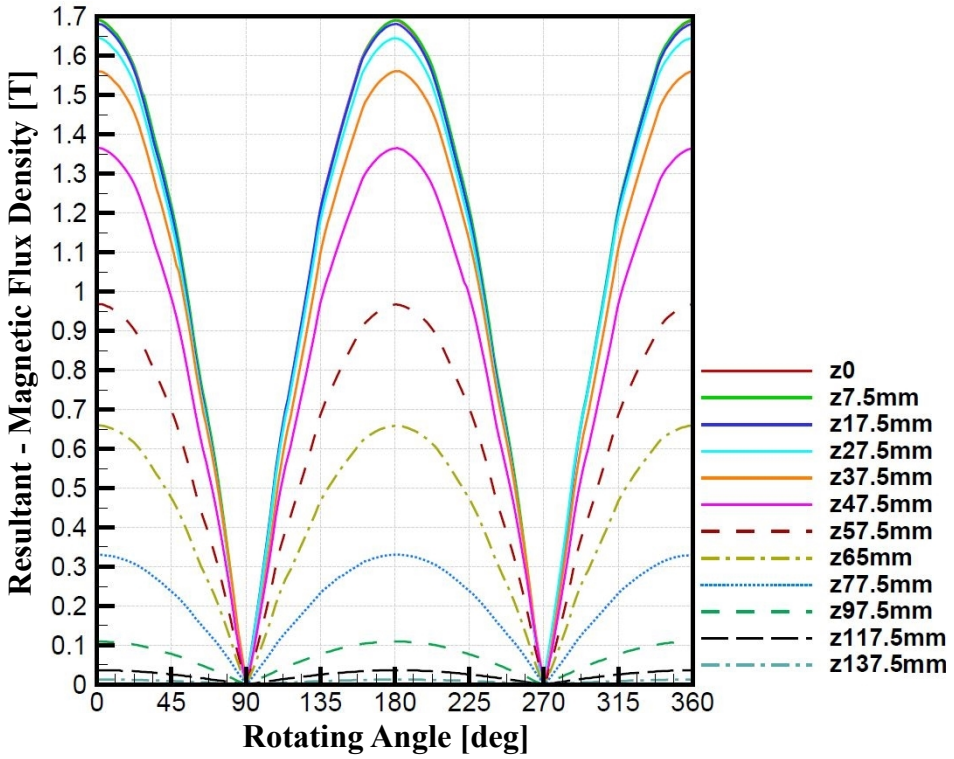

(a)

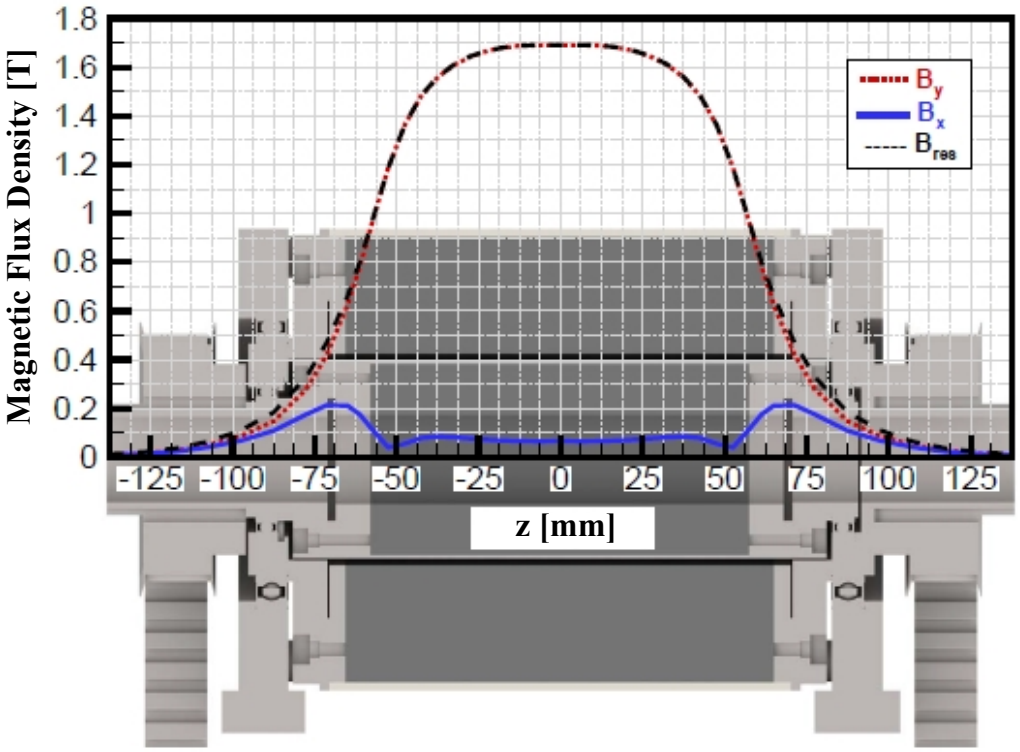

(b)

Figure 54 – (a) Experimental resultant magnetic flux density measurements as a function of the rotating angle for multiple positions along the z axis. (b) Experimental resultant magnetic flux density peak along the z-axis. Adapted from Trevizoli (2015).

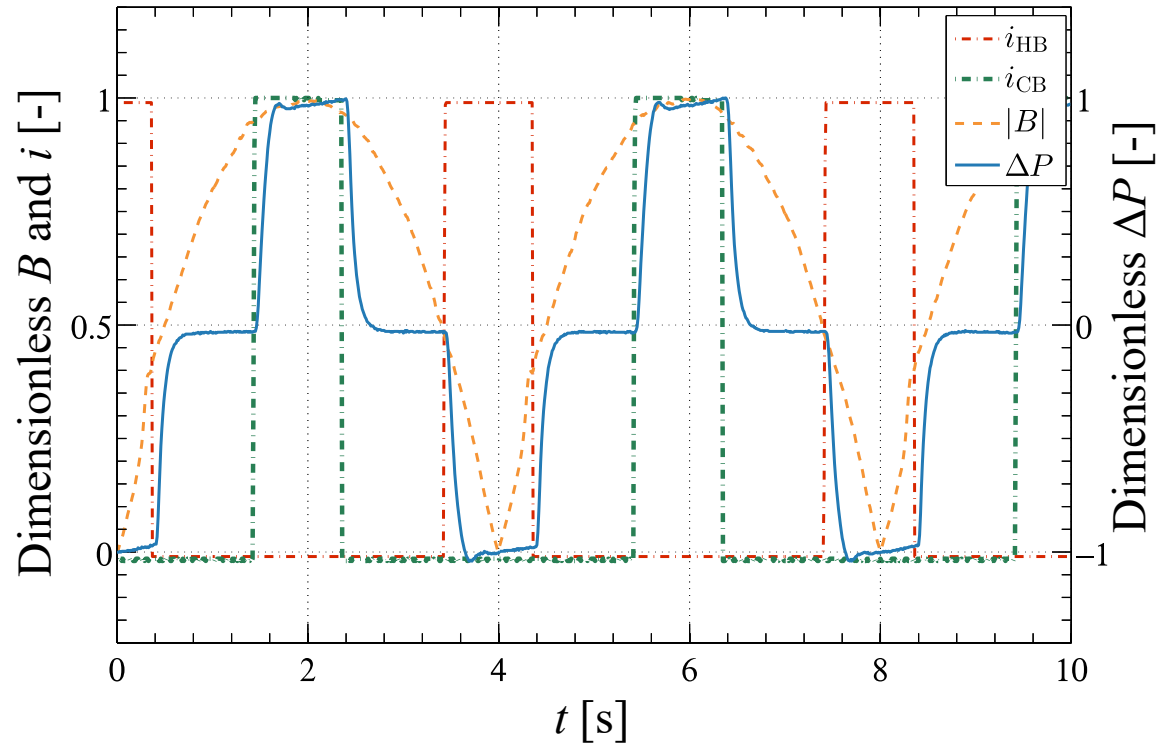

(a)

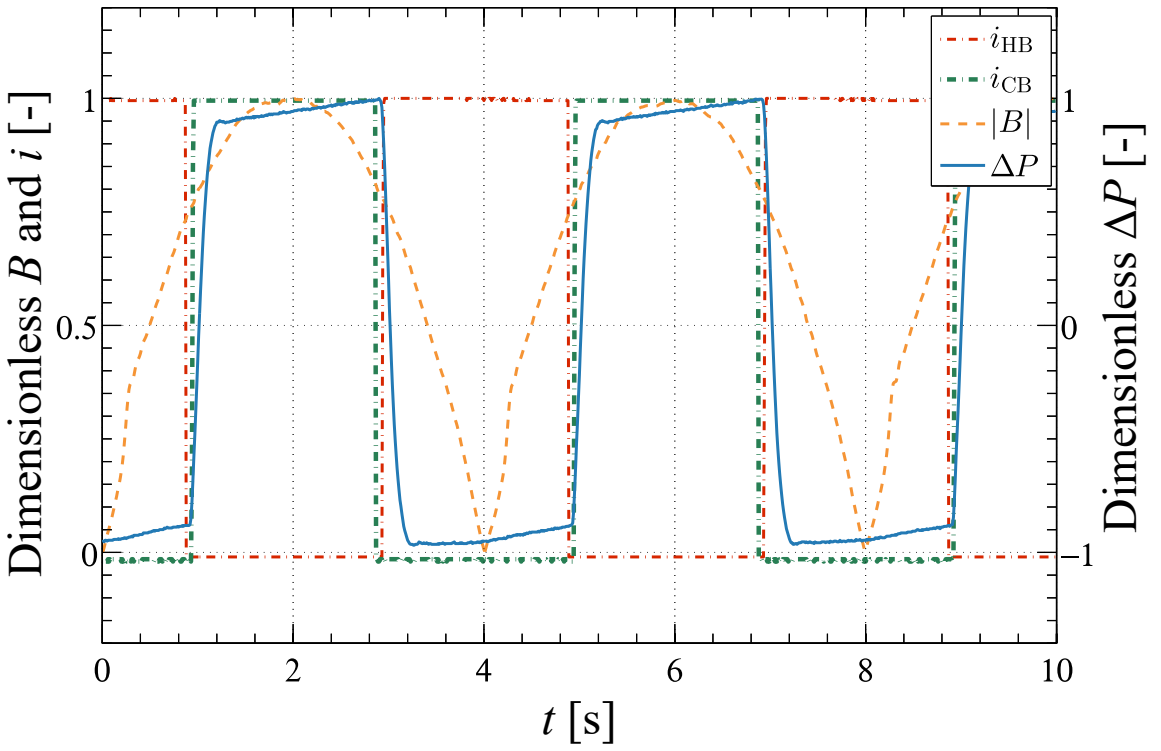

(b)

Figure 55 – Synchronization between the hydraulic, electric and magnetic waveforms in the experimental apparatus for blow fracions of (a) 25% and (b) 50%. Adapted from Nakashima et al. (2018).

obtained by averaging these values over a given number of cycles, according to the two expressions below:

$$\overline{\Delta P}_{\mathrm{CB}} = \frac{1}{\xi}\sum_{i=1}^{\xi}\left[\frac{1}{\tau_{\mathrm{CB}}}\int_{\tau_{\mathrm{CB}}}[P_{\mathrm{C,in}}(t) - P_{\mathrm{H,out}}(t)]dt\right] \tag{4.1}$$

$$\overline{\Delta P}_{\mathrm{HB}} = \frac{1}{\xi}\sum_{i=1}^{\xi}\left[\frac{1}{\tau_{\mathrm{HB}}}\int_{\tau_{\mathrm{HB}}}[P_{\mathrm{H,in}}(t) - P_{\mathrm{C,out}}(t)]dt\right] \tag{4.2}$$

where ξ is the number of cycles.

Two temperature controlled thermal baths are used to set the AMR inlet temperatures. These baths exchange heat with the heat transfer fluid through compact brazed plate heat exchangers which are intentionally oversized to guarantee that the fluid leaves the bath with the desired temperature. Thermocouples with an uncertainty of 0.2 K are positioned at various points of the system and are used to determine the desired performance parameters, namely the effectiveness in passive tests and cooling capacity in active tests. A summary of the instrumentation used in the apparatus can be found in Table 15.

Table 15 – Uncertainties of the measurement devices used in the apparatus.

Sensor / Transducer	Comp.	Model	Uncertainty
Pressure	Omega	PX613-200G5V	± 0.5 kPa
Thermocouple	Omega	SCPSS-020G-6	± 0.2 K
Coriollis mass flow meters	Krohne	Optimass 3300C-S04	± 1 %
Torque	HBM	T22/50Nm	± 0.3 N m
Hall effect	SEC Electronics	SS49E	-

In the present configuration, the apparatus has, as input parameters, the operating frequency given by the rotation speed of the magnet, the mass flow rate given by the pump, the temperature span given by the baths, and the blow fraction given by the control logic. The test procedure of a regenerator generally starts with the pressure drop tests, which have two purposes: establish an initial estimate of the mechanical stability of the material and determine the effective porosity (see Section 3.2). These tests consist of submitting the regenerator to steady flow isothermal experiments in which the pressure drop is measured as a function of the fluid flow rate. By knowing the parameters described in Tables 12 to 14, especially the particle diameter, the effective porosity becomes a function of the pressured drop, thus, these points can be used to determine the effective porosity by determining the value that best fits the data. Thus, DLS measurements to determine the particle diameter of the material are carried out prior to the pressure drop tests, which are usually performed daily to determine if the pressure drop is increasing and, consequently, the regenerator is breaking up.

The passive regeneration tests consist of submitting the regenerator to all stages of a regular AMR cycle except the magnetization and demagnetization. The two main

results of these tests are the time-dependent temperature profiles (traces) at the ends of the regenerator, which can be used to determine its effectiveness, and the dynamic pressure drop, which may be different from the steady flow unidirectional pressure drop. The regenerator effectiveness is determined through the following expressions:

$$\epsilon_{\mathrm{CB}} = \frac{\overline{T}_{\mathrm{reg,H,out}} - T_{\mathrm{reg,C,in}}}{T_{\mathrm{reg,H,in}} - T_{\mathrm{reg,C,in}}} \tag{4.3}$$

$$\epsilon_{\mathrm{HB}} = \frac{T_{\mathrm{reg,H,in}} - \overline{T}_{\mathrm{reg,C,out}}}{T_{\mathrm{reg,H,in}} - T_{\mathrm{reg,C,in}}} \tag{4.4}$$

where:

$$\overline{T}_{\mathrm{reg,H,out}} = \frac{1}{\xi} \sum_{i=1}^{\xi} \left[\frac{1}{\tau_{\mathrm{CB}}} \int_{\tau_{\mathrm{CB}}} T_{\mathrm{reg,H}}(t) dt \right] \tag{4.5}$$

$$\overline{T}_{\mathrm{reg,C,out}} = \frac{1}{\xi} \sum_{i=1}^{\xi} \left[\frac{1}{\tau_{\mathrm{HB}}} \int_{\tau_{\mathrm{HB}}} T_{\mathrm{reg,C}}(t) dt \right] \tag{4.6}$$

$$T_{\mathrm{reg,C,in}} = T_{\mathrm{C}} \tag{4.7}$$

$$T_{\mathrm{reg,H,in}} = T_{\mathrm{H}} \tag{4.8}$$

where $\mathrm{T_C}$ and $\mathrm{T_H}$ are the temperatures of the cold and hot baths, respectively. The values of $\mathrm{T_{reg,H}}$ are measured by thermocouple $\mathrm{T_{H,end}}$ and the values of $\mathrm{T_{reg,C}}$ are measured by thermocouple $\mathrm{T_{C,end}}$ (see Figure 53). In the case of the CV-HS-2 regenerator (Regenerator-3), it was noticed that the thermocouples $\mathrm{T_{C,end}}$ and $\mathrm{T_{H,end}}$ were not working properly and could not be replaced or fixed. Therefore, only during these tests, the values of $T_{\mathrm{reg,C,out}}$ were determined using thermocouple $T_{\mathrm{C,out}}$ and the values of $T_{\mathrm{reg,H,out}}$ were determined using thermocouple $T_{\mathrm{H,out}}$. Note that these equations rely on the assumption of balanced flow, requiring the imbalance-correcting logic to be working properly. Passive tests results are used mostly for validating non-MCE parts of the numerical model, namely the heat exchange and pressure drop resulting from the interaction between the solid porous medium and the fluid flows.

Lastly, active tests consist of submitting the regenerator to a complete AMR cycle under a known applied magnetic field variation. These tests are the simplest way to evaluate the performance of a regenerator under different conditions and are also the most integral part of the numerical model validation, encompassing all the physical phenomena relevant to it. The most important result of the active tests is the cooling capacity given by:

$$\dot{Q}_{\mathrm{c}} = \frac{1}{\xi} \sum_{i=1}^{\xi} \left[\frac{1}{\tau_{\mathrm{HB}}} \int_{\tau_{\mathrm{HB}}} \dot{m}(t) c_{\mathrm{p,f}} [T_{\mathrm{C}} - T_{\mathrm{reg,C,out}}(t)] \, dt \right] \tag{4.9}$$

where, once again, the values of $T_{reg,C,out}$ are measured by thermocouple $T_{C,end}$, except in the case of Regenerator-3. A more detailed description of the testing of each regenerator will be given in Section 5.1.

5 Results

This chapter will present all the relevant results that were obtained during the development of this dissertation. The first section will contain the model validation process based on the experimental results obtained with the two epoxy bonded regenerators analysed in this work (Regenerator-1 and Regenerator-2). The validation regarding Regenerator-3, which is not epoxy bonded, will be discussed near the end of the chapter due to its chronological placement in the development of the MRU regenerator. The validation section will then be followed by an analysis of the basic operating parameters of an AMR and their influence in the cooling capacity. These parameters include the mass flow rate, operating frequency, porosity and particle diameter. Next, an analysis of the layer and Curie temperature distribution will be exposed, followed by a void volume analysis. A brief discussion regarding deviations in the Curie temperature of the materials during manufacture is then made, and solutions to circumvent this problem are proposed. Up to this point in the chapter, all the results presented are not directly related to the design of the MRU regenerator, but the information yielded by them is important for the understanding of the fundamentals behind the design process, which is discussed in the following sections. These sections include a discussion of the manufacturing limitations which prevented some parameters from being changed, the integration of the AMR with the magnetic circuit and hydraulic sub-system and the decision process that was used to determine the MRU regenerator. Lastly, the model validation using the CV-HS-2 regenerator (Regenerator-3) is presented and a final redesign, which aimed to change the material of the regenerator to CV-HS-2, is discussed, with the final MRU regenerator being described.

5.1 Model Validation - Epoxy Bonded Regenerators

Chapter 4 presented a description of the three first-order test regenerators that were submitted to experimental tests to validate the numerical model. This section will focus specifically on the validation process of the epoxy-bonded regenerators (Regenerators-1 and 2), with the validation of Regenerator-3 being described in Section 5.7. The results are going to be presented separately for each regenerator since each went through a different testing routine, with the routine of Regenerator-2 being influenced in part by results obtained by Regenerator-1.

5.1.1 Regenerator-1

At the start of testing, most parameters related to the regenerator operation are known or can be prescribed, however, some other need to be determined before running the model, as detailed in Table 16. The intrinsic parameters of Regenerator-1 were already described in Section 4.1, among them the particle diameter, which is initially an unknown parameter. The particle diameter can be determined using dynamic laser scattering (DLS), which defines the distribution of diameter size for a sample containing a sufficient amount of particles. DLS results for Regenerator-1 are shown in Figure 56 and resulted on an average particle diameter of approximately 0.69 mm. With knowledge of the particle diameter, the regenerator can then be submitted to pressure drop tests to determine the effective porosity.

Table 16 – Known and unknown parameters of a regenerator test.

Known parameters	**Unknown Parameters**
MCM relative porosity (ε)	
Real porosity (ε_f)	
Frequency (f)	
Hot reservoir temperature (T_H)	
Temperature span (T_{span})	
Regenerator dimensions	Effective porosity (ε_{eff})
Number of layers	Particle diameter (d_P)
Curie temperatures (T_{Curie})	
Void volume length (L_{vv})	
Magnetic field profile	
Flow profile	
Heat transfer fluid	

5.1.1.1 Pressure Drop Tests

The effective porosity cannot be directly measured and needs to be indirectly obtained through experimental results. With knowledge of the particle diameter and the parameters shown in Table 16, the steady flow pressure drop becomes a function of the effective porosity ($\Delta P(\varepsilon_{eff})$) and thus one can be used to determine the other. To achieve that, steady flow isothermal experiments were carried out in which the pressure drop was measured as a function of the fluid flow rate and the value of ε_{eff} was adjusted to fit the fluid momentum equation to the experimental results. The result of this fit for Regenerator-1 is shown in Figure 57 together with the predicted results obtained using the real porosity (37.6%) as reference. These results were the original motivation for the implementation of an effective porosity since the experiment indicates that something in the porous medium is causing the pressure drop to be higher than predicted. The most remarkable difference in this porous medium compared to previously tested porous media (which showed good agreement with the model's

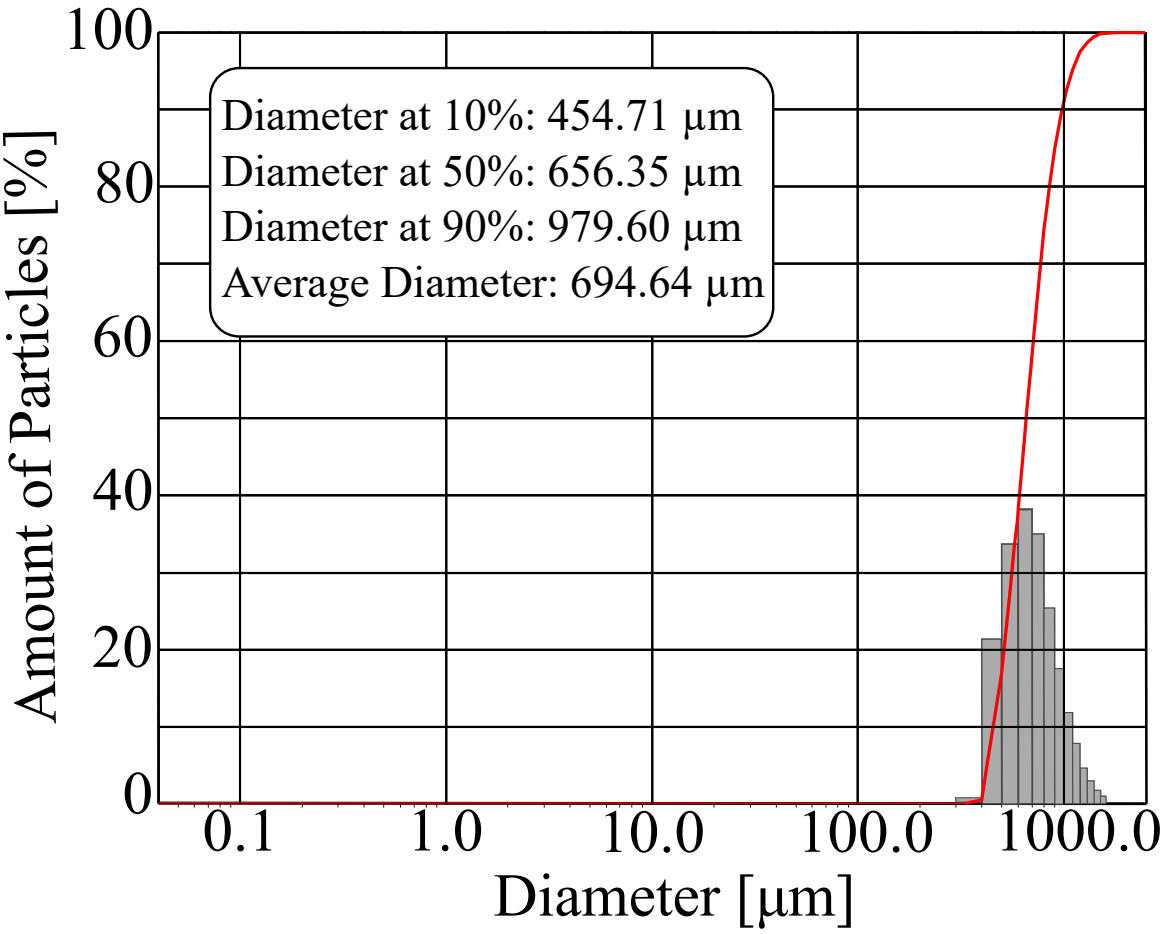

Figure 56 – DLS results for the MCM used in Regenerator-1 showing an average particle diameter of 0.69 mm. The red line indicates the cumulative amount of particles.

predictions, see Trevizoli (2015)) was the presence of epoxy. Thus, it was hypothesized that the epoxy was clogging the porous medium, increasing the pressure drop and reducing the heat exchange, which resulted in the adoption of an effective porosity.

A good fit for steady-state isothermal flow, however, does not initially guarantee that the model will accurately predict the pressure drop during actual operation, where flow acceleration is present due to the periodic changes in flow direction. Therefore, further evaluation using the pressure drop from active tests was done to check if this extrapolation could be done, with the results being shown in Figure 58. As can be seen, applying this fit to simulate AMR operation results in a good agreement with the experimental pressure drop results (<15%), which is not greatly affected by the temperature span. Finally, Figure 59 illustrates the good agreement between the experimental and numerical pressure drop profiles during one cycle of an active test that will be discussed in the next section, lending further strength to the effective porosity hypothesis.

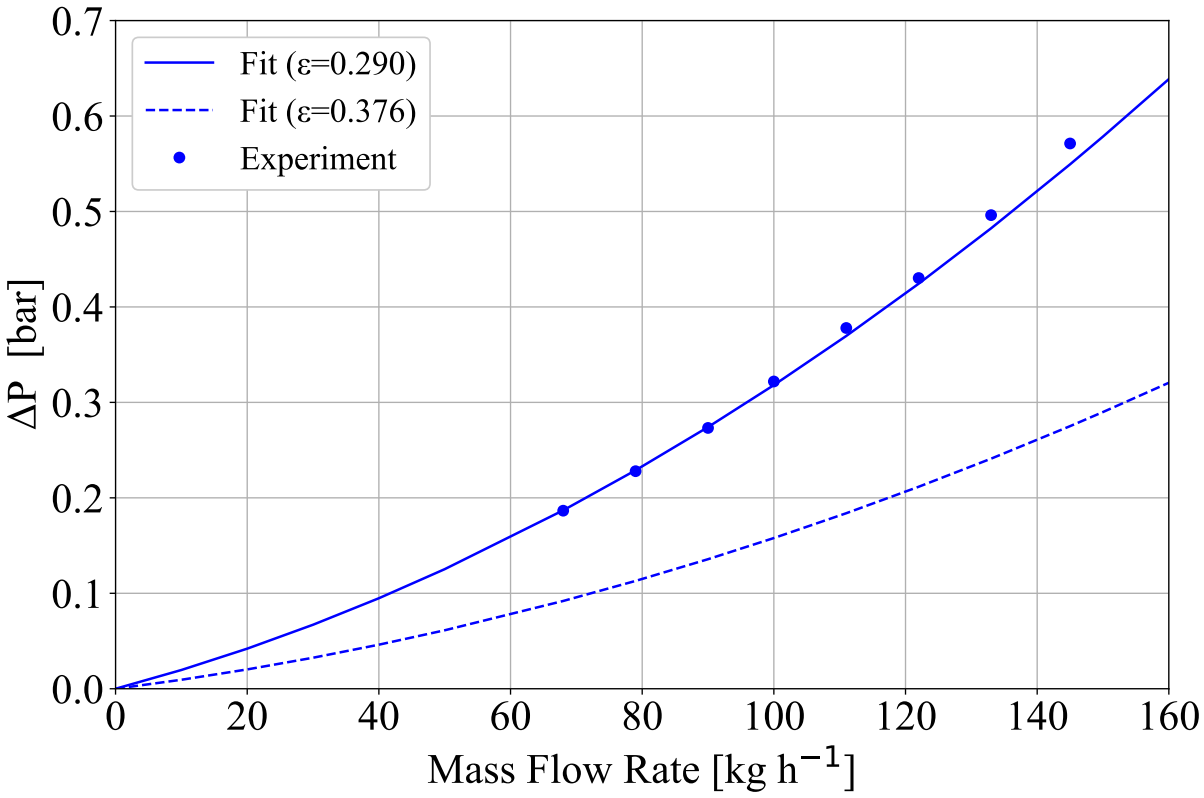

Figure 57 – Pressure drop fitting as a function of the mass flow rate in steady flow isothermal experiments of Regenerator-1 with the predicted pressure drop using the real porosity as reference.

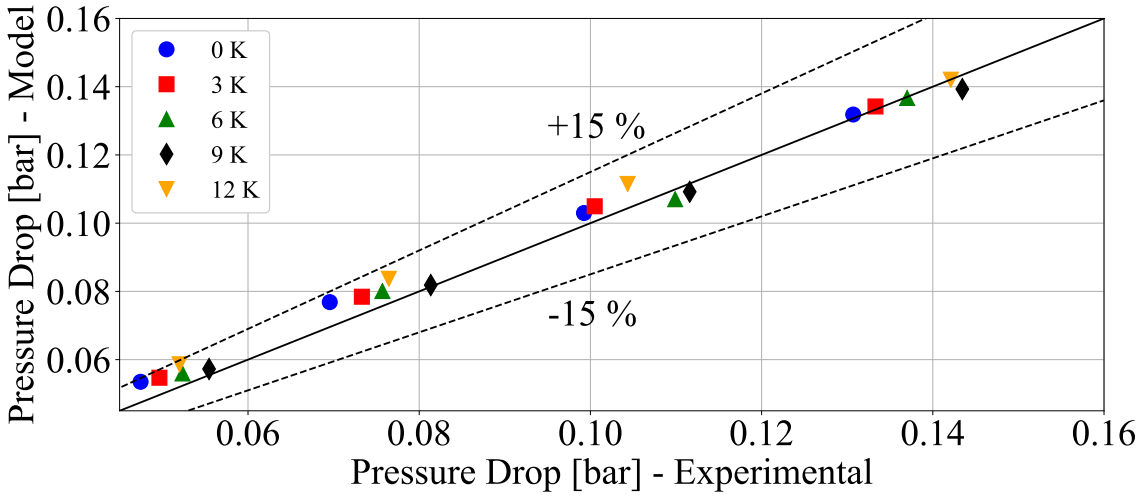

Figure 58 – Comparison between the numerical and experimental average pressure drop results for Regenerator-1 for different mass flow rates and temperature spans.

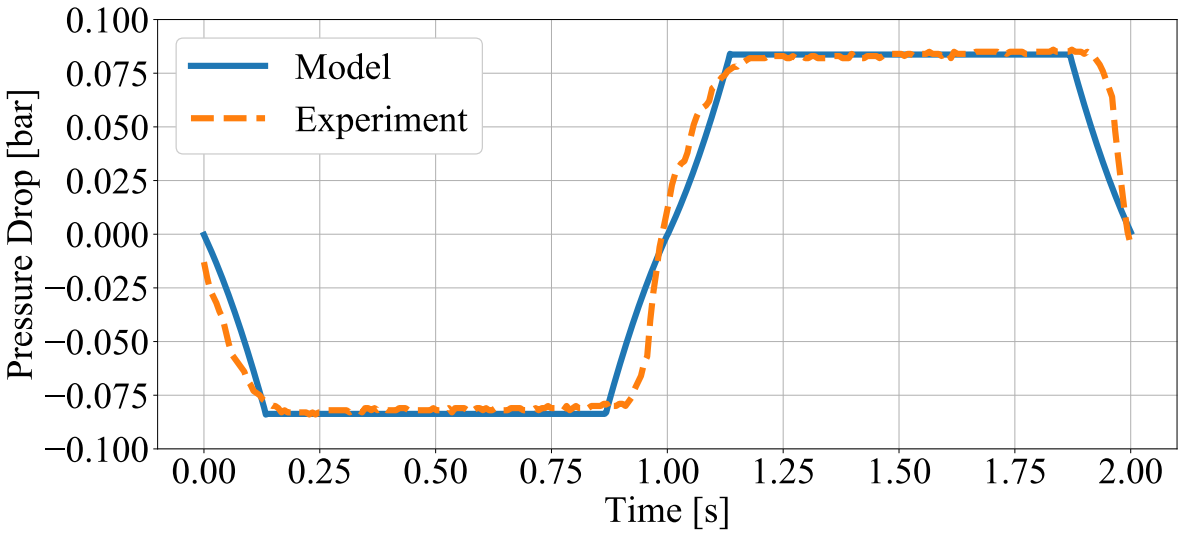

Figure 59 – Numerical and experimental results for the pressure drop during a cycle in Regenerator-1 for a mass flow rate of 40 kg h^{-1} and span of 12 K between the thermal reservoirs.

5.1.1.2 *Active Tests*

The final step of testing a regenerator involves the active tests. In these tests, the regenerator is placed inside a magnet which generates a known magnetic field profile (see Section 4.2) and goes through the entire AMR cycle (see Section 2.4.1). These tests will generate a time-dependent temperature variation (profile) for the fluid at the ends of the regenerator which can be used to determine the cooling capacity. In order to validate the model, a good agreement is required between both the numerical and experimental temperature profiles and the resulting cooling capacity. A summary of the test conditions can be found in Table 17, along with properties of Regenerator-1 which were already detailed in Section 4.1. The hot side temperature was chosen to be 309.15 K because preliminary tests showed that this condition resulted in the highest cooling capacities. The other operating parameters were chosen primarily due to limitations of the experimental apparatus. All tests were performed twice and the cooling capacity results that will be shown are the average between both results. The difference between the cooling capacity of tests under the same conditions was always below 1 W, and all but two cases had differences below 0.5 W.

Figures 60 and 61 show the temperature profile obtained experimentally and numerically in both ends of the regenerator during three cycles. The results show a good agreement between themselves, especially for the hot side. The sharp changes observed in the numerical temperature profiles (at odd seconds for the hot side and even seconds for the cold side) are the model response to changes in flow direction, according to the profile shown in Figure 59. Some slight differences between the cycles can be seen in the experimental profiles, however, they were considered to be sufficiently small to

Table 17 – General parameters of Regenerator-1 active tests.

Parameter	Value
Frequency	0.5 Hz
Mass flow rate	30 to 60 kg h^{-1}
Blow fraction	50%
Hot side temperature	309.15 K
Temperature span	0 to 12 K
Maximum field	1.69 T
Field profile	Rectified cosine
Fluid	2 % vol. ENTEK-water solution
Regenerator shape	cylinder
Regenerator length	50 mm
Regenerator diameter	24.3 mm
Curie temperature	299.9 K, 303.5 K and 307.0 K
Epoxy amount	2.7 wt.%
Housing material	AISI 304 Stainless steel
Housing thickness	0.5 mm

assume that the periodic steady state was reached. The temperature profiles for the other test conditions can be found in Appendix B.

Finally, Figure 62 shows a comparison between the numerical and experimental AMR cooling capacity curves as a function of the temperature span for all mass flow rates. A typical AMR performance curve behaviour is observed, with the cooling capacity decreasing with the temperature span and higher mass flow rates having higher zero-span cooling capacities but reaching lower temperature spans. The average deviation for the zero-span cooling capacity was smaller than 7%, and the numerical results followed the experimental trends fairly well. The model showed a tendency to slightly overestimate the cooling capacity at lower mass flow rates while the behaviour at higher mass flow rates is more unpredictable. The average deviation of the cooling capacity in percentage points increases with the span, but mostly due to the smaller cooling capacity values. The absolute average deviation of the cooling capacity reaches a peak at the span of 3 K (1.66 W) and is minimal at the span of 0 K (0.90 W), which shows that the model has a tendency to underestimate the initial drop of the cooling capacity with the temperature span, but corrects itself as the span rises. One important characteristic of these profiles is that the cooling capacity starts to sharply decrease after the temperature span of 6 K. This value is usually closely related with the span between the Curie temperatures of the regenerator, which in this case was near 7 K. While other parameters may have an influence on the exact position of this point, most numerical and experimental results did not deviate from the Curie temperature span by more than 1 K. This is true as long as the hot reservoir temperature is properly chosen and the flow imbalance is minimum. Thus, precise knowledge of the Curie temperatures of each layer, especially the first and last ones, is extremely important to properly predict

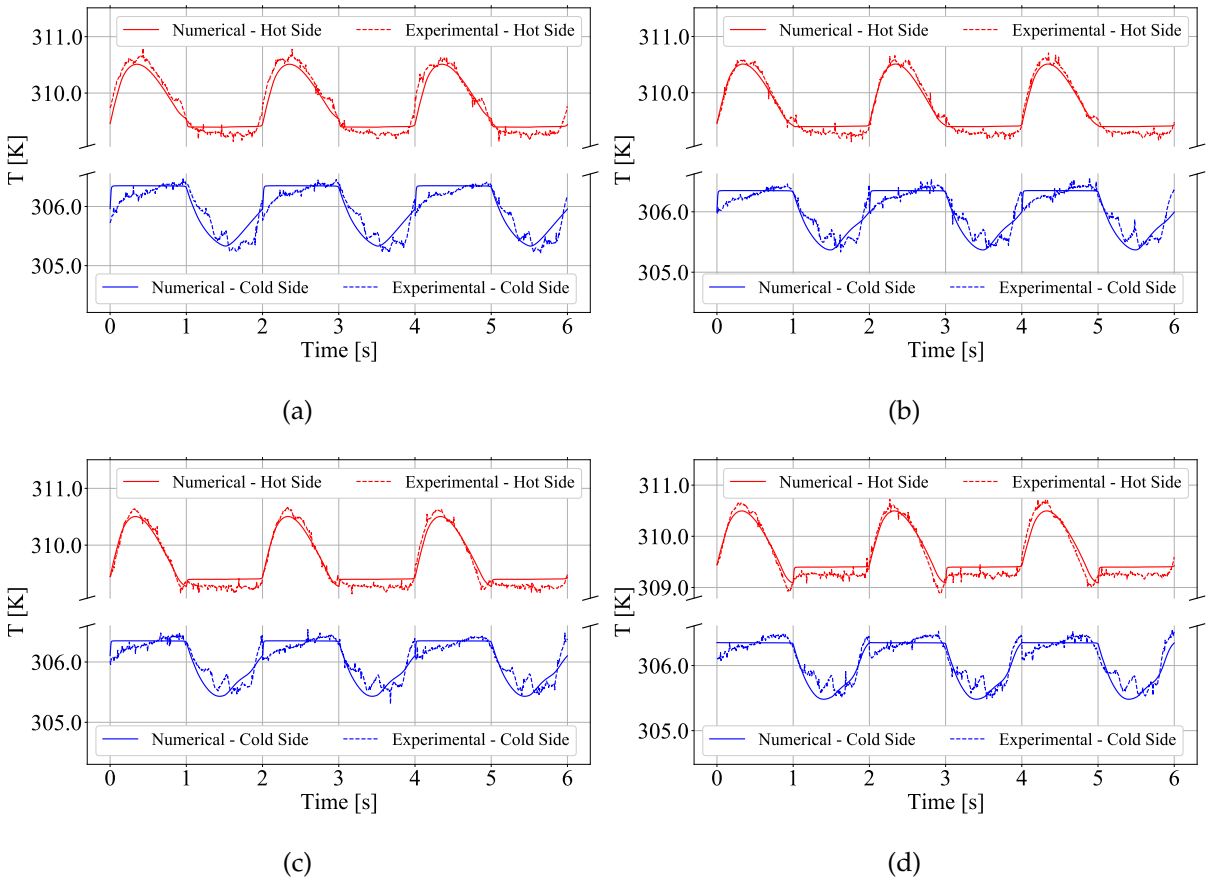

Figure 60 – Comparison between the numerical and experimental temperature profiles at the hot and cold ends of Regenerator-1 during three cycles. The cycle frequency is 0.5 Hz, the temperature span is 3 K and the mass flow rate is (a) 30, (b) 40, (c) 50 and (d) 60 kg h^{-1}.

the behaviour of the AMR performance curve.

The results shown in Figure 62 along with the temperature profiles at the ends of the regenerator were considered sufficient to validate the model against this regenerator. The main takeaways from this validation processes were:

- The effective porosity proved to be efficient at reproducing the experimental pressure drop behaviour of the regenerator;
- The value of effective porosity measured in steady flow tests can be used to model transient regimes without significant deviations on the results;
- The temperature profiles at the ends of the regenerator generated by the model exhibited a good agreement with the experimental results, with the main differences being caused by the flow waveform;
- The cooling capacity curve is accurately predicted by the model provided that the Curie temperatures are properly measured;

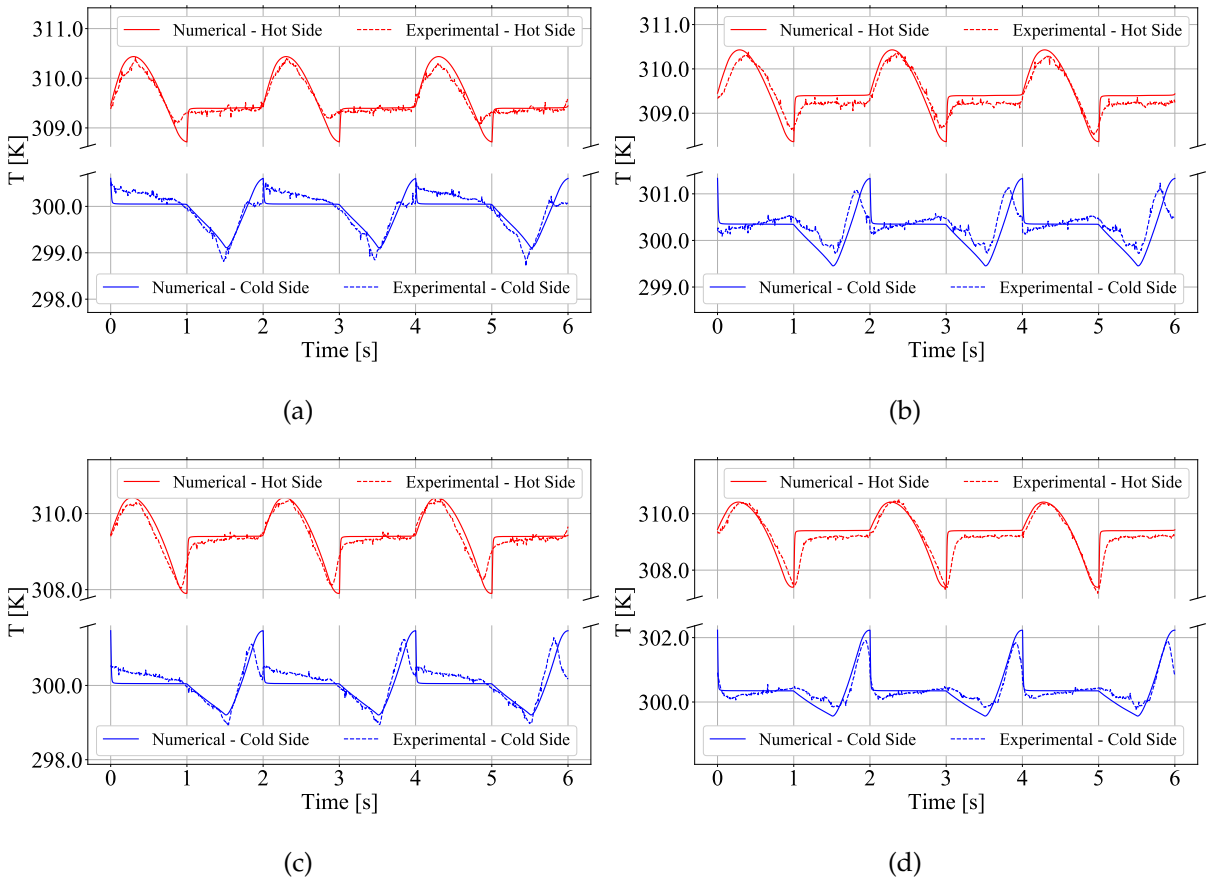

Figure 61 – Comparison between the numerical and experimental temperature profiles at the hot and cold ends of Regenerator-1 during three cycles. The cycle frequency is 0.5 Hz, the temperature span is 9 K and the mass flow rate is (a) 30, (b) 40, (c) 50 and (d) 60 kg h^{-1}.

- While the heat transfer was not directly compared in this analysis, it can be considered validated by the good agreement shown by the cooling capacity results, but further tests should be done.

5.1.2 *Regenerator-2*

The initial procedure applied to Regenerator-2 is identical to the one described for Regenerator-1, with the intrinsic parameters of the regenerator already described in Section 4.1 and the known and unknown parameters described in Table 16. The particle diameter was once again measured using dynamic laser scattering (DLS), see Figure 63, and was approximately equal to 0.65 mm. With knowledge of the particle diameter, the regenerator can then be submitted to pressure drop tests to determine the effective porosity.

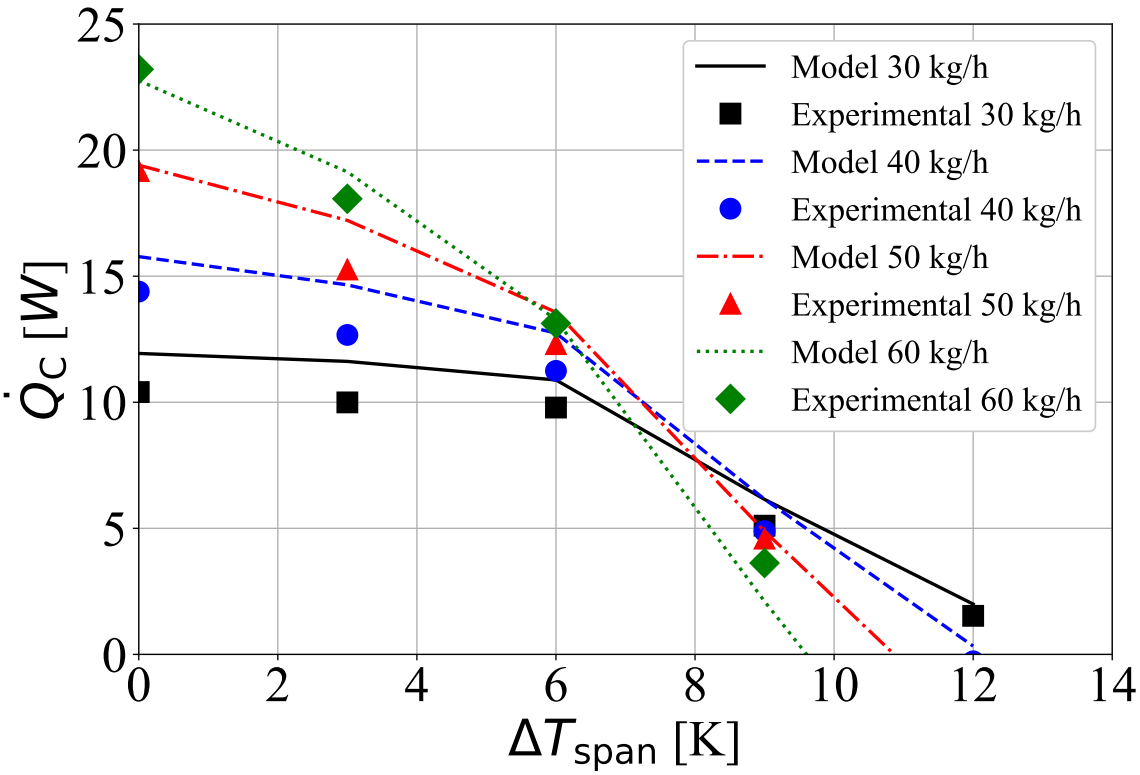

Figure 62 – AMR performance curves (experimental data vs. model results) for Regenerator-1 for mass flow rates of 30, 40, 50 and 60 kg h^{-1}. The cycle frequency was 0.5 Hz, while the hot reservoir temperature was 309.15 K.

5.1.2.1 *Pressure Drop and Passive Tests*

The main purpose of the pressure drop tests for Regenerator-2 was the same as for Regenerator-1: determine the effective porosity. However, they were also used to monitor the integrity of the porous medium during the tests, with any increase in pressure drop serving as an indicator of disintegration of the epoxy-bonded porous structure. The fitting of the effective porosity yielded a value of 27%, smaller than for Regenerator-1, as shown in Figure 64. This effective porosity was considered further evidence that the epoxy was clogging the regenerator since its value was once again much smaller than the real porosity (38%). Figure 65 shows the results of using the effective porosity to estimate the pressure drop in the passive tests. Similarly to Regenerator-1, the effective porosity shows good agreement when predicting the pressure drop of the periodic steady state, especially for the frequency of 0.5 Hz. The deviation is once again consistently smaller than 15% except for the lowest mass flow rate where the pressure drop is considerably low and thus more sensitive to small deviations.

Next, the regenerator was subjected to passive experiments, which were used to validate the parts of the model not related to the MCE, mainly the heat transfer and losses due to epoxy and void volumes. In these experiments, the regenerator was

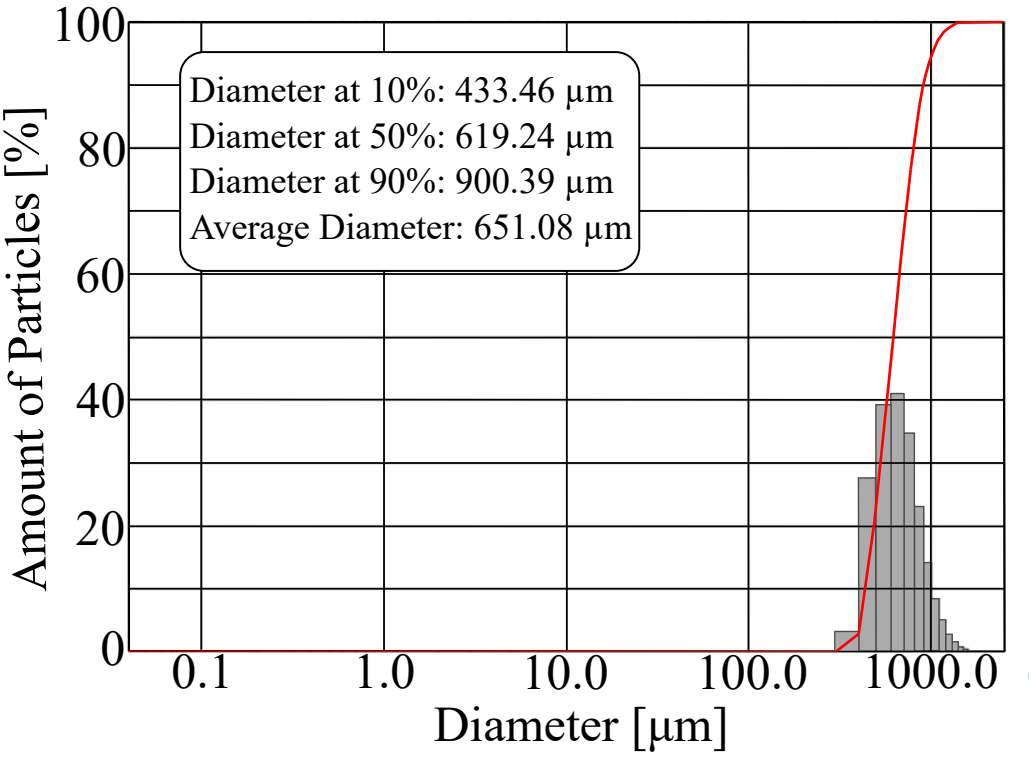

Figure 63 – DLS results for the MCM used in Regenerator-2 showing an average particle diameter of 0.65 mm. The red line indicates the cumulative amount of particles.

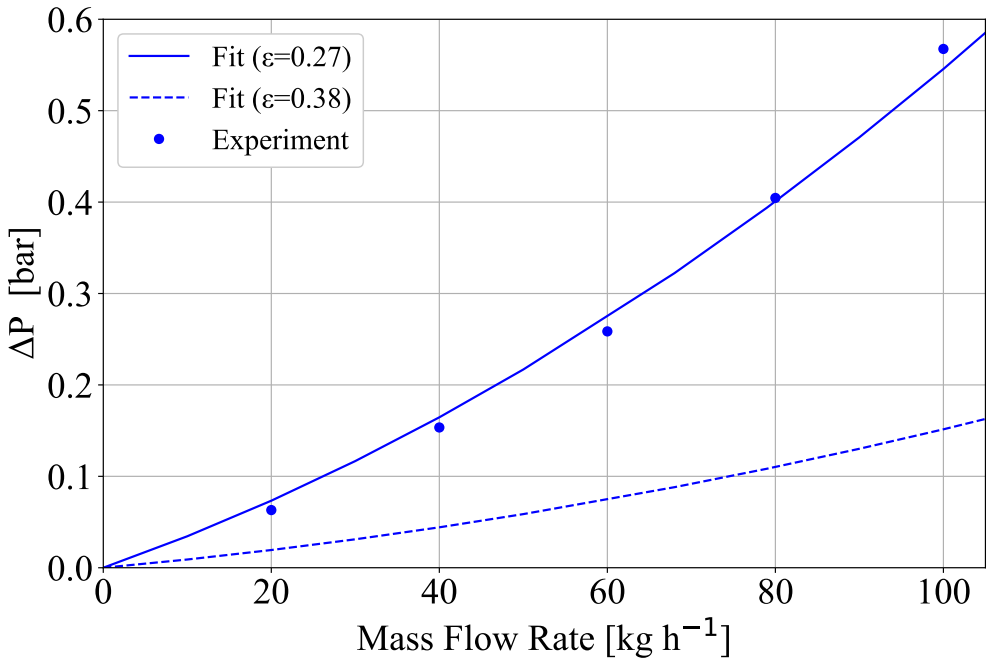

Figure 64 – Pressure drop fitting as a function of the mass flow rate in steady flow isothermal experiments of Regenerator-2 with the predicted pressure drop using the real porosity as reference.

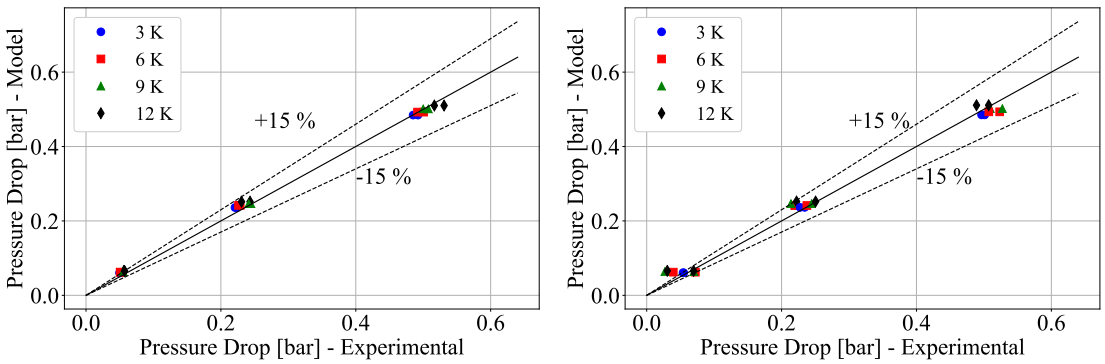

Figure 65 – Comparison between the numerical and experimental average pressure drop results for Regenerator-2 for different mass flow rates and temperature spans operating with a blow fraction of 50% and frequency of (a) 0.5 and (b) 0.75 Hz.

removed from inside the magnet and operated between two thermal reservoirs with set temperatures. The temperatures at both ends of the regenerator were measured during the cycle and used to determine its effectiveness. In the model, the regenerator was simulated by setting a constant, 0 T field. This configuration guarantees that the term relating to the MCE becomes zero and that the properties of the MCM will only be a function of temperature. The effectiveness can then be determined from the temperature profiles at the ends of the regenerator. Three different correlations for the interstitial heat transfer correlation were tested: the one proposed by Wakao & Kaguei (1982), the one proposed by Kuwahara, Shirota & Nakayama (2001) and the one proposed by Pallares & Grau (2010).

The conditions of the passive tests of Regenerator-2 are shown in Table 18. It is important to note that the blow fraction of 25% was only used in tests at 0.5 Hz due to limitations of the apparatus. These cases were run in the model using all three correlations described above and the values of effectiveness were compared. The correlation proposed by Pallares & Grau (2010) showed the best agreement with the results, as shown in Table 19. Figures 66 and 67 show a comparison between experimental and numerical effectiveness results for Regenerator-2 operating with a blow fraction of 50% at 0.5 Hz, for all given mass flow rates and temperature span. The difference between the measured effectiveness of the spans was small (< 3% for all cases) and was mostly caused by slight imbalances that could not be corrected by the apparatus and which were considered in the model. The results for the other frequency and blow fraction can be found in Appendix B. The agreement between the results is considerably good, with all but two of the numerical points falling within the limits of the experimental results considering the thermocouple uncertainty of 0.2 K. The average deviation between the numerical and experimental effectivenesses was 2.24%,

as already shown in Table 19. The highest deviation observed was of 7.7% for the cold blow (20 kg h^{-1}, 3 K, 0.75 Hz) and of 7.4% for the hot blow (100 kg h^{-1}, 12 K, 0.5 Hz, 25% blow fraction). The model had a tendency to overestimate the effectiveness of the cold blow for all cases at 0.5 Hz and blow fraction of 25% and for most cases with a blow fraction of 50%, with the exception of the highest mass flow rates and highest spans. The effectiveness of the hot blow was also overestimated for all cases operating at a blow fraction of 25%, while cases with a blow fraction of 50% overestimated the effectiveness at lower mass flow rates and underestimated it at higher mass flow rates.

Table 18 – General parameters of Regenerator-2 passive tests.

Parameter	Value
Frequency	0.5 and 0.75 Hz
Mass flow rate	20, 60 and 100 kg h^{-1}
Blow fraction	25% and 50%
Hot side temperature	304 K
Temperature span	3 to 12 K
Fluid	2 % vol.. ENTEK-water solution
Regenerator shape	cylinder
Regenerator length	50 mm
Regenerator diameter	23 mm
Curie temperature	298.95 K, 299.6 K and 302.5 K
Epoxy amount	2.7 wt.%
Housing material	AISI 304 Stainless steel
Housing thickness	0.5 mm

Table 19 – Average deviation in the effectiveness results for the three proposed heat exchange correlations.

Correlation	Average Effectiveness Deviation
Pallares & Grau (2010)	2.24 %
Kuwahara, Shirota & Nakayama (2001)	3.16 %
Wakao & Kaguei (1982)	2.76 %

Comparing the effectiveness is not, however, enough to validate the heat exchange model, since great variations in the heat exchange may not result in great variations in the effectiveness, especially for high values of NTU. Table 19 helps to illustrate this, with three different correlations all obtaining considerably low average deviations of the effectiveness. Thus, it is necessary to also compare the temperature profile at the cold and hot ends of the regenerator obtained by the model and the experimental results. Figures 68 to 70 show the comparison between said temperature profiles for different operating conditions during three operation cycles. As can be seen, most cases show a good agreement between the numerical and experimental results. The most notable difference between the results is once again the presence of sharp changes in the numerical temperature profiles, which are due to the changes in the

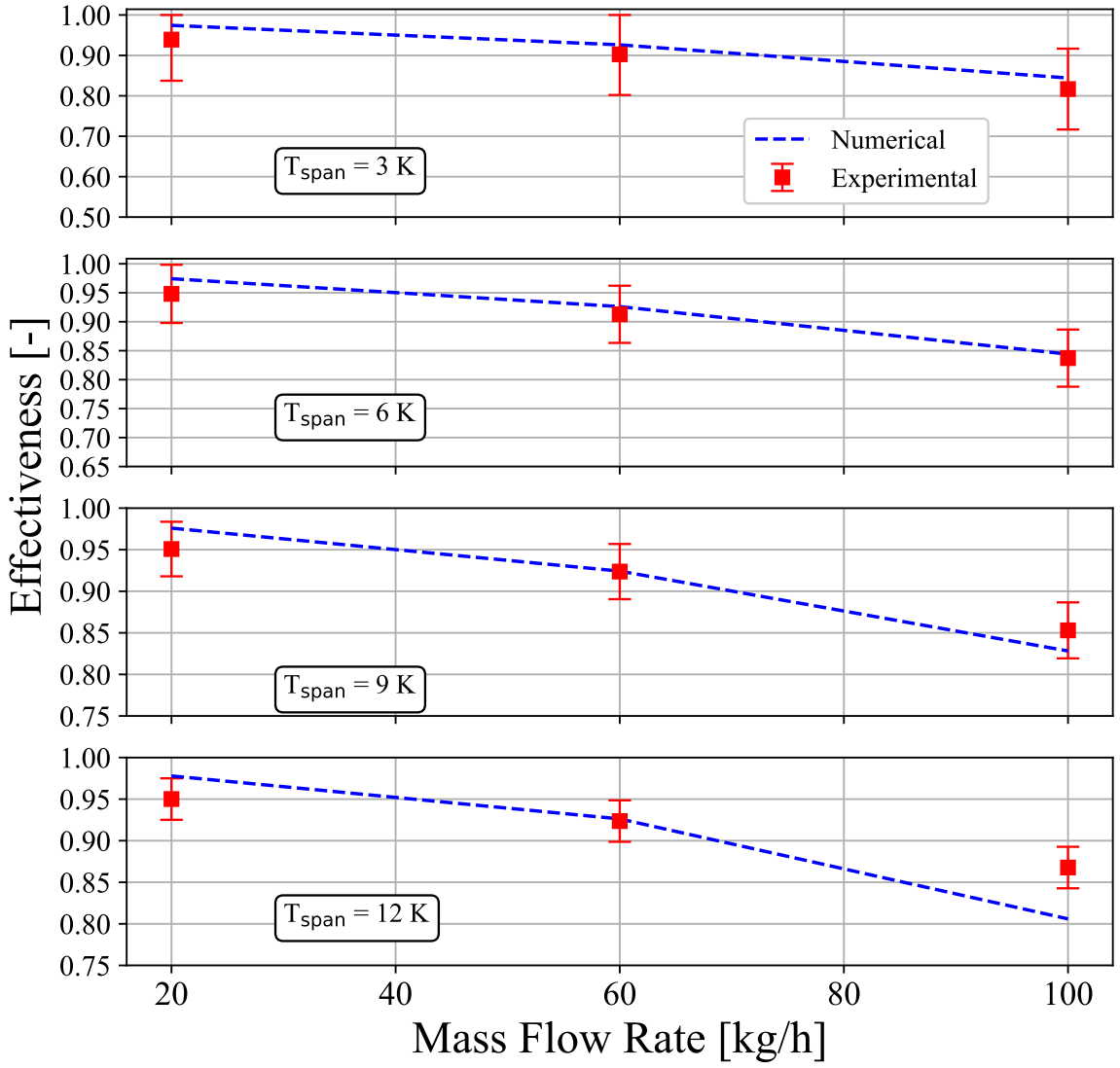

Figure 66 – Effectiveness results for the cold blow of Regenerator-2 for a frequency of 0.5 Hz and blow fraction of 50%. The model used the correlation proposed by Pallares & Grau (2010).

flow direction, according to the waveform of the fluid flow. It can also be seen that the cycles in the experimental results are not exactly the same, however, the differences are considerably small, which indicates that the periodic steady state was achieved in the experiment. The differences between the model and the experiment are more apparent in cases with low mass flow rate (20 kg h^{-1}) and tend to be less pronounced at higher mass flow rates (100 kg h^{-1}). There are multiple explanations for this phenomenon: (i) lower mass flow rates result in higher values of effectiveness and thus smaller differences in the temperature profile become more apparent, (ii) the effects of the void volume are more pronounced at lower mass flow rates and factors that cannot be accounted by the model such as the exact positioning of the thermocouple within the void volume become more relevant, and (iii) the small flow imbalance that cannot

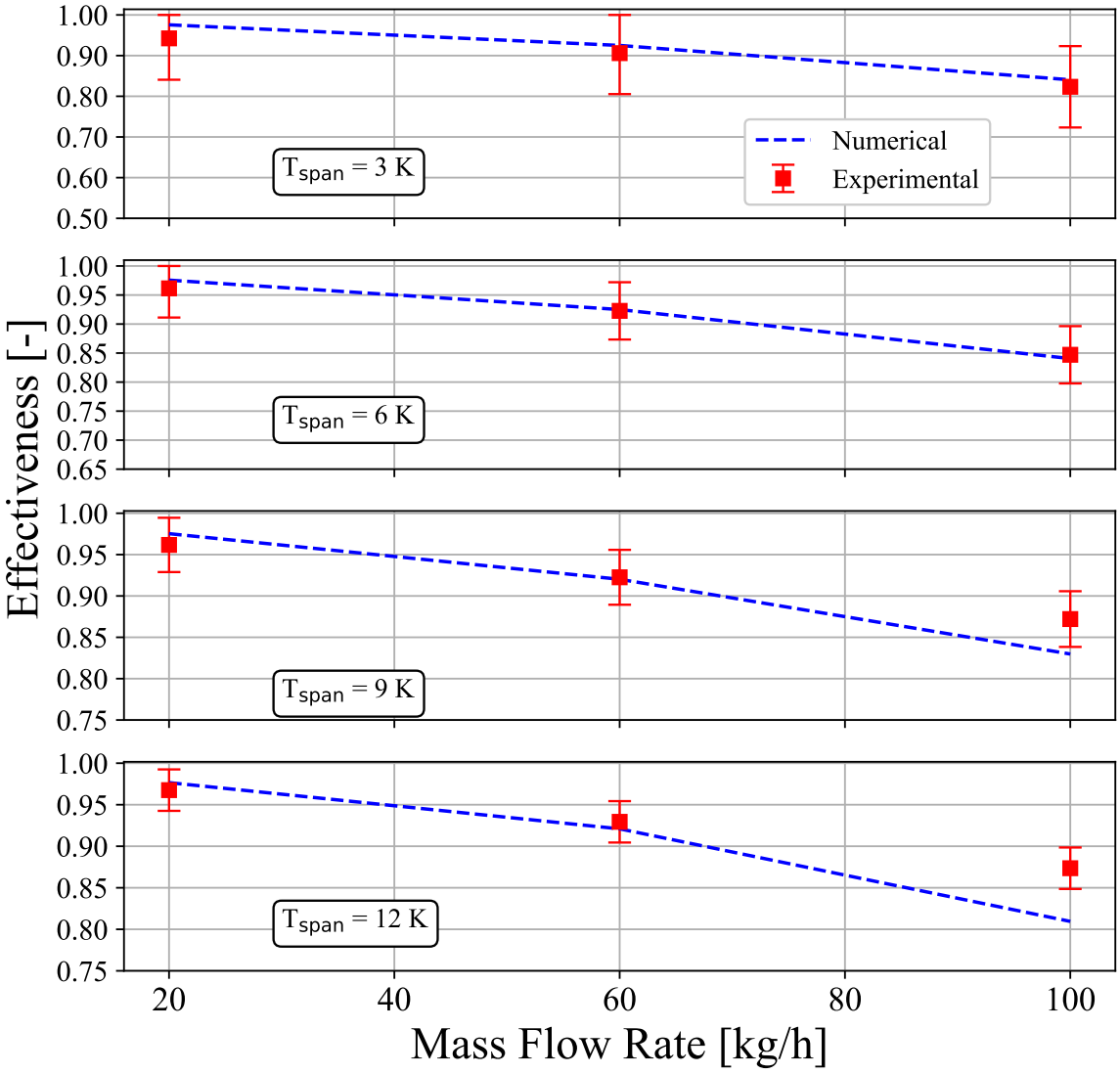

Figure 67 – Effectiveness results for the hot blow of Regenerator-2 for a frequency of 0.5 Hz and blow fraction of 50%. The model used the correlation proposed by Pallares & Grau (2010).

be controlled is more relevant at the lower mass flow rates. However, due to the overall good effectiveness and temperature profile results, along with the fact that the interest of this work is in regenerators operating at high mass flow rates, these results were considered satisfactory to validate the heat exchange of the model.

As mentioned in Section 4.1, Regenerator-2 was broken by the time it was submitted to active tests and this was translated into very low cooling capacity results which could not be used to validate the model. To illustrate this, Figure 71 shows the increase in the pressure drop between the active and passive tests, with the pressure drop at 100 kg h^{-1} becoming almost three times higher. This was considered evidence that the CV-HS material was breaking like CV-H and that Regenerator-2 could not be further tested. The main takeaways from the present experiments were:

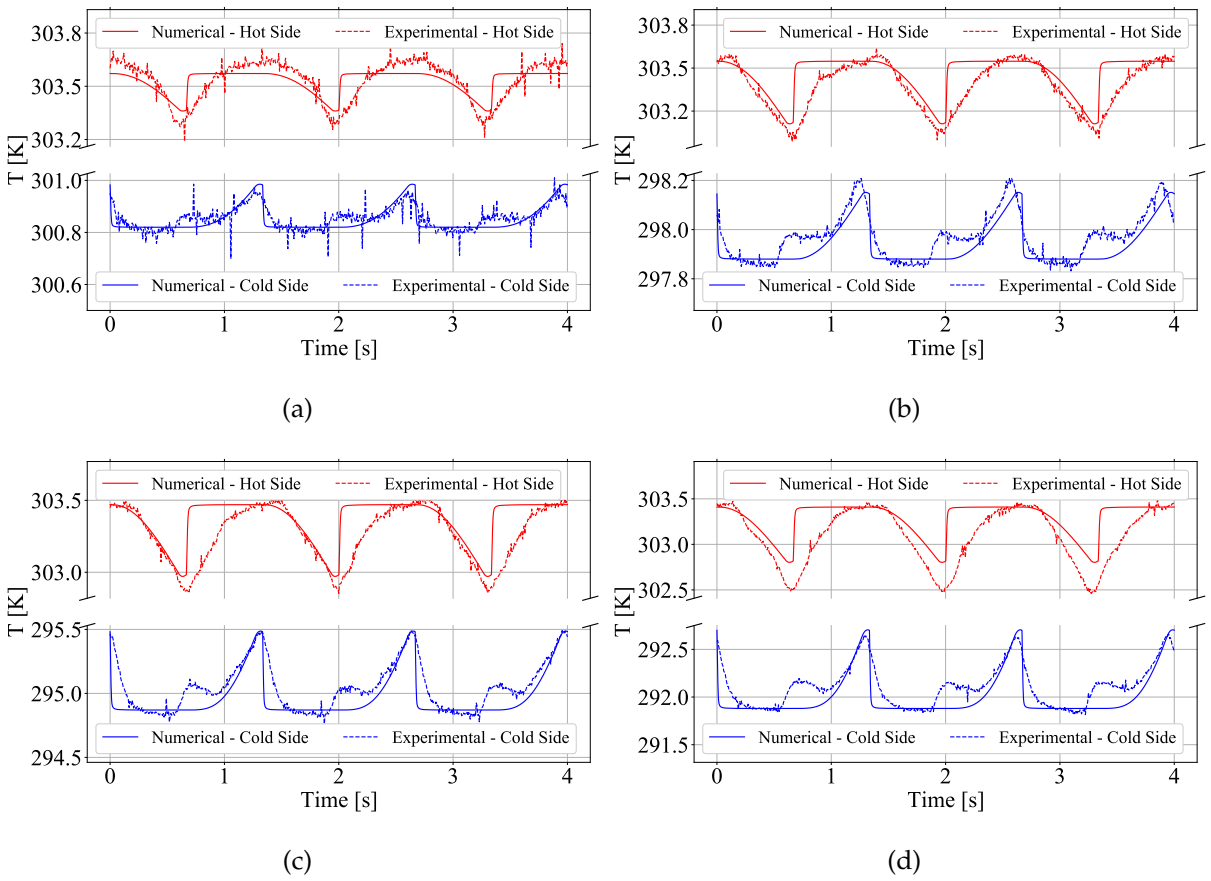

Figure 68 – Comparison between the numerical and experimental temperature profiles at the hot and cold ends of Regenerator-2 during three cycles of the passive tests. The cycle frequency is 0.75 Hz, the blow fraction is 50%, the mass flow rate is 20 kg h^{-1} and the temperature span is (a) 3, (b) 6, (c) 9 and (d) 12 K.

- The effective porosity was further confirmed to be efficient at predicting the pressure drop behaviour of the regenerator;
- The temperature profiles at the ends of the regenerator produced by the model exhibit a good agreement with the experimental results, with the main differences being caused by the flow waveform;
- The agreement of the profiles is usually worse at lower mass flow rates, which may be a consequence of the greater effect of the flow imbalance and the void volumes;
- The correlation proposed by Pallares & Grau (2010) had the best agreement with the data, but the other correlations also showed good results;
- Assuming that the porous media are similar and considering the cooling capacity results, there is a strong possibility that the heat exchange model was also adequate to represent Regenerator-1;

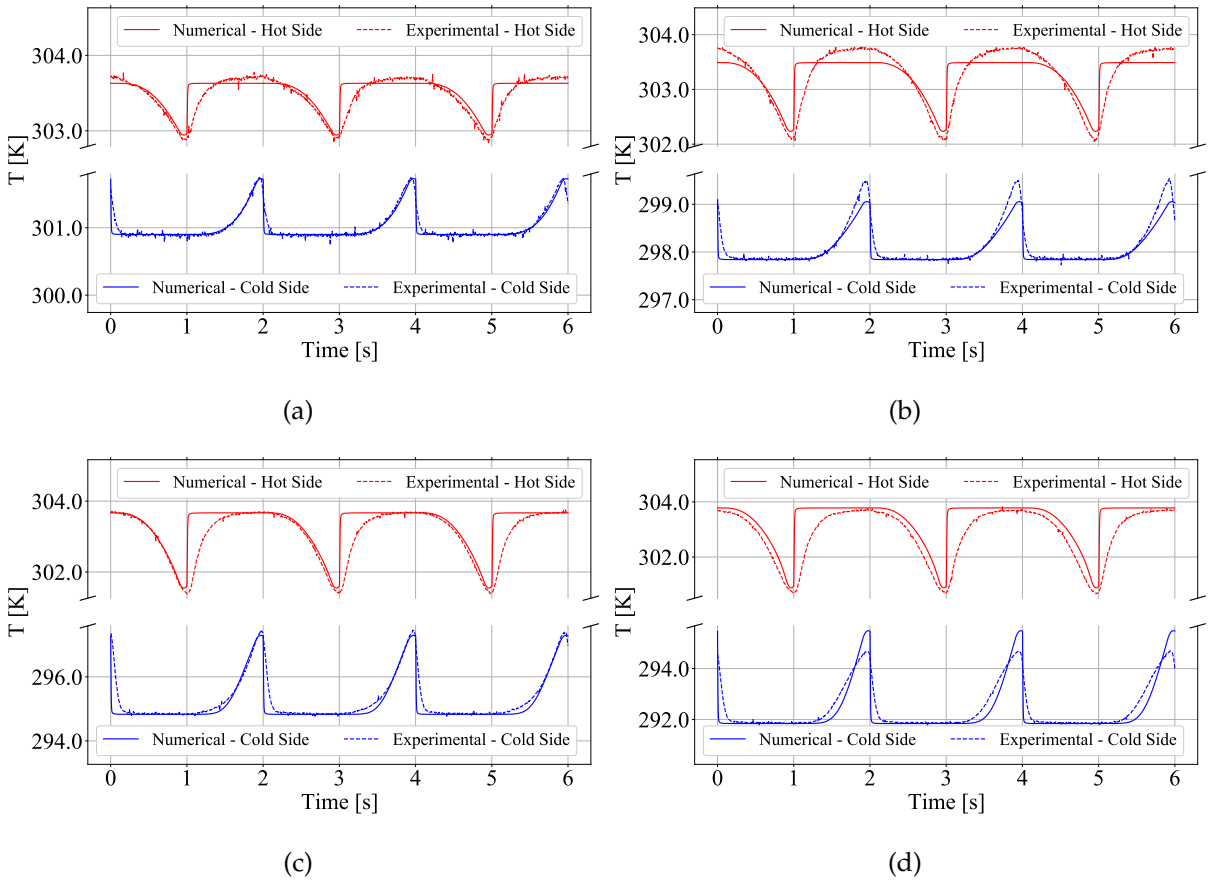

Figure 69 – Comparison between the numerical and experimental temperature profiles at the hot and cold ends of Regenerator-2 during three cycles of the passive tests. The cycle frequency is 0.5 Hz, the blow fraction is 50%, the mass flow rate is 60 kg h^{-1} and the temperature span is (a) 3, (b) 6, (c) 9 and (d) 12 K.

- By the same logic, there is a strong possibility that the model would also be able to accurately represent the active results of Regenerator-2, if those were available.

5.2 Basic AMR Operating Parameters

There are many different operating parameters that could influence the performance of an AMR. Some of these parameters need to be carefully selected before manufacturing the regenerator, such as the Curie temperature and layer distribution, the void volume size, the regenerator dimensions, the magnetic circuit that will generate the magnetic field and the hydraulic system that will provide the fluid flow. These parameters will be thoroughly analysed in further sections. Other parameters are, to an extent, independent of the regenerator and magnetic circuit, and may be adjusted after their manufacture if necessary. These parameters include the mass flow rate, operating frequency, temperature span (mainly for testing) and blow fraction. Finally, there are the operating parameters that are limited or cannot be changed due to manufacturing

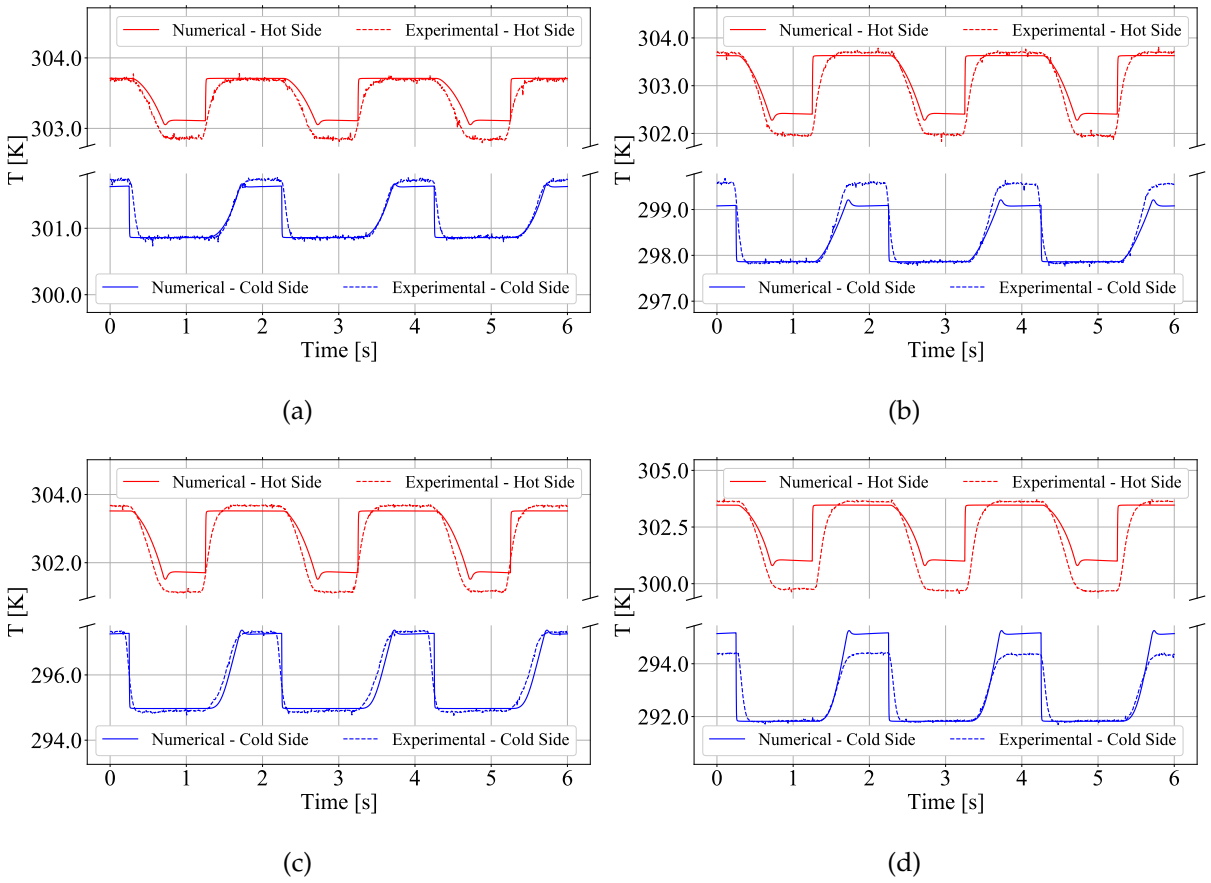

Figure 70 – Comparison between the numerical and experimental temperature profiles at the hot and cold ends of Regenerator-2 during three cycles of the passive tests. The cycle frequency is 0.5 Hz, the blow fraction is 25%, the mass flow rate is 100 kg h^{-1} and the temperature span is (a) 3, (b) 6, (c) 9 and (d) 12 K.

limitations or intrinsic characteristics of the material. These parameters include the particle diameter, the different porosities and the amount of epoxy in the porous medium. This section will focus on the latter two kinds of parameters, more specifically the mass flow rate, operating frequency, porosity and particle diameter, showing their influence on the cooling capacity and how they affect the tests required to determine the first kind of parameter.

Table 20 shows the basic properties of the fictitious regenerator which will be used as the reference for all analyses done in this section. The geometry was chosen because it yielded cooling capacities near the value needed for the MRU project and for having characteristics similar to those expected for the final regenerator configuration. Unlike the regenerators tested in Section 5.1, this regenerator has a rectangular cross section, which is closer to the section that will be used in the regenerator to be designed for the MRU. The Curie temperature distribution factor and number of layers will be described in Section 5.3. Finally, the reference operating conditions are shown in Table 21. In this analysis, the field and flow profiles are idealized as ramp and step profiles, respectively. The blow and maximum and minimum field fractions are both

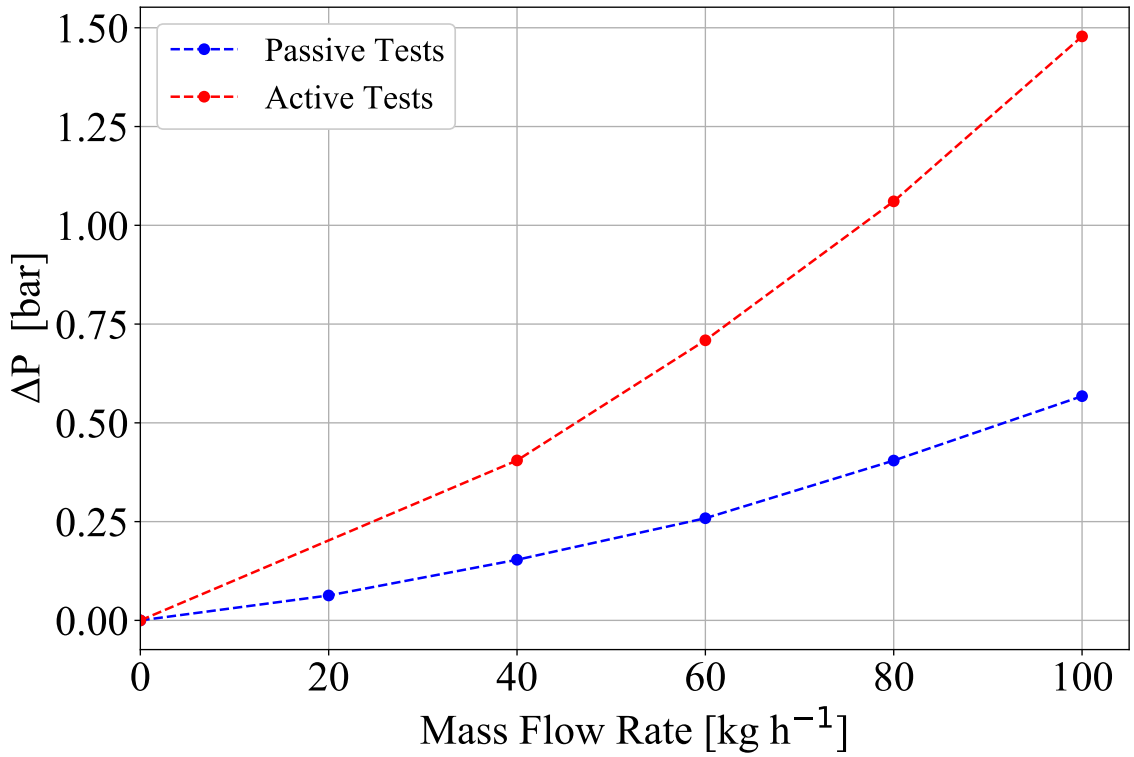

Figure 71 – Increase of the pressure drop between the active and passive tests of Regenerator-2.

35%, a choice that will be discussed in sections below. Figure 72 illustrates both profiles during one cycle of the regenerator. The losses due to the casing heat transfer in these and further analyses were neglected because they were shown to have a neglectable effect on the cooling capacity for regenerators of this scale, but severely increased the computational time required to run the model.

Table 20 – Properties of the fictitious regenerator for the basic parametric analysis.

Name	Fict. Regenerator
MCM relative porosity (ε)	0.45
Real porosity (ε_f)	0.34
Effective porosity (ε_{eff})	0.27
Regenerator height	50 mm
Regenerator width	60 mm
Regenerator length	150 mm
Number of layers	15
Curie temperature distribution factor (CTDF)	-2 K
Heat transfer fluid	2 % vol. ENTEK-water solution
Particle diameter	0.65 mm
Material	CV-HS
Epoxy concentration	2.7 wt.%
Void volume	0 mm^3

Table 21 – Reference operating conditions for the basic parametric analysis.

Operating Conditions	Values
Frequency	1.5 Hz
Temperature span	30 K
Maximum applied magnetic flux density	1.0 T
Hot side temperature (T_H)	316.15 K
Applied field profile	Ramp
Blow profile	Step
Blow fraction	35%
High and low field fractions	35%

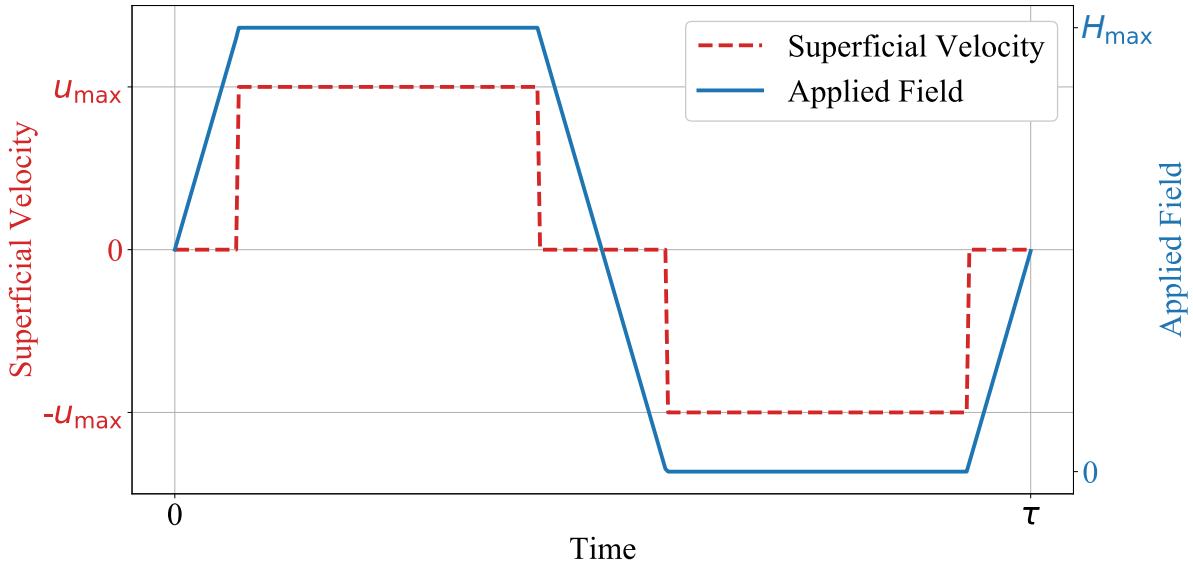

Figure 72 – Idealized flow and applied field profiles used in the analysis.

5.2.1 *Mass Flow Rate*

Most studies regarding regenerators focus on the influence of the utilization instead of the mass flow rate or frequency specifically. However, since these parameters are independent, and the utilization is not well defined for first-order magnetocaloric materials due to the behaviour of the specific heat capacity of the solid matrix, they will be analysed separately. The influence of the mass flow rate in the cooling capacity is fairly straightforward. The cooling capacity increases with the mass flow rate until a maximum value is reached, beyond which the cooling capacity starts to decrease. This happens because after this point the effects of the viscous dissipation due to the pressure drop start to dominate the phenomenon, which hinders the cooling capacity. The position of the peak can change if the regenerator is altered, and tends to be at higher mass flow rates for "better" regenerators (higher heat transfer, lower pressure drop, larger size, greater MCE).

Figure 73 shows the usual behaviour of the cooling capacity as a function of the mass flow rate obtained by the model for a regenerator at 4 different conditions,

highlighting the point of peak capacity. The first one, the reference, is the regenerator operating under what was chosen to be considered the normal conditions, and is used only as a means to compare the behaviour of the other regenerators. It had a peak cooling capacity at around 600 kg h^{-1}. The second regenerator had its pressure drop decreased by halving the percentage of pores blocked by the epoxy. As can be seen, this improved the overall performance of the regenerator and shifted the peak cooling capacity to a mass flow rate closer to 700 kg h^{-1}. The third regenerator had the maximum value of the magnetic field applied to it increased by 50%, which considerably increased its cooling capacity and shifted the peak to values over 800 kg h^{-1}. Finally, the last regenerator had its heat transfer coefficient between the solid and fluid phases artificially increased by 10 times, resulting in much better performance, so the peak capacity was shifted to mass flow rates over 1100 kg h^{-1}. This, however, should not be interpreted as saying that improving the heat exchange is better than increasing the applied field, which in turn is better than reducing the pressure drop. The cases were chosen only to show different changes in the cooling capacity profile. In fact, the improvement depends on how much these parameters can actually be improved. While a reduction in epoxy clogging could be achieved with just a few changes in the fabrication process, increasing the applied field by 50% would require profound changes in the magnetic circuit, increasing its price considerably, and increasing the heat exchange 10 times is, for all intents and purposes, impossible without radical conceptual changes in the regenerator, making a comparison between the three configurations unfair. Thus, if the objective is to maximize the cooling capacity, different regenerators must be compared not at the same mass flow rate, but with each one operating at its optimal mass flow rate. The only exception to this should be if the optimal mass flow rate of a regenerator surpasses the limits of the hydraulic system, in which case it should be analysed at the highest mass flow rate possible.

5.2.2 *Operating Frequency*

The operating frequency is usually analysed alongside the mass flow rate, since both are used to determine the utilization. However, its effect on the cooling capacity is considerably less straightforward than that of the mass flow rate, due to its indirect influence on many other operating parameters. Increasing the frequency reduces the period of the magnetization and demagnetization processes, which, in general, reduces the heat transfer losses. However, it also reduces the periods of the blows, which need to be long enough to allow the fluid to properly exchange heat with the solid matrix (see Fourier number in Section 3.6.3). This is especially important for large epoxy-coated spheres, which is the case for first-order regenerators. Not only that, due to the reduced periods, a higher pressure drop would be required to displace the same amount of fluid. Due to this competing effects, each regenerator is expected to have an optimal operating frequency, much like the mass flow rate. However, unlike the mass

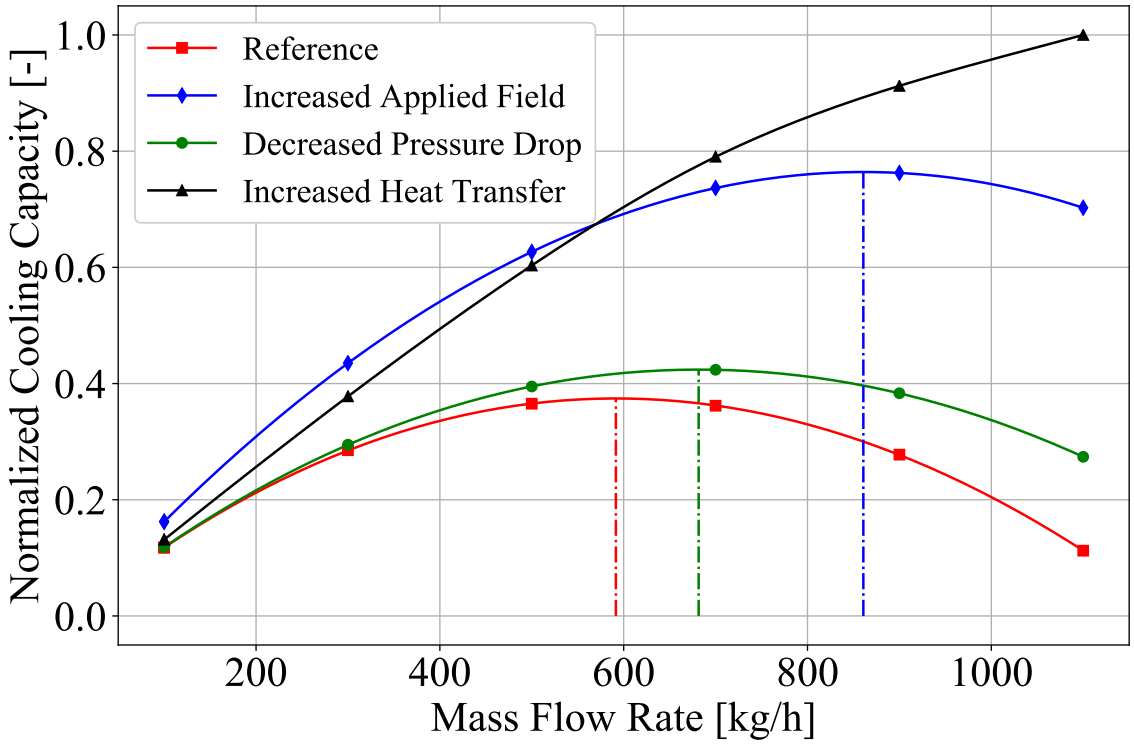

Figure 73 – Cooling capacity as a function of the mass flow rate and the effects of decreasing the pressure drop (by removing half of the epoxy blockage), increasing the applied magnetic field by 50% and increasing the heat transfer coefficient by 10 times.

flow rate, higher operating frequencies are considerably harder to achieve, especially for reciprocating magnet systems with bulky components. Thus, reaching the optimal operating frequency is often impossible. Similarly to the mass flow rate, regenerators with better heat transfer, higher applied field and more material tend to have higher optimal frequencies.

Figure 74 shows the behaviour of the cooling capacity for the reference regenerator at different frequencies. As can be seen, increasing the frequency from 0.5 Hz to 1.5 Hz greatly increases the cooling capacity because the effect of reducing the magnetization and demagnetization times is much greater than the losses due to the reduction of heat transfer time. Increasing the frequency from 1.5 Hz to 2.5 Hz also increases the cooling capacity, but considerably less. After that, the effect of the reduction of the heat transfer time begins to dominate, so raising the frequency from 2.5 Hz to 3.5 Hz stops increasing the cooling capacity. In this case, it is clear that the ideal operating frequency lies somewhere between 2.5 Hz and 3.5 Hz.

The dimensionless parameter that represents the effect of the frequency on the heat exchange is the Fourier number, which was defined in Section 3.6.3. A large Fourier number implies that the thermal wave reaches far into the sphere, while a low

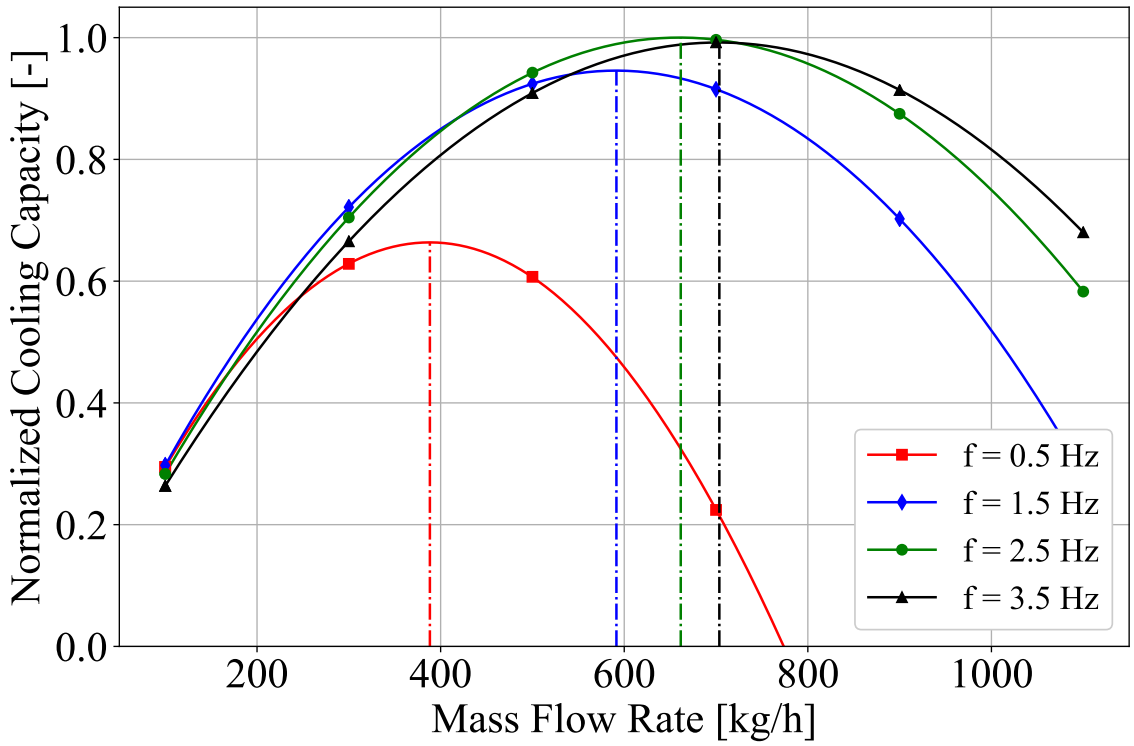

Figure 74 – Cooling capacity of the test regenerator as a function of the mass flow rate for different operating frequencies.

Fourier numbers implies the opposite. Thus, higher frequencies are associated with lower Fourier numbers and consequently hinder the heat exchange. Another parameter that greatly affects the Fourier number is the particle diameter: larger particles require more heat exchange time for the heat wave to reach their center, decreasing the Fourier number. Therefore, it can be predicted that the same regenerator with larger particles would reach peak cooling capacity at lower frequencies. Figure 75 shows cooling capacity results for the same regenerator with a particle diameter of 0.8 mm and it can clearly be seen that the peak cooling capacity was shifted from the original 2.5 Hz region to values closer to 1.5 Hz, as expected.

Finally, Figure 76 shows the cooling capacity as a function of the Fourier number for three different particle diameters. It can be seen that all cases reach the highest cooling capacity at Fourier numbers between 1 and 2, which correspond to different frequencies for each particle diameter (the larger the particle, the lower the frequency). This information can be used to predict the optimal frequency as a function of the particle diameter, or vice-versa. For a given regenerator, however, the optimal value of the Fourier number may shift depending on the operating conditions such as heat transfer rate and the magnetization period of the material, so care needs to be taken when using this method.

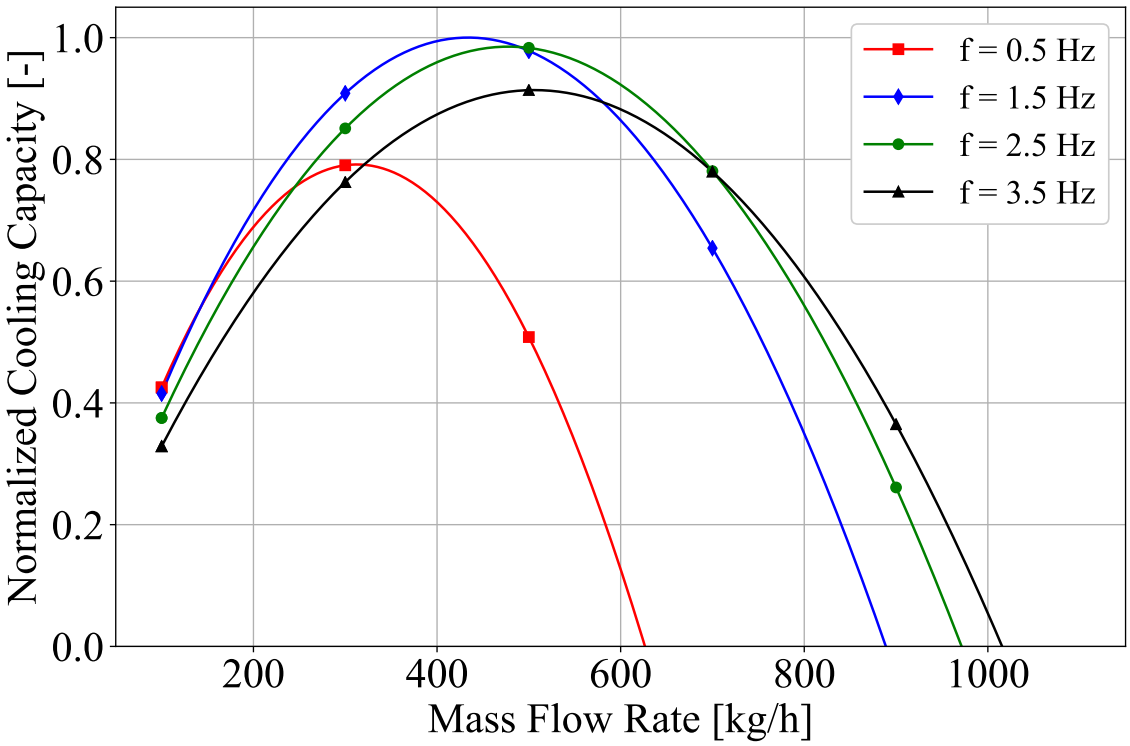

Figure 75 – Cooling capacity of the fictitious regenerator with a larger particle diameter (0.8 mm) as a function of the mass flow rate for different operating frequencies.

5.2.3 *MCM Porosity*

As described in Chapter 3, three porosities are needed to fully describe the regenerator: the MCM porosity (ε), the real porosity (ε_f) and the effective porosity (ε_{eff}). The MCM porosity considers only the volume occupied by the magnetocaloric material, the real porosity also includes the epoxy and the effective porosity includes the blockage caused by the epoxy.

The MCM porosity is related to the amount of magnetocaloric material in the regenerator with the amount of MCM increasing as ε decreases. Decreasing ε also increases the surface area density of the regenerator (β) and the interstitial heat transfer coefficient (h), increasing the heat transfer. However, it also increases the pressure drop, which is detrimental for the performance. Thus, the cooling capacity is expected to initially increase with the reduction of the MCM porosity until the pressure drop becomes so high that the cooling capacity starts to decrease. Figure 77 shows this phenomenon for a regenerator without epoxy which can be fully represented by only the MCM porosity (ε=ε_f=ε_{eff}). As can be seen, decreasing the porosity is always beneficial for the cooling capacity within the usual range of values because the cross sectional area is considerably large. Thus, an extreme value of porosity (0.10) is also shown to illustrate that the pressure drop does eventually start to dominate the phenomenon. However,

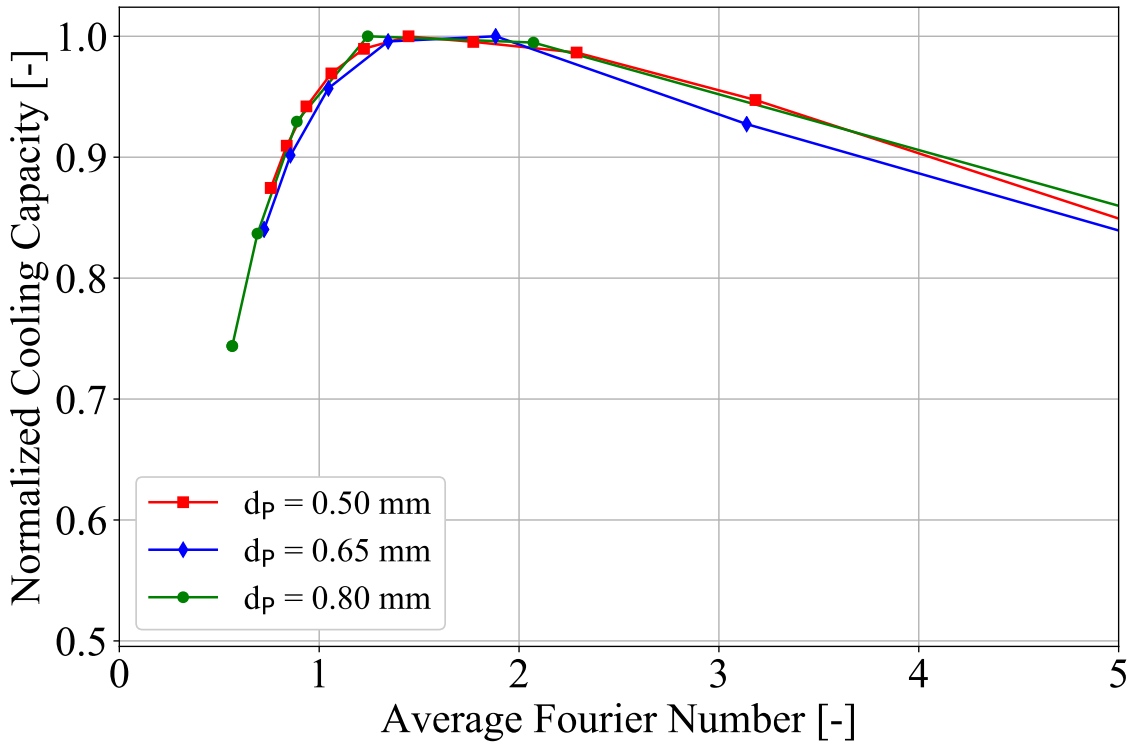

Figure 76 – Cooling capacity of the fictitious regenerator as a function of the Fourier numbers for three different particle diameters.

smaller regenerators, which are usually more affected by the pressure drop, may begin seeing cooling capacity drops at higher values of ε.

5.2.4 *Epoxy*

By adding epoxy, the real porosity becomes different from the MCM porosity ($\varepsilon > \varepsilon_t$). Changing the value of the real porosity is equivalent to changing the amount of epoxy added to the regenerator and its influence in the cooling capacity can, therefore, be seen as the influence of the epoxy. Unlike the MCM porosity, decreasing the value of the real porosity (adding more epoxy) does not increase the amount of magnetocaloric material, which is the main benefit of decreasing ε. Still, it increases the surface area density of the regenerator, but the overall heat transfer is reduced due to a thicker epoxy layer around the spheres. Figure 78 shows the influence of the real porosity on the heat transfer coefficient for a fixed MCM porosity of 0.45 and without considering any clogging. As can be seen, the heat transfer coefficient does in fact decrease as more epoxy is added, and the losses are greater for smaller particle diameters, since the thickness of the epoxy layer is greater in these cases. While a heat transfer coefficient reduction of around 10% is not necessarily high, the epoxy also has other deleterious effects to the performance.

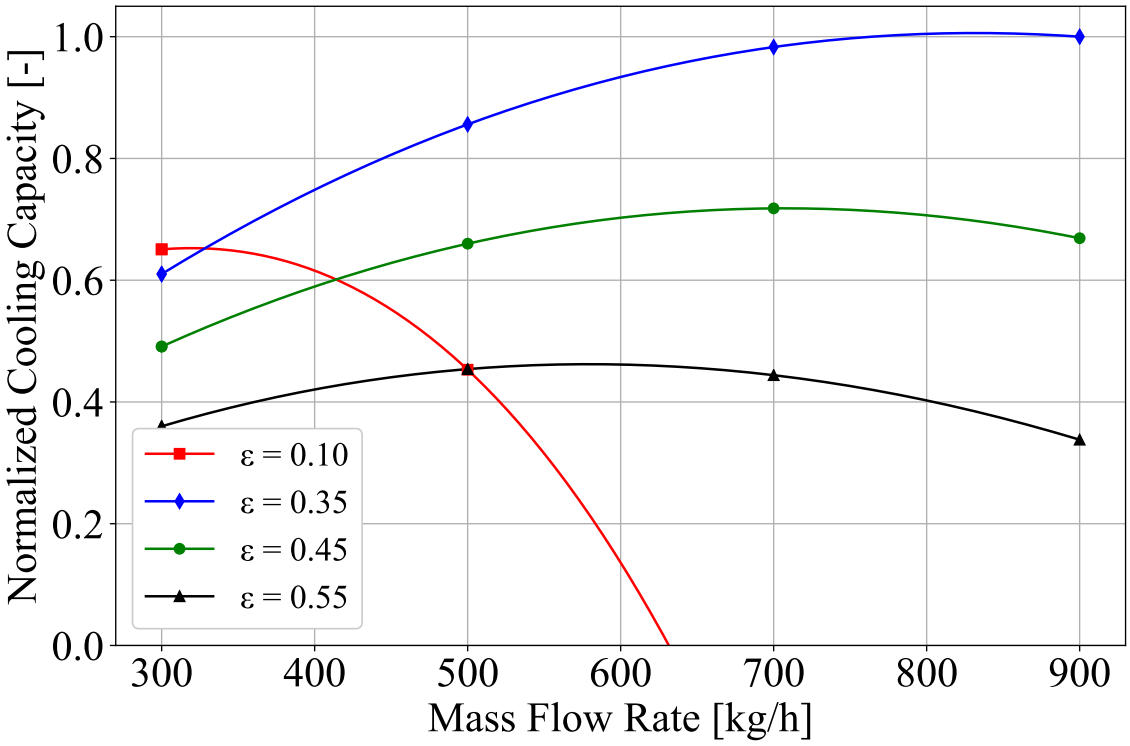

Figure 77 – Cooling capacity as a function of the mass flow rate and the effects of decreasing the MCM porosity for a regenerator without epoxy (ε=ε_f=ε_{eff}).

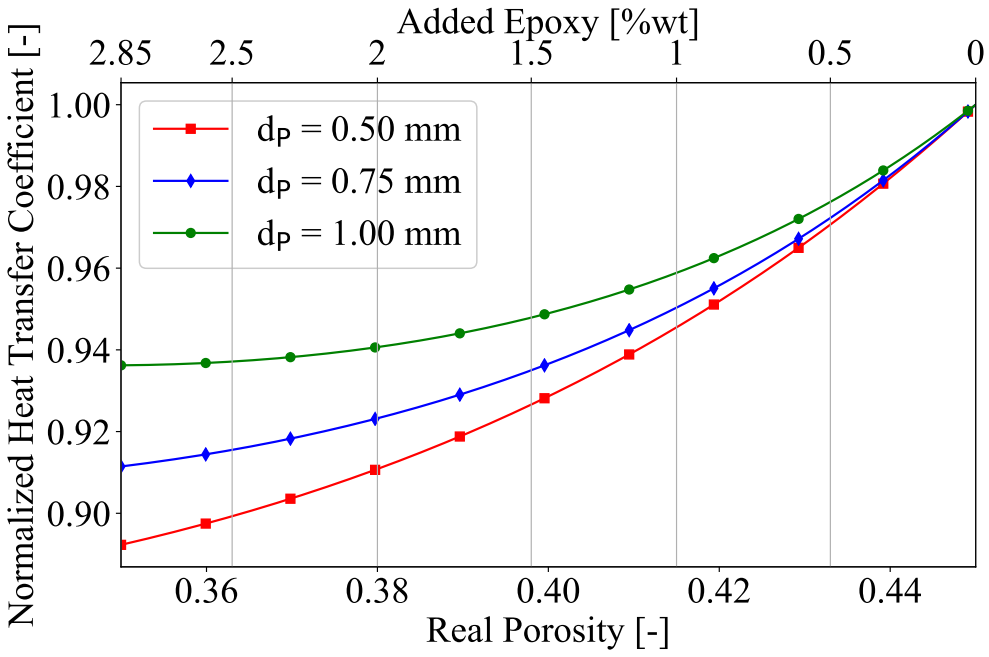

Figure 78 – Effect of the epoxy on the heat transfer coefficient for different particle diameters in a regenerator with a MCM porosity of 0.45.

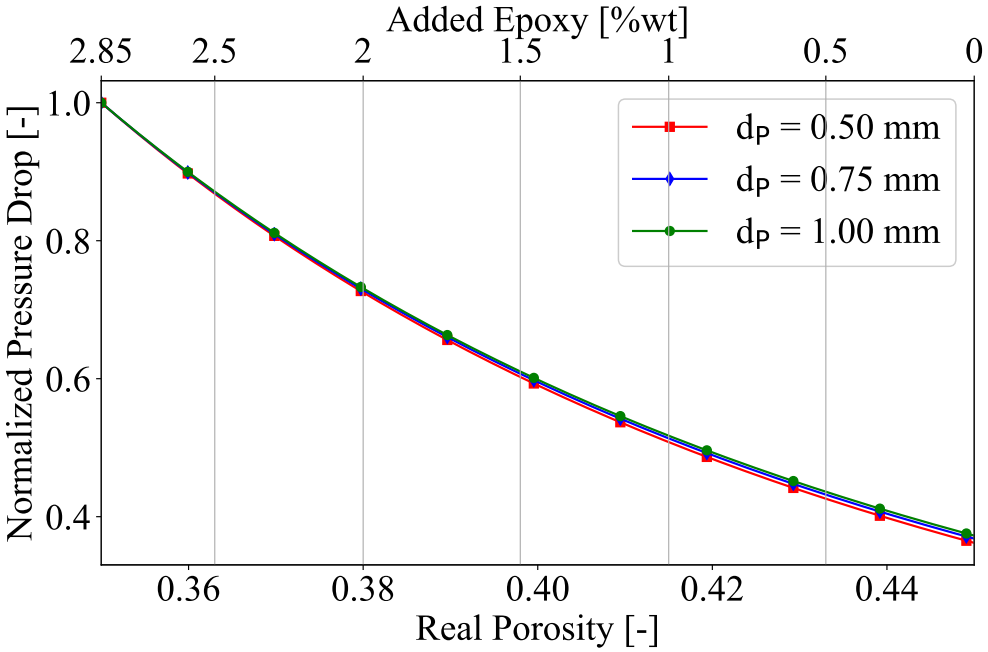

Figure 79 – Effect of the epoxy in the pressure drop for different particle diameters in a regenerator with a MCM porosity of 0.45.

As already discussed, adding epoxy increases the pressure drop by reducing the porosity. For the expected range of values for the porosity in the regenerator, the epoxy can more than double the total pressure drop in the porous medium, as shown in Figure 79. While the increase in pressure drop does not seem to be greatly influenced by the particle diameter, it can be seen that it starts increasing almost exponentially for smaller porosities which makes adding more epoxy even worse for the cooling capacity.

Additionally, the epoxy also causes clogging of the porous medium, decreasing the value of the effective porosity (ε_{eff}), which further increases the pressure drop and reduces the heat transfer area. The results presented so far do not consider this phenomenon and already show a considerable decrease in heat transfer and increase in pressure drop. Figure 80 shows the influence of the clogging on the heat transfer (product between the interstitial heat transfer coefficient and heat exchange area) of a regenerator with $\varepsilon_{\text{MCM}} = 0.45$ and $\varepsilon_{\text{f}} = 0.35$. As can be seen, the reduction in the heat transfer area caused by the clogging can considerably hinder the heat transfer. Experimental results show that $\varepsilon_{\text{eff}} \approx \varepsilon_{\text{f}} - 0.07$ which would result in a decrease of around 30% in the heat transfer for this regenerator. Lastly, the pressure drop is further increased by the clogging, since the effective porosity is even smaller than the real porosity. As can be seen in Figure 81, this increase can become prohibitively high if the clogging becomes too excessive.

All of the above losses add up and greatly affect the resulting cooling capacity of the regenerator. Figure 82 shows a comparison between the cooling capacity with

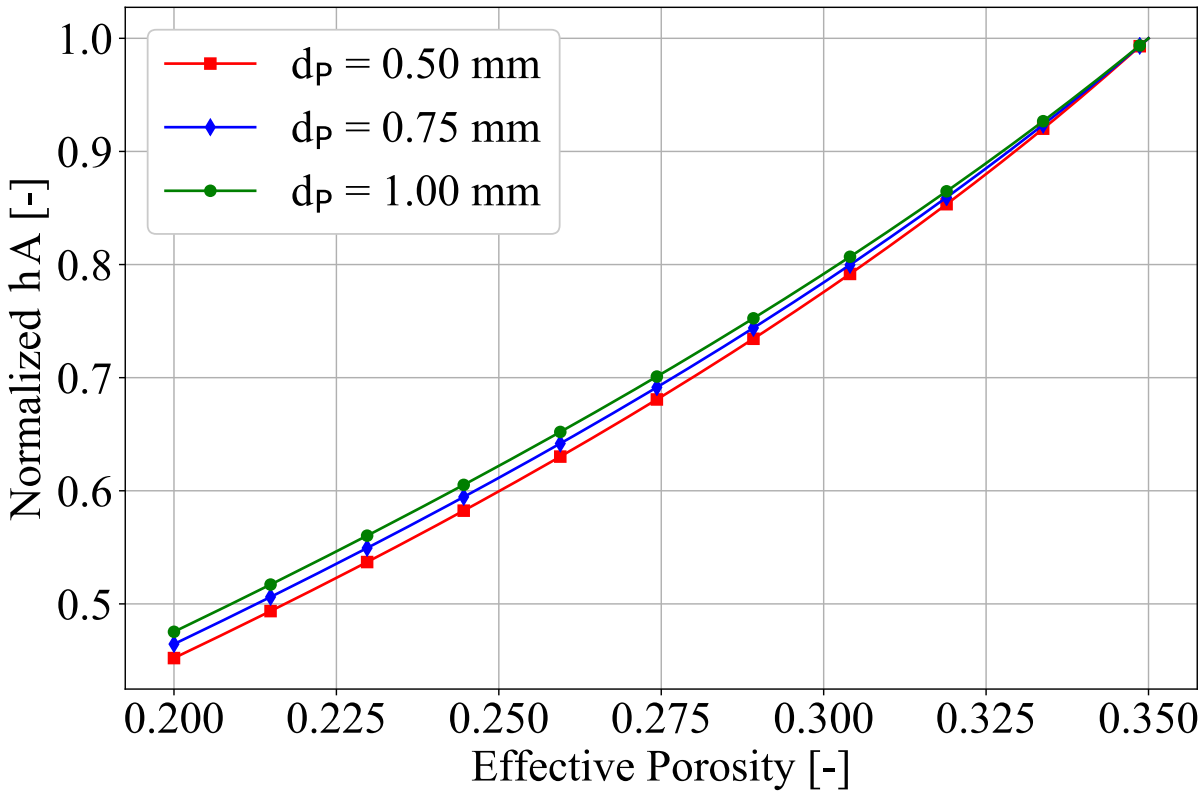

Figure 80 – Effect of the epoxy clogging on the product hA for different particle diameters in a regenerator with a MCM porosity of 0.45 and real porosity of 0.35.

and without epoxy, with the clogging effect considered separately. It can be inferred from the previous results that the addition of the epoxy is not the main cause of the reduction in cooling capacity. Rather, it is the clogging that really affects performance (in this case reducing the peak cooling capacity by around 25% in relation to the reference without epoxy). However, considering all the regenerators with epoxy that were tested in this work, it does not seem possible to add epoxy to the structure of the regenerator without causing clogging, so it is not possible, in principle, to build a regenerator with the integrity provided by epoxy and without the main negative effects that come with it. Thus, the best way to get rid of the negative effects of epoxy is, in principle, to use a material with enough mechanical integrity so that it does not require the addition of epoxy to the porous medium.

5.3 Multilayer and Curie Temperature Distribution

Due to the nature of the magnetocaloric effect in materials with a first-order phase transition, the selection of the number of layers and the distribution of Curie temperatures is extremely important for the operation of the regenerator. The choice of an appropriate Curie temperature profile ensures a more efficient use of the material

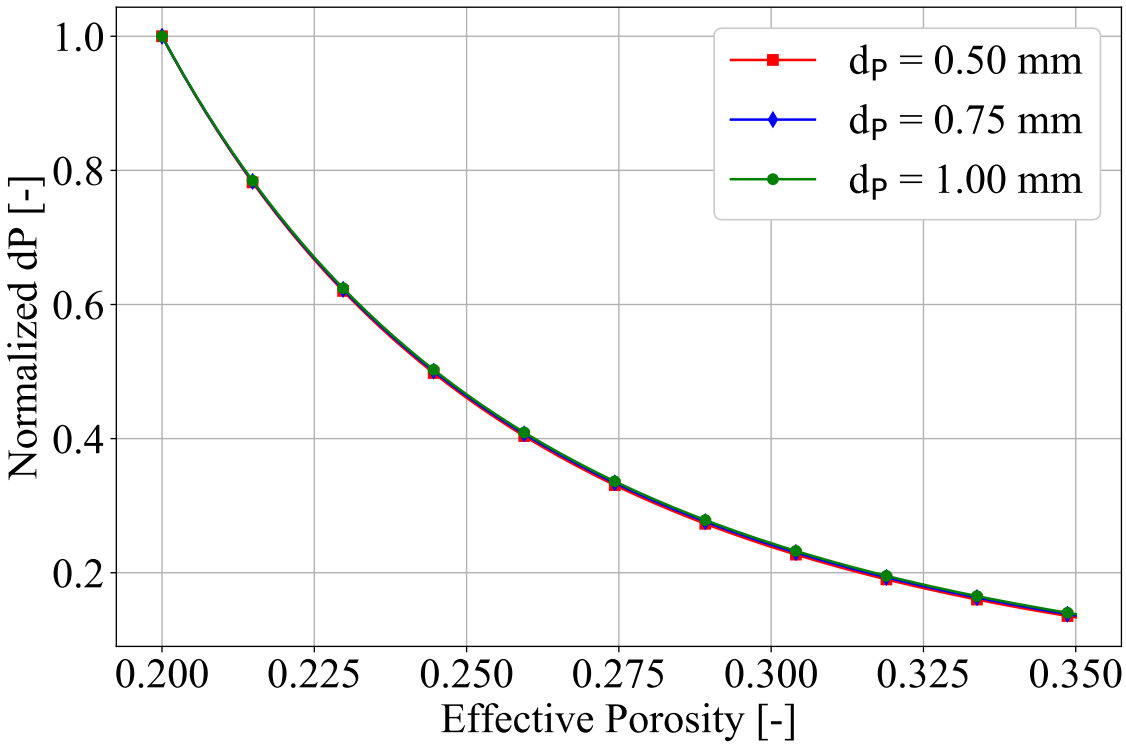

Figure 81 – Effect of the epoxy clogging on the pressure drop for different particle diameters in a regenerator with a MCM porosity of 0.45 and real porosity of 0.35.

in generating the magnetocaloric effect, reducing the mass necessary to obtain the desired cooling capacity. The peak of the magnetocaloric effect is observed around the Curie temperature at a 0-T magnetic flux density, with the peak being shifted to higher temperatures at a rate of approximately 4.6 K/T for the analyzed materials, a phenomenon which was already discussed in Chapter 2.

An ideal regenerator would be composed of an infinite number of layers along its length, each with an average peak temperature of MCE equivalent to the average temperature of its position. In practice, manufacturing and cost limitations prevent the use of a large number of layers, creating the need to optimize this parameter in order to achieve high cooling capacities using a reasonably priced, manufacturable regenerator. This section will focus on analyzing the influence of the number of layers and the distribution of Curie temperatures on the performance of a fictitious regenerator, with characteristics similar to those expected to be found in the regenerator to be designed. This influence will be tested at different operating conditions, in order to determine if they affect the ideal distribution of layers and, if this occurs, how this influence can be explained and predicted.

The characteristics of the analyzed regenerator are illustrated in Table 22, and are very similar to the regenerator used in Section 5.2. In addition, the operating

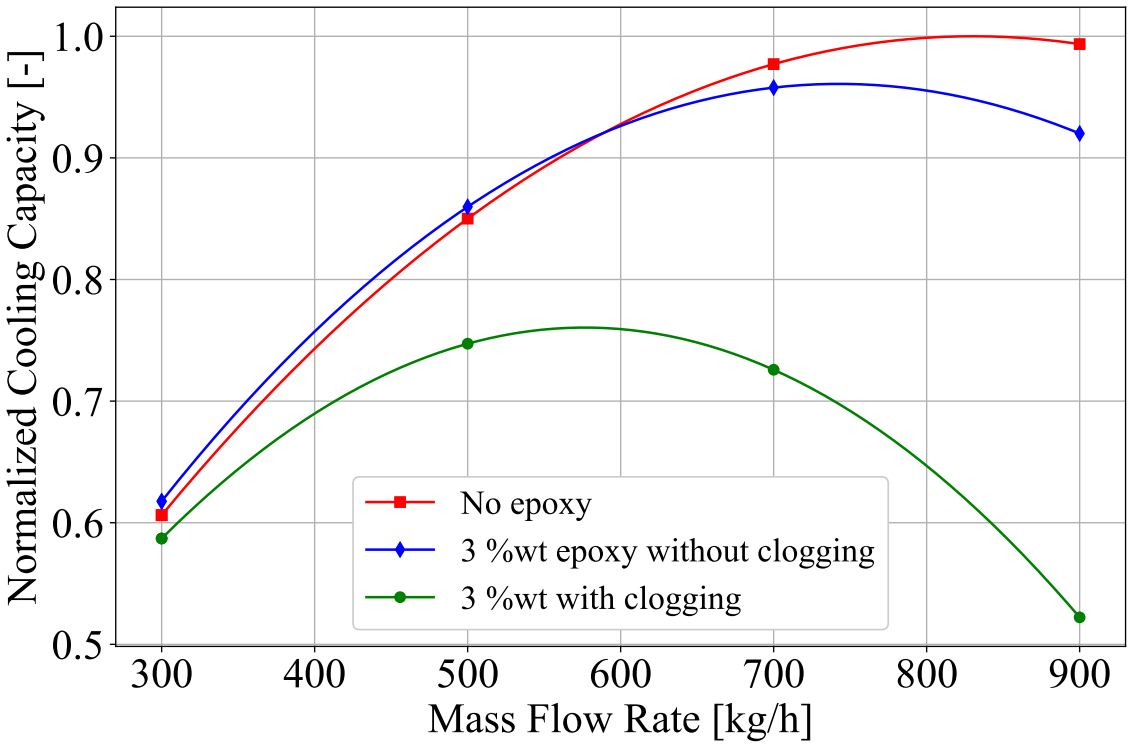

Figure 82 – Effect of the epoxy on the cooling capacity of the reference regenerator with a MCM porosity of 0.35.

conditions to which the regenerator will be subjected can be found in Table 23.

Table 22 – Properties of the fictitious regenerator.

Name	Fict. Regenerator
MCM relative porosity (ε)	0.45
Real porosity (ε_f)	0.34
Effective porosity (ε_{eff})	0.27
Regenerator height	50 mm
Regenerator width	60 mm
Regenerator length	150 mm
Number of layers	To be determined
Curie temperature distribution factor (CTDF)	-3, -2, -1, 0 K
Heat transfer fluid	2 % vol. ENTEK-water solution
Particle diameter	0.65 mm
Material	CV-HS
Epoxy concentration	2.7 wt.%
Void volume	0 mm^3

In this analysis, the field and flow profiles are once again idealized as ramp and step profiles, respectively. The regenerator has a length of 150 mm, so the length of each layer will be equal to that value divided by the number of layers. The value of the Curie temperature in each layer is a function of both the temperature span and

Table 23 – Operating conditions for the layers distribution analysis.

Operating Conditions	Values
Frequency	1.5 Hz
Temperature span	20, 30 K
Number of layers (N)	5, 9, 13, 17, 21
Mass flow rate	300, 500, 700, 900 kg h^{-1}
Maximum applied magnetic flux density	0.5, 1, 1.5 T
Hot side temperature (T_H)	316.15 K
Applied field profile	Ramp
Blow profile	Step
Blow fraction	35%
High and low field fractions	35%

the number of layers, being calculated (from highest to lowest) using the following expression:

$$T_{\text{Curie,n}} = TH - \frac{T_{\text{span}}}{N-1} n + CTDF \text{ for } n = 0 \text{ to } N-1 \tag{5.1}$$

where *CTDF* is the Curie temperature distribution factor shown in Table 22. Thus, in the case where $CTDF = 0$ K, the highest Curie temperature will coincide with the temperature of the hot reservoir and the lowest with that of the cold reservoir, while the others are distributed linearly between these values. In the case of $CTDF = -1$ K, the highest Curie temperature will be 1 K below the temperature of the hot reservoir and the lowest will be 1 K below the temperature of the cold reservoir, and so on.

Figure 83 shows the results of cooling capacity as a function of the CTDF and the number of layers. Similar to the results obtained by Lei et al. (2015), moving the Curie temperature to lower values considerably increases the cooling capacity obtained. The results indicate that a CTDF of -3 K tends to yield the best cooling capacity results, especially for the lower numbers of layers. At higher numbers of layers the difference between CTDFs of -2 and -3 K becomes nearly nonexistent, with both yielding the highest cooling capacity. This difference is reduced even more at higher mass flow rates, which do not seem to affect the influence of the number of layers and Curie temperature distribution in any other way. However, the number of layers appears to have a slight influence on the cooling capacity dependence on the mass flow rate, as illustrated in Figure 84. In an AMR, the cooling capacity increases with the mass flow rate until it reaches a maximum value, where the pressure drop becomes so great that it starts to impair the capacity (see Section 5.2.1). Analyzing the results, it is possible to notice that, for smaller numbers of layers, increasing the number of layers shifts the peak capacity to higher values of mass flow rate, further assisting in increasing the performance of the regenerator.

An increase in cooling capacity with the number of layers is intuitively expected, since with more layers the MCE peak temperature profile is better adjusted to

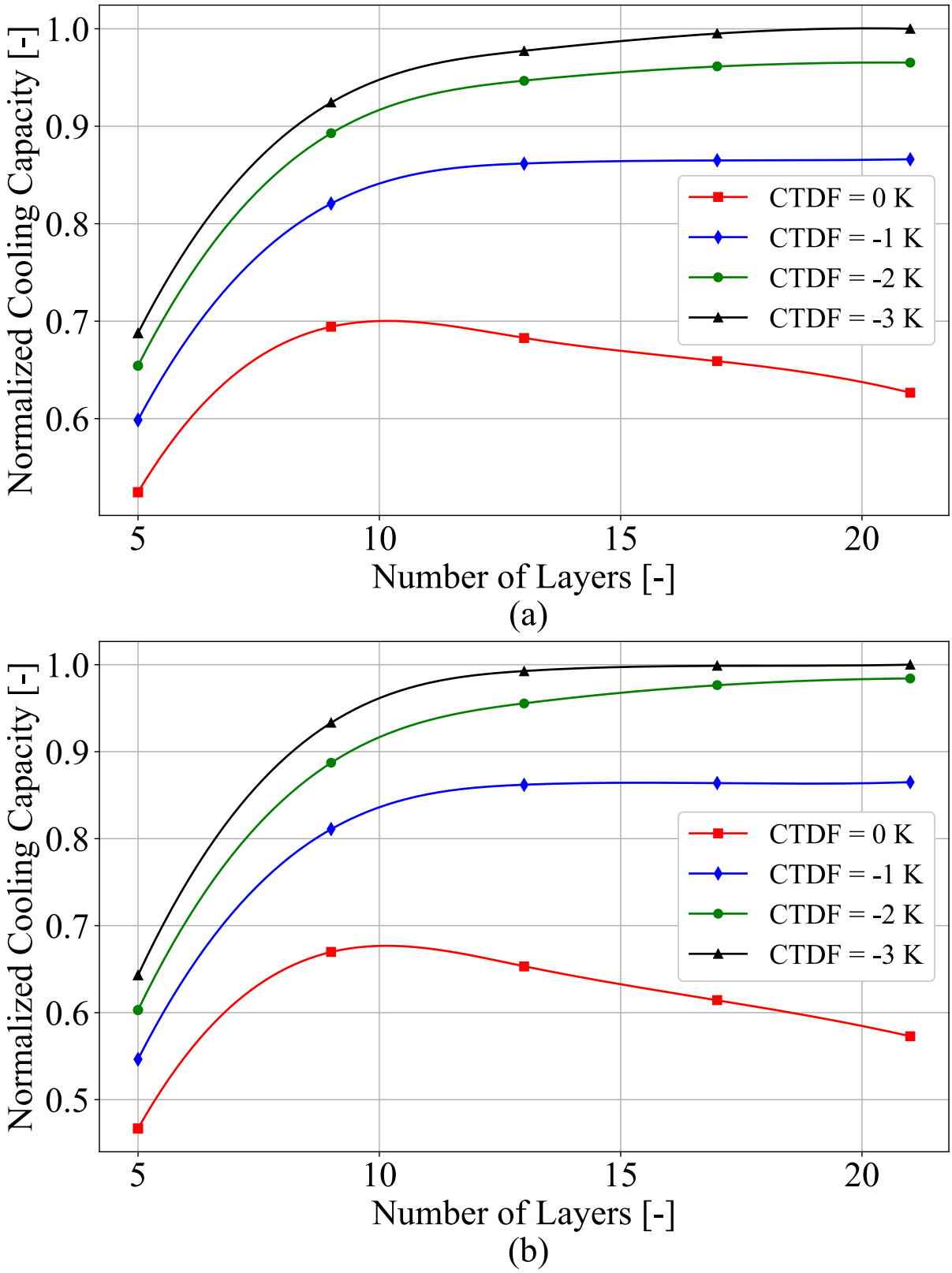

Figure 83 – Part 1 - Influence of the CTDF and the number of layers on the cooling capacity of the fictitious regenerator operating at a frequency of 1.5 Hz, maximum applied magnetic flux density of 1 T, temperature span of 30 K and mass flow rate of (a) 300, (b) 500, (c) 700 and (d) 900 kg h^{-1}.

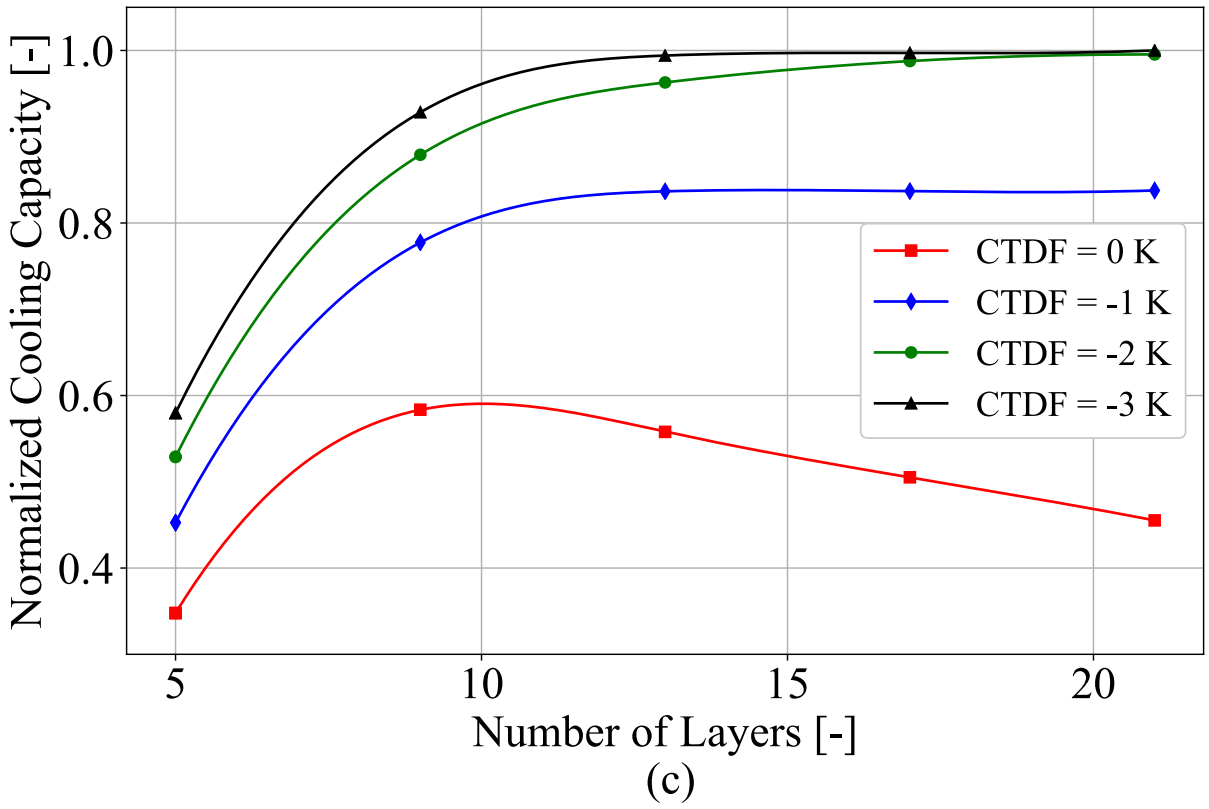

(c)

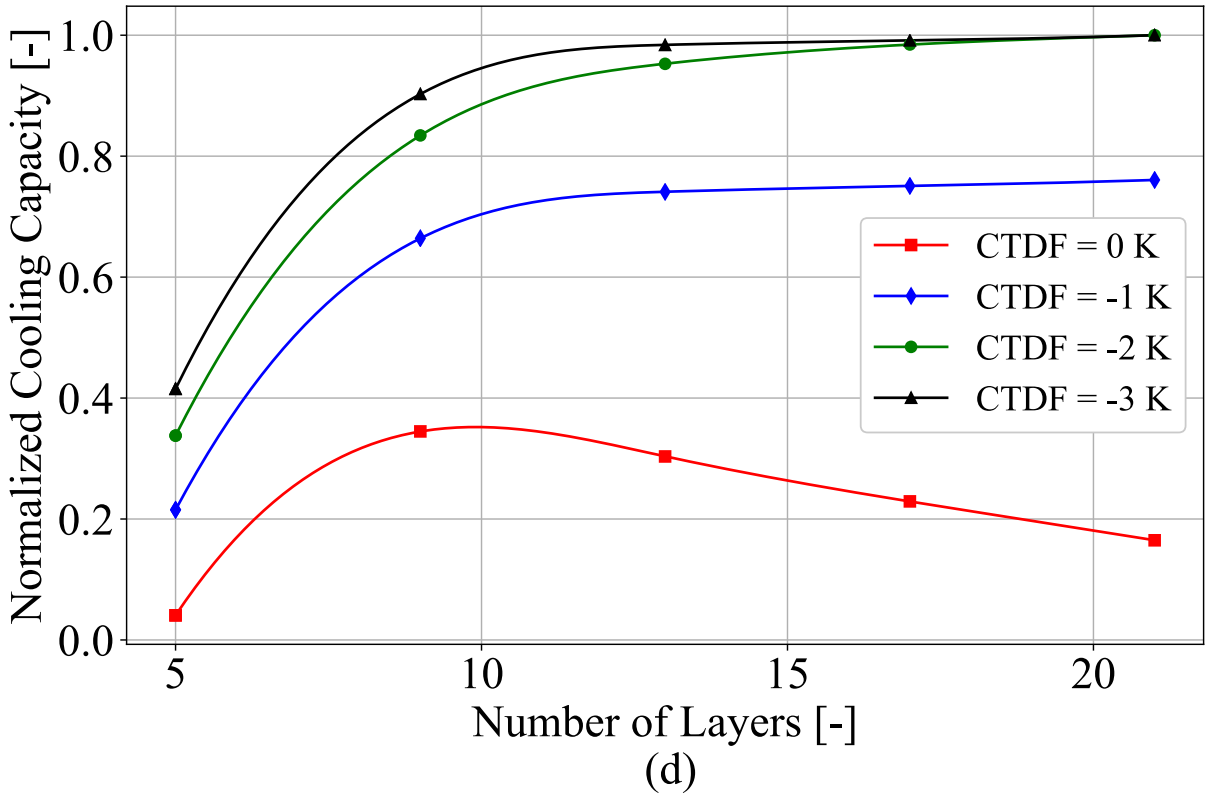

(d)

Figure 83 – Part 2 - Influence of the CTDF and the number of layers on the cooling capacity of the fictitious regenerator operating at a frequency of 1.5 Hz, maximum applied magnetic flux density of 1 T, temperature span of 30 K and mass flow rate of (a) 300, (b) 500, (c) 700 and (d) 900 kg h^{-1}.

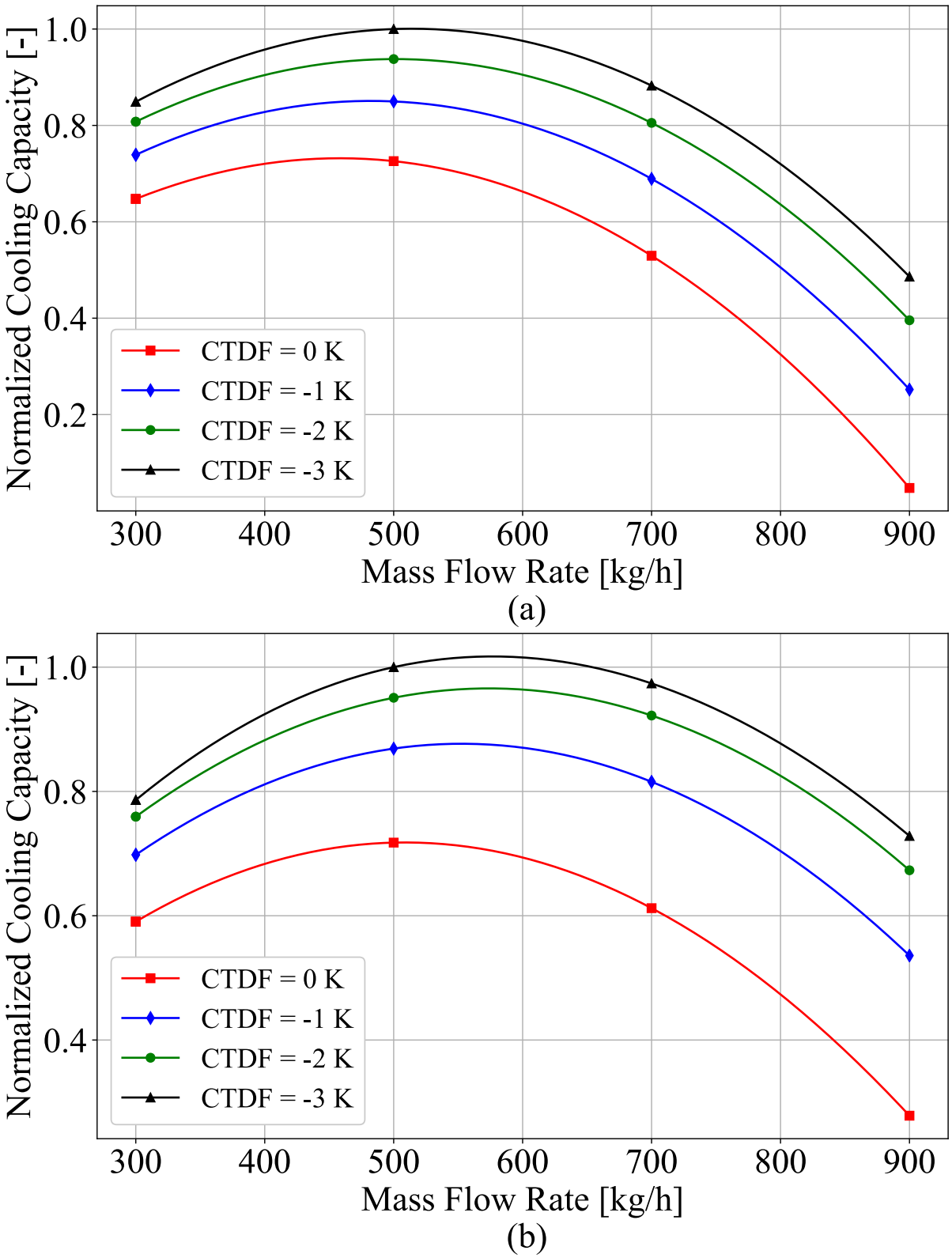

Figure 84 – Part 1 - Influence of the CTDF and mass flow rate on the cooling capacity of the fictitious regenerator operating at a frequency of 1.5 Hz, maximum applied magnetic flux density of 1 T and temperature span of 30 K with (a) 5, (b) 9, (c) 13 and (d) 21 layers.

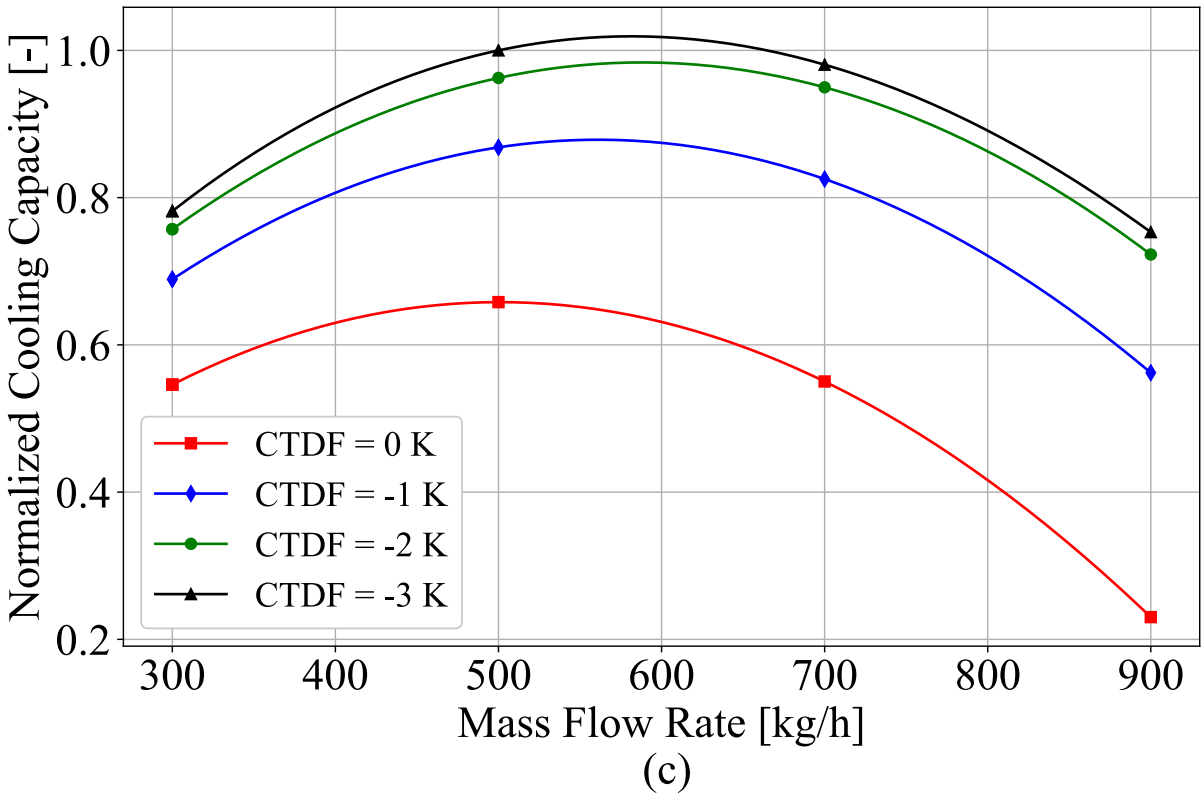

Figure 84 – Part 2 - Influence of the CTDF and mass flow rate on the cooling capacity of the fictitious regenerator operating at a frequency of 1.5 Hz, maximum applied magnetic flux density of 1 T and temperature span of 30 K with (a) 5, (b) 9, (c) 13 and (d) 21 layers.

the temperature profile of the regenerator, increasing the total magnitude of the effect. Figure 85 illustrates this phenomenon as seen in the model. The x-axis represents the position of each control volume along the regenerator and the y-axis represents the normalized absolute value of the integration of all MCE terms (see Equation 3.14) for each volume during demagnetization. In other words, higher y-axis values represent a higher MCE. As can be seen, the regenerator with more layers has a high magnetocaloric effect along its entire length, while the regenerator with fewer layers has higher MCE peaks, but also large regions where its value is considerably reduced. When all those effects are combined, the intensity of the MCE in the regenerator with 21 layers is approximately 66% higher than in the regenerator with 5 layers. The existence of the highest peaks in the regenerator with fewer layers can be explained by the fact that longer layers are more likely to have one point where the average temperature of the regenerator coincides with the value that maximizes the MCE.

A phenomenon that needs to be highlighted is the behavior of the cooling capacity with CTDF = 0 K, where a decrease in capacity is observed with the increase in the number of layers. This behavior differs from that found by Lei et al. (2015), but can also be explained by the intensity of the magnetocaloric effect. Figure 86 shows the MCE intensity for the regenerator operating with CTDF = 0 K with 9 and 21 layers. As can be seen, due to the choice of CTDF, the 21-layer regenerator, despite having several MCE peaks, does not reach high values over much of its length, especially in the region with lower Curie temperatures. Conversely, the 9-layer regenerator is able to achieve high MCE values along its entire length, despite still having regions with lower values. In view of this, it is much less clear which configuration has the greatest magnetocaloric effect and, therefore, the best performance, but further analysis shows that the intensity of the MCE in the regenerator with 9 layers was around 10% higher than in the regenerator with 21 layers, corroborating with the results shown in Figure 83. This shows that increasing the number of layers in a regenerator can, sometimes, be detrimental to its performance, if the Curie temperature profile is not carefully selected according to the desired application. Therefore, before deciding the number of layers, the ideal profile needs to be properly tested and determined.

One parameter that greatly influences the number of layers required to maximize the cooling capacity of a regenerator is the temperature span associated with the envisaged application. After all, this is what determines the temperature range within which the Curie temperatures will have to be allocated. Smaller temperature spans generate a temperature profile that requires less layers to be accurately followed, converging to the limiting case of a 0 K span which would need only one layer. On the other hand, larger temperature spans require more layers, since the temperature variation along the regenerator also increases, converging mathematically to the case of an infinite span with infinite layers. This phenomenon is illustrated in Figure 87, where the results for the regenerator operating at a temperature span of 20 K are compared to

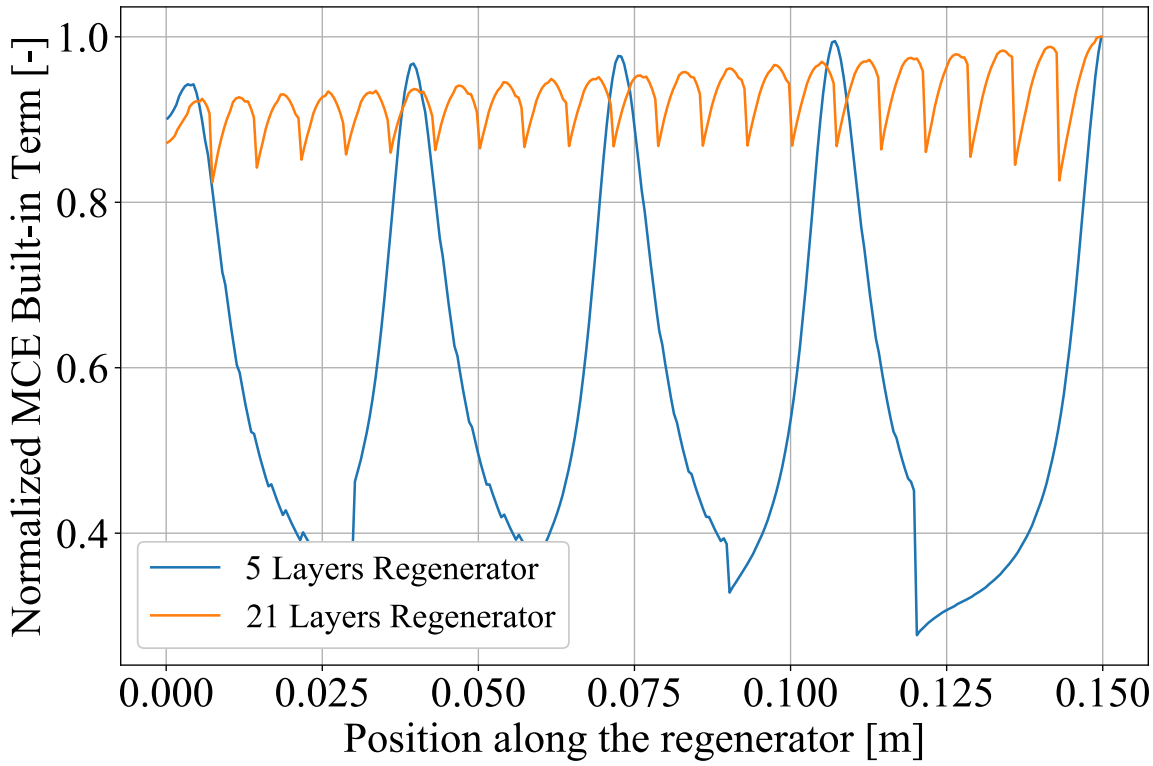

Figure 85 – Intensity of the MCE for regenerators with 5 and 21 layers and a CTDF of -2 K. The operating conditions were a frequency of 1.5 Hz, a mass flow rate of 300 kg h^{-1}, a temperature span of 30 K and a maximum applied magnetic flux density of 1 T.

the results obtained under the same conditions, but instead with a temperature span of 30 K. As can be seen, with 5 layers, the regenerator operating at a span of 20 K already reached values of over 80% of the maximum cooling capacity, while for a span of 30 K it has not reached 60%. While the proportions may change, the same phenomenon is seen regardless of mass flow rate, maximum applied field and operating frequency. In fact, the operating frequency, like the mass flow rate, does not seem to have any effect on the ideal CTDF or number of layers, as can be seen in Figure 88, which shows the results for a regenerator operating at a frequency of 1 Hz and is very similar to the ones obtained at 1.5 Hz.

Lei et al. (2015) suggested that the reason for the increase of the cooling capacity for values of CTDF around -2 K is the increase of the temperature which corresponds to the MCE peak with the magnetic field. In other words, while the Curie temperature is a constant value for a given material, the average peak temperature of the MCE is a function of the applied field and, for the analysed materials, will always be higher than the Curie temperature (if there is an applied field). In order to maximize the MCE, this temperature (and not the Curie temperature) must be as close as possible to the temperature of the material. To confirm the explanation by Lei et al. (2015), the same

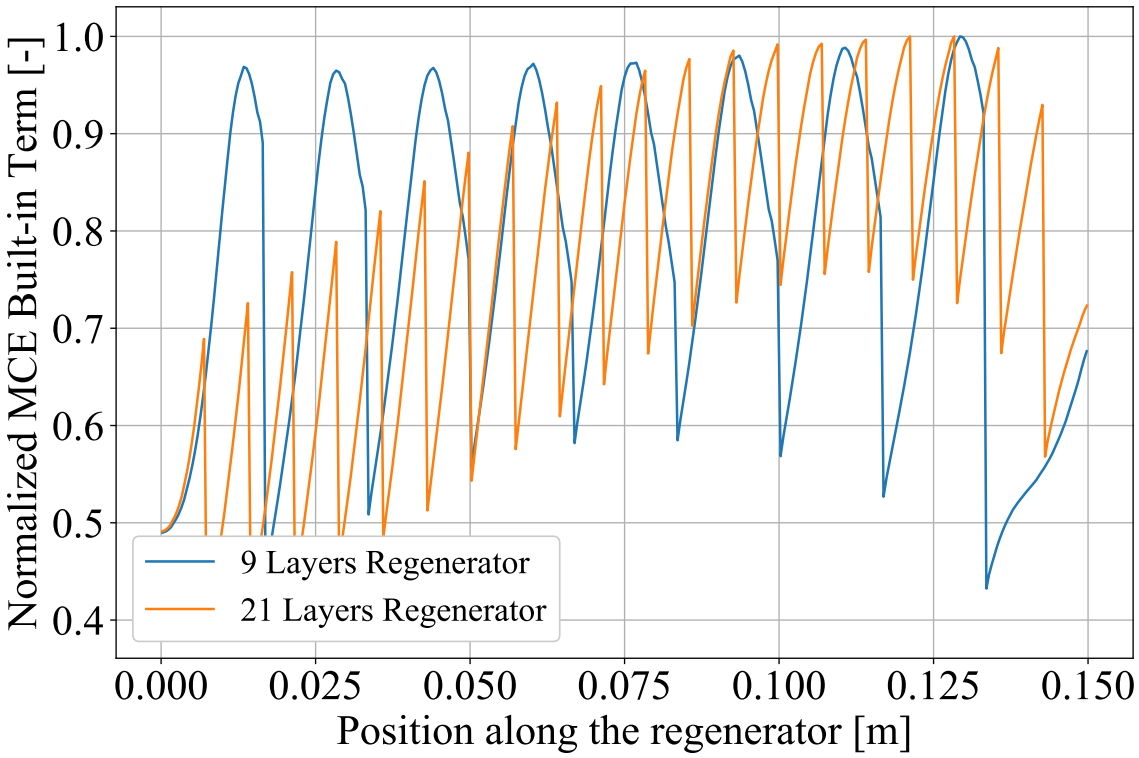

Figure 86 – Intensity of the MCE for regenerators with 9 and 21 layers and a CTDF of 0 K. The operating conditions were a frequency of 1.5 Hz, a mass flow rate of 300 kg h^{-1}, a temperature span of 30 K and a maximum applied magnetic flux density of 1 T.

simulations were run with maximum applied magnetic flux densities of 0.5 and 1.5 T. If the assumption is right, the regenerator submitted to a lower field (0.5 T) would have an ideal CTDF closer to zero than the reference (1 T), since the influence of the shift of the MCE peak temperature would be smaller. On the other hand, the regenerator submitted to a higher field (1.5 T) would have an ideal CTDF further away from zero, since in this case the shift of the MCE peak would be even more significant. Figure 89 shows the results of these tests, and seems to confirm what has been proposed. For the applied field of 1.5 T, the CTDF of -3 K becomes consistently better than the CTDF of -2 K, indicating that the ideal CTDF shifted away from zero, while for the applied field of 0.5 T, the CTDF of -2 K starts to surpass the cooling capacity given by the CTDF of -3 K, indicating that the ideal profile is getting closer to a CTDF of 0 K.

Considering all that has been exposed, a few guidelines for designing the layer distribution of a regenerator can be proposed:

- Choosing an appropriate Curie temperature profile is of utmost importance. A badly chosen profile can severely hinder the regenerator performance and cannot be easily solved, since adding more layers will not continuously improve the cooling capacity and may actually reduce it;

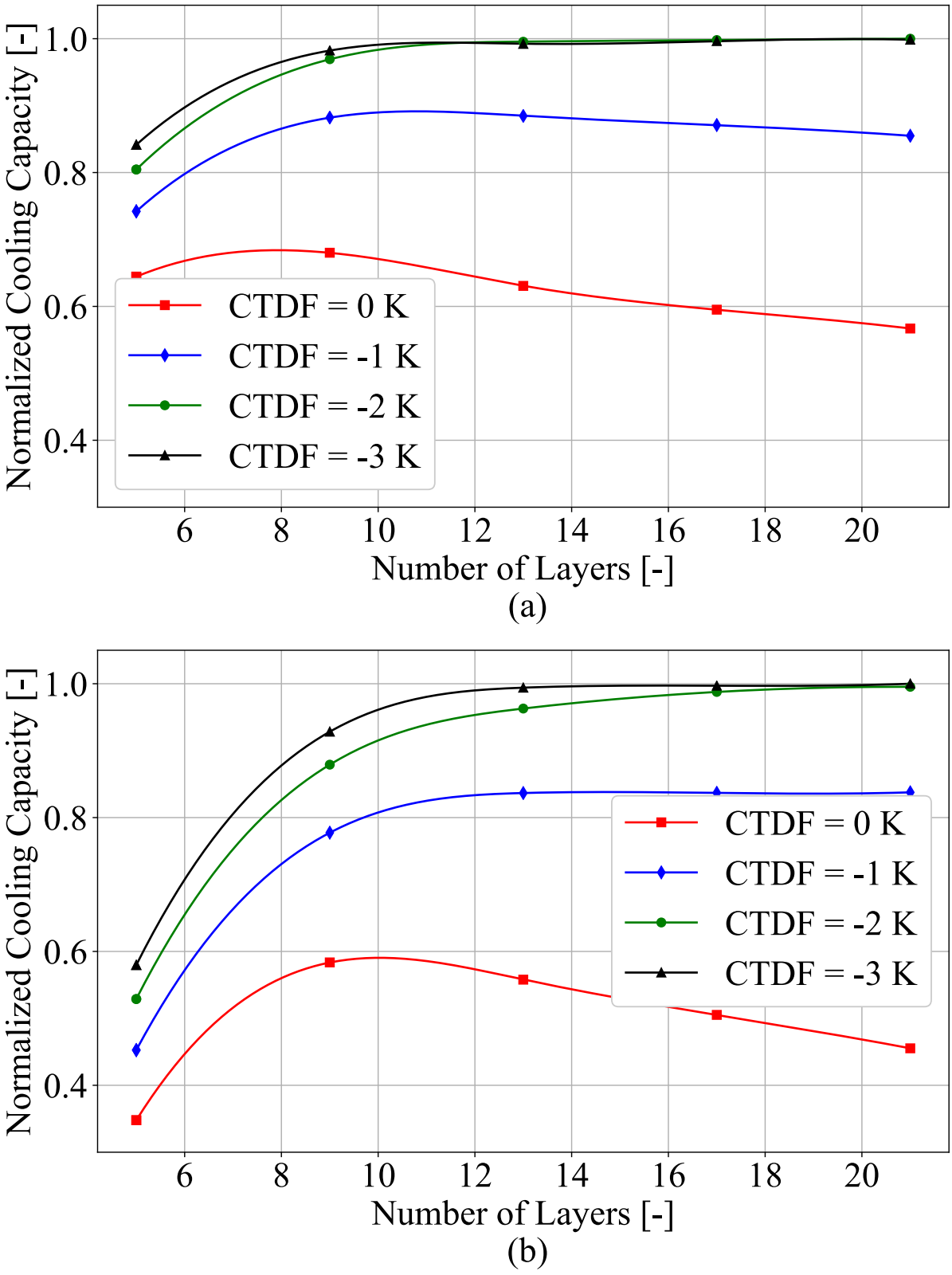

Figure 87 – Influence of the CTDF and number of layers on the cooling capacity of the fictitious regenerator operating at a frequency of 1.5 Hz, maximum applied magnetic flux density of 1 T, mass flow rate of 700 kg h^{-1} and temperature span of (a) 20 and (b) 30 K.

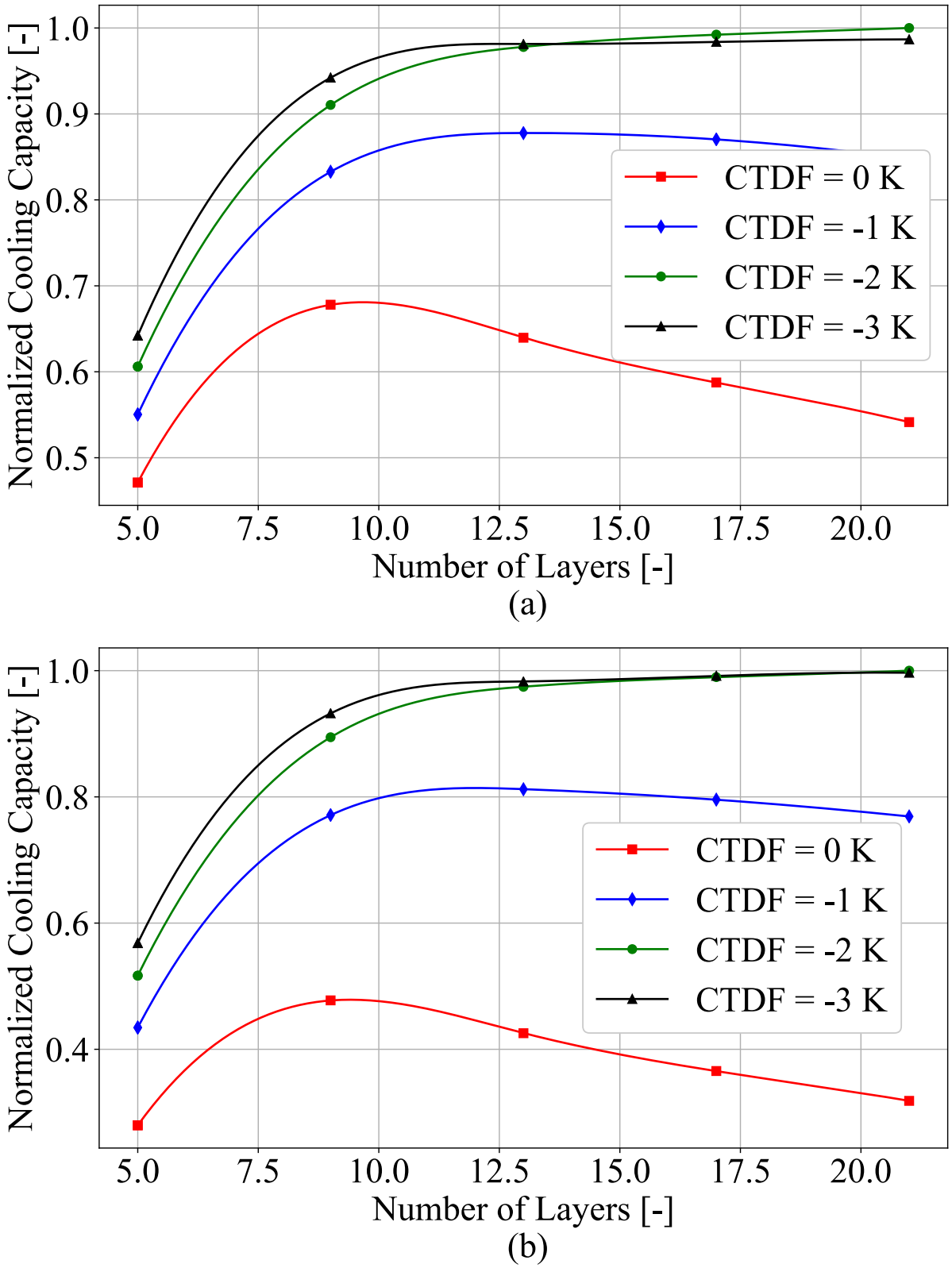

Figure 88 – Influence of the CTDF and number of layers on the cooling capacity of the fictitious regenerator operating at a frequency of 1.0 Hz, maximum applied magnetic flux density of 1 T, temperature span of 30 K and mass flow rate of (a) 500 and (b) 700 kg h^{-1}.

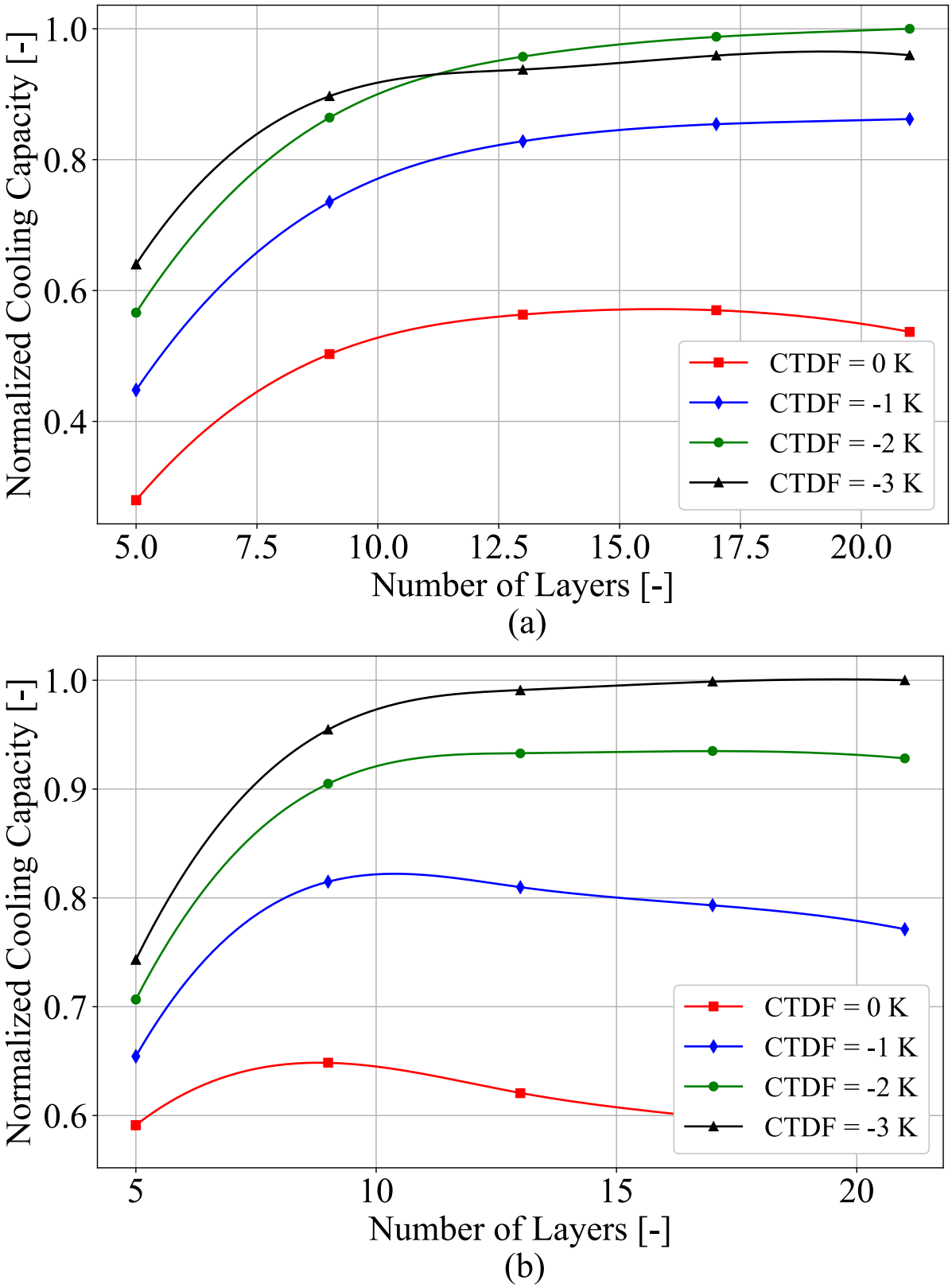

Figure 89 – Influence of the CTDF and the number of layers on the cooling capacity of the fictitious regenerator operating at a frequency of 1.5 Hz, temperature span of 30 K, mass flow rate of 300 kg h^{-1} and maximum applied magnetic flux density of (a) 0.5 and (b) 1.5 T.

- The ideal Curie temperature profile is directly influenced by the shift of the MCE peak temperature with the applied field. The larger the values of this shift and the applied field, the more negative the value of CTDF has to be;
- If an appropriate Curie temperature profile has been chosen, increasing the number of layers will increase the cooling capacity. However, the greater the number of layers, the less beneficial it will be to add a new one;
- Smaller temperature spans tend to require a smaller number of layers to reach high levels of cooling capacity;
- The operating frequency and mass flow rate do not seem to greatly influence the ideal Curie temperature distribution or number of layers.

5.4 Void Volume

The void volume is defined as the volume between the regenerator ends and their corresponding heat exchangers in which fluid remains after a blow without interacting with the thermal reservoirs, not contributing to the cooling capacity (or heat rejection). Additionally, this fluid then returns to the regenerator at a temperature that is usually higher than the hot reservoir (during the hot blow) or colder than than the cold reservoir (during the cold blow). This impairs the performance, because this fluid requires a greater heat exchange to reach a temperature lower than the cold reservoir (during the hot blow) or higher than the hot reservoir (during the cold blow). The fictitious regenerator and operating conditions used to determine how the void volume influences the cooling capacity are described in Tables 24 and 25.

Table 24 – Properties of the fictitious regenerator used in the void volume analysis.

Name	**Fict. Regenerator**
MCM relative porosity (ε)	0.45
Real porosity (ε_f)	0.34
Effective porosity (ε_{eff})	0.27
Regenerator height	50 mm
Regenerator width	60 mm
Regenerator length	150 mm
Number of layers	15
Curie temperature distribution factor (CTDF)	-2 K
Heat transfer fluid	2 % vol. ENTEK-water solution
Particle diameter	0.65 mm
Material	CV-HS
Epoxy concentration	2.7 wt.%

Initially, the regenerator was tested at different mass flow rates with different void volume sizes. The mass flow rates were chosen to be in the vicinity of the peak

Table 25 – Operating conditions for the void volume analysis.

Operating Conditions	Values
Frequency	1.5 Hz
Temperature span	30 K
Mass flow rate	Various
Maximum applied magnetic flux density	1 T
Hot side temperature (T_H)	316.15 K
Applied field profile	Ramp
Blow profile	Step
Blow fraction	35%
High and low field fractions	35%

capacity of the regenerator. The void volume size is defined as a percentage of the regenerator volume and represents the size of the void volume on one side of the regenerator, i.e., the percentage represents the size of only one of the void volumes and not the combined size of the ones in both sides. Since the model assumes the void volume to have the same cross-sectional area of the regenerator, this percentage is represented by the length of the void volume (L_{vv}). Figure 90 shows the effect of the void volume size on the cooling capacity of the test regenerator for different mass flow rates. The results were normalized so that the cooling capacity without void volumes for each mass flow rate had a value of 1. As can be seen, the losses due to the void volumes are much more relevant for lower mass flow rates, while larger mass flow rates require larger void volumes to present significant drops in cooling capacity. This is because at lower mass flow rates the volume of fluid displaced during a blow is smaller, so the fluid remaining in the void volume represents a higher percentage of the total fluid displacement.

Figure 91 shows the same results for cooling capacity, now normalized so that the maximum cooling capacity overall had a value of 1. As can be seen, if one were to design a regenerator without considering the void volume, a mass flow rate of around 500 kg h^{-1} would yield a higher cooling capacity and be selected. However, since the presence of a void volume is usually inevitable, a mass flow rate of 700 kg h^{-1} would be better for smaller void volumes (2.5% to 7.5%) and a mass flow rate of 900 kg h^{-1} would be more appropriate for large void volumes (greater than 7.5%). Regardless, the larger the void volume, the greater the loss would be in relation to the ideal case with no void volume.

In fact, an alternative way to analyze the void volume losses is through the void volume/displaced fluid ratio, rather than through the size of the void volume in relation to the regenerator. This method is particularly useful when comparing regenerators of different sizes. Larger regenerators tend to have greater losses for the same percentage of void volume because the actual size of the dead volume is greater for them. However, if the analysis is based on the void volume/displaced fluid ratio,

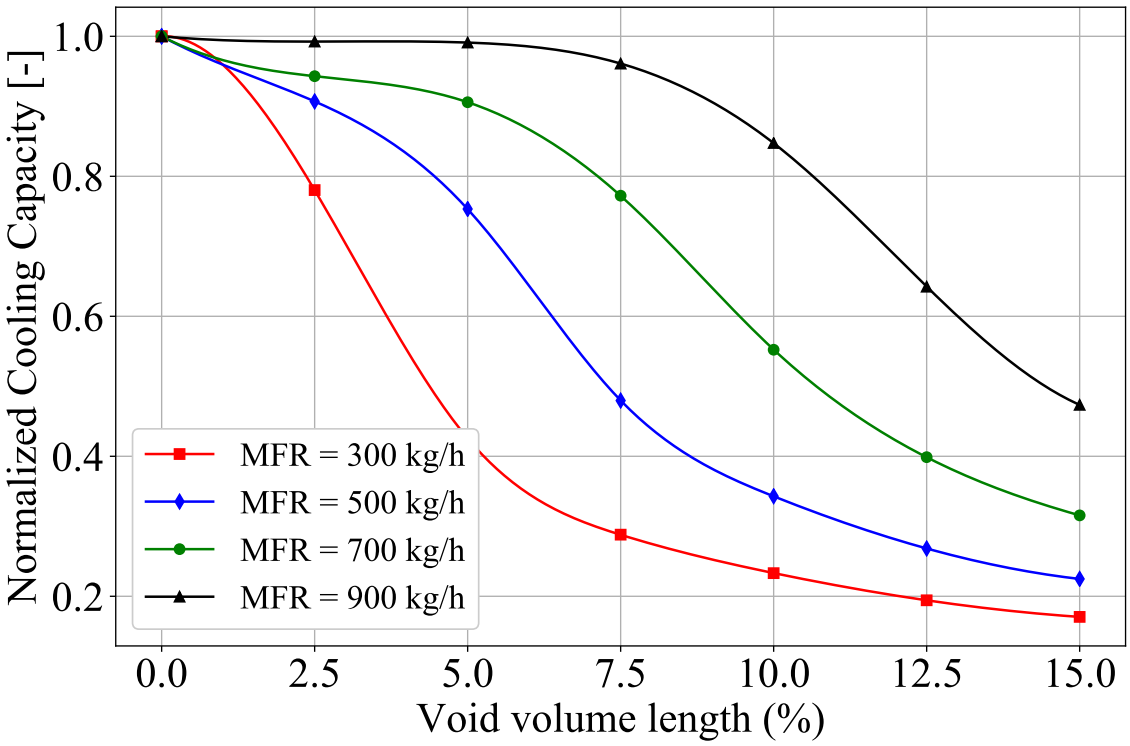

Figure 90 – Influence of the void volume size on the cooling capacity for different mass flow rates. The cooling capacity was normalized so that it had a value of 1 without void volumes for each mass flow rate.

the size of the regenerator has little influence on the void volume losses, producing equivalent values for different regenerator sizes. This can be seen in Figure 92 where the drop in cooling capacity for various mass flow rates and void volume sizes is shown for three regenerators, each with a different length. While there is some variation, the overall losses in all regenerators are considerably close for similar values of void volume/displaced fluid ratio.

Therefore, the best way to minimize void volume losses is to reduce the ratio between the size of the void volume and the total volume of fluid displaced in each blow. This can be achieved in two ways: reducing the size of the void volumes or increasing the volume of displaced fluid. The first approach is not influenced by other parameters of the regenerator and is mostly dictated by the hydraulic system, therefore, the following analysis will focus on the second approach, assuming the void volume size is the smallest possible in each case.

The usual way to increase the volume of displaced fluid during a blow is by increasing the mass flow rate. However, as Figure 91 already showed, while this may minimize the void volume losses, it will not guarantee the maximum cooling capacity for the given size of the void volume. Therefore, to minimize the void volume losses the aim should be to maximize the mass flow rate at which the peak capacity is observed

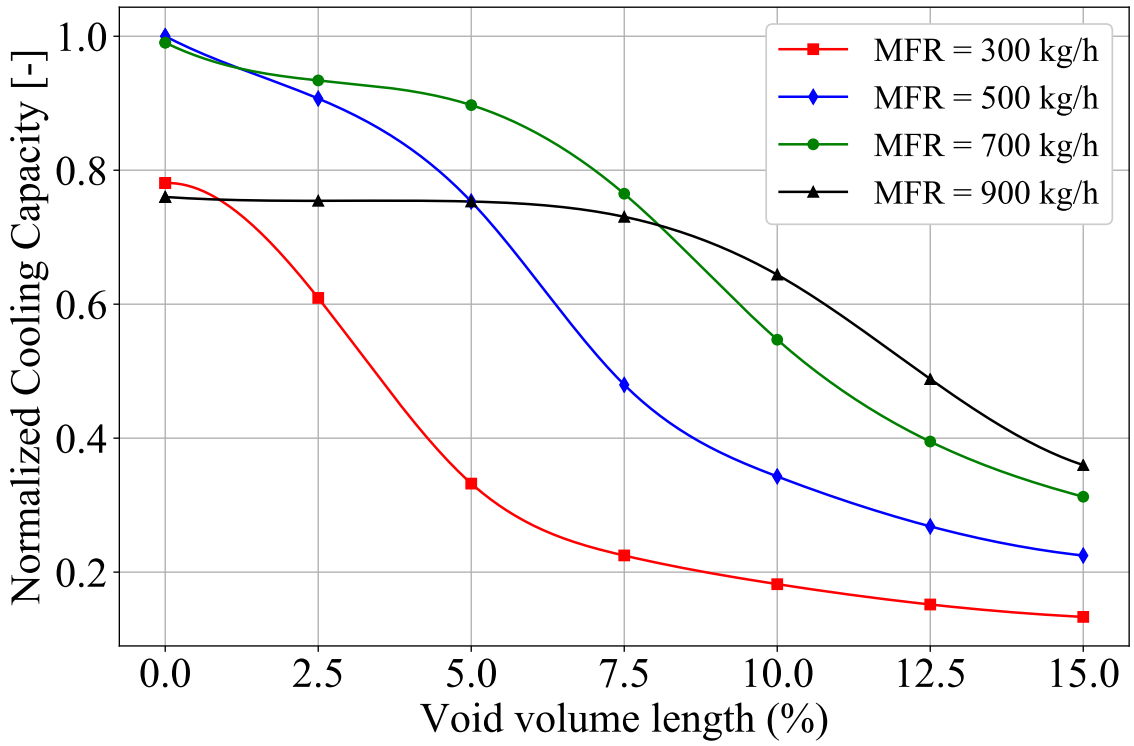

Figure 91 – Influence of the void volume size on the cooling capacity for different mass flow rates. The cooling capacity was normalized so that the maximum cooling capacity had a value of 1.

and the simplest way to achieve that is by reducing the regenerator pressure drop (see Section 5.2.1). Again, there are two main ways to achieve this without making fundamental changes to the system: increasing the effective porosity and increasing the cross-sectional area of the regenerator. To illustrate this, Figure 93 shows the comparison between the drop in the peak cooling capacity of the baseline regenerator with the drops in a regenerator with a larger height (75 mm) and in a regenerator without blockages caused by epoxy ($\varepsilon_{\text{eff}} = \varepsilon_{\text{f}}$). As discussed above, this occurred because reducing the pressure drop increased the peak mass flow rate from 500 kg h^{-1} for the baseline regenerator to 700 kg h^{-1} for the other regenerators.

Besides the ratio between the volume of displaced fluid and the void volume, there is another operating factor that affects the void volume losses: the temperature span. As observed by Jacobs & Zimm (2008) smaller temperature spans are associated with larger cooling capacities and, consequently, the difference between the outlet temperature of a blow and the inlet temperature of the next blow will be greater, increasing the influence of the fluid that remains in the void volume. This phenomenon can actually be extrapolated to any changes in the system that increase the cooling capacity without changing the fluid/void volume ratio, however, it is most pronounced and easiest to observe with the temperature span. Figure 94 shows the drop in cooling

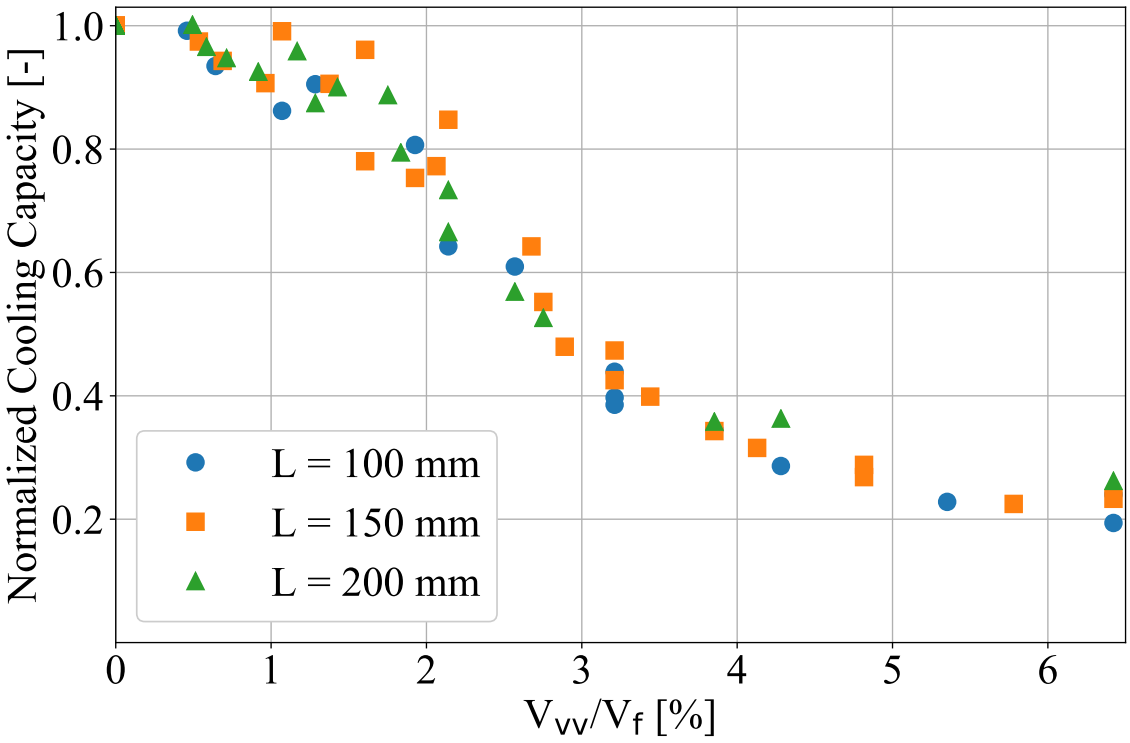

Figure 92 – Void volume losses for three regenerators with different lengths. Data points were obtained at various mass flow rates (between 100 kg h^{-1} and 1300 kg h^{-1}) and void volume sizes (between 0% and 15% of the regenerator volume). The cooling capacity was normalized so that it had a value of 1 without void volumes for each mass flow rate.

capacity for the test regenerator at temperature spans of 10 K, 20 K and 30 K. As discussed, the losses at smaller spans are higher than at larger spans, with the difference being especially significant at void volume percentages of around 5%. However, it is important to note that not only the absolute value of cooling capacity is considerably higher at smaller temperature spans, but the mass flow rate that yields the higher cooling capacity also tends to increase. Thus, if the system is able to reach higher mass flow rates, the resulting void volume loss may be reduced by increasing the fluid/void volume ratio.

Finally, a few guidelines can be proposed when trying to minimize the void volume losses in a regenerator:

- The void volume should be as small as possible;
- The ratio between the void volume and the volume of displaced fluid during a blow should be as low as possible without hindering the cooling capacity;
- Because of this, the ideal mass flow rate when considering the void volumes may be higher than in cases where the void volumes are not taken into account;

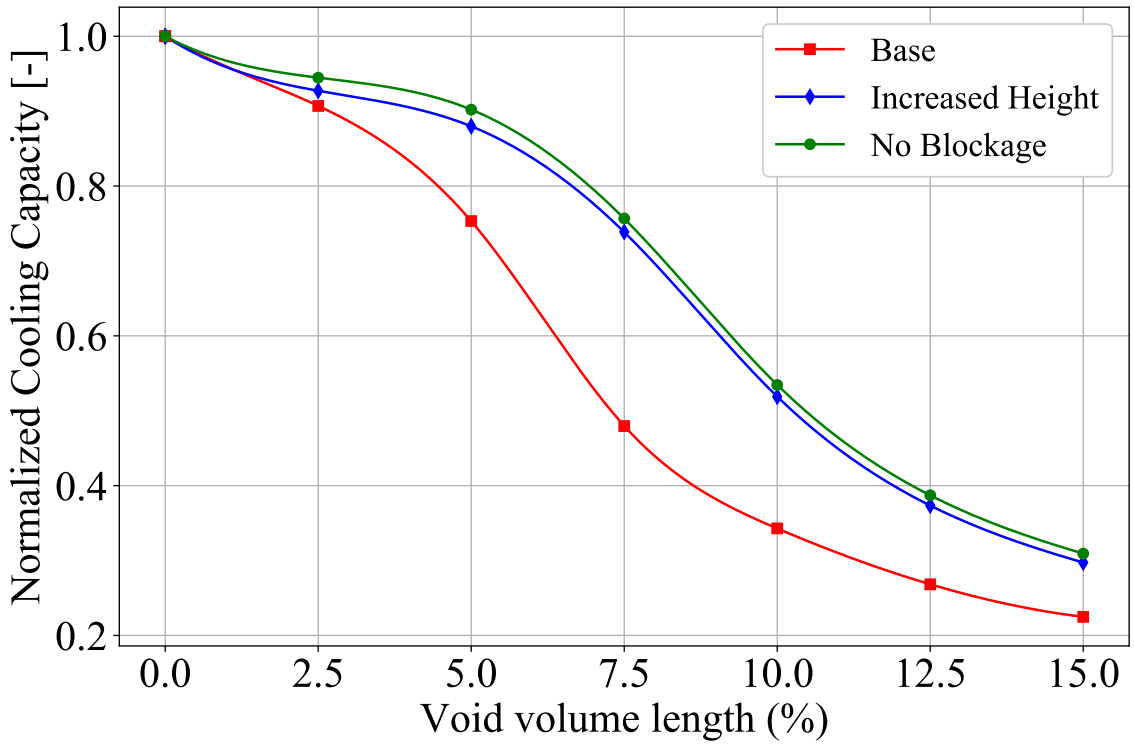

Figure 93 – Comparison between the void volume losses of the baseline regenerator with regenerators with lower pressure drops. The reduced pressure drop was achieved by increasing the height of the regenerator and by removing the blockage caused by epoxy. This caused the peak capacity mass flow rate without void volume to be increased from 500 kg h^{-1} for the base regenerator to 700 kg h^{-1} for the other regenerators.

- The best way to decrease the void volume/volume of displaced fluid ratio is by reducing the pressure drop inside the regenerator, either by increasing the effective porosity or the cross-sectional area, increasing the mass flow rate of the peak cooling capacity.

5.5 Deviations of the Curie Temperature

Most of the characteristics and operating conditions of an active magnetic regenerator can be manufactured with or set to an acceptable degree of accuracy. However, the Curie temperatures of the materials do not follow this trend and have to be treated with greater care, as shown by Lei et al. (2015). During manufacture, it is usual to expect an absolute tolerance of +/- 2 K in the value of the Curie temperature, i.e., a material with a target Curie temperature of T_{Curie} could end up as a material with any Curie temperature between T_{Curie} - 2 K and T_{Curie} + 2 K. However, the value of this error appears to be approximately the same for all Curie temperatures manufactured in the same batch. Therefore, the total error of the Curie temperature of each layer can

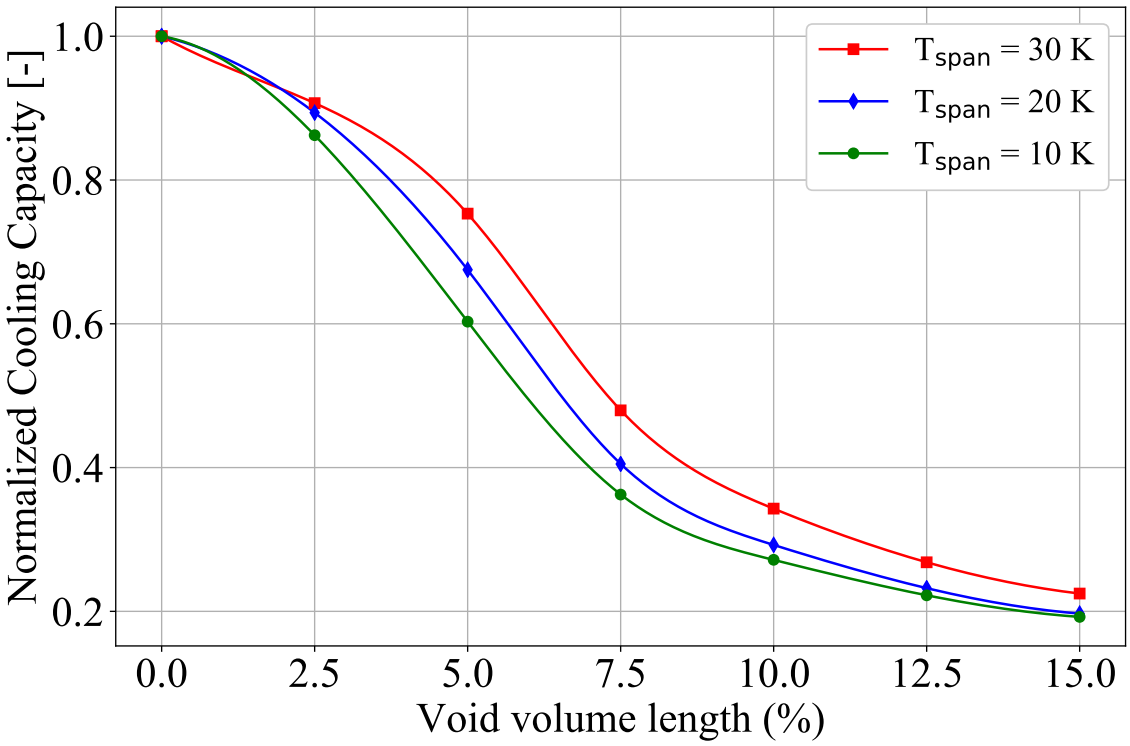

Figure 94 – Effect of the temperature span on the void volume losses for the test regenerator. The mass flow rate was kept constant at 500 kg h^{-1} and the other parameters are listed in Tables 24 and 25.

be divided into two parts: a systematic error which is the same for all layers and a smaller random error, specific to each layer. The systematic error represents absolute tolerance and, therefore, can vary between -2 K and 2 K while the random error can be represented by a normal distribution with zero mean and standard deviation of 0.4 K, based on previously obtained manufacturing results.

In order to determine the effect of this variation on the cooling capacity, the regenerator presented in Section 5.4 operating at peak cooling capacity was tested multiple times with each of five values of systematic error (-2 K, -1 K , 0 K, +1 K and +2 K) and the random systematic error applied to its Curie temperature profile. The average loss in cooling capacity is shown in Figure 95, where the resulting average cooling capacity for each value of systematic error is shown as a percentage of the cooling capacity of the reference case (without deviations). As can be seen, the larger the absolute value of the systematic error, the greater the loss in the cooling capacity. Moreover, positive values of systematic error seem to be considerably worse for the cooling capacity than negative values, which is expected given the results shown in Section 5.3.

This poses a considerable challenge to the design of the regenerators, since this presumably unpredictable and unavoidable deviation may result in drops in the cooling

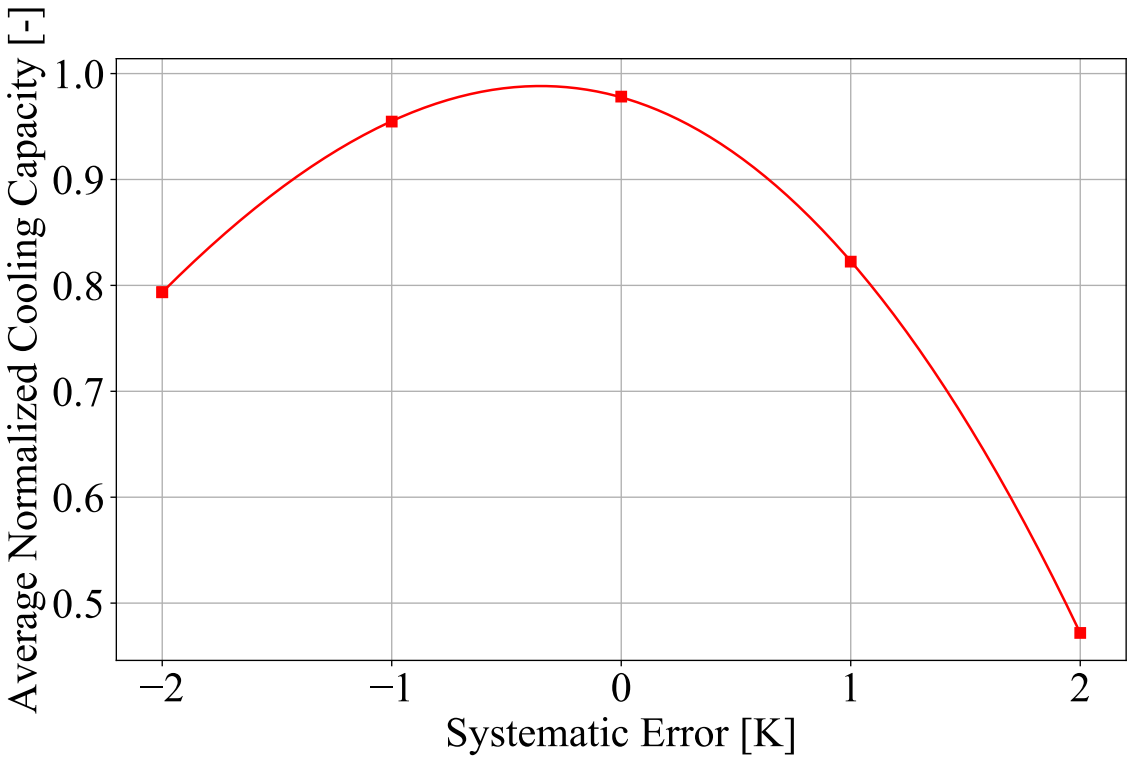

Figure 95 – Average resulting cooling capacity as a function of the systematic error in the Curie temperature. The random error had a standard deviation of 0.4 K. The results were normalized considering the cooling capacity without any deviation in the Curie temperatures.

capacity of more than 50%. Thus, preventive measures need to be taken to mitigate these losses. These measures involve manufacturing extra materials with selected Curie temperatures that can be used to replace other materials in the regenerator if necessary. One of the most cost-effective methods to achieve this is to manufacture two extra materials, one with a Curie temperature 2 K lower than the lowest one required for the regenerator and another with a Curie temperature 2 K higher than the highest one in the regenerator. That way, since the gap between the Curie temperatures of the layers is usually smaller than 2 K, the maximum absolute value of the systematic error is reduced to 1 K. This method, however, is limited by the cost of manufacturing said materials and is also less effective if the gap between the Curie temperatures is high.

Therefore, there also needs to be a way to ensure that the material being manufactured is used in the best possible way, regardless of the resulting Curie temperatures. This can be achieved through changes in the length of each layer, so that each point along the regenerator has the most appropriate Curie temperature among those that have been manufactured. A description of the method and routine applied to determine the ideal length of each layer is shown in Appendix C. By itself, this method is already quite powerful, allowing for increases in cooling capacity over 60% in cases

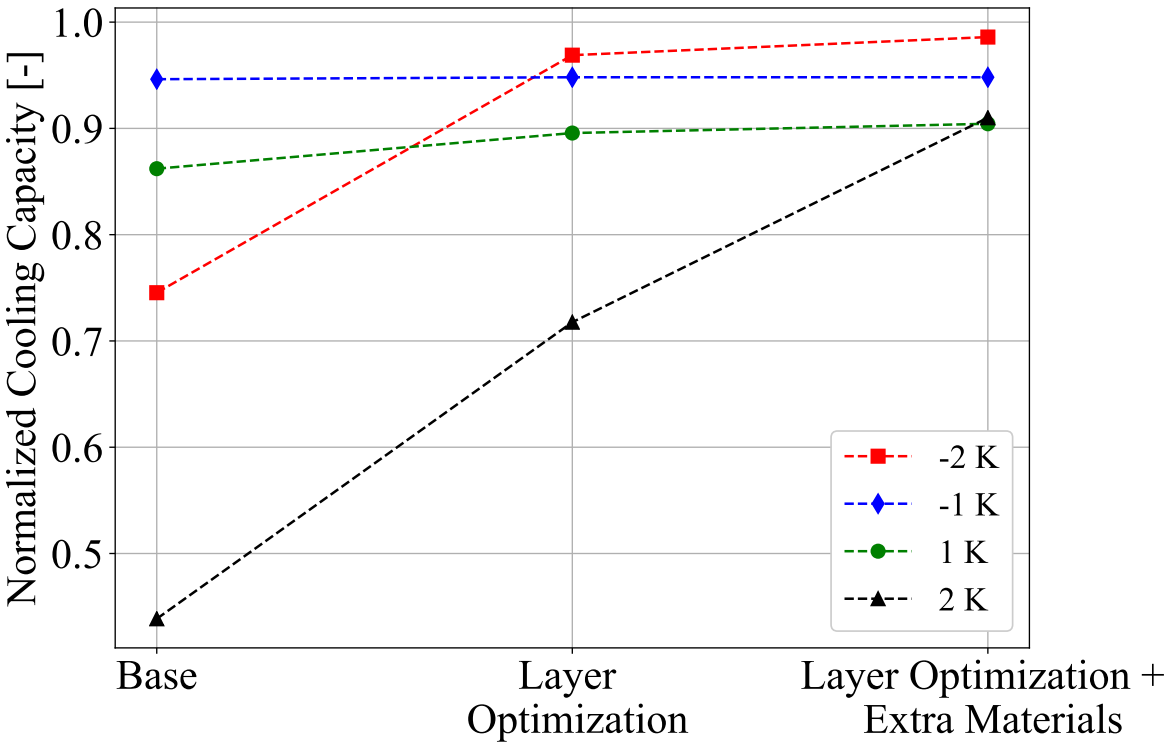

Figure 96 – Effect of the layer length optimization and use of extra materials in the cooling capacity of four specific cases with different systematic errors. The results were normalized considering the cooling capacity without any deviation in the Curie temperatures.

with systematic errors of + 2 K. It cannot, however, reach the equivalent cooling capacity without deviations unless the deviations themselves are very small. Thus, the ideal scenario is to use this optimization along with manufacturing extra materials, which increases the pool of Curie temperatures that can be used, minimizing the systematic error. Figure 96 shows the effects of the length layer optimization with and without extra materials in cases with non-zero systematic errors. As can be seen, the use of both methods guarantees a much more predictable loss in cooling capacity due to the deviations and caps it at around 10%. This happens because both methods are particularly effective when the systematic error has an absolute value of 2 K and are less helpful when the absolute value is 1 K. Meanwhile, the overall losses increase with the absolute value of the deviation, which balances this effect and results in a fairly constant overall loss in performance.

The drawback of both solutions is the same: an increase in the quantity of material that needs to be manufactured. Manufacturing extra Curie temperatures not only adds to the total mass of material, but also increases the complexity of the manufacturing process, which may further increase the costs. Meanwhile, the optimization of the layer lengths inevitably results in layers which are larger than initially predicted, a

phenomenon that is usually observed at the ends of the regenerator and requires these layers to have more mass of material. Since the length of the layers is unpredictable before the Curie temperatures are known (i.e, before manufacturing), an extra amount of all materials will need to be manufactured in order to make this correction practical.

5.6 Designing a Regenerator for a Magnetic Refrigeration Unit

All results previously presented in this chapter pertain to characteristics of the regenerator which are either independent from the other sub-systems of a refrigeration unit (e.g., particle diameter and porosity) or which can be prescribed during operation (e.g., frequency and mass flow rate). This section will focus on analysing parameters which are directly related to other systems, namely the hydraulic sub-system and the magnetic circuit, while taking into account how these parameters affect said systems. These analyses will then be used as a backdrop for the design of the regenerator to be applied in a Magnetic Refrigeration Unit (MRU) with requirements that will be described further ahead. While this section presents maps showing the path that was taken to define the final regenerator and magnet for the system, it is important to note that a good portion of the optimizations that led to the final design were made elsewhere, using a model that integrated all relevant components of the MRU including systems that are not directly related to the regenerator. This semi-empirical model, which can be found in Peixer (2020), used the knowledge developed in the present work along with information from models of the other systems to predict the performance of the MRU as a whole. This was done so because the semi-empirical model, while not as reliable as the more detailed models such as the one described in this work, was able to run hundreds of thousands of cases fairly quickly, while the other models required to much computation power and were too slow to achieve this.

5.6.1 Flow and Field Profiles

As described in Section 2.4.1, an AMR cycle operating according to the Brayton cycle is divided into four processes: adiabatic magnetization, isofield cold blow, adiabatic demagnetization and isofield hot blow. While this is the sequence that these processes should follow ideally, it is not the way they are implemented in practice, both in terms of waveforms (fluid flow and magnetic field change) and their synchronization. Therefore, the aim of this section is to determine how the field and flow profiles affect each other and how they should be conceived in order to maximize performance. This will then be translated into guidelines for the selection of the valves and control system that will control the flow within the regenerator in the MRU.

For this analysis, the same regenerator from Table 24 was used, and the operating conditions are also similar, as shown in Table 26, with the main differences being the blow fractions and the high and low field fractions of 25%, instead of 35%, which were changed to allow ratios between blow and high field of up to 2. As can be seen, the field profile will be kept constant in this analysis and behave as a ramp in order to better represent a real profile generated by a magnet. Therefore, all test conditions will be created by changing the flow profile, aiming to emulate a real situation with an already existing magnet, in which the field profile is unchangeable, but the flow profile may still be altered. The flow profile will start as a simple step profile and eventually be modified into a ramp profile with different opening and closing times, similarly to a real valve.

Table 26 – Operating conditions for the flow and field profile analysis.

Operating Conditions	**Values**
Frequency	1.5 Hz
Temperature span	30 K
Mass flow rate	Various
Maximum applied magnetic flux density	1 T
Hot side temperature (T_H)	316.15 K
Applied field profile	Ramp
Blow profile	Step and Ramp
Blow fraction	Varied
High and low field fractions	25%

5.6.1.1 Instantaneous Flow Profile

An instantaneous (step change) flow profile is the simplest configuration since it disregards any potential closing and opening times for the valve that controls the flow. This configuration can be used to study two different parameters: the ratio between the periods of each profile and the synchronization between them. The ratio between the periods is simply defined as the ratio between τ_{Blow} and τ_{HF}, both shown in Figure 97. The synchronization is defined by τ_D, also shown in Figure 97, which is the time difference between the center of the high (or low) field profile (B_c) and the center of the high (or low) velocity profile (u_c). If $\tau_D = 0$, the profiles are considered synchronized, if τ_D is positive, the flow profile is delayed in relation to the field profile (as in Figure 97), and if τ_D is negative, the flow profile is ahead of the field profile.

Figure 98 shows the cooling capacity results for the regenerator operating at 300 and 600 kg h^{-1}. In both cases, it can be seen that the cooling capacity peaks when the blow period is equal to the high field period. However, higher mass flow rates also reach high cooling capacities for τ_{Blow}/τ_{HF} values of up to 1.4, and immediately start dropping if τ_{Blow}/τ_{HF} dips below 1. Meanwhile, lower mass flow rates maintain high

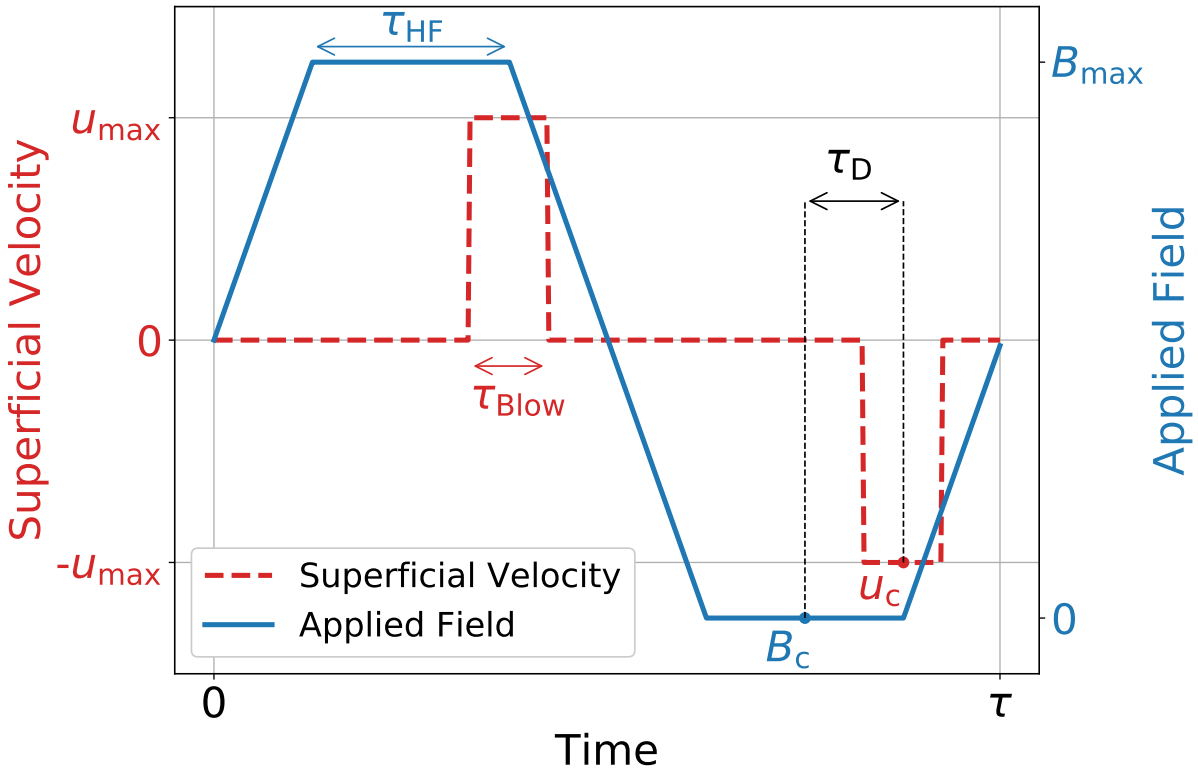

Figure 97 – Representation of the ramp applied field and instantaneous flow profiles, with the releveant periods highlighted. τ_{Blow} is the blow period, τ_{HF} is the high field period and τ_D is the time lag, which is positive when the blow is delayed in relation to the applied field.

cooling capacities at values closer to 1 from both sides, ranging from around 0.9 to 1.2. The likely explanation for this is that higher values of τ_{Blow} allow for the same volume of fluid to be displaced with a lower mass flow rate and thus, pressure drop. Because of this, cases with high mass flow rate are more sensitive to the effects of increasing the value of τ_{Blow} due to them being greatly affected by the pressure drop, while cases with low mass flow rate do not have the same response and will not favor greater values of τ_{Blow}.

Regarding synchronization, the cooling capacity reaches its peak when both profiles are perfectly synchronized ($\tau_D = 0$) and reduces continuously as it moves away from that configuration. The reduction is greater if the flow profile gets ahead of the field profile ($\tau_D < 0$), thus, when designing the control of the system, the target should be $\tau_D = 0$ with any unavoidable tolerance preferably only allowing $\tau_D > 0$, in order to minimize the drop in performance.

5.6.1.2 *Ramp Flow Profile*

As shown in the last section, the cooling capacity reaches its maximum value when the profiles are synchronized and $\tau_{Blow} = \tau_{HF}$, thus, this section will focus in

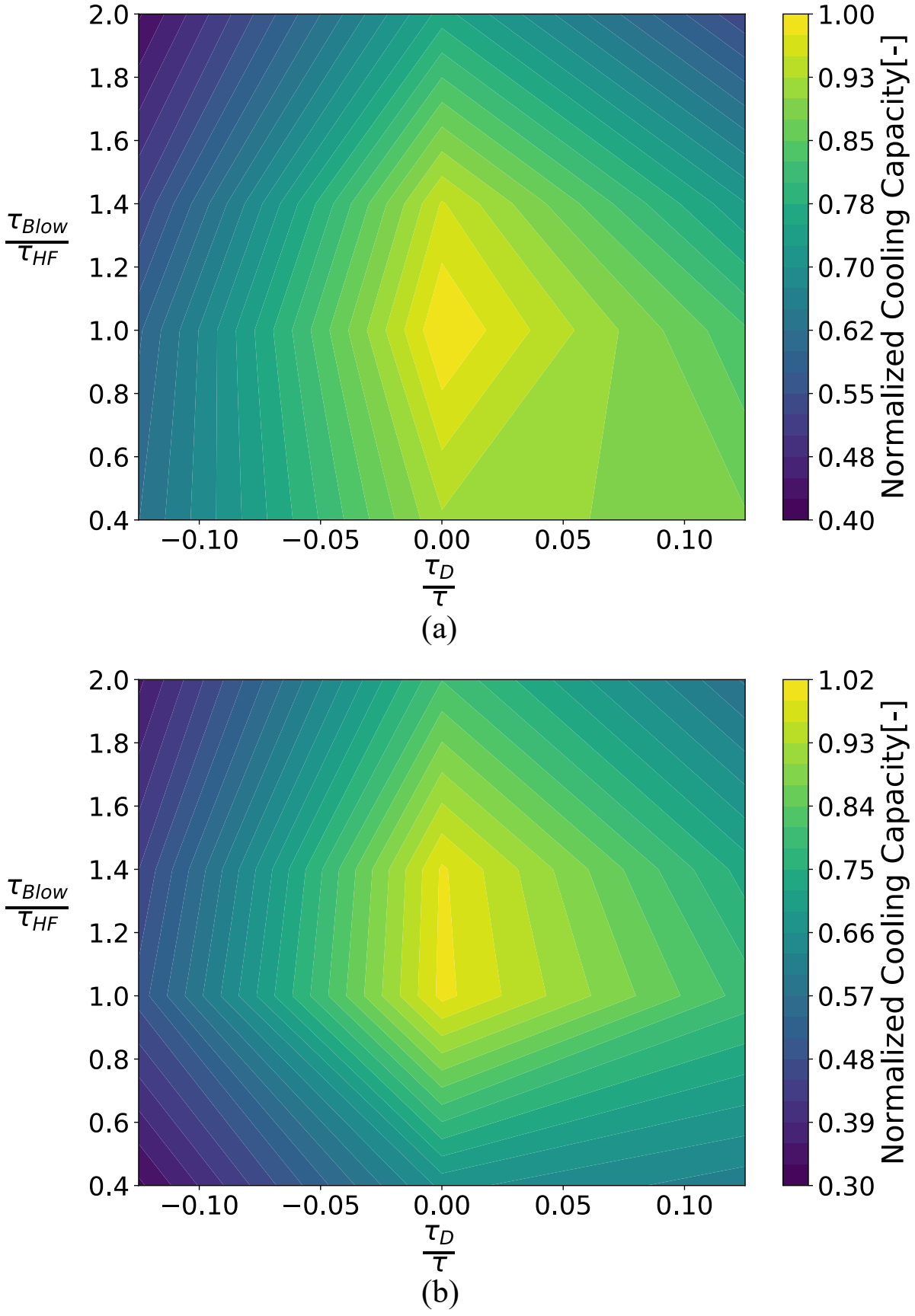

Figure 98 – Influence of synchronization (τ_D) and the ratio between τ_{Blow} and τ_{HF} on the cooling capacity for mass flow rates of (a) 300 and (b) 600 kg h^{-1}.

cases that satisfy these conditions. The ramp flow profile is more complex than the instantaneous profile and thus requires more parameters to be fully described, as shown in Figure 99. τ_{Op} is the opening period of the ramp profile, i.e., the time it takes to go from a no-flow condition to the maximum flow condition. τ_{Cl} is the closing period and the opposite of the opening period, i.e., the time it takes to go from a maximum flow condition to a no-flow condition. These values are not necessarily the same, especially in real applications such as valves which usually have $\tau_{Cl} > \tau_{Op}$. The ramp period (τ_{Ramp}) is defined as the sum of both these periods. τ_b is the high flow period and in this analysis this value will be kept equal to τ_{HF} instead of τ_{Blow}. Lastly, the synchronization will initially be defined as when u_c (half of the blow period) happens at the same time as B_c (half of the applied magnetic field period).

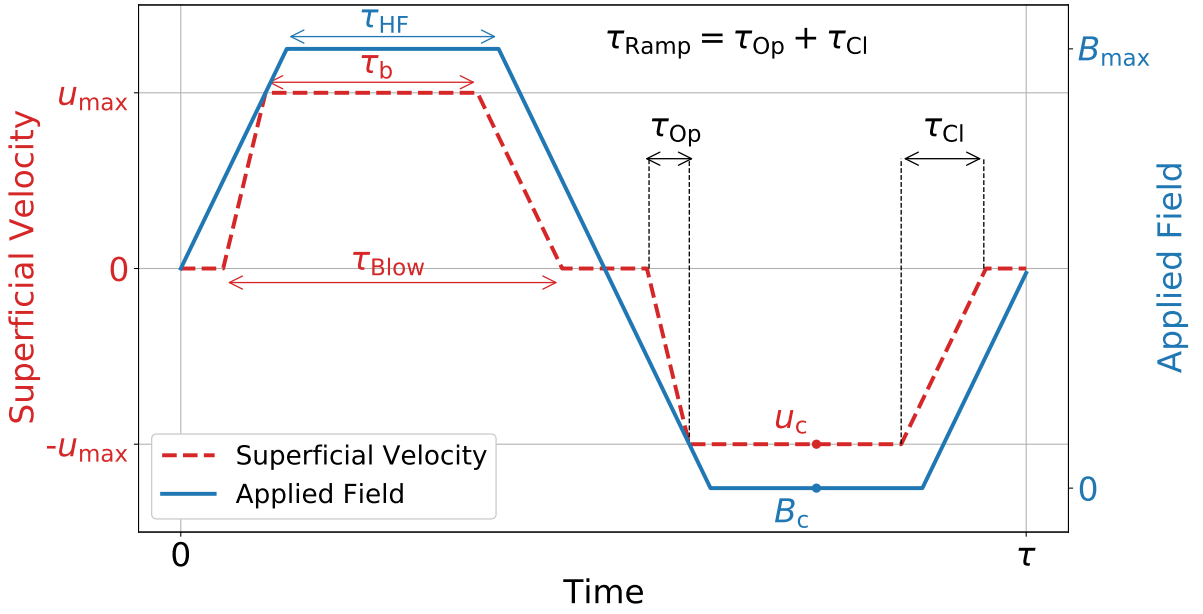

Figure 99 – Representation of the ramp-like field and flow profiles, with the relevant periods highlighted. τ_{Blow} is the blow period, τ_{HF} is the high field period, τ_b is the high blow period, τ_{Op} is the valve opening period, τ_{Cl} is the valve closing period and τ_{Ramp} is the ramp period.

Since the synchronization and τ_b are kept constant, the main variables in the ramp profile become the size of τ_{Ramp}, which represents how fast the flow starts and stops, and the relation between τ_{Op} and τ_{Cl}, which accounts for imbalances in the flow profile that are inevitable in practical applications. Figure 100 shows the influence of these variables on the cooling capacity for mass flow rates of 300 and 600 kg h^{-1}. It can be seen that increasing the value of τ_{Ramp} is detrimental to the cooling capacity, with the highest cooling capacity invariably happening at the lowest values of τ_{Ramp}. Thus, the flow profile should be as close as possible to the instantaneous profile. Regarding τ_{Op} and τ_{Cl}, the results show that a longer opening time is better for the cooling capacity than a longer closing time. However, the main reason for this increase is actually the indirect time lag caused by the different opening and closing times. Increasing the

opening time is similar to delaying the flow profile, which, as shown in Section 5.6.1.1, is better for the cooling capacity than having it occurring earlier, which is the case for longer closing times.

To further evaluate the effect of the opening and closing times, another analysis was carried out in which the synchronization was changed to guarantee that τ_{HF} and τ_b occur at the same time, as shown in Figure 101. The results for this analysis are shown in Figure 102, and are exactly the opposite of the previous results regarding the opening and closing periods. In this case, smaller opening times reduce the percentage of the flow taking place earlier than B_c (center of the magnetic field "wave") and increase the cooling capacity, while shorter closing times have the opposite effect. Thus, since valves have shorter opening than closing times, this type of synchronization is ideal for most practical applications.

5.6.1.3 Real Valve Profile

Before making conclusions based solely on the analysis of ramp-like profiles, it is necessary to determine if these idealized profiles accurately represent the results that would be obtained using real valves to operate the system. In order to achieve this, several valves were tested and the flow profiles produced by them were implemented in the model and then compared to the equivalent ramp-like profiles. Based on experiments that followed the method described in dos Santos et al. (2020), two valves were considered to have the best profiles for implementation in the model and were used in this analysis: one manufactured by Asco (ASCO SC8210-112) and another manufactured by Danfoss (Danfoss 032U1251). Figure 103 shows an example of the flow profiles generated by these valves along with an equivalent ramp-like profile that aims to emulate the actual valve behavior.

The flow profiles shown above were used to simulate the regenerator operating under different conditions of frequency (0.5 Hz, 1.5 Hz and 2.5 Hz), mass flow rate (500, 700 and 900 kg h^{-1} and applied magnetic flux density (1.0 and 1.15 T). Figure 104 shows the deviation between the results obtained using the actual valve profile and the equivalent ramp profile. From these results, it can be inferred that the ramp profile represents a system that is similar to the one being operated using a valve, with an average error of 3.5% for the Asco valve and 1.4% for the Danfoss valve. These results were considered accurate enough to justify the representation of actual valve profiles using idealized ramp-like profiles.

The results obtained in Section 5.6.1.2 can be used to create guidelines for the relation between the flow and field profiles and, consequently, for the selection of the MRU valves. These guidelines are:

- The ideal configuration has both profiles synchronized, however, if this is not achievable, it is better to have the flow delayed in relation to the applied field;

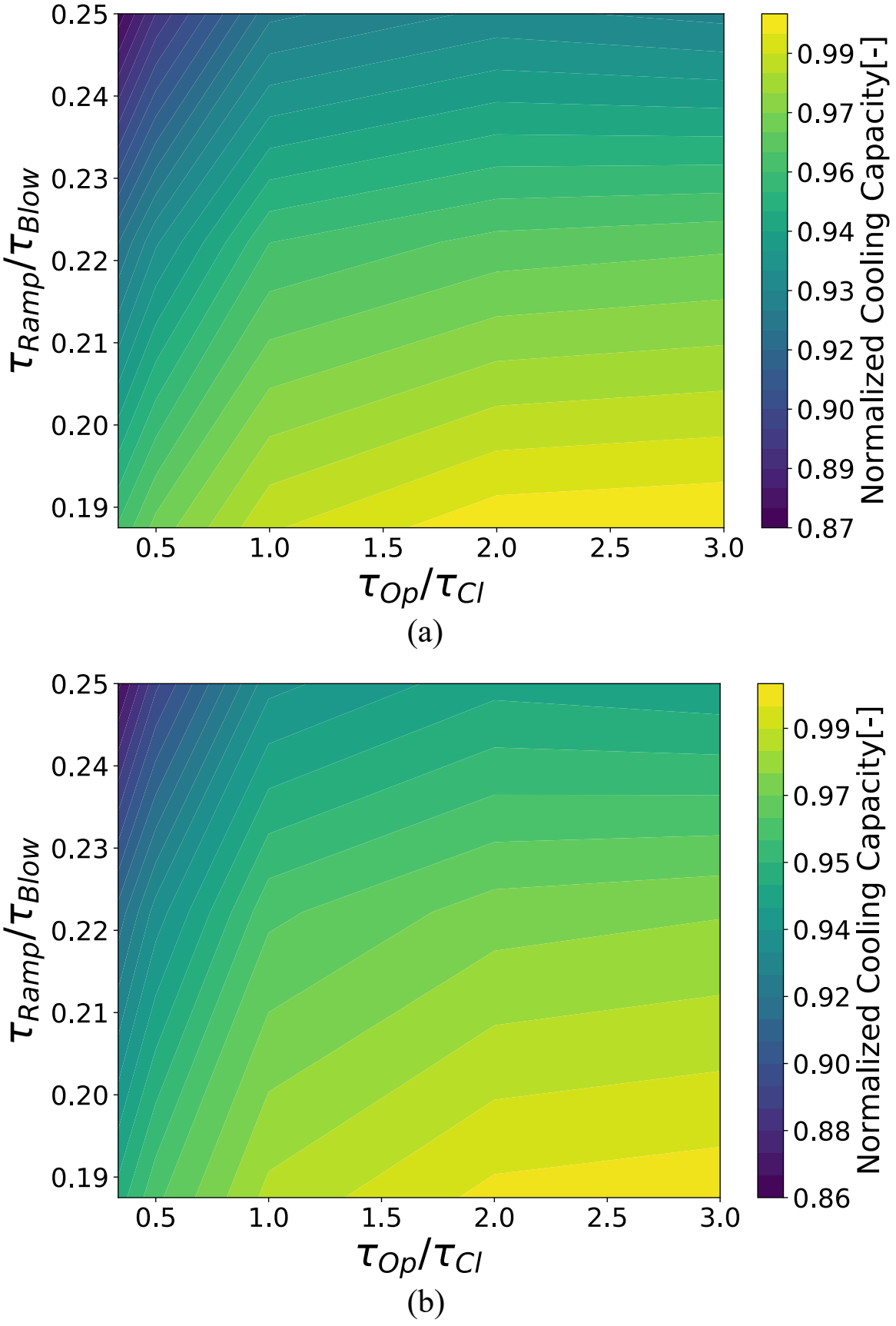

Figure 100 – Influence of the ramp period (τ_{Ramp}) and the ratio between τ_{Op} and τ_{Cl} on the cooling capacity for mass flow rates of (a) 300 and (b) 600 kg h^{-1}.

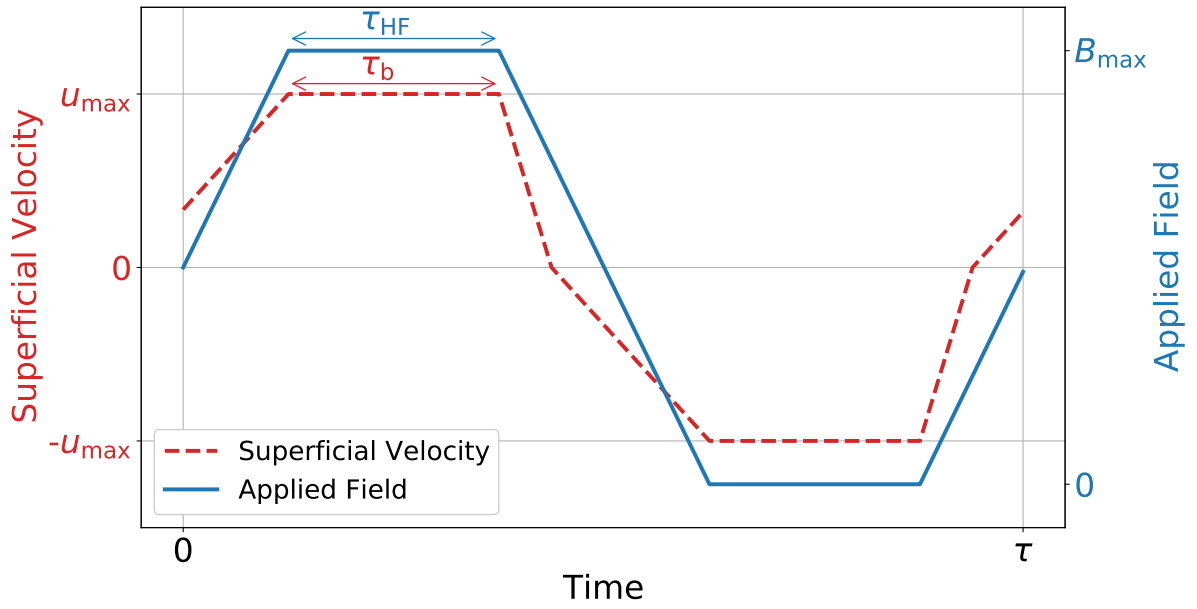

Figure 101 – Representation of the ramp applied field and flow profiles, with the alternate synchronization where τ_{HF} and τ_b coincide.

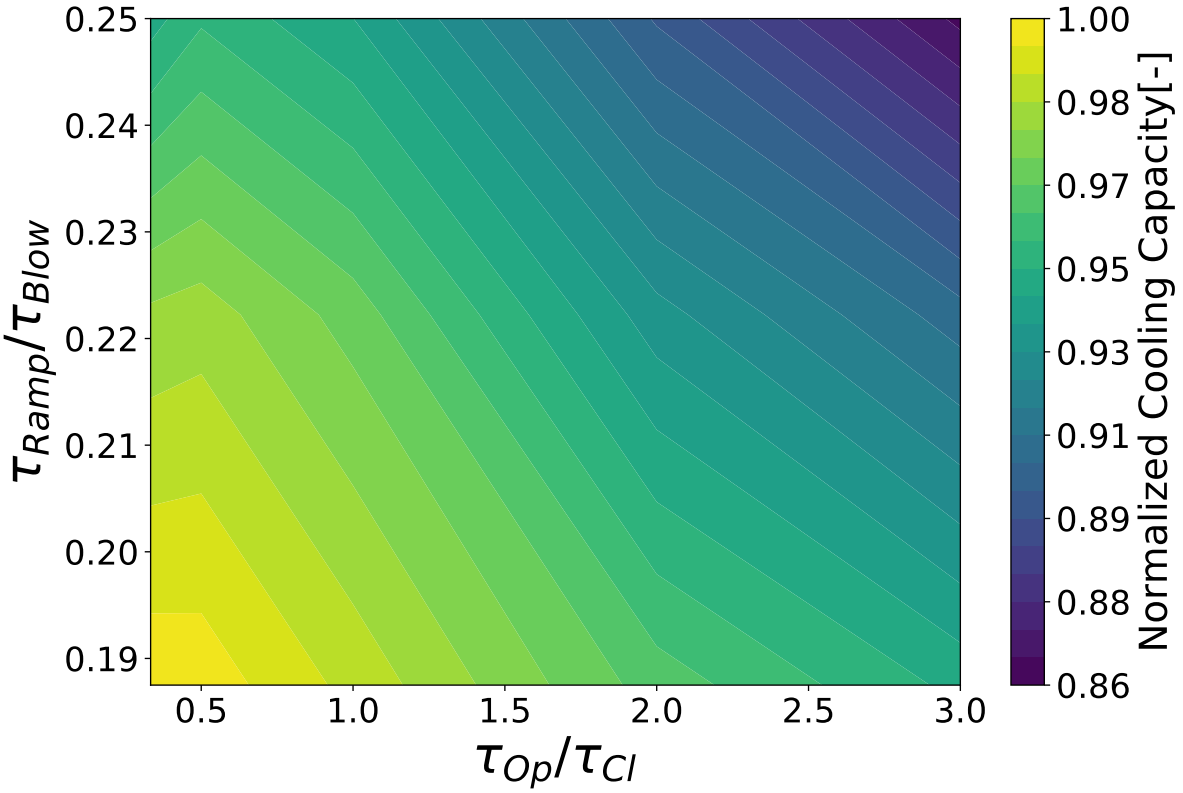

Figure 102 – Influence of the ramp period (τ_{Ramp}) and the ratio between τ_{Op} and τ_{Cl} on the cooling capacity with the alternate synchronization for a mass flow rate of 600 kg h^{-1}.

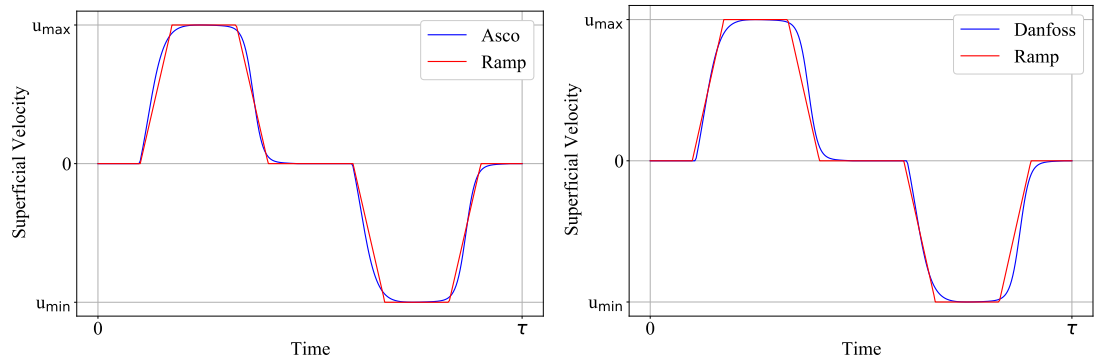

(a) (b)

Figure 103 – Flow profiles generated by the (a) Asco and (b) Danfoss valves with their equivalent ramp-like profiles.

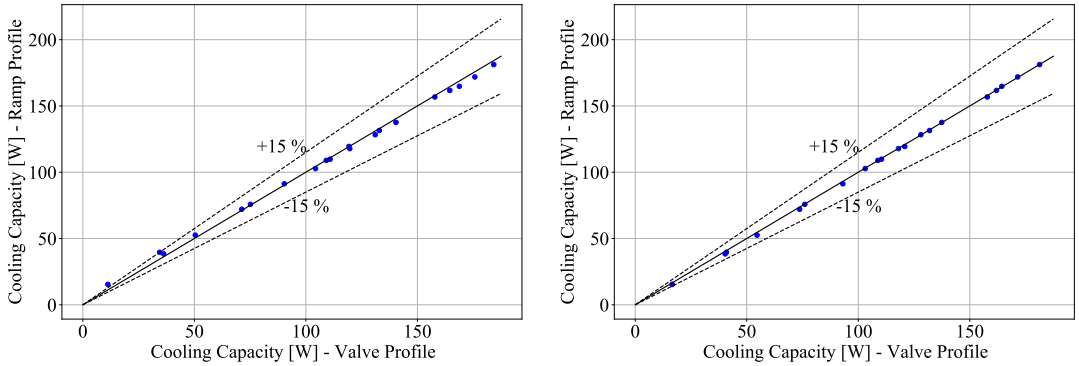

(a) (b)

Figure 104 – Comparison between numerical result obtained using a ramp-like flow profile and the expected flow profile of the (a) Asco and (b) Danfoss valve (f = 1.0 Hz).

- The highest cooling capacities are obtained when $\tau_{Blow} = \tau_{HF}$ (instantaneous profile) or $\tau_b = \tau_{HF}$ (ramp profile and valves);
- In ramp-like flow profiles, the ramp period should be as small as possible;
- If the hydraulic system generates an opening time which is shorter than the closing time (usual case for valves), the synchronization should guarantee that τ_b and τ_{HF} occur at the same time;
- If the hydraulic system produces an opening time which is longer than the closing time , the synchronization should guarantee that B_c and u_c occur at the same time;

5.6.2 *Integrated Design with the Magnetic Circuit*

This section will focus on the integration between the AMR and the magnetic circuit, which is essential to guarantee the optimum performance of the refrigerator.

There are three main ways in which the regenerator and the magnetic circuit can interact with each other: through their lengths, through the gap size *versus* the cross section of the regenerator and through the flow profile *versus* the magnetic field profile. Each of these ways will be analyzed in this section aiming to maximize the cooling capacity obtained while maintaining the size of the magnetic circuit at acceptable values, avoiding considerable increases in the cost of the system.

5.6.2.1 Regenerator and Magnet Length

The relationship between the length of the regenerator and the length of the magnet is, in many ways, the simplest to analyze. Both parameters are independent, i.e., a change in the length of the regenerator does not automatically imply a change in the length of the magnet, and vice-versa. However, as the focus of the project is to maximize the cooling capacity, these parameters end up becoming dependent on each other due to the need to achieve this objective. Table 27 shows all the parameters that were varied in order to perform this analysis, as well as their values. The parameters not mentioned in the table are the same as those in Section 5.4.

Table 27 – Parametric ranges considered in the regenerator and magnet length analysis.

Name	**Fict. Regenerator**
Mass flow rate	300, 500, 700 and 900 kg h^{-1}
Maximum applied magnetic flux density	1.0, 1.25 and 1.5 T
Regenerator length	100, 125, 150, 175 and 200 mm
Temperature span	10 and 30 K
L_{mag}/L_{reg}	5/6, 1, 7/6, 8/6, 9/6, 10/6, 11/6 and 2

The way in which the length of the magnet affects performance is also quite simple. In general, the variation of the magnetic field is maximum in the center of the magnet and decreases as the edges are approached. Because of that, an ideal magnet would have an infinite length and the field variation would be maximum throughout the regenerator. In practice, the length of the magnet is finite and must be determined by a trade-off analysis. On the one hand, increasing the length of the magnet ensures greater field variation over the entire regenerator, which increases the cooling capacity. On the other hand, the mass of the magnet increases linearly with the length and, consequently, so does its cost. In addition, there is an increase in the complexity of the magnet assembly, since it consists of the union of several smaller pieces, which have a limited length. Thus, if the length exceeds certain values, more parts will be needed to manufacture the magnet.

The effect of the regenerator length is fairly similar to the effect of the mass flow rate: increasing the length initially benefits the cooling capacity since the mass of MCM increases linearly with the length, consequently increasing the MCE. However, increasing the length also increases the pressure drop in the regenerator, which hinders

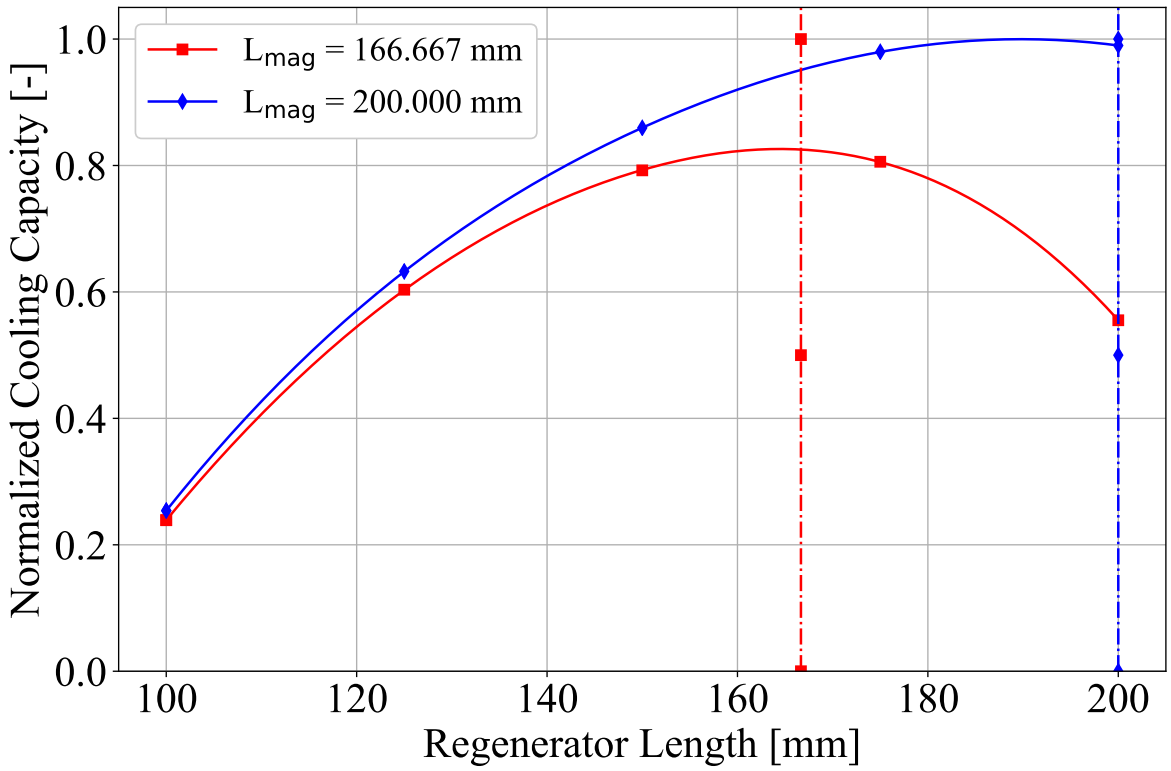

Figure 105 – Effect of the regenerator length on the cooling capacity for two fixed magnet lengths. The vertical lines are used to highlight the value of the magnet length at the x axis.

the cooling capacity. Thus, as for the mass flow rate, after a certain length the effect of increasing the pressure drop outweighs the effect of having more material, and the capacity begins to decrease. This is especially true for a fixed magnet length, since all material added with the increase in length is placed at positions progressively further away from the center of the magnet and, therefore, with lower magnetic field variation. Figure 105 shows this behaviour for two different regenerator lengths (166.667 and 200 mm). As can be seen, the cooling capacity increases until the length of the regenerator reaches values close to that of the magnet, beyond which the cooling capacity starts to decrease. Thus, in order to further increase the cooling capacity, the magnet length needs to be increased along with the length of the regenerator.

Figure 106 shows the cooling capacity as a function of the regenerator length when the ratio L_{mag}/L_{reg} is kept constant, i. e., the increase in the regenerator length is accompanied by a proportional increase in the magnet length. Since the magnet is also getting larger, the cooling capacity continues to increase even for larger regenerators. However, the effect of the pressure drop still exists, causing the increase in cooling capacity to decrease with increasing length of the regenerator. It can be expected that, for sufficiently large values of regenerator length, the cooling capacity will stop increasing or even start to decrease. The value of the ratio L_{mag}/L_{reg} does not appear to have an effect

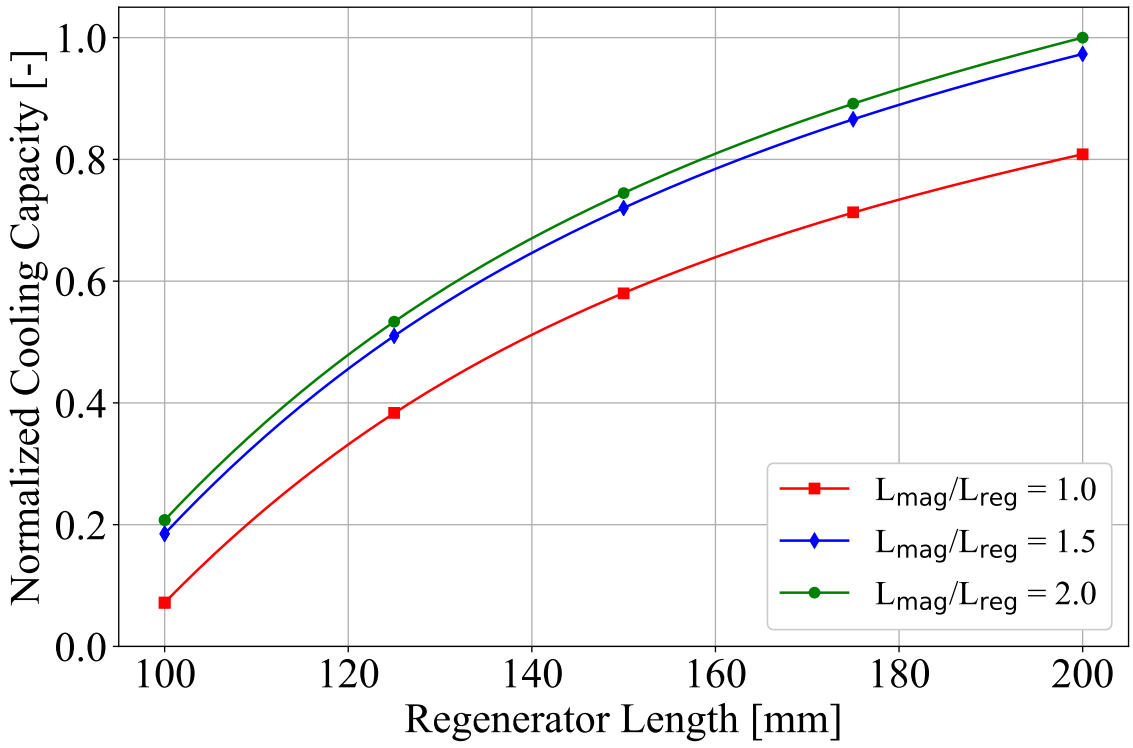

Figure 106 – Effect of the regenerator length on the cooling capacity for different $\frac{L_{mag}}{L_{reg}}$ ratios at peak mass flow rate.

on the behavior of the cooling capacity with the length of the regenerator (derivative of the curves), but larger values of L_{mag}/L_{reg} result in higher absolute values of cooling capacity.

The effects of the L_{mag}/L_{reg} ratio can be further seen in Figure 107, which shows the cooling capacity results for all conditions described in Table 27. The cooling capacity for L_{mag}/L_{reg} = 2 was considered equivalent to the case with an infinite magnet, and used as a reference for normalization. With the exception of some outliers, the effect of L_{mag}/L_{reg} is quite similar for all operating conditions, especially at values closer to 2. The outliers, although physically consistent, represent unlikely operating conditions, with short regenerators operating at mass flow rates that are higher than the value associated with the highest cooling capacity. Thus, in the context of engineering design, such points can be neglected, resulting in Figure 108.

Considering the standard deviation, the behaviour of the cooling capacity with L_{mag}/L_{reg} can be considered practically independent of all the other parameters that were varied if L_{mag}/L_{reg} is large enough. For values around unity or smaller, this assumption becomes less correct, and each case needs to be analysed individually. This analysis, however, does not take into consideration the cost of the assembly, which will usually be an important factor in determining the final lengths of the magnet and regenerator. In fact, while a value of L_{mag}/L_{reg} greater than 1.2 may be the best considering only

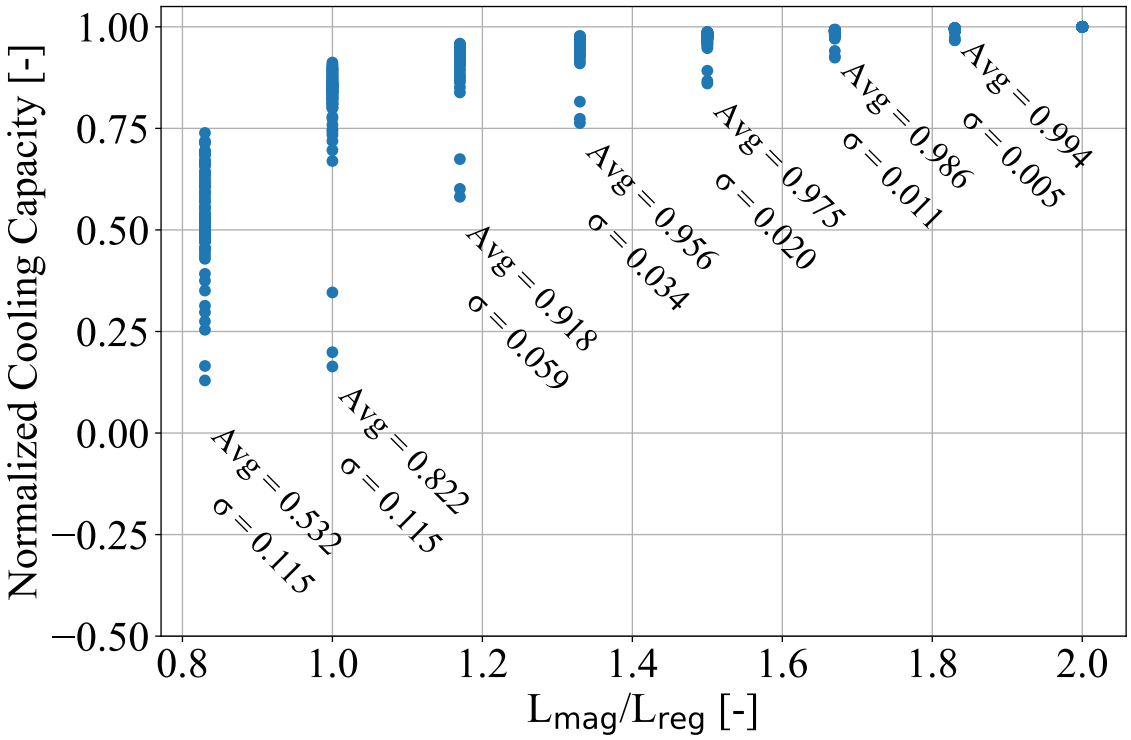

Figure 107 – Effect of the ratio $\frac{L_{mag}}{L_{reg}}$ in the cooling capacity, including outliers.

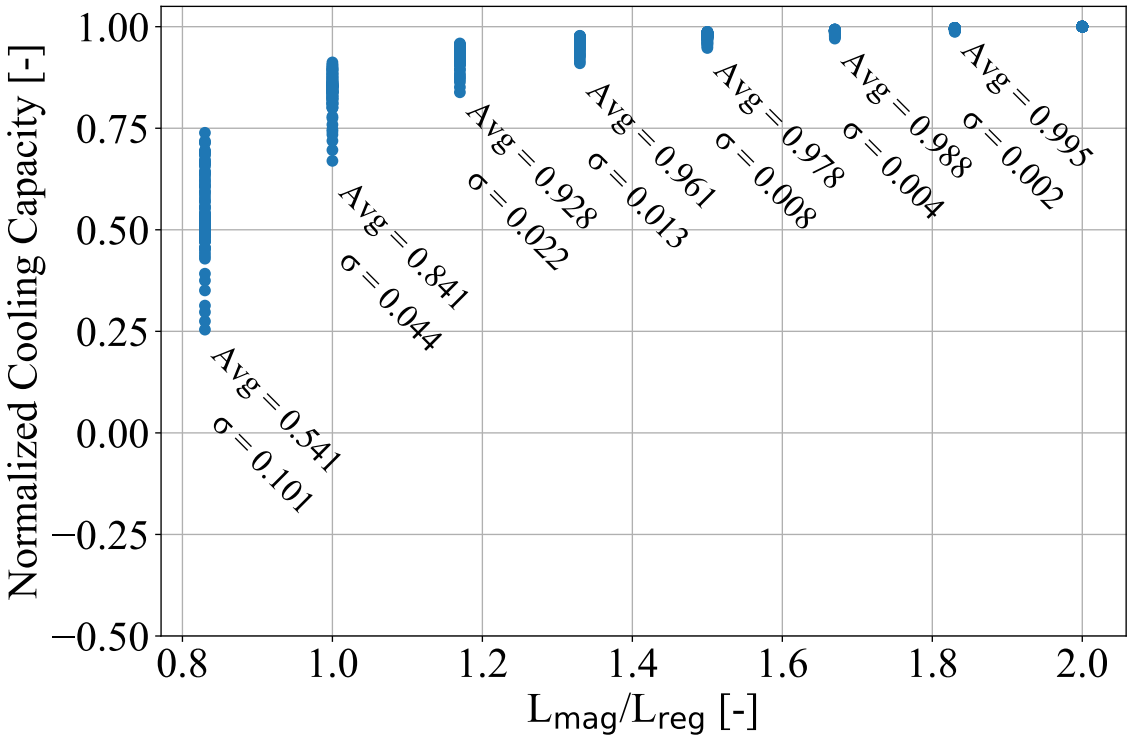

Figure 108 – Effect of the ratio $\frac{L_{mag}}{L_{reg}}$ in the cooling capacity, excluding outliers.

the cooling capacity, when the variable cost is introduced, a value of L_{mag}/L_{reg} closer to unity with a slightly larger regenerator may be the optimal choice. A more in-depth analysis of the effect of the cost can be found in (PEIXER, 2020).

5.6.2.2 Air Gap

In the magnetic cooling system configuration evaluated in the present section, the regenerator is positioned inside an air gap between two concentric cylinders, where the inner cylinder is made of iron and the outer one contains both iron and magnetic material (NdFeB). Figure 109 shows a schematic representation of the regenerators positioned within the air gap, which is located between the outer radius of the inner cylinder (R_2) and the inner radius of the outer cylinder (R_3). δ_v is the radial gap between the regenerator beds and the cylinders while δ_h is the azimuthal gap between the regenerator beds, with both mainly comprising the regenerator wall and air gaps to avoid friction. The sizes of the gaps are independent of the magnetic configuration and will be kept constant in this analysis. The main parameters in Figure 109 that have a considerable influence in the regenerator and overall performance of the system are the radii, R_i, which affect the system in different ways:

- Internal Radius of the Internal Cylinder (R_1) - Altering the value of R_1 does not affect the size of the air gap. Decreasing its value increases the amount of iron and the overall weight and cost of the magnetic circuit, however, it has to be considerably smaller than R_2 to guarantee a good magnetic profile within the air gap. Overall, it is the radius that least affects the performance of the regenerator;

- Outer Radius of the Internal Cylinder (R_2) - One of the radii that forms the air gap. For a fixed (R_3), increasing the value of R_2 directly decreases the height of the air gap, consequently decreasing the height of the regenerator. However, higher values of R_2 also allow for slightly wider regenerator beds, and smaller gap heights increase the maximum applied field within the air gap, leading to a trade-off situation. Increasing the value of R_2 also increases the amount of iron within the inner cylinder, adding to both weight and cost;

- Inner Radius of the External Cylinder (R_3) - One of the radii that forms the air gap. For a fixed (R_2), decreasing the value of R_3 directly decreases the height of the air gap, consequently decreasing the height of the regenerator. It also slightly decreases the width of the regenerator beds by reducing the average radius of the gap. However, this also increases the mass of magnetic material in the external cylinder and reduces the height of the air gap, increasing the maximum applied field considerably more than when increasing the value of R_2, leading to another trade-off situation. Decreasing the value of R_3 also increases the amount of both iron and magnetic material in the outer cylinder, which increases the weight

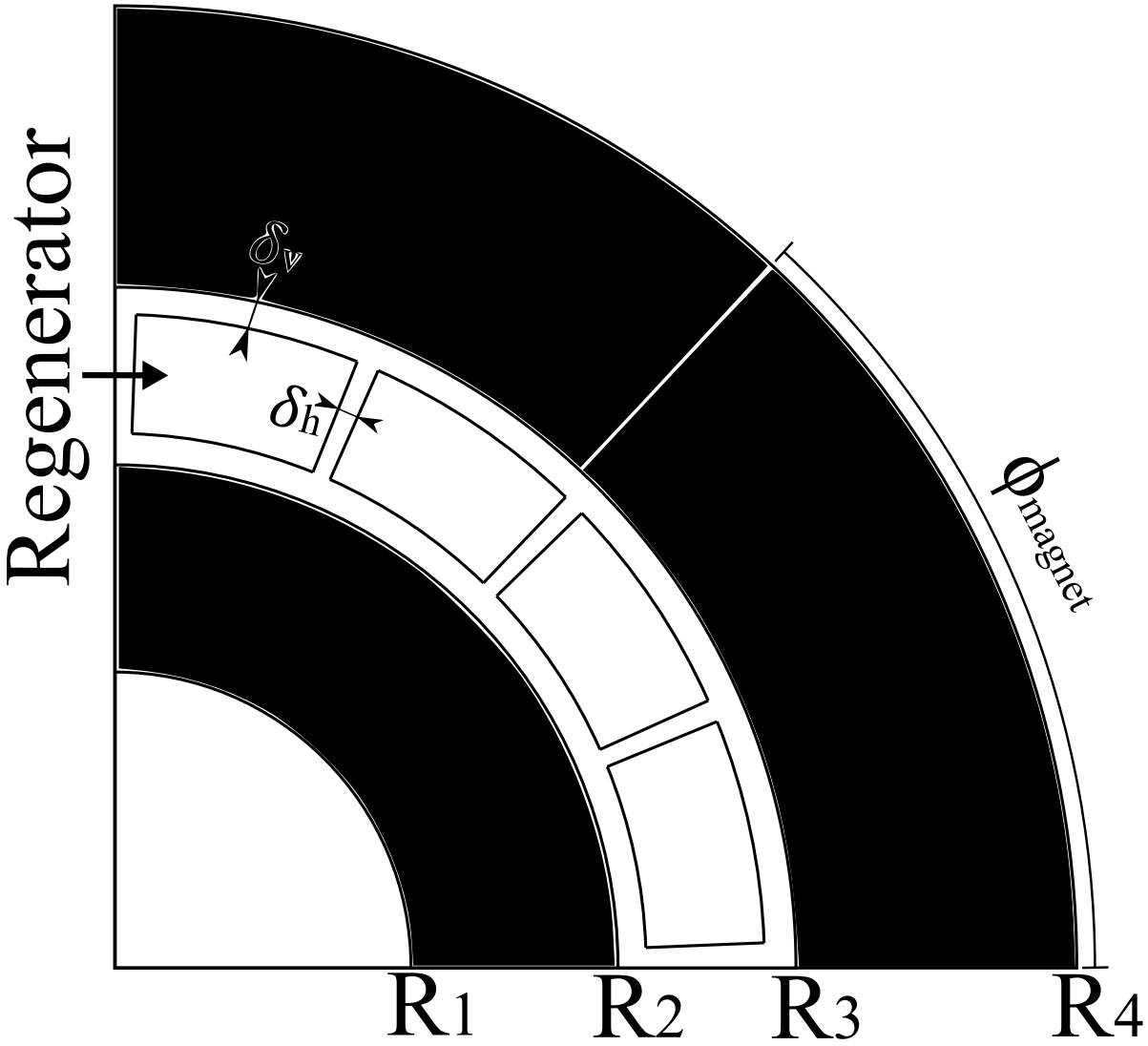

Figure 109 – Representation of the regenerators within the air gap in the magnetic circuit, with the relevant radii highlighted.

and especially the cost of the system, since the magnetic material is much more expensive;

- Outer Radius of the External Cylinder (R_4) - Altering the value of R_4 does not affect the size of the air gap. Increasing the size of R_4 increases the amount of magnetic material in the outer cylinder, therefore increasing the maximum applied field within the air gap. However, this also results in a substantial increase of the total mass of magnetic material, which considerably drives up the cost of the magnetic circuit.

Since the influence of R_1 in the regenerator is negligible when compared to the influence of the other radii, it will not be analysed further. Figure 110 illustrates how each of the radii affect the gap height, maximum applied field, iron mass and magnet mass, as discussed above. As can be seen, the gap height linearly decreases with R_2 and

linearly increases with R_3. The maximum applied field increases with R_2 and decreases with R_3 because of the gap size reduction (and, in the case of R_3, the addition of more magnetic material), so this increase will not necessarily translate into an increase of cooling capacity. Increasing R_4, on the other hand, increases the maximum applied field without changing the gap, so it can be expected to strictly increase the cooling capacity. However, increasing R_4 also results in the highest increase in the mass of both iron and magnetic material, which translates into a higher increase in cost.

To illustrate this, Figure 111 shows how the cooling capacity of the system is influenced by the outer radius of the external cylinder, R_4, when all other radii are kept constant. As already discussed above, there is no trade-off between cooling capacity and R_4, in fact, as can be seen in the results, the cooling capacity continuously increases with R_4 without ever reaching a maximum value. However, the increase in cooling capacity shows an approximately linear behaviour, while the mass of magnetic material increases quadratically with R_4 (see Figure 110), thus, as R_4 increases, more material needs to be added to yield the same increase in cooling capacity. This can also be seen in Figure 111, where the specific cooling capacity ($\dot{Q}_c/M_{\text{magnet}}$) actually decreases with R_4.

Figure 112 shows the influence of R_3 on the cooling capacity, which, as expected, is not as straightforward as the influence of R_4. Due to the trade-off between maximum applied field and gap height, there is an optimal value of R_3 which maximizes the cooling capacity. Moving away from this optimal value will reduce the cooling capacity, but the drop is lower for cases where R_3 is increased (larger gaps). This might be because the regenerator in question has a high pressure drop and the increase in the cross-sectional area given by the increase in the gap is more beneficial than the increase in the applied field given by reducing R_3. Because of that, when cost is considered, the optimal value may be shifted to higher values of R_3 which have a smaller mass of magnet material.

Finally, Figure 113 shows the influence of R_2 on the cooling capacity, which is fairly similar to the influence of R_3. Due to the maximum applied field vs gap height trade-off, an optimal value of R_2 which maximizes the cooling capacity can be found. However, the reduction of cooling capacity when moving away from this point is more uneven than for R_3. Once again, moving into values that increase the gap height (smaller R_2) is less detrimental to the cooling capacity because of the high pressure drop, but since the inner cylinder is not comprised of magnetic material, the loss in maximum applied field is smaller than for R_3, reducing even more the drop in cooling capacity.

5.6.2.3 Magnet Angle

As shown in Figure 109, only a region of the rotor (outer magnet) is comprised of magnetic material while the other part is comprised of iron. The size of this region

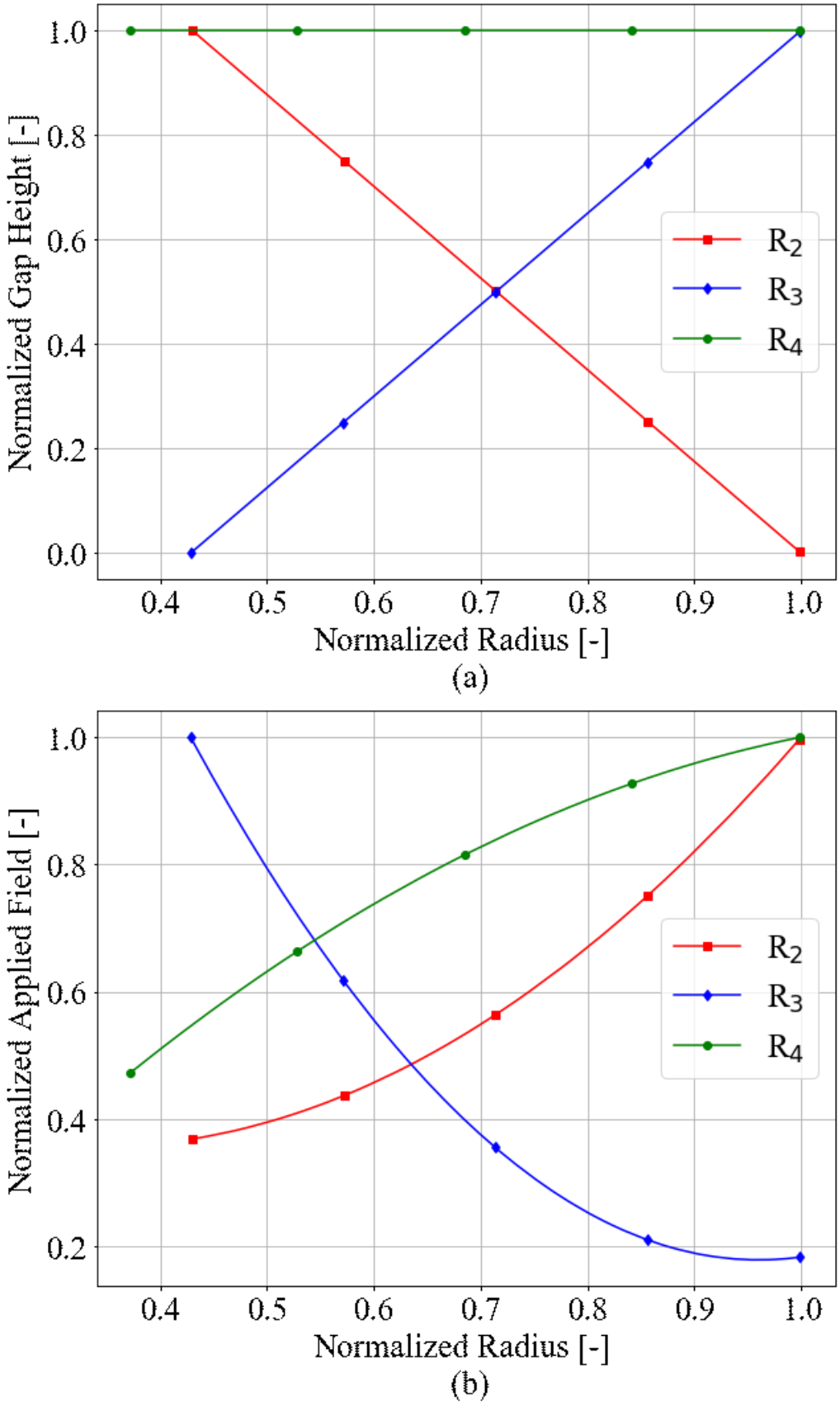

Figure 110 – Part 1 - Influence of the magnetic circuit radii (R_2, R_3 and R_4) in the (a) gap height, (b) maximum applied field, (c) iron mass and (d) magnet mass.

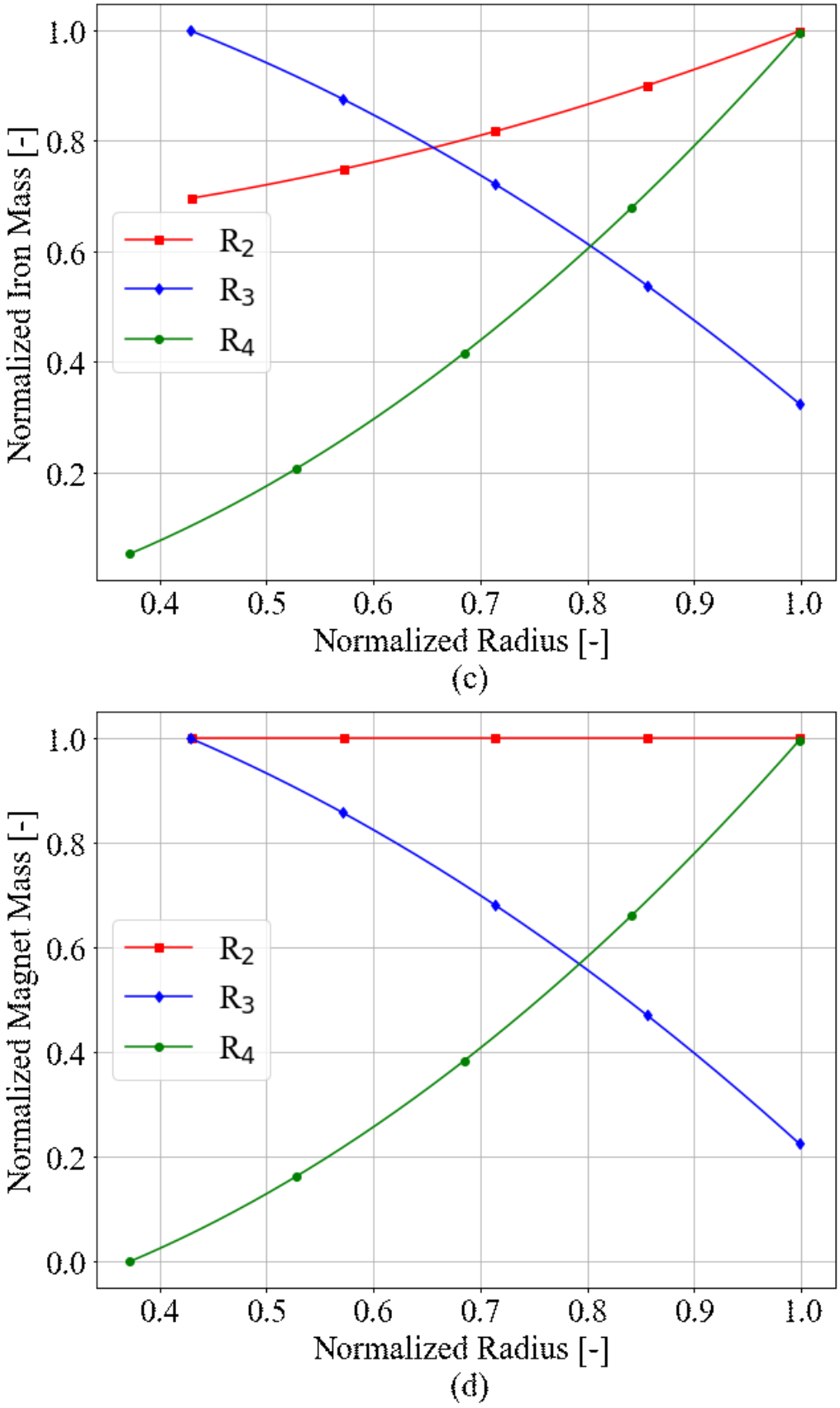

Figure 110 – Part 2 - Influence of the magnetic circuit radii (R_2, R_3 and R_4) in the (a) gap height, (b) maximum applied field, (c) iron mass and (d) magnet mass.

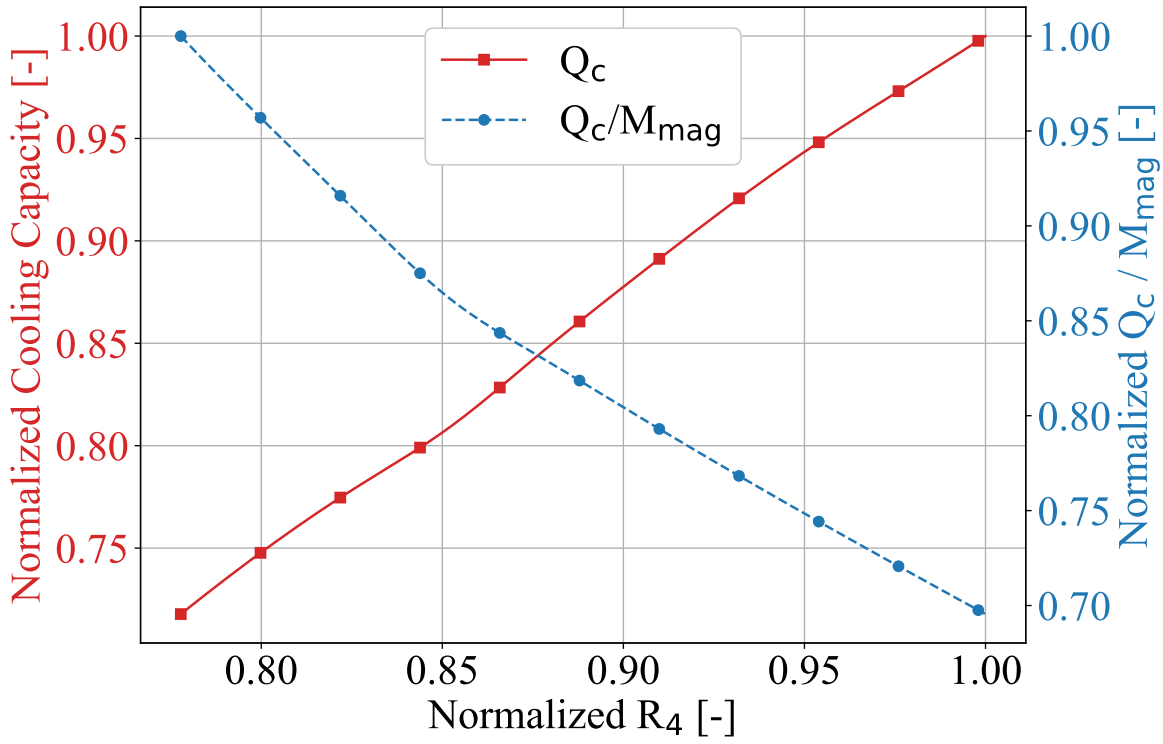

Figure 111 – Influence of the outer radius of the external cylinder (R_4) on the cooling capacity and specific cooling capacity of the system.

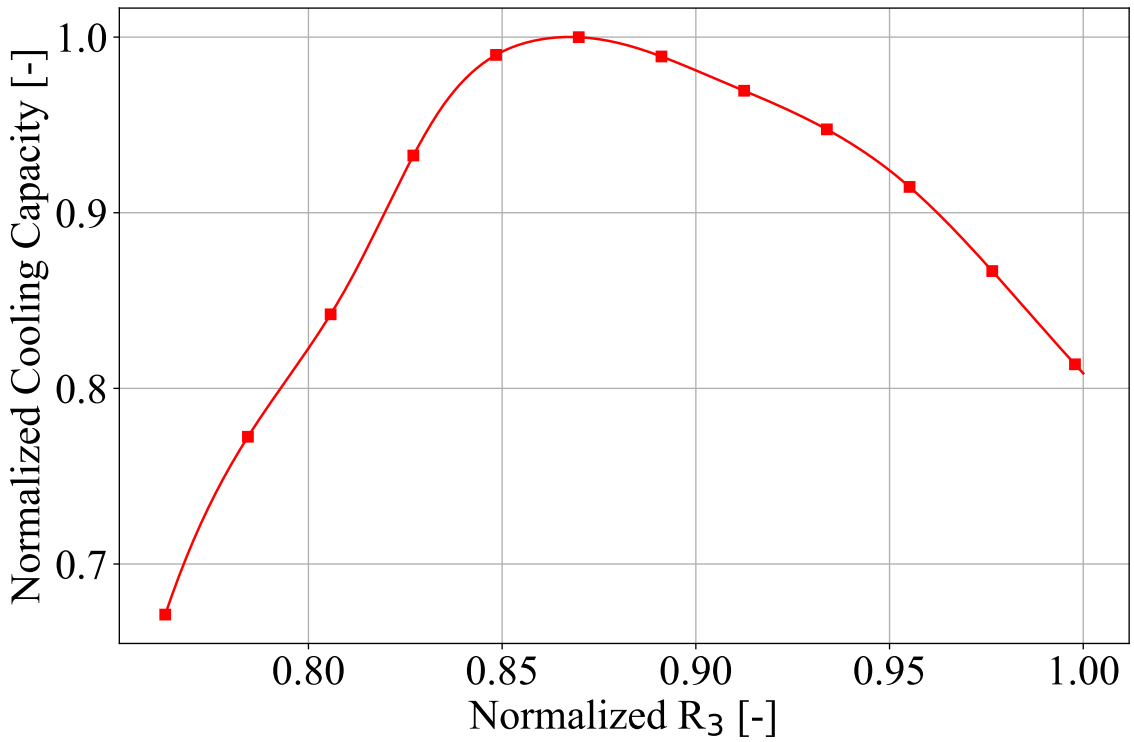

Figure 112 – Influence of the inner radius of the external cylinder (R_3) on the cooling capacity of the system.

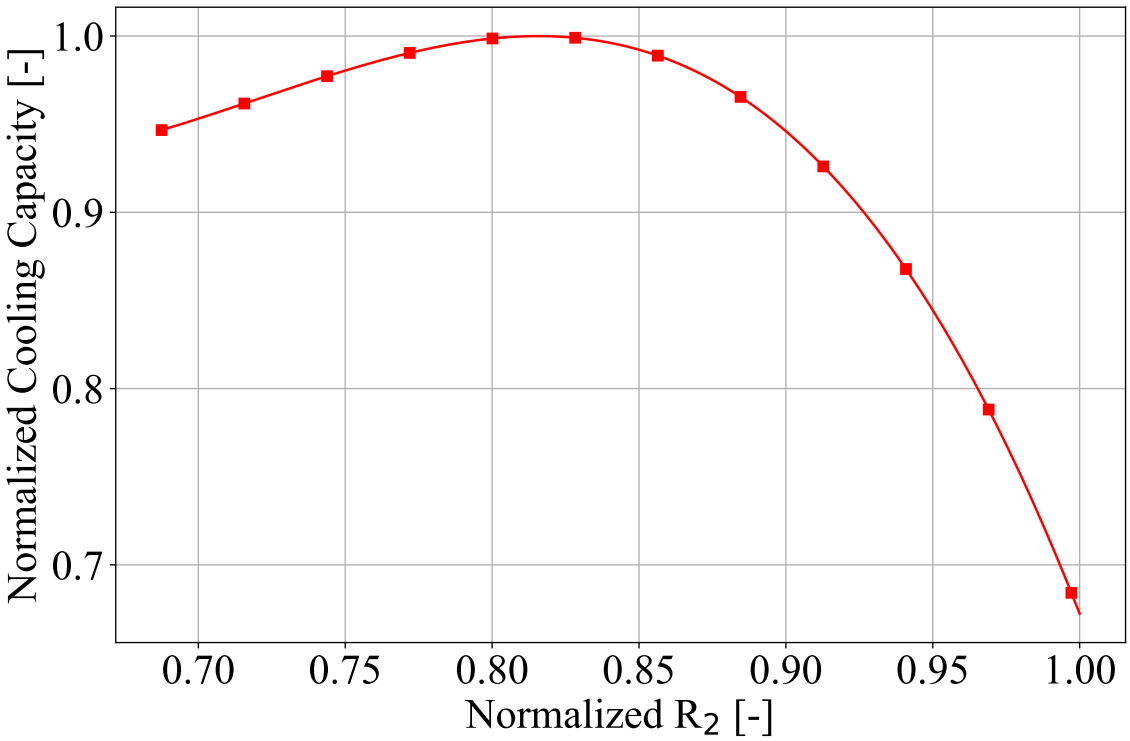

Figure 113 – Influence of the outer radius of the internal cylinder (R_2) on the cooling capacity of the system.

is defined by the angle ϕ_{magnet}, which delimits the transition point between the two materials. The influence of the value of ϕ_{magnet} on the magnetic field and, consequently, the cooling capacity, is not as straightforward as the influence of the other parameters like the radii and length. Figure 114 shows the magnetic profiles obtained by an external model for the same magnet with ϕ_{magnet} values of 30°, 40° 50° and 60° (CATTELAN, 2020). The edges and discontinuities of the profiles are numerical in origin and are not expected to exist in a profile created by a real magnet. The figure shows that reducing the value of ϕ_{magnet} initially does not significantly reduce the maximum value of B (disregarding the discontinuities), but instead reduces the high field period while increasing the low field period. While this has an effect on the cooling capacity, most of the potential loss is expected to be eliminated by adjusting the blow fractions, as shown by the results presented in Section 5.6.1. However, greater reductions in the value of ϕ_{magnet} start to also decrease the value of B_{max}, which is expected to reduce the cooling capacity in a way that cannot be compensated by adjustments in the flow profile.

To determine the influence of ϕ_{magnet} on the cooling capacity, the profiles shown in Figure 114 were smoothed and inserted into the model. Then, the fictitious regenerator was tested under the different operating conditions shown in Table 28. The instantaneous (step change) flow profile was chosen to simplify the analysis. Figure 115 shows the cooling capacity results obtained in this analysis. They show that the

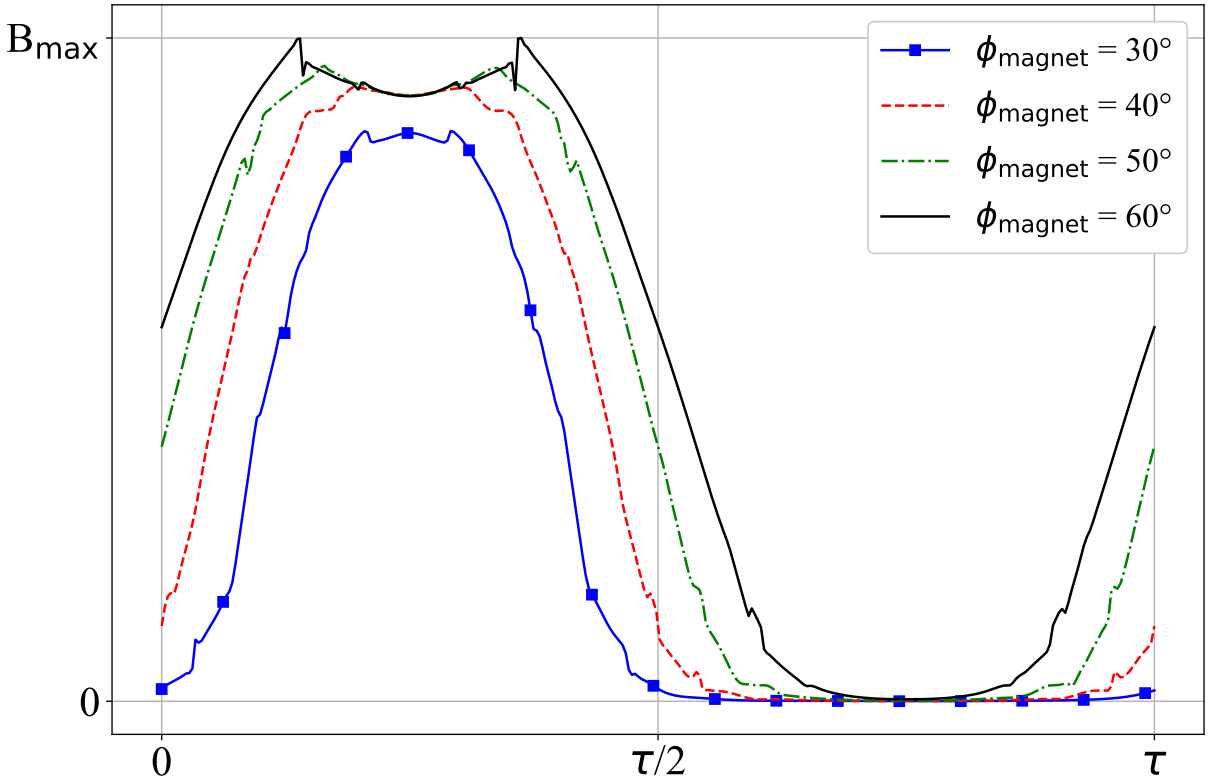

Figure 114 – Modeled applied magnetic flux density profiles created by the same magnet with different values of ϕ_{magnet}.

cooling capacity reaches its peak at ϕ_{magnet} values of 50° and 60°, has a small drop when ϕ_{magnet} reaches 40° (6.7% average) and drops considerably at 30° (32.9 % average). The cases where the cooling capacity was higher at 50° than 60° were assumed to be caused by the discontinuities seen in the 60° profile, which, when smoothed, created regions of large negative magnetic flux density variations during the high field period. However, the differences in cooling capacity at 50° and 60° were considered negligible. This is an important result because it shows that using a ϕ_{magnet} value of 40° instead of 60° will have a very small influence on the cooling capacity while reducing the magnet mass by 33 %.

Table 28 – Parameters evaluated in the magnet angle analysis.

Name	Fict. Regenerator
Mass flow rate	500 and 900 kg h^{-1}
Regenerator length	100 and 170 mm
Height	55 and 65 mm
Frequency	0.5 and 2.5 Hz
Flow profile	Instantaneous
ϕ_{magnet}	30°, 40°, 50° and 60°

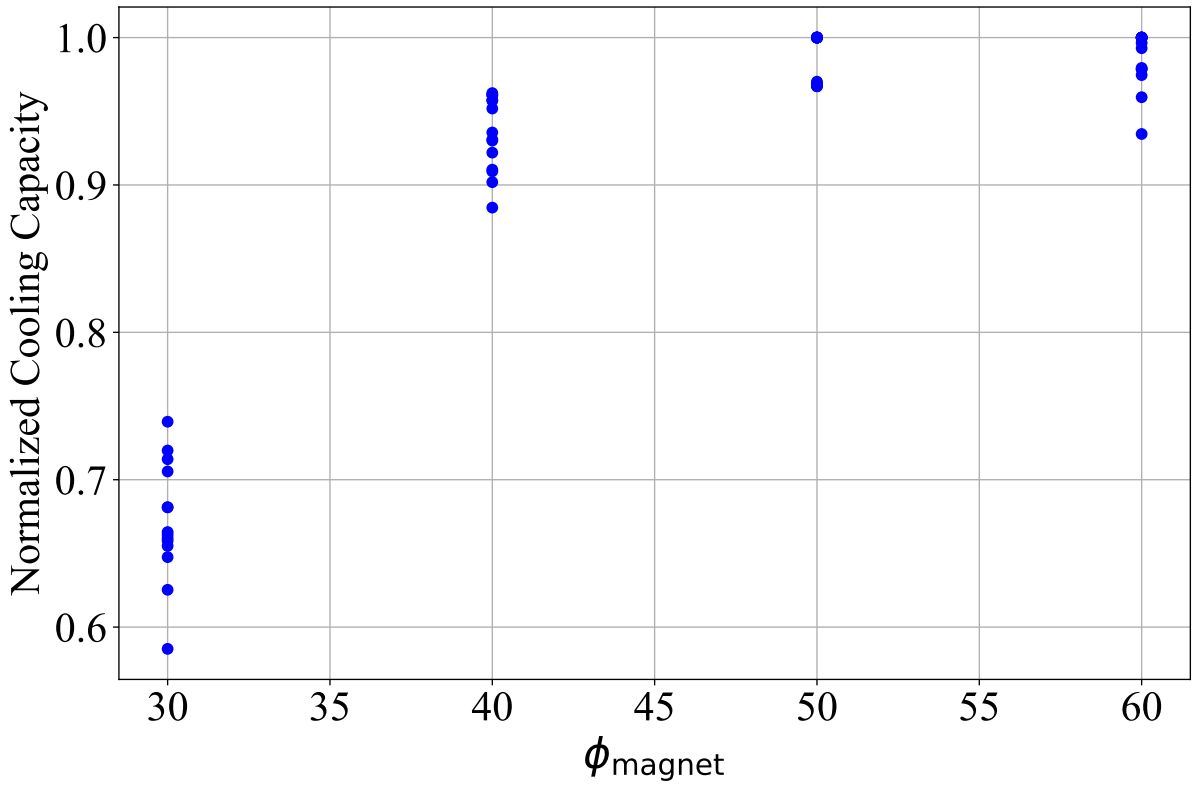

Figure 115 – Normalized cooling capacity as a function of ϕ_{magnet} for the cases shown in Table 28.

5.6.3 *Definition of the MRU Regenerator*

The results presented so far in this section provided valuable insights on how the regenerator interacts with the other systems, paving the way for the selection of the MRU regenerator. However, it did not contribute to narrow down the range of parameters associated with the design of the present MRU regenerator. To do that, the first step is to define the main requirements of the MRU regenerator, which are:

- The system should have a cooling capacity of 9000 BTU/h (approximately 2637 W). Nevertheless, values above 2500 W are considered acceptable to achieve lower costs and because, according to the Brazilian standard that can be found in Portaria... (2020), the cooling capacity of a device should reach at least 92 % of the declared value, which, for 2637 W, would be equal to 2426 W;

- The temperature span in the regenerator should be 29 K, with a hot side temperature of 316 K;

- The porous medium should be comprised of spheroidal La-Fe-Si-based particles. The particle diameter should be as small as possible;

- The material should have sufficient mechanical integrity and chemical stability to sustain multiple hours of operation;

- The proposed operating conditions, specifically mass flow rate, blow fraction and frequency, should be achievable by the hydraulic system and the unit as a whole;

- The total cost should be as low as possible, a condition which is generally achieved by minimizing the magnet mass.

Some of these requirements can be met simply by choosing the appropriate material, which, in this analysis, is the original CV-HS with a proposed epoxy concentration of 3.5 wt%. This material was originally selected because, at the time, it was believed to have the best mechanical integrity (which was proven to be false), while the epoxy concentration was deliberately chosen as a high value to guarantee mechanical integrity and potentially increase the safety of the project. The temperature span in the regenerator was determined based on the heat exchangers selected by Peixer (2020) to reach the desired temperature span between the reservoirs. The particle diameter, MCM porosity and effective porosity of the regenerator could not be modified or optimized because they were a result of the manufacturing process of the material and, therefore, were harder to control. Because of this, these parameters were estimated based on the test regenerators presented in Section 4.1 and were kept constant during the entire design process. The other parameters of the regenerator are mostly influenced by the desired cooling capacity, the temperature span and the total cost of the unit. Table 29 shows a summary of all MRU regenerator parameters, including the ones that cannot be changed and the ones that need to be determined. Besides the parameters that were already described, the table also presents the number of regenerator beds (16). The reason for this value is twofold: first, this number would require a cooling capacity of 162.5 W per regenerator bed to reach 2600 W, which was considered a realistic value to be achieved within the scope of the project, and second, the number 16 allows for a large number of different blow fractions in which a whole number of regenerators is under a blow condition at each time. For example, a blow fraction of 50% would have 8 regenerators going through the hot blow and 8 regenerators going through the cold blow, while a blow fraction of 37.5% would have 6 going through each blow and 4 at no-blow at any instant. These configurations make the control and hydraulic systems much easier to design since the end of the blow in one regenerator is always synchronized with the start of a blow in another. Lastly, the value of the void volume was going to be affected by the final shape and operating conditions of the regenerator, however, this influence is hard to quantify and correlate with the other parameters. Thus, the void volume of the experimental apparatus was scaled up to match an expected final configuration of the regenerator, resulting in a value of 5883 mm^3. This value was used

in all analyses and, to consider this hypothesis, the final regenerator was submitted to a void volume analysis, as will be shown ahead.

Table 29 – Summary of the MRU regenerator parameters.

AMR Set Parameters	**Value**
MCM porosity (ε)	0.45
Real porosity (ε_f)	0.334
Effective porosity (ε_{eff})	0.27
Particle diameter	0.65 mm
Number of regenerators	16
Material	CV-HS
Void volume	5883 mm^3
AMR Design Parameters	**Value**
Height	TBD
Width	TBD
Length	TBD
Curie temperature distribution	TBD
Layer length	Evenly distributed
Operation Parameters	**Value**
Hot reservoir temperature	316.15 K
Temperature span	29 K
Applied field profile	TBD
Blow fraction	TBD
Mass flow rate	TBD
Frequency	TBD

5.6.3.1 Definition of the Number of Layers

The number of layers of the regenerator is almost exclusively determined by the desired temperature span and manufacturing limitations. As shown in Section 5.3, increasing the number of layers may considerably increase the cooling capacity, but this effect becomes less noticeable as more layers are added. For the desired span, the increase becomes practically unnoticeable after around 18 layers. However, as mentioned in Section 5.5, there is also an expected deviation in the Curie temperature of the material of around 2 K during manufacturing. Because of that, good practices require a relative difference between two Curie temperatures in adjacent layers to be around 2 K. Thus, it was determined that the regenerator would have 15 layers, guaranteeing a high cooling capacity while also keeping the difference between the Curie temperatures of the layers at approximately 2 K. Regarding the CTDF, the results of Section 5.5 show that a value between -2 K and -3 K should be chosen in order to maximize the cooling capacity. For the MRU regenerator, a value of -2 K was chosen, mainly because it was less sensitive to negative deviations in the Curie temperature and because it tended to show better results in the layer length optimization process. The final layer distribution of the regenerator is shown in Table 30.

Table 30 – Curie temperature distribution of the MRU regenerator.

Layer	Curie Temperature [K]
1	285.15
2	287.22
3	289.29
4	291.36
5	293.44
6	295.51
7	297.58
8	299.65
9	301.72
10	303.79
11	305.86
12	307.93
13	310.00
14	312.08
15	314.15

5.6.3.2 *Definition of the Regenerator Dimensions*

The regenerator bed dimensions (height, width and length) directly affect the magnetic circuit, so a coupling between the AMR and magnet models is required. While the cross-section of a regenerator bed is treated as rectangular shaped, Figure 109 shows that it actually has the shape of a circular wedge. To account for that, the height of the bed is assumed to be the height of the wedge:

$$H_{\text{reg}} = R_3 - R_2 - 2\delta_{\text{v}} \tag{5.2}$$

while the width of the regenerator bed is corrected so that the rectangular cross-section has the same area as the circular wedge. In terms of the magnet circuit radii, this results in:

$$W_{\text{reg}} = \frac{1}{2H_{\text{reg}}}\left(\frac{2\pi}{N} - \frac{2\delta_{\text{h}}}{(R_3 + R_2)}\right)\left[(R_3 - \delta_{\text{v}})^2 - (R_2 + \delta_{\text{v}})^2\right] \tag{5.3}$$

where N is the number of regenerator beds. These equations are powerful links to integrate the regenerator to the magnetic circuit, since they relate each combination of height and width to a single corresponding combination of R_2 and R_3. The values of δ_{h} and δ_{v} were set at 4 and 3 mm, respectively to accommodate the casing and air gap between the regenerators and between the regenerators and the magnetic circuit, respectively.

The main constraint behind the design of the MRU was the required cooling capacity, while the main goal was slowly determined to be to reduce the cost in order to guarantee the feasibility of the project. Due to the size of the magnetic circuit, its mass was the parameter that most affected the cost, even though the price per

kilogram of magnetocaloric material was higher (PEIXER, 2020). However, due to manufacturing and cost limitations, the size of the regenerator must also be limited. Thus, the design process consisted of finding the regenerator which reached the desired cooling capacity (2500 W) with the smallest magnetic circuit possible, while maintaining the regenerator reasonably sized. The first step taken to find this regenerator was to run several simulations with different configurations and operating conditions in order to better understand the behaviour of the cooling capacity. Table 31 shows the intervals in which each parameter was varied during this analysis.

Table 31 – Ranges of parameters tested during the regenerator dimensions analysis.

Parameter	**Interval**
Mass flow rate	450 - 1000 kg h^{-1}
Operating frequency	1.0 - 4.0 Hz
Regenerator height	35 - 55 mm
Regenerator width	40 - 80 mm
Regenerator length	150 - 190 mm
Maximum applied magnetic flux density	1.0 - 1.3 T
Field profile	Ramp
Magnetic circuit length	190 mm
High and low field fractions	25%
Blow fraction	25% - 50%

The length of the magnetic circuit was set at 190 mm mainly for manufacturing reasons. Previous analyses showed that regenerators with less than 150 mm were not likely to reach the desired cooling capacity, thus, the magnet length needs to be larger than that. As mentioned before, the magnet is built by bonding together smaller pieces to form a circuit. Since the maximum lengths of these pieces only reached values up to 95 mm, overall magnet lengths larger than 190 mm would likely require a third magnet piece and increase the complexity of the magnetic circuit. Because of that, 190 mm was selected for it is the largest length safely achievable without increasing complexity, while also being at the top of the expected value range for the length of the regenerator, ensuring that the ratio L_{mag}/L_{reg} remains greater or equal than unity. The high and low field fractions of 25 % were selected to represent the high field fraction obtained with a magnet in which $\phi_{magnet} = 40^{o}$. The frequency and mass flow rate ranges were selected to guarantee operating conditions that were expected to be achievable by the hydraulic system.

Figure 116 shows the behaviour of the peak cooling capacity, i.e., obtained by operating at optimal values of frequency, mass flow rate and blow fraction within the given ranges, as a function of the height and width of the regenerator for three given lengths: 150, 170 and 190 mm. The maximum applied magnetic flux density in all cases was 1.0 T. The results show that the length of 170 mm requires smaller AMR cross-sections than the others in order to reach the desired cooling capacity of 2500

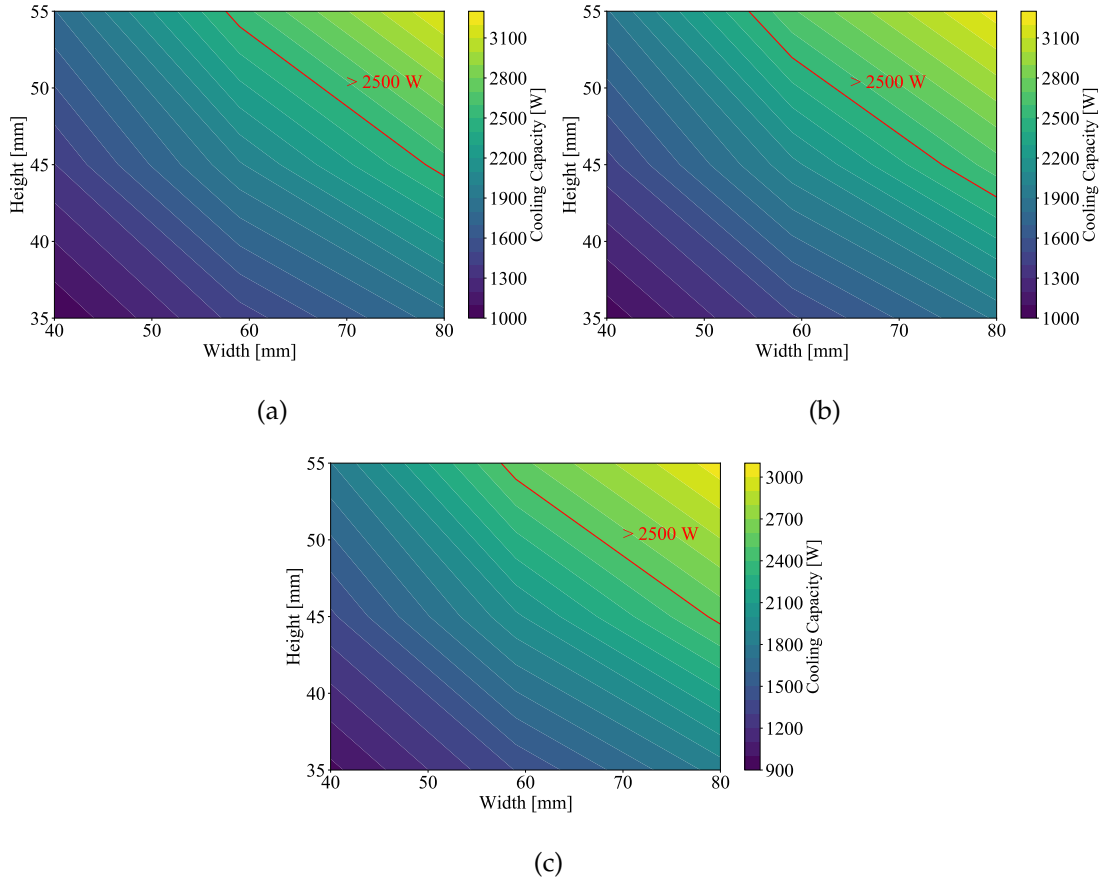

Figure 116 – Peak cooling capacity maps representing the influence of the height and width of the regenerator beds on the cooling capacity. The maximum applied magnetic flux density was 1.0 T and the length of the regenerator was (a) 150, (b) 170 and (c) 190 mm.

W, implying that 170 mm is near an optimal value. However, all cases require large regenerators to reach 2500 W, ranging from approximately 55 mm × 59 mm to 45 mm × 80 mm for the lengths of 150 and 190 mm and from 57 mm × 55 mm to 43 mm × 80 mm for the length of 170 mm. The smaller regenerator amongst these cases would have a mass of approximately 2 kg of MCM, which adds up to 32 kg when all 16 regenerators are considered.

Because of the design limitations discussed in Section 5.6.3, the best way to reduce the size of the regenerator is to increase the magnetic flux density which will indirectly increase the size of the magnetic circuit. However, as shown by the results in Figure 117, this allows much smaller regenerators to reach the desired cooling capacity, which results in smaller gaps that require smaller magnets to reach higher magnetic flux densities. Because of that, the best way to integrate the regenerator to the magnetic circuit is to determine the minimum magnetic flux density required to reach the desired cooling capacity for each regenerator configuration. Figure 118 shows these results and, as expected, smaller regenerators require larger magnetic flux densities, with the smallest ones in the tested range requiring values over 1.30 T. These results are

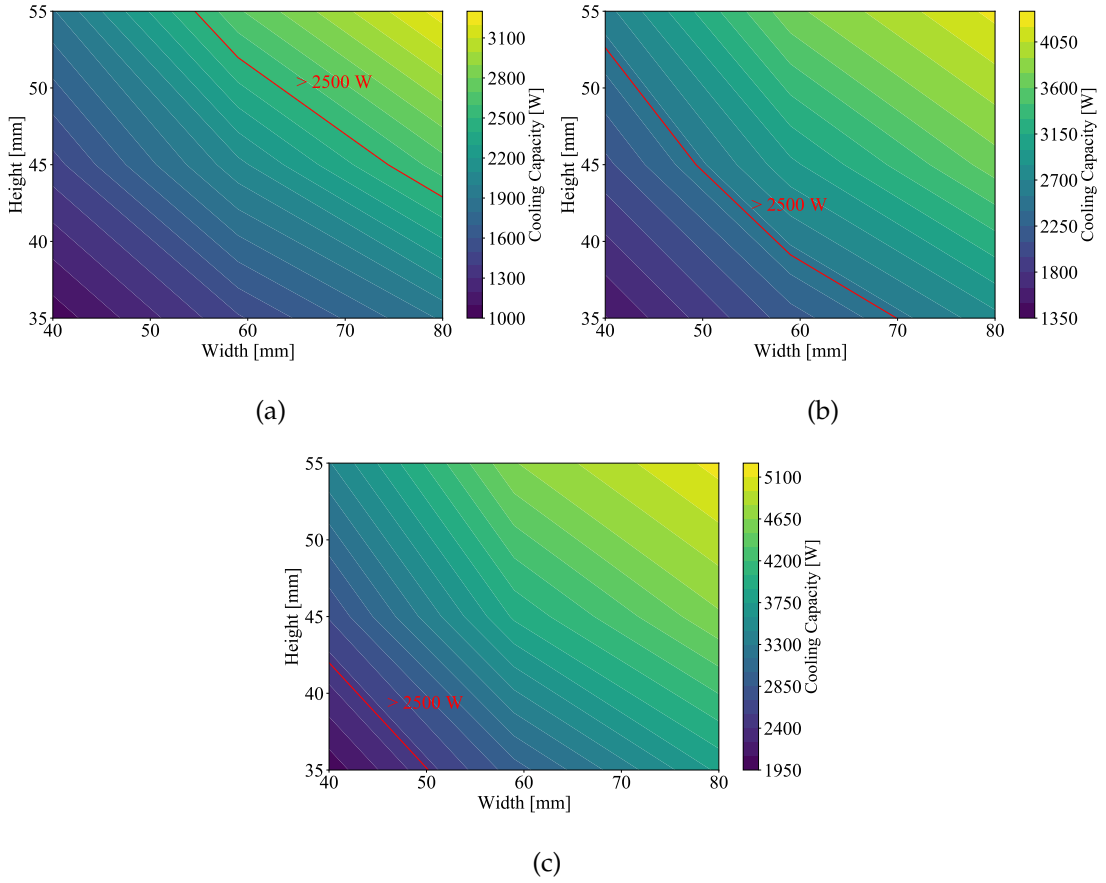

Figure 117 – Peak cooling capacity maps representing the influence of the height and width of the regenerator on the cooling capacity. The length of the regenerator was 170 mm and the maximum applied magnetic flux density was (a) 1.00, (b) 1.15 and (c) 1.30 T.

extremely important since while the height and width give the values of R_2 and R_3, the magnetic flux density allows for an estimation of R_4. Generally, higher values of magnetic flux density require larger magnets (larger differences between R_4 and R_3). However, as mentioned above, smaller gaps need smaller magnets to reach the same value of magnetic flux density resulting in a trade-off which may yield an optimal value, or range of values, for the height and width of the regenerator which minimizes the magnet mass.

The magnet is comprised of an internal and external cylinders, but only the external cylinder contains magnetic material and thus it is responsible for the largest fraction of its cost. While only part of the external cylinder contains magnetic material (determined by the value of ϕ_{magnet}), its mass is directly proportional to the volume of this cylinder, which is defined by the following expression:

$$V_{\text{magnet}} = \pi(R_4^2 - R_3^2)L_{\text{magnet}} \tag{5.4}$$

This expression shows that the volume increases with the difference between R_3 and R_4 and, for a constant difference, it also increases with the value of each radius. The value

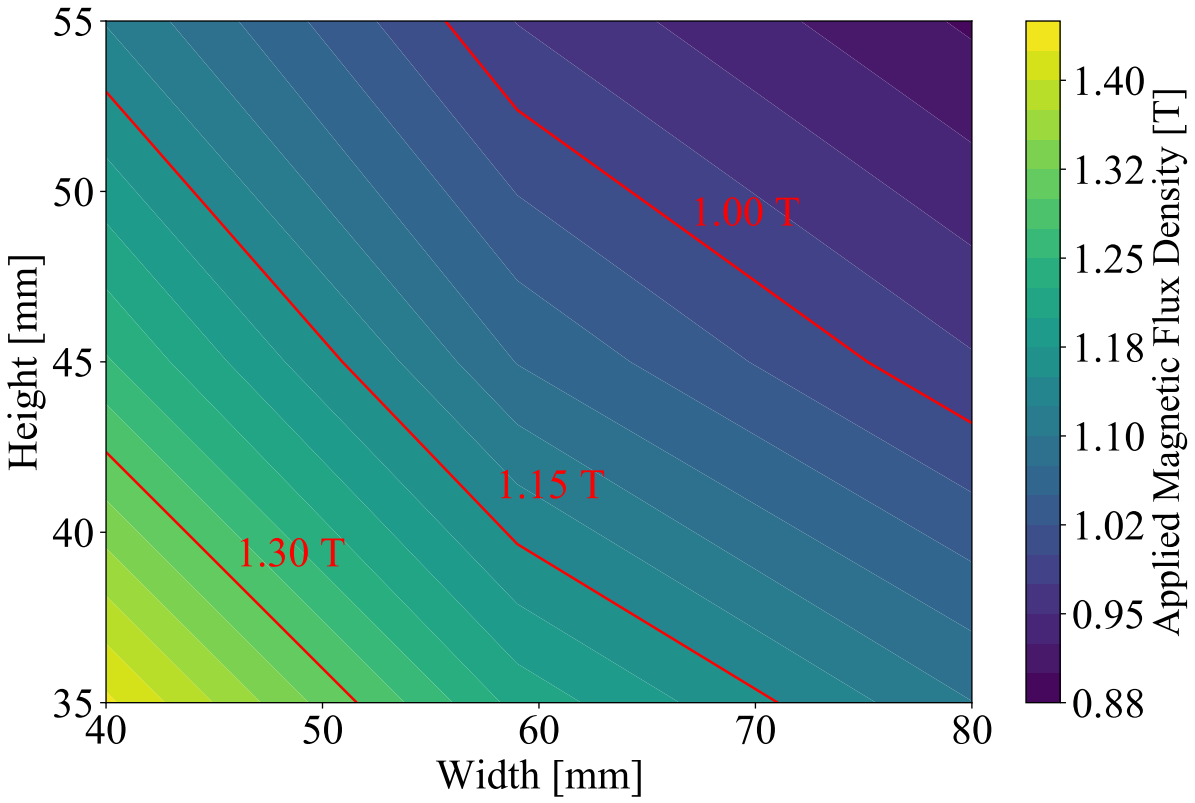

Figure 118 – Map of the estimated applied magnetic flux density required to reach a peak cooling capacity of 2500 W.

of R_3 mainly increases with the width of the regenerator. However it also increases slightly with the height. Meanwhile, the difference between R_3 and R_4 increases with the required value of the magnetic flux density. Thus, smaller regenerators need smaller values of R_3 but larger differences between R_3 and R_4 to reach higher values of magnetic flux density. On the other hand, larger regenerators need larger values of R_3, but the difference between R_3 and R_4 is expected to be much smaller. This effect is yet another trade-off between the size of the regenerator and the size of the magnetic circuit which will result in an optimal regenerator configuration. To determine this optimal configuration, Equations 5.2 and 5.3 were used to determine the values of R_2 and R_3 for all the heights and widths within the test range, while the data shown in Figure 118 were used as input to an external magnetic circuit model (CATTELAN, 2020) which estimated the value of R_4 needed to generate the desired magnetic flux density. These values were then applied to Equation 5.4 and resulted in the map shown in Figure 119. This map shows that the magnet volume, and therefore magnetic circuit cost, reaches a minimum around a 45 mm $\times$ 60 mm regenerator, with smaller heights also resulting in small magnets. It is important to note that all these tests assumed an idealized magnetic profile, which invariably increases the cooling capacity. Because of that, while the optimal region is not expected to be affected, the final volume of the magnetic circuit will be larger than the values shown in Figure 119.

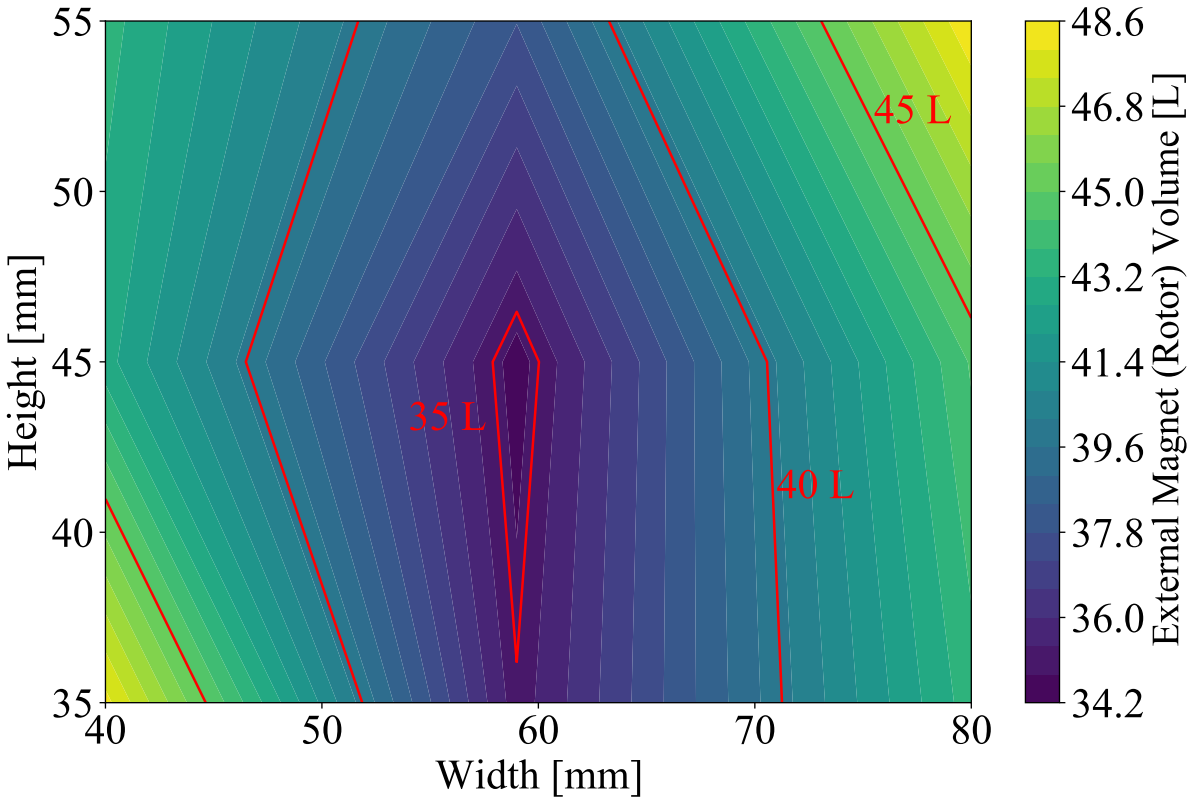

Figure 119 – Map of the estimated external magnet required to reach a peak cooling capacity of 2500 W for a 170 mm regenerator.

The data presented in Figure 119 were supplied to the semi-empirical model developed by Peixer (2020), which was also fed data from a more robust magnet model, so several simulations were run to find an optimal configuration aiming to minimize the magnet mass and reduce power consumption when possible. The final dimensions of the regenerator, as shown in Table 32, were determined to be 45 mm × 59 mm × 170 mm (height × width × length), falling precisely within the optimal range of the preliminary analysis.

Table 32 – MRU design parameters after the determination of the Curie temperature distribution and the integration with the magnetic circuit.

AMR Design Parameters	**Value**
Height	45 mm
Width	59 mm
Length	170 mm
Curie temperature distribution	-2 K, 15 layers
Layer length	Evenly distributed
Magnet Design Parameters	**Value**
R_2	135 mm
R_3	186 mm
R_4	315 mm

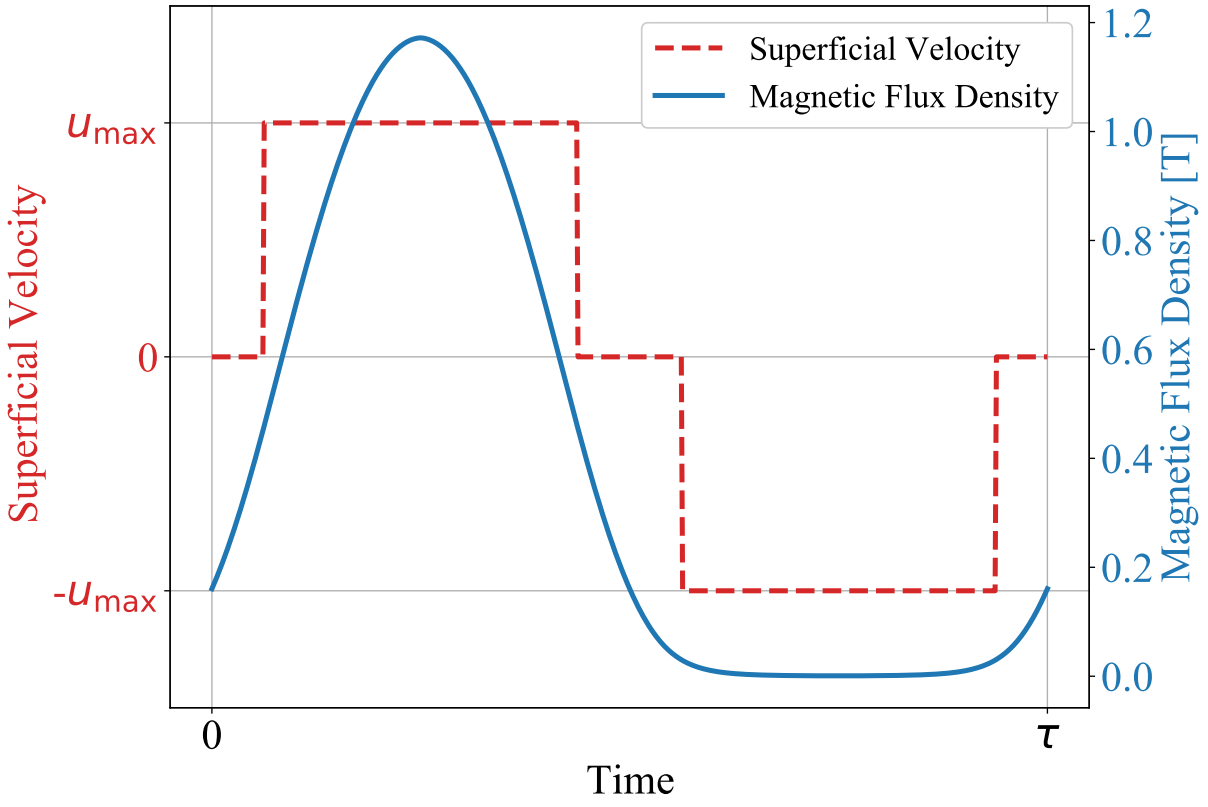

Figure 120 – Magnetic profile generated by the final magnetic circuit with a generic instantaneous blow profile (blow fraction of 37.5%) for reference.

5.6.3.3 *Definition of the Operating Parameters*

The definitions presented in the previous section, which are summarized in Table 32, can be used to determine the final applied magnetic field profile with a much higher degree of precision using a detailed model. Figure 120 shows this profile along with a generic instantaneous blow profile with a blow fraction of 37.5 % for reference. This magnetic profile, unlike the idealized ramp-like profiles, does not have an easily discernible high field fraction, but it does have a low field fraction around 37.5%, which is larger than the high field fraction. This happens as a result of the ϕ_{magnet} value of 40° and was already expected. However, this requires, once again, an ideal blow fraction and synchronization between the profiles to be determined. Due to limitations of the hydraulic system, it is not possible to have different blow fractions between the hot and cold blow and thus a single ideal blow fraction needs to be determined. Furthermore, a search needs to once again be done to determine the ideal operating conditions, namely mass flow rate and frequency, of the regenerator.

To determine these conditions, a final sweep of the operating conditions within the ranges shown in Table 33 was performed. The results, which are illustrated in Figure 121, show that the ideal blow fraction for this magnetic profile was 37.5 %, which roughly corresponds to the low field fraction and requires 6 regenerator beds

to be going through the hot blow and 6 regenerator beds to be going through the cold blow at any given time. The optimal frequency was determined to be 2.5 Hz, with higher values not greatly compromising the cooling capacity. The mass flow rate which maximized the cooling capacity in these conditions was 900 kg h^{-1}. With this, Table 29 can be completed, resulting in Table 34.

Table 33 – Interval of parameters tested during the regenerator operating conditions analysis.

Parameter	Interval
Mass flow rate	800 - 1000 kg h^{-1}
Operating frequency	1.5 - 3.5 Hz
Regenerator height	45 mm
Regenerator width	59 mm
Regenerator length	170 mm
Maximum applied magnetic flux density	1.17 T
Field profile	Figure 120
Magnetic circuit length	190 mm
High and low field fractions	Figure 120
Blow fraction	25% - 50%

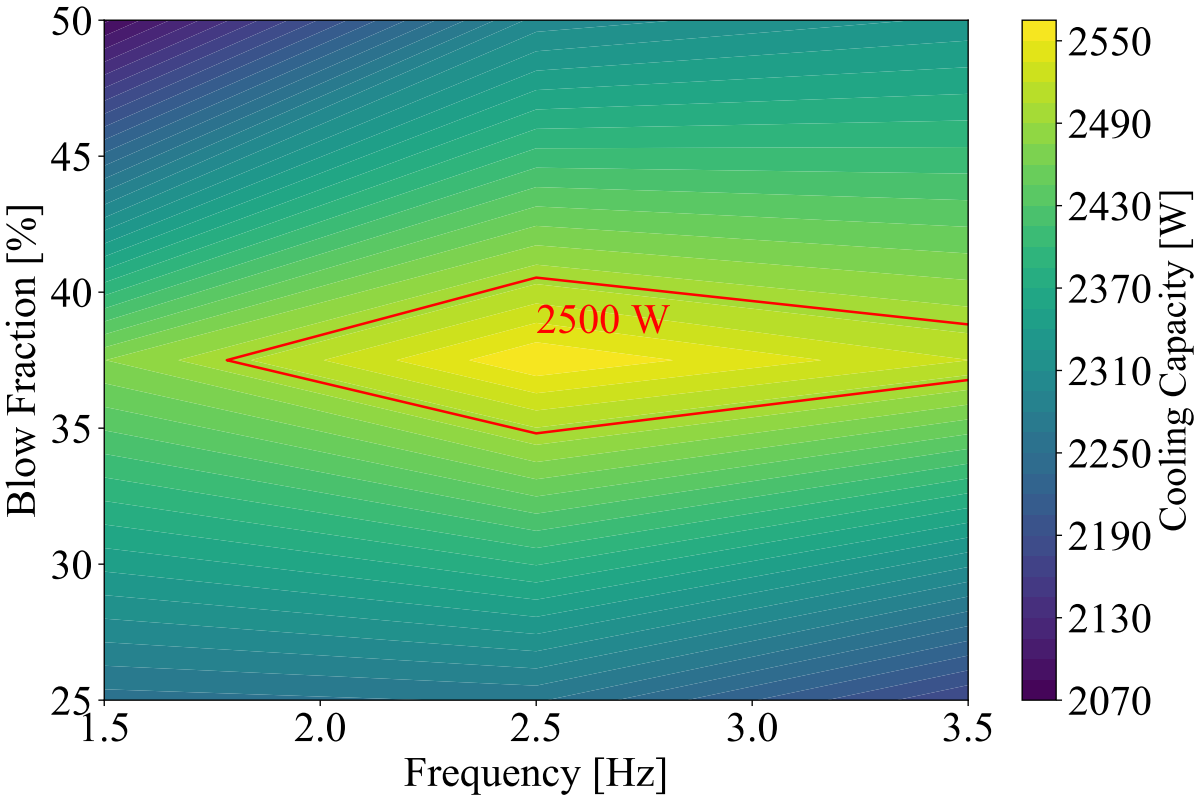

Figure 121 – Map of the peak cooling capacity obtained as a function of the operating frequency and blow fraction for the conditions shown in Table 33.

Table 34 – Summary of the final MRU regenerator parameters.

AMR Set Parameters	**Value**
MCM porosity (ε)	0.45
Real porosity (ε_f)	0.334
Effective porosity (ε_{eff})	0.27
Particle diameter	0.65 mm
Number of regenerators	16
Material	CV-HS
Void volume	5883 mm^3
AMR Design Parameters	**Value**
Height	45
Width	59
Length	170
Curie temperature distribution	-2 K, 15 layers
Layer length	Evenly distributed
Operation Parameters	**Value**
Hot reservoir temperature	316.15 K
Temperature span	29 K
Applied field profile	Figure 120
Blow fraction	37.5 %
Mass flow rate	900 kg h^{-1}
Operating frequency	2.5 Hz

The void volume analysis, which was proposed at the beginning of this section, was carried to determine the maximum acceptable void volume size for the regenerator. Figure 122 shows the results of this final analysis, with the 5883 mm^3 highlighted for reference. The results show that the cooling capacity remains above the desired 2500 W for void volume sizes up to 10000 mm^3, thus defining the maximum acceptable void volume. Conversely, reducing the void volume size from the original 5883 mm^3 does not have a great impact on the cooling capacity, making any attempt of reducing it to improve performance inconsequential. With that analysis completed, the final parameters shown in Table 34 were considered acceptable.

With the final operating conditions determined, ASCO SC8210-112 valves were selected for controlling the blows. The selection process which determined the valves can be found in Santos (2020). The flow profiles given by the valves operating at conditions similar to the ones described in Table 34 were inserted in the model, resulting in the final flow and applied magnetic flux density profiles shown in Figure 123. Due to the high frequency, the profile did not approach the ramp-like profiles shown in the previous cases. However, after proper synchronization (shown in Figure 123), the cooling capacity was estimated to be of 2535 W. This synchronization process estimated equivalent values of τ_b based on the mass of displaced fluid and matched it with the low field period of the magnetic profile, according to what was exposed in Section 5.6.1.2.

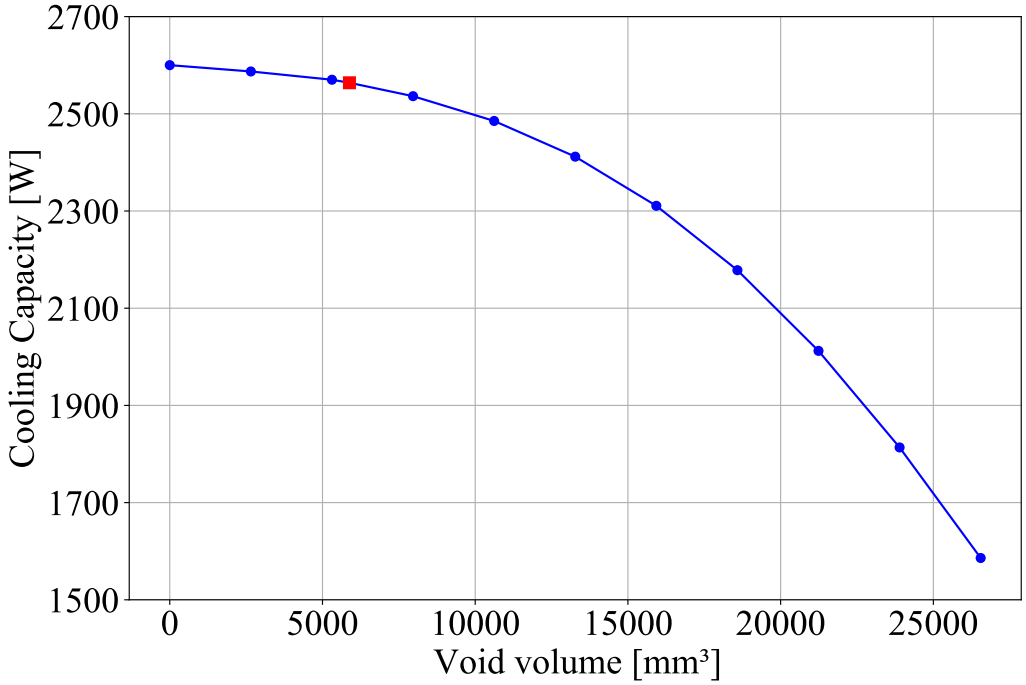

Figure 122 – Cooling capacity of the final regenerator for the expected operating conditions as a function of the void volume size. The void volume used to design the regenerator is highlighted by the red square.

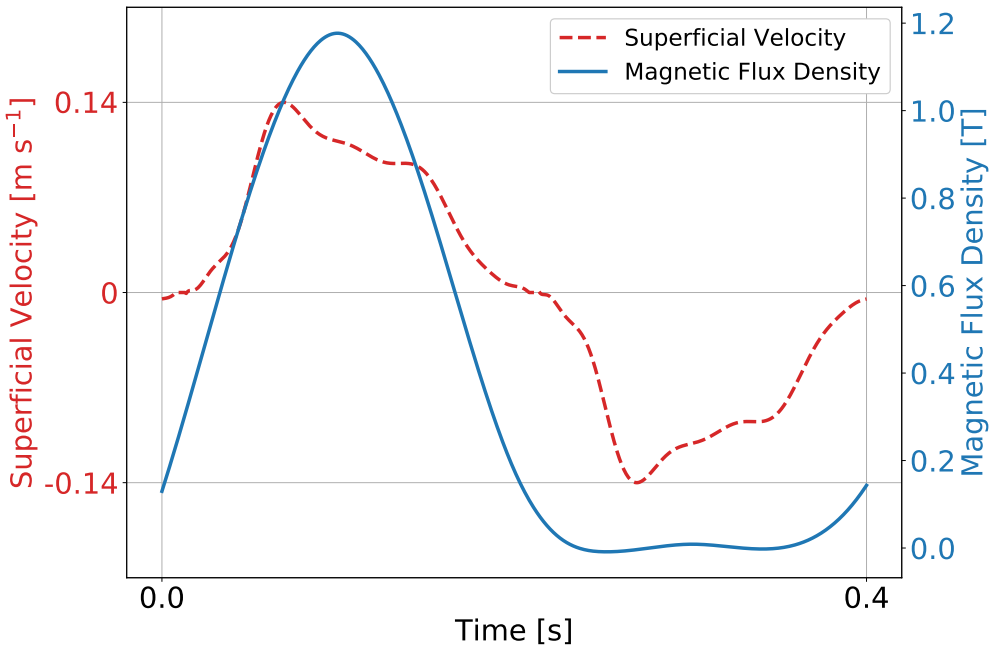

Figure 123 – Final magnetic and flow profiles of the AMR cycle.

5.7 First-Order Regenerators without Epoxy

At the final stages of the work presented in this dissertation, Vacuumschmelze was able to develop a new kind of La-Fe-Si based material, called CV-HS-2, which showed a better mechanical integrity than regular CV-HS and CV-H. This new de-

velopment raised the possibility of using a La-Fe-Si-based regenerator without the addition of epoxy. This possibility was later confirmed by the tests that will be shown in this section. As demonstrated in Section 5.2.4, the epoxy quantities normally added to the regenerator can severely compromise the resulting cooling capacity, so the prospect of a regenerator that did not need epoxy to remain mechanically intact was quite promising. Additionally, measurements of magnetic properties have shown that CV-HS-2 has a magnetocaloric effect on par with some samples of the original CV-H, albeit smaller than the average CV-H material, as shown in Section 4.1. However, DLS results showed that this material had an average particle diameter of approximately 0.75 mm (see Figure 124), which is larger than the average CV-H and CV-HS material and will negatively affect the performance if not reduced. These results indicate that, considering that smaller particle diameters are attainable, CV-HS-2 has the potential to perform better than CV-HS from the magnetocaloric point of view, requiring only confirmation of its superior mechanical integrity. With that in mind, several passive and active experimental tests were carried out on a CV-HS-2 regenerator (see Test Regenerator-3 in Section 4.1). Since this regenerator does not have epoxy in its composition and is made of a new material, a new validation had to be made in order to confirm that the model can accurately predict its performance.

5.7.1 Pressure Drop Tests Without Epoxy

The first step of the validation involves determining the effective porosity, which can be achieved through pressure drop experiments. This was once again achieved through steady flow experiments in which the pressure drop was measured as a function of the fluid flow rate, with the value of ε_{eff} being adjusted to fit the momentum equation to the results, as discussed in Section 5.1. Unlike the other regenerators, Regenerator-3 showed a considerable and consistent difference between the pressure drop of each blow, i.e., the pressure drop was dependent on the direction of the flow. In this case, the hot blow showed consistently higher pressure drops than the cold blow. This phenomenon can either be caused by the morphology of the porous medium or by an imbalance between the flows, which may remain undetected by the Coriolis effect mass flow meters. To account for that, the fitting was performed using the average pressure drop between the blows. The best agreement was found when the effective porosity was set at 0.28, with the results being shown in Figure 125. This effective porosity result is very close to the ones obtained for the regenerators with epoxy. This result is not in line with the original assumption that the epoxy was clogging the porous medium and increasing the pressure drop, since the removal of epoxy should have increased the effective porosity if that hypothesis was true. This regenerator, however, had extra polymeric grids between each layer which increased the pressure drop, but even when this effect and the effect of the empty casing pressure drop were removed,

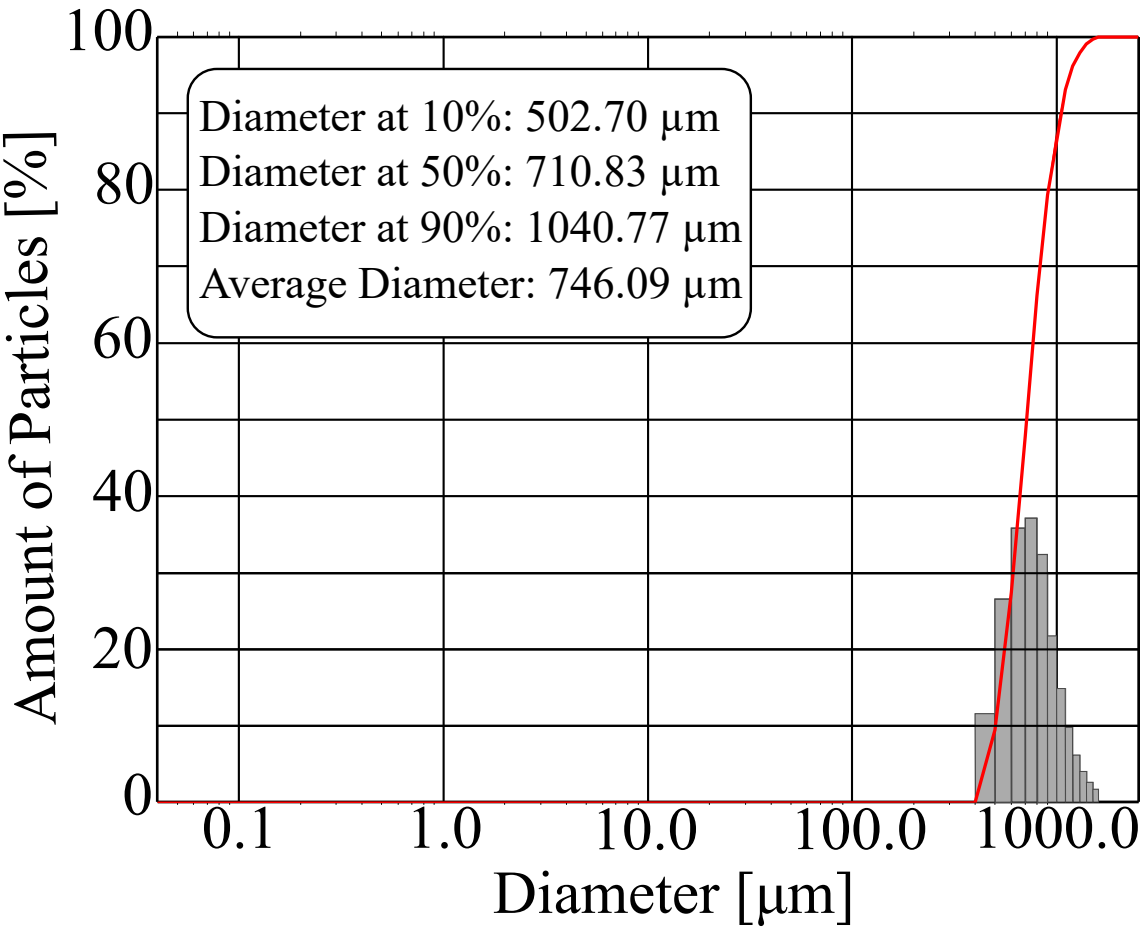

Figure 124 – DLS results for the MCM used in Regenerator-3 showing an average particle diameter of 0.746 mm. The red line indicates the cumulative amount of particles.

the effective porosity remained considerably below the real porosity which is known to be close to 0.39. Similar results with stainless steel spheres did not behave the same way, with the real porosity correctly predicting the pressure drop once all other effects were removed. Thus, the increase in pressure drop is most likely being caused by the porous medium, but further studies are needed to determine the explanation for this phenomenon. This explanation may be, but is not limited to:

- The particle size distribution of the material spans a wide range of values, which may result in a porous medium configuration that increases the pressure drop;
- The tortuosity of the porous medium, which was not considered in this analysis, may play an important role in the pressure drop;
- The assembly process of the regenerator may include processes which are unintentionally clogging part of the porous medium;
- Since there is no bonding material, the expected accommodation of the particles

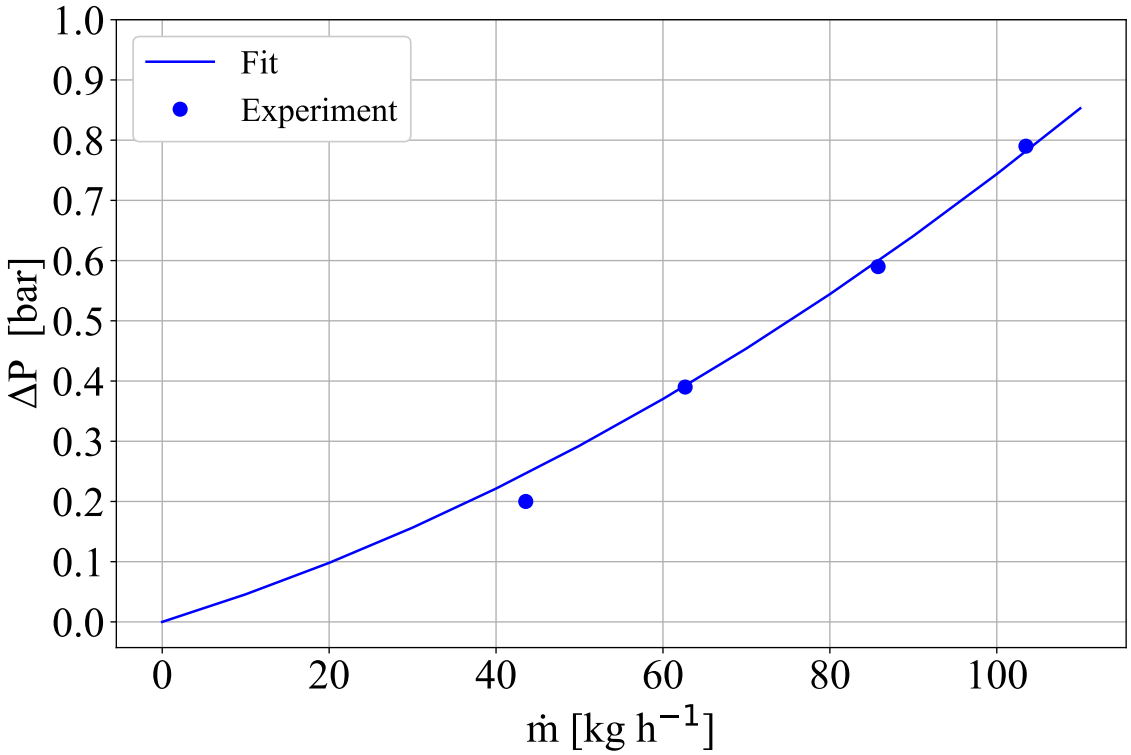

Figure 125 – Comparison between experimental and numerical results of effectiveness for the CV-HS-2 regenerator without epoxy.

within the porous medium might be clogging parts of the regenerator, increasing the pressure drop.

5.7.2 *Passive Tests Without Epoxy*

After the effective porosity was determined, passive tests were carried out to analyse if the model correctly predicted the regenerator heat transfer behaviour. Unlike previous regenerators, the effective porosity was not used in the heat transfer correlation, and no corrections were made to the heat transfer area density, which was determined using Equation 3.33. These tests are slightly different from the passive tests performed in Section 5.1, as the thermocouples that measured the temperatures at the ends of the regenerator could not be used and so the temperature was measured further down the channels, as explained at the end of Section 4.2. The distance between the ends of the regenerator and the thermocouples was determined to be 110 mm in a channel with a diameter of 4.2 mm. The model was changed accordingly to allow the calculation of a temperature profile in an equivalent position, but this added an extra uncertainty to the results. The test conditions of the passive tests are shown in Table 35.

Figures 126 and 127 show a comparison between the experimental and numerical effectiveness results for the cold and hot blows of the test regenerator operating at

Table 35 – General parameters of Regenerator-3 passive tests.

Parameter	Value
Operating frequency	0.5 and 0.75 Hz
Mass flow rate	40 to 100 kg h^{-1}
Blow fraction	37.5%
Hot side temperature	296.15 K
Temperature span	4 to 16 K
Fluid	2 % vol. ENTEK-water solution
Regenerator shape	cylinder
Regenerator length	109 mm
Regenerator diameter	24 mm
Curie temperature	278.70 K, 284.06 K, 288.88 K, 294.05 K and 300.56 K
Layer Lengths	24.8 mm, 24.8 mm, 24.8 mm, 24.8 mm and 9.8 mm
Epoxy amount	0 wt.%
Housing material	AISI 304 Stainless steel
Housing thickness	0.5 mm

0.75 Hz, using the time-dependent temperature profiles at each end of the AMR. Some aspects of the results differ from what was originally expected, namely the fact that the effectiveness does not necessarily decrease with the mass flow rate. The reasons for this phenomenon are hypothesized to be twofold: (i) the temperature profile is being measured with a thermocouple that is not directly at the end of the regenerator and thus the delay between the fluid leaving the regenerator and reaching the thermocouple affects the effectiveness results and (ii) this regenerator was the most affected by flow imbalance and slight deviations (smaller than a 0.5 kg h^{-1} difference between the blows) greatly affect the effectiveness results, especially in the numerical simulations. Because of the uncertainty of the Coriolis-effect mass flow meters, especially for high frequencies, it was impossible to determine the flow imbalance so precisely, and this was reflected in the numerical results. Despite this, there is good agreement between the results, especially for the cold blow, where only one numerical data point fell outside the uncertainty bar of the experimental result. For the hot blow, a tendency to overestimate the effectiveness is observed, especially at higher mass flow rates. Numerically, the hot blow effectiveness was observed to be affected more by imbalances which increased the mass of fluid displaced during said blow, which might indicate a tendency in the experiment flow imbalance which was not being corrected by the flow imbalance logic. This would also explain the higher pressure drop consistently observed during the hot blow.

Additionally, Figures 128 and 129 show a comparison between the numerical and experimental temperature profiles 110 mm away from the ends of the regenerator for temperature spans of 8 and 12 K. As expected from the effectiveness results, the agreement between the profiles is not as good as the agreement seen for Regenerators 2 and 3. The profile is also different from the ones seen in the passive tests of Regenerator-

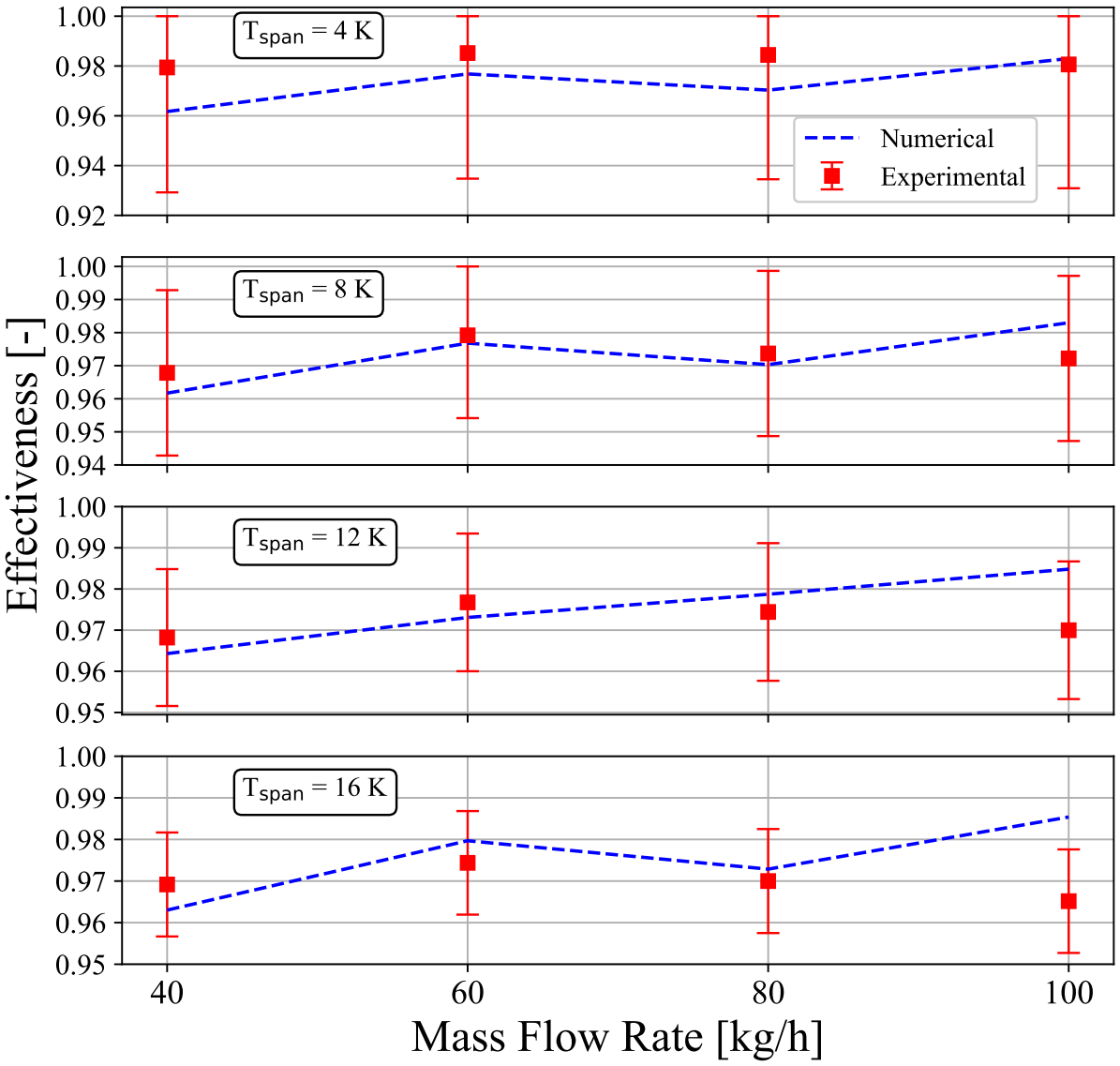

Figure 126 – Comparison between experimental and numerical results of effectiveness for Regenerator-3 during the cold blow operating at 0.75 Hz.

2 because of the thermocouple positioning: while the thermocouples near the ends of the regenerators used in the Regenerator-2 tests are affected by the inlet and outlet of the blows, the thermocouples used in the Regenerator-3 tests are only affected by the outlets. Because of that, temperature profiles for Regenerator-2 reached a constant value that corresponded to the hot or cold reservoirs temperatures, which were the temperatures of the inlets of the blows. Meanwhile, the Regenerator-3 temperature profiles reached a constant value at whatever temperature the fluid in the thermocouple had when the blow ended, since the inlet of the other blow does not flow past the thermocouple.

Furthermore, the numerical results show a small deviation in the form of a ridge for the cold side and a valley for the hot side before following the overall shape

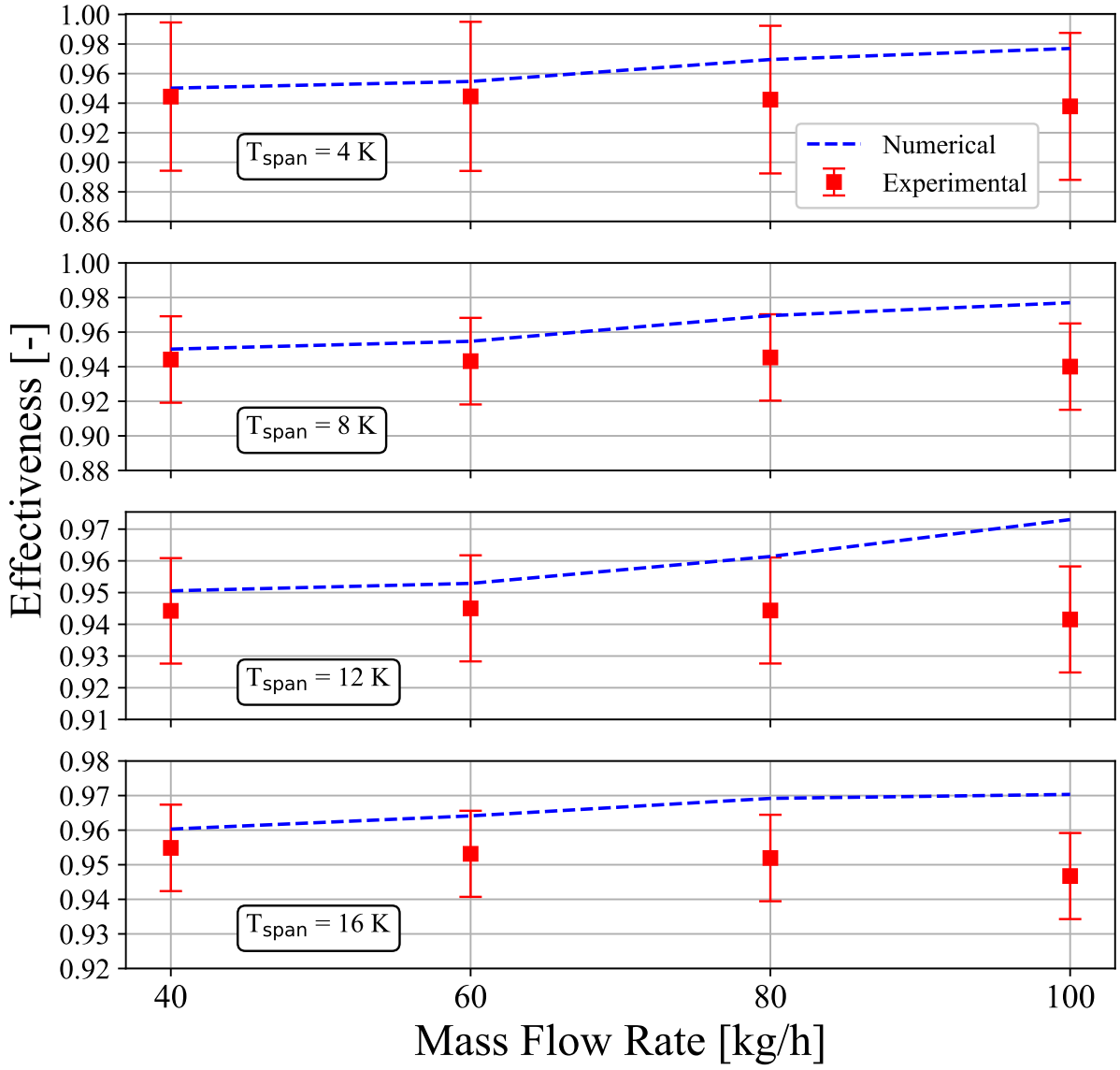

Figure 127 – Comparison between experimental and numerical results of effectiveness for Regenerator-3 during the hot blow operating at 0.75 Hz.

of the profile. This can also be seen in the experimental results, especially at lower mass flow rates. This deviation is a result of the fluid that remained in the volume between the thermocouple and the end of the regenerator during the previous blow passing around the thermocouple. Its effect is more relevant and visible at smaller mass flow rates because this volume represents a larger proportion of the volume of displaced fluid. While the model does predict this phenomenon (and its decrease with the mass flow rate), it seems to overestimate it when compared to the experimental results. The temperature profiles for the other temperature spans and the results for the tests at 0.5 Hz can be found in Appendix B.

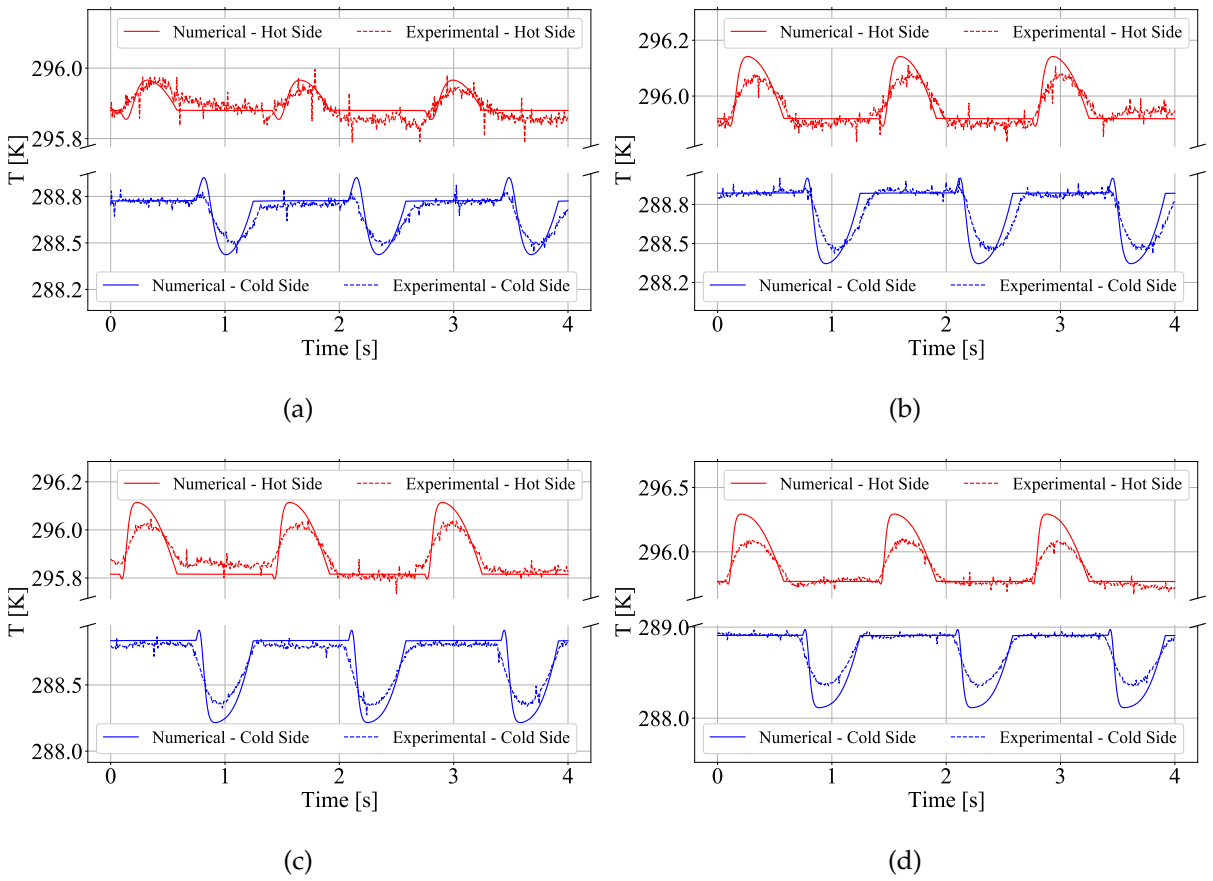

Figure 128 – Comparison between the numerical and experimental temperature profiles at approximately 110 mm from the hot and cold ends of Regenerator-3 during three cycles. The cycle frequency is 0.75 Hz, the temperature span is 8 K and the mass flow rate is (a) 40, (b) 60, (c) 80 and (d) 100 kg h^{-1}.

5.7.3 *Active Tests Without Epoxy*

Lastly, active regenerator tests were performed on the regenerator in order to determine its performance curves and compare them to the numerical results. The operating conditions were the same as the ones shown in Table 35 with the rectified cosine applied field used in the active tests of Regenerator-1. The results for 0.5 Hz and 0.75 Hz are shown in Figure 130 (a) and (b), respectively. A mass imbalance of 2% favoring the hot blow was assumed in all cases, meaning that the fluid displacement during the hot blow was 2% higher than in the cold blow. This imbalance was not observed in the experimental cases, but fell within the mass flow rate uncertainty of all of them. The numerical results under this condition were also considerably better than when considering no imbalance at all or an imbalance favoring the cold blow, which lend further strength to the hypothesis that there was a systematic imbalance favoring the hot blow, especially when allied with the higher pressure drops observed in the hot blow during testing. The numerical results showed a tendency to overestimate the cooling capacity, except for the cases operating at 0.5 Hz and 40 kg h^{-1}. The numerical results

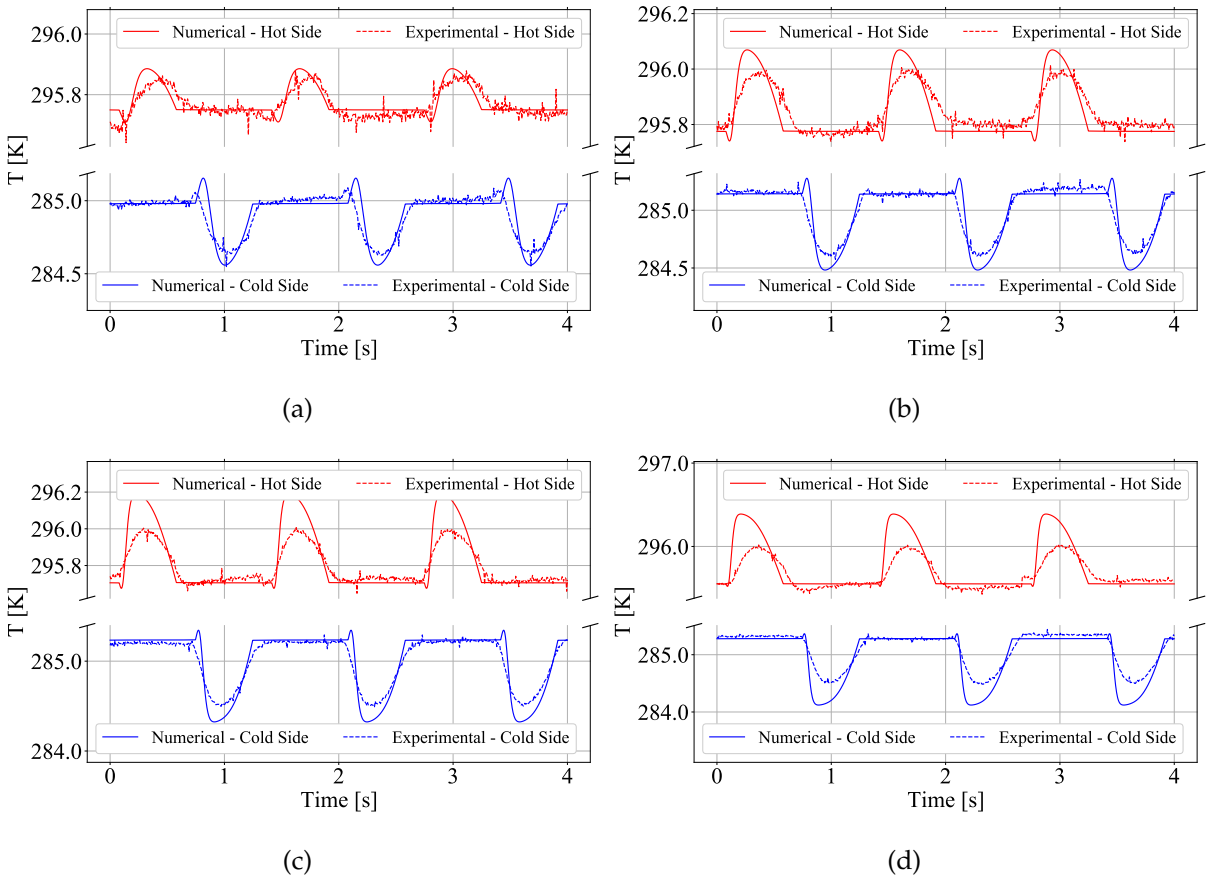

Figure 129 – Comparison between the numerical and experimental temperature profiles at approximately 110 mm from the hot and cold ends of Regenerator-3 during three cycles. The cycle frequency is 0.75 Hz, the temperature span is 12 K and the mass flow rate is (a) 40, (b) 60, (c) 80 and (d) 100 kg h^{-1}.

also showed a tendency to overestimate the maximum temperature span reached by the regenerator at 0.5 Hz which was not observed at 0.75 Hz. This happened mainly because the experimental results at 0.5 Hz reached smaller spans than at 0.75 Hz, while the numerical results reached around the same span regardless of the frequency. As mentioned in section 5.1, under normal operating conditions, the maximum temperature span for a given mass flow rate is usually determined by the span between the hot side temperature and the lowest Curie temperature, which in this case is approximately 18 K. Thus, the maximum temperature span should not be heavily influenced by the operating frequency, lending further credence to the numerical results. The mass imbalance, however, is expected to affect the maximum temperature span, indicating that the experimental results at 0.5 Hz were more affected by the imbalance than the results at 0.75 Hz.

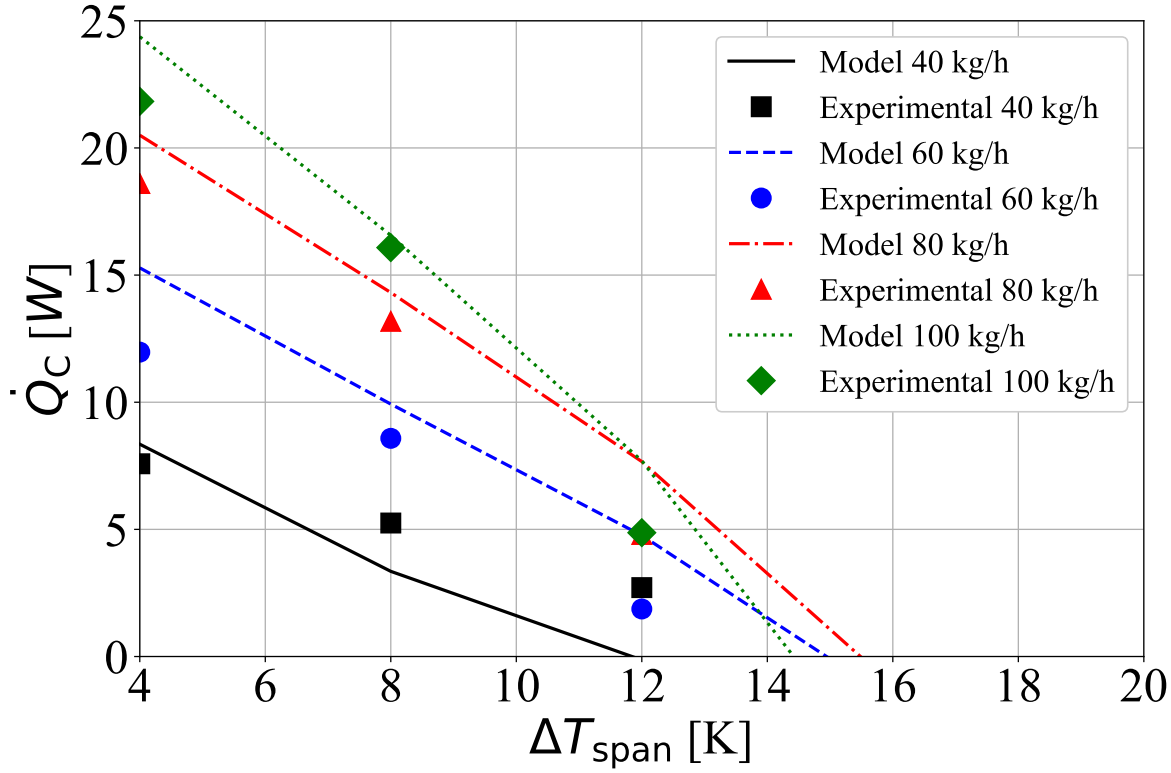

(a)

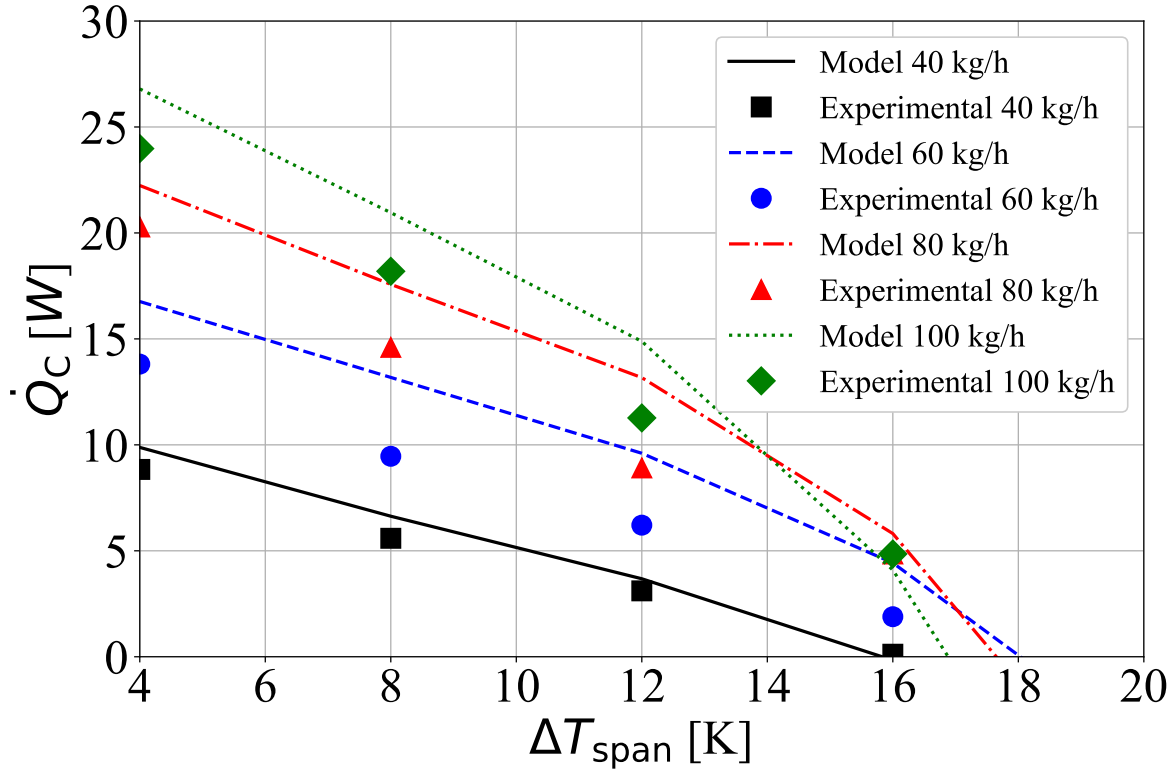

(b)

Figure 130 – Experimental and numerical cooling capacity results for the test regenerator operating at a blow fraction of 37.5 %, hot side temperature of 296.15 K, and a frequency of (a) 0.5 Hz and (b) 0.75 Hz.

5.8 MRU CV-HS-2 Regenerator Without Epoxy

The design process described in Section 5.6.3 was initially performed under a precarious assumption: that the CV-HS material would be able to withstand the stress of the AMR operation. After this was proven to be false by the tests described in Section 4.1, another precarious assumption was made: that the final material, which would have a mechanical integrity able to withstand the stress of operation, would have magnetocaloric properties similar to those of CV-HS. This was proven false by the property measurement results of CV-HS-2, which showed it had better magnetocaloric properties than CV-HS. In fact, CV-HS-2 proved to have several advantages over CV-HS, namely:

- Better magnetocaloric properties, close to those of the original CV-H;
- Better mechanical integrity, allowing it to withstand over 200 hours of operation;
- A porous medium configuration that could reach porosities under 40%, which was not possible even for CV-H regenerators;
- Ability to operate without epoxy, improving the heat exchange.

The removal of epoxy was originally expected to also decrease the pressure drop and, while this was not observed, CV-HS-2 also did not show any noticeable increase in pressure drop in relation to the other materials. The more concerning result was the particle diameter of 0.746 mm which by itself was enough to neutralize all of the previously described advantages. However, discussions with the supplier about the manufacturing process and the origin of the samples used in Regenerator-3 resulted in the conclusion that the material could be expected to reach particle diameters closer to those of CV-H and CV-HS, i.e., 0.65 mm.

In addition to this new material, modifications in the heat exchangers allowed the temperature span in the regenerator to be reduced from 29 K to 26 K, potentially allowing the reduction of the number of layers. These developments greatly increased the predicted cooling capacity of the regenerator, creating the potential to reduce its size and, consequentially, its cost, which at that point was much higher than expected. The magnet, on the other hand, had already been ordered and could not be changed, which prevented some parameters of the regenerator from being changed. The regenerator parameters that did not affect the magnetic circuit were the operating conditions (frequency, mass flow rate, blow fraction), the regenerator length and the layer distribution. Table 36 shows a summary of all the regenerator parameters which were changed with the advent of the new material, the ones that remained the same due to the limitations given by the magnetic circuit and the ones that could be changed and needed to be redesigned.

Table 36 – Summary of the CV-HS-2 regenerator parameters.

AMR Set Parameters	**Value**
MCM porosity (ε)	0.39
Real porosity (ε_f)	0.39
Effective porosity (ε_{eff})	0.28
Particle diameter	0.65 mm
Number of regenerators	16
Material	CV-HS-2
Void volume	5883 mm^3
Height	45
Width	59
AMR Design Parameters	**Value**
Length	TBD
Curie temperature distribution	-2 K, TBD layers
Layer length	Evenly distributed
Operating Parameters	**Value**
Hot reservoir temperature	316.15 K
Temperature span	26 K
Applied field profile	Figure 120
Blow fraction	TBD
Mass flow rate	TBD
Operating frequency	TBD

Because the target of this optimization was to reduce cost, the first step taken was to decrease the regenerator length, which was expected to have the greatest effect on its cost. Under the original operating conditions the new regenerator was obtaining cooling capacities around 3100 W, approximately 25% more than the required 2500 W and thus a similar, slightly larger, reduction in length was expected. A new sweep of operating conditions was done in order to determine the optimal cooling capacity for different lengths of the regenerator, with the results shown in Figure 131 (a). A length of 130 mm (reduction of 30%) was chosen as it resulted in a cooling capacity above 2700 W, which allowed for a reduction in the number of layers. Another important result of this sweep was that the optimal operating condition was very close to that of the original regenerator, and thus no great changes would need to be done to the hydraulic system. The new span of 26 K resulted in an initial estimate of 13 layers for the regenerator, but smaller values were also tested. Figure 131 (b) shows the results for the cooling capacity of the 130 mm regenerator as a function of the number of layers, keeping a CTDF of -2 K. The results showed that 12 layers were sufficient to reach a cooling capacity of 2638 W, which is nearly exactly the original target of 9000 BTU/h.

The final operating conditions and parameters of the regenerator, including its expected final cooling capacity can be found in Table 37. The required mass of each layer and their Curie temperature can be found in Table 38.

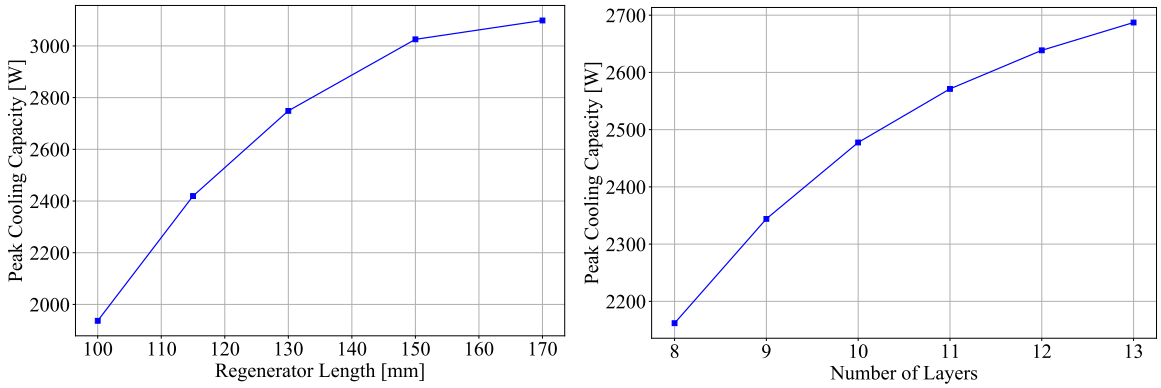

(a) (b)

Figure 131 – (a) Peak cooling capacity of the regenerator as a function of its length. (b) Cooling capacity of a 130 mm regenerator as a function of the number of layers.

Table 37 – Summary of the CV-HS-2 regenerator final parameters.

AMR Set Parameters	**Value**
MCM porosity (ε)	0.39
Real porosity (ε_f)	0.39
Effective porosity (ε_{eff})	0.28
Particle diameter	0.65 mm
Number of regenerators	16
Material	CV-HS-2
Void volume	5883 mm^3
Height	45 mm
Width	59 mm
AMR Design Parameters	**Value**
Length	130 mm
Curie temperature distribution	-2 K, 12 layers
Layer length	Evenly distributed
Operating Parameters	**Value**
Hot reservoir temperature	316.15 K
Temperature span	26 K
Applied field profile	Figure 120
Blow fraction	37.5%
Mass flow rate	800 kg h^{-1}
Operating frequency	2.5 hz
Cooling Capacity	**2638 W**

Table 38 – Final Curie temperatures and masses of the 12 layers.

Curie Temperature	Mass
288.15 K	2.02 kg
290.51 K	2.02 kg
292.88 K	2.02 kg
295.24 K	2.02 kg
297.60 K	2.02 kg
299.97 K	2.02 kg
302.33 K	2.02 kg
304.70 K	2.02 kg
307.06 K	2.02 kg
309.42 K	2.02 kg
311.79 K	2.02 kg
314.15 K	2.02 kg
Total Mass	**24.24 kg**

6 Final Remarks

This dissertation is part of a series of different works involved in a project with the ultimate goal of designing a magnetic refrigeration unit with a cooling capacity of 9000 BTU/h between 22ºC and 35ºC. This worked focused specifically on the regenerator and its integration with the other systems of the MRU. To achieve this, a numerical model was developed and adapted to represent the AMR and to allow the integration of the parameters that originated from the other systems, namely the flow and field profiles. Because the goal was to design a regenerator using first-order materials, namely La-Fe-Si alloys, thermophysical properties of these materials had to be measured and treated for proper implementation in the model. The model consisted of solving three governing equations: the momentum and energy equations of the fluid phase and the energy equation of the solid phase. The magnetocaloric effect was included in the model using the built-in method, which consists of adding an energy source term to the solid energy equation. The calculation of the MCM and other closure relationships needed to solve the equations were exposed. Two extra governing equations, which account for the casing and void volume losses, were also described along with their required closure relationships. The influence of the epoxy in the heat exchange was described along with the simplifying assumptions involved. The solution method consisted of applying the finite volume method to all governing equations except the fluid momentum equation, which was solved directly. For the interpolation of the temperature values, the Weighted Upstream Differencing Scheme (WUDS) was used. The integration process and resulting coefficients of all the equations were presented, along with the boundary conditions. A mesh analysis to determine the required temporal and spatial meshes was carried out and it was concluded that, to estimate the cooling capacity, temporal and spatial meshes of 640 elements were considered converged. For the energy balance, however, more refined meshes were required.

The model was initially validated through experimental tests of two first-order regenerators bonded with epoxy which were submitted to pressure drop, passive and active tests in the experimental apparatus described in Chapter 4. These tests also showed that two of the materials that were tested, CV-H and CV-HS, did not meet the required mechanical integrity to sustain several hours of operation expected from the MRU. During the pressure drop tests, it was observed that both epoxy bonded regenerators showed a higher pressure drop than expected when considering their measured porosities and particle diameters. It was hypothesized that this phenomenon was being caused by the epoxy, which was clogging the porous medium and hampering the fluid flow through it. This phenomenon was included in the model through a new porosity, named effective porosity, which was estimated through unidirectional

pressure drop tests and was meant to represent the actual pore network volume through which the fluid was able to flow. Once this porosity was included, the agreement between the experimental and numerical pressure drops was considered satisfactory, and thus this method was cemented in the model. Passive tests were performed on one of the regenerators, which were used to determine the best interstitial heat transfer correlation for the model. The agreement between the results was evaluated through the effectiveness and the temperature profiles at the ends of the regenerators. The correlation proposed by Pallares & Grau (2010) was determined to best represent the experimental results and was used in the model. Active tests were done to the other regenerator to determine its performance. Chronologically, these tests were done before the passive tests, but the interstitial heat transfer correlation used was the same. The comparison between the model and the experiments was done in terms of the cooling capacity results and temperature profiles at the ends of the regenerator.

Using the model, a description of the basic operating parameters of the regenerator was made. These consisted of the intrinsic parameters of the regenerator that could not be designed due to manufacturing limitations, e.g., the porosity, particle diameter and epoxy concentration and operating parameters that could be changed during operation, namely the mass flow rate and frequency. The former parameters had their influence in the cooling capacity described to illustrate what could be improved if substantial changes in the manufacturing process were effected, but ultimately these changes could not be done, and these parameters had little influence in the design process since their values were fixed. The latter parameters (operating frequency and mass flow rate) were described to expose the concept of peak cooling capacity, which would repeatedly be used in the design process. The influence of the Curie temperature distribution and number of layers was subsequently described, an analysis which would then be used to determine the layer configuration of the final regenerator. Next, the influence of the void volume was presented, with a special emphasis on how its losses behave and how to minimize them. Lastly in these sections, the matter of deviations in the Curie temperature of the materials during manufacture was addressed. Depending on the deviations, this phenomenon could considerably reduce the regenerator performance and thus a process of optimizing the length of the layers for a given set of Curie temperatures was proposed in order to minimize this performance reduction.

To start the design of the regenerator, the influence of the relation between the field and flow profiles in the cooling capacity was analysed. This study aimed to determine the ideal ratio between the periods of the profiles and the ideal synchronization between them that would maximize cooling capacity. At the end, guidelines for the valve selection were proposed considering the results that were obtained. Next, the relation between the shape of the regenerator and the shape of the magnet was analysed. This section focused mainly on the relation between the cooling capacity and the magnet mass, which was one of the most important aspects of the project due to

its cost. Next, the requirements of the MRU regenerator were exposed, with the target cooling capacity being reduced from 2637 W to 2500 W due to costs. A brief analysis of the set (unalterable) parameters of the regenerator was done to justify why these were not included in the design process, but were instead kept fixed during the entire analysis. The selection of the material was also discussed, with CV-HS being chosen as the reference material for the design process. This was done because, at the time, the material had not yet been tested, but CV-H had already been determined to not have the required mechanical integrity. This was followed by the selection of the number of layers and Curie temperature distribution, which relied heavily on the analysis that was described previously. The selection of the regenerators dimensions was then discussed, and it was determined that dimensions around 45 mm × 60 mm × 170 mm minimized the magnet mass, which was the main criterion for the selection of the regenerator. Lastly, the optimal operating parameters were determined and the void volume analysis was described. The valves of the hydraulic system were selected and the model was run using the final magnetic and hydraulic profiles, predicting a final cooling capacity of 2535 W.

After this process, it was determined that CV-HS would not be able to withstand the stress required to operate under the AMR cycle and another material, CV-HS-2, was developed. Its magnetocaloric properties were determined to be better than those of CV-HS, which could allow for a reduction of the regenerator mass. Furthermore, it was expected to have sufficient mechanical integrity to not require epoxy in its assembly. A regenerator of this material was then tested and its pressure drop tests showed the same increased pressure drop observed in the previous regenerators. This meant that the epoxy clogging hypothesis was at least incomplete, and the model continued to use an effective porosity to account for this phenomenon. The regenerator was then submitted to passive and active tests, and the agreement between the numerical and experimental results were satisfactory, but not as good as the ones obtained for the previous regenerators. However, this could be attributed to the extra uncertainties in these tests due to mass imbalances and a new positioning of thermocouples. This material showed no signs of degradation after over 200 hours of operation and was thus selected to be used in the MRU regenerator. The model was then used to try and reduce the size of the regenerator through the use of this better material, but options were limited because the magnet was already being manufactured. This reduction was then translated into a smaller length and a smaller number of layers, which was also possible because of a reduction of 3 K in the temperature span. The final regenerator was changed so as to have a length of 130 mm (versus the original 170 mm) and 12 layers instead of 15 and is expected to reach precisely 9000 BTU/h.

6.1 Recommendations for Future Work

Considering the advancements and conclusions reached in this work, and analysing what has yet to be improved in this work and in magnetic refrigeration in general, the following recommendations for future works are proposed:

- To manufacture and test the regenerator within the system that was designed in this work and guarantee a complete validation under the expected operating conditions. While the validation process was an integral part of this work, there might be unpredictable consequences of operating at high cooling capacities which were not observed in the smaller scale tests;
- To design similar systems focusing on other design metrics, namely COP and pressure drop, instead of cooling capacity;
- To run more tests using CV-HS-2 regenerators without epoxy and perform further testing of the porous medium to determine the origin of the increase in pressure drop and add it to the model;
- To develop new methods of interpolating the measured properties of magnetocaloric materials for different fields which are more reliable and better represent the data for all cases;
- To test other, non-La-Fe-Si based first-order magnetocaloric materials and compare their performance results with the ones obtained using La-Fe-Si alloys;
- To develop new magnetocaloric materials which have better mechanical integrity and magnetocaloric properties. While there are many aspects that can still be improved in magnetic refrigeration, today the materials cost and performance are one of the main factors preventing the technology from reaching widespread use;
- To analyse and design a similar regenerator using different porous media configurations, namely micro channels, which are increasingly gaining prominence in the field;
- To expand the layer length optimization method, which is currently being used only to compensate deviations in the manufacturing process, in order to use it to increase the cooling capacity and performance in general;
- To develop a more detailed model of the porous medium in order to better describe the phenomena observed in this work, including an option to consider the fluid trapped inside the clogging as part of the solid phase.

Bibliography

ACKERMAN, R. A. *Cryogenic Regenerative Heat Exchangers*. [S.l.]: New York: Plenum Press, 1997.

AHARONI, A. Demagnetizing factors for retangular ferromagnetic prisms. *Journal of Applied Physics*, v. 93, p. 3432–3434, 1998.

APREA, C.; GRECO, A.; MIORINO, A.; C., M. A comparison between rare earth and transition metals working as magnetic materials in an amr refrigerator in the room temperature range. *Applied Thermal Engineering*, v. 91, p. 767–777, 2015.

ARNOLD, D. S.; TURA, A.; RUEBSAAT-TROTT, A.; ROWE, A. Design improvements of a permanent magnet active magnetic refrigerator. *International Journal of Refrigeration*, v. 37, p. 99–105, 2014.

BAHL, C. R. H.; NIELSE, K. k. The effect of demagnetization on the magnetocaloric properties of gadolinium. *Journal of Applied Physics*, v. 105, 2009.

Barbosa Jr., J. R.; LOZANO, J.; TREVIZOLI, P. Magnetocaloric refrigeration research at the inct in cooling and thermophysics. In: *Proceedings of the ENCIT 2014*. [S.l.: s.n.], 2014.

BARCLAY, J. A.; STEYERT, W. A. Patent, *Active Magnetic Regenerator*. 1982.

BASSO, V.; KüPFERLING, M.; CURCIO, C.; BENNATI, C.; BARCZA, A.; KATTER, M.; BRATKO, M.; LOVELL, E.; TURCAUD, J.; COHEN, L. Specific heat and entropy change at the first order phase transition of La(Fe-Mn-Se)$_{13}$-H compounds. *Journal of Applied Physics*, v. 118, 2015. Disponível em: ⟨http://dx.doi.org/10.1063/1.4928086⟩.

BASSO, V.; SASSO, C. P.; KÜPFERLING, M. A Peltier cells differential calorimeter with kinetic correction for the measurement of $c_p(H,T)$ and $\Delta s(H,T)$ of magnetocaloric materials. *The Review of scientific instruments*, v. 81, n. 11, p. 113904, 2010.

BERGMAN, T. L.; LAVINE, A. S.; INCROPERA, F. P.; DEWITT, D. P. *Fundamentals of Heat and Mass Transfer*. 7. ed. [S.l.]: John Wiley & Sons, 2011.

BEZ, H. N. *Magnetocaloric materials and first order phase transitions*. Tese (Doutorado) — Technical University of Denmark, 2016.

BEZ, H. N.; NAKASHIMA, A. T. D.; LANG, G. B.; LIMA, B. S.; MACHADO, A. J. S.; LOZANO, J. A.; BARBOSA JR., J. R. Performance assessment and layer fraction optimization of gd-y multilayer regenerators for near room-temperature magnetic cooling. *International Journal of Air-Conditioning and Refrigeration*, v. 28, 2020.

BEZ, H. N.; NAVICKAITĖ, K.; LEI, T.; ENGELBRECHT, K.; BARCZA, A.; BAHL, C. R. H. Epoxy bonded La(Fe,Mn,Si)$_{13}$H$_z$ as a multi layered active magnetic regenerator. In: *Seventh IIF-IIR International Conference on Magnetic Refrigeration at Room Temperature, Thermag VII*. [S.l.: s.n.], 2016.

BJøRK, R.; BAHL, C. R. H.; INSINGA, A. R. Topology optimized permanent magnet systems. v. 437, p. 78–85, 2017.

BJøRK, R.; BAHL, C. R. H.; KATTER, M. Magnetocaloric properties of $LaFe_{13-x-y}Co_xSi_y$ and commercial grade gd. *Journal of Magnetism and Magnetic Materials*, v. 322, p. 3882–3888, 2010.

BJøRK, R.; BAHL, C. R. H.; SMITH, A.; PRYDS, N. Optimization and improvement of halbach cylinder design. *Journal of Applied Physics*, v. 104, 2008.

BJøRK, R.; BAHL, C. R. H.; SMITH, A.; CHRISTENSEN, D. V.; PRYDS, N. An optimized magnet for magnetic refrigeration. *Journal of Magnetism and Magnetic Materials*, v. 322, p. 3324–3328, 2010.

BOUCHARD, J.; NESREDDINE, H.; GALANIS, N. Model of a porous regenerator used for magnetic refrigeration at room temperature. *International Journal of Heat and Mass Transfer*, v. 52, p. 1223–1229, 2009.

BOUCHEKARA, H. R. E. H.; KEDOUS-LEBOUC, A.; YONNET, J. P.; CHILLET, C. Multiobjective optimization of amr systems. *International Journal of Refrigeration*, v. 37, p. 63–71, 2014.

BROWN, G. V. Magnetic heat pumping near room temperature. *Journal of Applied Physics*, v. 47, p. 3673–3680, 1976.

CATTELAN, L. F. P. *Design and Optimization of Magnetic Circuits for applications in refrigeration using COMSOL Multiphysics*. 2020. Personal Communication.

COEY, J. M. D. *Magnetism and magnetic materials*. [S.l.]: Cambridge University Press, 2010.

dos Santos, D.; DUTRA, S. L.; do Rosário, G. N.; SILVA, M. C. R.; RIBEIRO, M. C.; LORENZONI, A. M.; PEIXER, G. F.; CADENA, J. A. L.; BARBOSA JR., J. R. Design and experimental validation of a fluid flow management system based on solenoid valves for a large magnetic refrigerator. In: *18th Brazilian Congress of Thermal Sciences and Engineering*. [S.l.: s.n.], 2020.

DRAGUTINOVIC, G. D.; BACLIC, B. S. *Operation of Counterflow Regenerations, Computational Mechanics publications*. [S.l.]: Billerica, 1998.

DUTRA, S. L.; NAKASHIMA, A. T. D.; HOFFMANN, G.; LOZANO, J. A.; BARBOSA JR., J. R. Using electrovalves as a flow distribution system for an active magneticregenerator. In: *24th ABCM International Congress of Mechanical Engineering (COBEM)*. [S.l.: s.n.], 2017.

ENGELBRECHT, K. *A numerical model of an active magnetic regenerator refrigerator refrigeration system*. Dissertação (Mestrado) — University of Wisconsin-Madison, 2004.

ENGELBRECHT, K. *A numerical model of an active magnetic regenerator refrigerator with experimental validation*. Tese (Doutorado) — University of Wisconsin-Madison, 2008.

ENGELBRECHT, K.; TUŠEK, J.; ERIKSEN, D.; LEI, T.; LEE, C. Y.; PRYDS, N. A regenerative elastocaloric device: experimental results. *Journal of Physics D: Applied Physics*, v. 50, 2017.

ENGELBRECTH, K.; ERIKSEN, D.; BAHL, C. R. H.; BJØRK, R.; GEYTI, J.; LOZANO, J. A.; NIELSEN, K. K.; SAXILD, F.; SMITH, A.; PRYDS, N. Experimental results for a novel rotary active magnetic regenerator. *International Journal of Refrigeration*, v. 35, p. 1498–1505, 2012.

ERGUN, S. Fluid flow through packed collumn. *Chemical Engineering Progress*, v. 48, p. 89–94, 1952.

FORTKAMP, F. P.; LANG, G. B.; LOZANO, J. A.; BARBOSA JR., J. R. Design trade-offs for an active magnetic regenerator device. *Applied Thermal Engineering*, v. 165, 2020.

FORTKAMP, F. P.; LOZANO, J. A.; Barbosa Jr., J. R. Analytical solution of concentric two-pole halbach cylinders as apreliminary design tool for magnetic refrigeration systems. *Journal of Magnetism and Magnetic Materials*, v. 444, 2017.

FRANCO, V.; BLáZQUEZ, J.; INGALE, B.; CONDE, A. The magnetocaloric effect and magnetic refrigeration near room temperature: materials and models. *Annual Review of Materials Research*, v. 42, p. 305–342, 2012.

GANJEHSARABI, H.; DINCER, I.; GUNGOR, A. Analysis and optimisation of a cascade active magnetice regenerative refrigeration system. *International Journal of Exergy*, v. 19, p. 143–160, 2016.

GRECO, A.; APREA, C.; MAIORINO, A.; MASSELLI, C. A review of the state of the art of solid-state caloric cooling processes at room-temperature before 2019. *International Journal of Refrigeration*, v. 106, p. 66–88, 2019.

GSCHNEIDNER, K. A.; PECHARSKY, V. K. Thirty years of near room temperature magnetic cooling: Where we are today and future prospects. *International Journal of Refrigeration*, v. 31, p. 945–961, 2008.

GUNN, D. J. Transfer of heat or mass to particles in fixed and fluidised beds. *International Journal of Heat and Mass Transfer*, v. 21, p. 467–476, 1978.

HADLEY, G. R. Thermal conductivity of packed metal powders. *International Journal of Heat and Mass Transfer*, v. 29, p. 909–920, 1986.

HAUSEN, H. *Heat Transfer in Counterflow, Parallel-Flow and Cross-Flow*. [S.l.]: New York: McGraw-Hill Co., 1983.

HE, J.; CHEN, J.; WU, C. The influence of heat-transfer laws on the performance of a magnetic stirling refrigeration cycle. *International Journal of Ambient Energy*, v. 24, p. 75–82, 2003.

HOFFMANN, G. *Estudo e desenvolvimento de estratégias de controle para sistemas de refrigeração magnética*. Dissertação (Mestrado) — Federal University of Santa Catarina - UFSC, 2020.

HOFFMANN, G.; DUTRA, S. L.; CARDOSO, P. O.; NAKASHIMA, A. T. D.; LOZANO, J. A.; BARBOSA JR., J. R. Actuation and control of electric valves for a magnetic refrigerator. In: *24th ABCM International Congress of Mechanical Engineering (COBEM)*. [S.l.: s.n.], 2017.

HU, J.; XIAO, J. New method for analysis of active magnetic regenerator in magnetic refrigeration at room temperature. *Cryogenics*, v. 35, p. 10–104, 1995.

JACOBS, S.; AURINGER, J.; BOEDER, A.; CHELL, J.; KOMOROWSKI, L.; LEONARD, J.; S., R.; ZIMM, C. The performance of a large-scale rotary magnetic refrigerator. *International Journal of Refrigeration*, v. 37, p. 84–91, 2014.

JACOBS, S.; ZIMM, C. Modeling magnetic refrigeration. In: *Delft Days on Magnetocalorics)*. [S.l.: s.n.], 2008.

JAYARAMAN, T. V.; BOONE, L.; SHIELD, J. E. Near room temperature magnetic entropy changes in as-cast $Gd_{100-x}Mn_x$ (x=0, 5, 10, 15, and 20 at.%) alloys. *Journal of Alloys and Compounds*, v. 509, p. 1411–1417, 2011.

JAYARAMAN, T. V.; BOONE, L.; SHIELD, J. E. Magnetocaloric effect and refrigerant capacity in melt-spun gd-mn alloys. *Journal of Alloys and Compounds*, v. 345, p. 153–158, 2013.

KAMRAN, M. S.; AHMAD, H. O.; WANG, H. S. Review on the developments of active magnetic regenerator refrigerators – evaluated by performance. *Renewable and Sustainable Energy Reviews*, v. 133, 2020.

KAVIANY, M. *Principles of Heat Transfer in Porous Media*. 2. ed. [S.l.]: Springer, 1995.

KIROL, L. D.; MILLS, J. L. Numerical analysis of thermomagnetic generators. *Journal of Appiled Physics*, v. 56, p. 824–828, 1984.

KITANOVSKI, A. Energy applications of magnetocaloric materials. *Advanced Energy Materials*, 2020.

KITANOVSKI, A.; PLAZNIK, U.; TUŠEK, J.; POREDOŠ, A. New thermodynamic cycles for magnetic refrigeration. *International Journal of Refrigeration*, v. 37, p. 28–35, 2014.

KITANOVSKI, A.; TUŠEK, J.; TOMC, U.; PLAZNIK, U.; OŽBOLT, M.; POREDOŠ, A. *Magnetocaloric Energy Conversion from Theory to Applications*. [S.l.]: Springer, 2015.

KLEIN, S. A. *Engineering Equation Solver (EES) Professional Version*. 2013. V9.339, F-Chart Software, Madison, WI.

KOCH, D. L.; BRADY, J. F. Dispersion in fixed beds. *Journal of Fluid Mechanics*, v. 154, p. 399–427, 1985.

KUPPAN, T. *Heat Exchanger Design Handbook*. 2. ed. [S.l.]: Marcel Dekker, 2000.

KUWAHARA, F.; SHIROTA, M.; NAKAYAMA, A. A numerical study of interfacial convective heat transfer coefficient in two-energy equation model for convection in porous media. *International Journal of Heat and Mass Transfer*, v. 44, p. 1153–1159, 2001.

LANG, G. B. *Development of an Active Magnetic Regenerator Model Using the Finite Volumes Method for a Magnetic Refrigeration Application*. Bachelor's Thesis — Federal University of Santa Catarina - UFSC, 2018.

LEE, J.; NOMURA, T.; DEDE, E. M. Topology optimization of halbach magnet arrays using isoparametric projection. *Journal of Magnetism and Magnetic Materials*, v. 432, p. 140–153, 2017.

LEI, T.; ENGELBRECHT, K.; NIELSEN, K. K.; VEJE, C. T. Study of geometries of active magnetic regenerators for room temperature magnetocaloric refrigeration. *Applied Thermal Engineering*, v. 111, p. 1232–1243, 2017.

LEI, T.; NIELSEN, K. K.; ENGELBRECHT, K.; BAHL, C. R. H.; BEZ, H. N.; VEJE, C. Sensitivity study of multi-layer active magnetic regenerators using first order magnetocaloric material La(Fe,Mn,Si)$_{13}$H$_y$. *Journal of Applied Physics*, v. 118, 2015.

LI, C. H.; FINLAYSON, B. A. Heat transfer in packed beds - a reevaluation. *Chemical Engineering Science*, v. 32, p. 1055–1066, 1977.

LIONTE, S.; VASILE, C.; SIROUX, M. Numerical analysis of a reciprocating active magnetic regenerator. *Applied Thermal Engineering*, v. 75, p. 871–879, 2015.

LORENZ, L.; KEVLISHVILI, N. Designing of halbach cylinder based magnetic assembly for a rotating magnetic refrigerator.part 1: Designing procedure. *International Journey of Refrigeration*, v. 73, p. 246–256, 2017.

LOZANO, J.; PEIXER, G.; FORTKAMP, F.; NAKASHIMA, A.; DUTRA, S.; LANG, G.; HOFFMANN, G.; de Sá, N.; CALOMENO, R.; de Oliveira, M.; ANTUNES, L.; SANTOS, V.; BEZ, H.; BARBOSA JR., J. R. Designing a magnetic wine cooler. In: *Eighth International Conference on Caloric Cooling, Thermag VIII*. [S.l.: s.n.], 2018.

LOZANO, J. A. *Designing a Rotary Magnetic Refrigerator*. Tese (Doutorado) — Federal University of Santa Catarina - UFSC, 2015.

LOZANO, J. A.; CAPOVILLA, M. S.; TREVIZOLI, P. V.; ENGELBRECHT, K.; BAHL, C. R. H.; BARBOSA JR., J. R.; PRATA, A. T. Development of a novel rotary magnetic refrigerator. *International Journal of Refrigeration*, v. 68, p. 187–197, 2016.

MALISKA, C. R. *Transferência de Calor e Mecânica dos Fluidos Computacional*. 2. ed. [S.l.]: LTC, 2004.

MOMEN, A. M.; ABDELAZIZ, O.; GLUESENKAMP, K.; VINEYARD, E.; BENEDICT, M. Thermofluid analysis of magnetocaloric refrigeration. In: *Proceedings of the ASME (2014) international mechanical engineering congress and exposition*. [S.l.: s.n.], 2014.

MONFARED, B. Design and optimization of regenerators of a rotary magnetic refrigeration device using a detailed simulation model. *International Journal of Refrigeration*, v. 88, p. 260–274, 2018.

NAKASHIMA, A. T. D. *Avaliação teórica e experimental da influência do perfil temporal doescoamento sobre a performance de um regenerador magnético-ativo*. Dissertação (Mestrado) — Federal University of Santa Catarina - UFSC, 2017.

NAKASHIMA, A. T. D.; DUTRA, S. L.; HOFFMANN, G.; CARDOSO, P. O.; LOZANO, J. A.; BARBOSA JR., J. R. Performance assessment of solenoid valves as flow distributors for an active magnetic regenerator. In: *8th International Conference on Caloric Cooling*. [S.l.: s.n.], 2018.

NAKASHIMA, A. T. D.; FORTKAMP, F. P.; de Sá, N. M.; dos Santos, V. M. A.; HOFFMANN, G.; PEIXER, G. F.; DUTRA, S. L.; RIBEIRO, M. C.; LOZANO, J. A.; BARBOSA JR., J. R. A magnetic wine cooler prototype. *International Journal of Refrigeration*, 2020.

NAKASHIMA, A. T. D.; Sá, N. M. D.; SANTOS, V. M. A. D.; HOFFMANN, G.; LOZANO, J. A.; BARBOSA JR., J. R. Performance assessment of a magnetic wine cooler prototype. In: *Proceedings of the Ninth IIR International Conference on Caloric Cooling and Applications of Caloric Materials, THERMAG IX*. [S.l.: s.n.], 2020.

NAVICKAITĖ, K.; BEZ, H. N.; LEI, T.; BARCZA, A.; VIEYRA, H.; BAHL, C. R. H.; ENGELBRECHT, K. Experimental and numerical comparison of multi-layered $La(Fe,Mn,Si)_{13}H_y$ active magnetic regenerators. *International Journal of Refrigeration*, v. 86, p. 322–330, 2018.

NELLIS, G.; KLEIN, S. *Heat Transfer*. [S.l.]: Cambridge University Press, 2009.

NIELSEN, K. K. *Numerical modeling and analysis of the active magnetic regenerator*. Tese (Doutorado) — Technical University of Denmark, 2010.

NIELSEN, K. K.; BAHL, C. R. H.; SMITH, A.; ENGELBRECHT, K.; OLSEN, U. L.; PRYDS, N. The influence of non-magnetocaloric properties on the amr performance. In: *Proceeding in 5th International Conference on Magnetic Refrigeration at Room Temperature (THERMAG V)*. [S.l.: s.n.], 2012.

NIELSEN, K. K.; TUŠEK, J.; ENGELBRECHT, K.; SCHOPFER, S.; KITANOVSKI, A.; BAHL, C. R. H.; SMITH, A.; PRYDS, N.; POREDOŠ, A. Review on numerical modeling of active magnetic regenerators for room temperature applications. *International Journal of Refrigeration*, v. 34, p. 603–616, 2011.

OLIVEIRA, P. A.; TREVIZOLI, P. V.; BARBOSA JR., J. R.; PRATA, A. T. A 2d hybrid model of the fluid flow and heat transfer in a reciprocating active magnetic regenerator. *International Journal of Refrigeration*, v. 35, p. 98–114, 2012.

OZGUMUS, T.; MOBEDI, M.; OZKOL, U. Determination of kozeny constant based on porosity and pore to throat size ratio in porous medium with rectangular rods. *Engineering Applications of Computational Fluid Mechanics*, v. 8, p. 308–318, 2014.

OZGUMUS, T.; MOBEDI, M.; OZKOL, U.; NAKAYAMA, A. Thermal dispersion in porous media = a review on approaches in experimental studies. *6th International Advanced Technologies Symposium*, p. 266–271, 2011.

PALLARES, J.; GRAU, F. X. A modification of a nusselt number correlation for forced convection in porous media. *International Communications in Heat and Mass Transfer*, v. 37, p. 1187–1190, 2010.

PATANKAR, S. *Numerical Heat Transfer and Fluid Flow*. [S.l.]: Hemisphere Publishing Corporation, 1980.

PECHARSKY, V. K.; GSCHNEIDER, K. A. j. Giant magnetocaloric effect in $Gd_5(Si_2Ge_2)$. *Physical Review Letters*, v. 78, p. 4494–4497, 1997.

PECHARSKY, V. K.; GSCHNEIDER, K. A. J. Magnetocaloric effect and magnetic refrigeration. *Journal of Magnetism and Magnetic Materials*, v. 200, p. 44–56, 1999.

PECHARSKY, V. K.; GSCHNEIDER, K. A. j. Advanced magnetocaloric materials: What does the future hold? *International Journal of Refrigeration*, v. 29, p. 1239–1249, 2006.

PEIXER, G. F. *Integrated Design and Optimization of a Magnetic Cooling System for Air-Conditioning Applications*. Dissertação (Mestrado) — Federal University of Santa Catarina - UFSC, 2020.

PEIXER, G. F.; LOZANO, J. A.; BARBOSA JR., J. R. Performance evaluation of amrs using different casings. In: *Book of Abstracts of the Danish Days on Caloric Materials and Devices (Poster Session), Roskilde, Denmark*. [S.l.: s.n.], 2017. p. 84.

PETERSEN, T. F.; PRYDS, N.; SMITH, A.; HATTEL, J.; SCHMIDT, H.; KNUDSEN, H. Two-dimensional mathematical model of a reciprocating room-temperature active magnetic regenerator. *International Journal of Refrigeration*, v. 31, p. 432–443, 2008.

PORTARIA Nº 234, de 29 de junho de 2020. [S.l.], 2020.

QIAN, S.; YU, J.; YAN, G. A review of regenerative heat exchange methods for various cooling technologies. *Renewable and Sustainable Energy Reviews*, v. 69, p. 535–550, 2017.

ROWE, A.; TURA, A.; DIKEOS, J.; CHAHINE, R. Near room temperature magnetic refrigeration. *Proceedings of the International Green Energy Conference*, 2005.

ROY, S.; PONCET, S.; SORIN, M. Sensitivity analysis and multiobjetcive optimization of a parallel-plate active magnetic regenerator using a genetic algorithm. *International Journal of Refrigeration*, v. 75, p. 276–285, 2017.

SANTOS, D. dos. *Sistema de Gerenciamento Hidráulico para uma Unidade de Refrigeração Magnética*. Bachelor's Thesis — Federal University of Santa Catarina - UFSC, 2020.

SARLAH, A. *Thermohydraulic properties of heat regenerators in magnetic refrigerator*. Tese (Doutorado) — University of Ljubljana, 2008.

SATO, M.; ISHII, Y. Simple and approximate expressions of demagnetizing factors of uniformly magnetized rectangular rod and cylinder. *Journal of Applied Physics*, v. 66, p. 983–985, 1989.

SCHMIDT, F.; WILMOOT, A. J. *Thermal Energy Storage and Regeneration*. [S.l.]: Hemispehere Publishing Co., 1981.

SHAH, R.; SEKULIĊ, D. P. *Fundamentals of Heat Exchanger Design*. [S.l.]: John Wiley Sons, Inc., 2003.

SMAILLI, A.; CHAHINE, R. Thermodynamic investigation of optimum active magnetic regenerators. *Cryogenics*, v. 38, p. 247–252, 1998.

SMITH, A. Who discovered the magnetocaloric effect. *The European PHysical Journal H*, v. 38, p. 507–517, 2013.

SMITH, A.; BAHL, C. R. H.; BJØRK, R.; ENGELBRECHT, K.; NIELSEN, K. K.; PRYDS, N. Materials challenges for high performance magnetocaloric refrigeration devices. *Advanced Energy Materials*, v. 2, p. 1288–1318, 2012.

STEYERT, W. A. Stirling-cycle rotating magnetic refrigerators and heat engines for use near room temperature. *Journal of Applied Physics*, v. 49, p. 1216–1226, 1978.

TEYBER, R.; TREVIZOLI, P. V.; CHRISTIAANSE, T. V.; GOVINDAPPA, P.; I., N.; ROWE, A. Permanent magnet design for magnetic heat pumps using total cost minimization. *Journal of Magnetism and Magnetic Materials*, v. 442, p. 87–96, 2017.

TISHIN, A. M. Magnetocaloric effect in lanthanide materials. *Journal of Alloys and Compounds*, v. 250, p. 635–641, 1997.

TREVIZOLI, P. *Development of Thermal Regenerators for Magnetic Cooling Applications*. Tese (Doutorado) — Federal University of Santa Catarina - UFSC, 2015.

TREVIZOLI, P. V.; Barbosa Jr., J. R. Entropy generation minimization analysis of oscillating-flow regenerators. *International Journal of Heat and Mass Transfer*, v. 87, p. 347–358, 2015.

TREVIZOLI, P. V.; BARBOSA JR., J. R.; FERREIRA, R. T. S. Experimental evaluation of a gd-based linear reciprocating active magnetic regenerator test apparatus. *International Journal of Refrigeration*, v. 34, p. 1518–1526, 2011.

TREVIZOLI, P. V.; BARBOSA JR., J. R.; OLIVEIRA, P. A.; CANESIN, F. C.; FERREIRA, R. T. S. Assessment of demagnetization phenomena in the performance in the performance of an active magnetic regenerator. *International Journal of Refrigeration*, v. 35, p. 1043–1054, 2012.

TREVIZOLI, P. V.; LOZANO, J. A.; PEIXER, G. F.; BARBOSA JR., J. R. Design of nested halbach cylinder arrays for magnetic refrigeration applications. *Journal of Magnetism and Magnetic Materials*, v. 395, p. 109–122, 2015.

TREVIZOLI, P. V.; NAKASHIMA, A. T.; PEIXER, G. F.; BARBOSA JR., J. R. Performance evaluation of an active magnetic regenerator for cooling applications - part i: Experimental analysis and thermodynamic performance. *International Journal of Refrigeration*, v. 72, p. 192–205, 2016.

TURA, A.; ROWE, A. Permanent magnet magnetic refrigerator design and experimental characterization. *International Journal of Refrigeration*, v. 34, p. 628–639, 2011.

TUŠEK, J.; KITANOVSKI, A.; PREBIL, I.; POREDOŠ, A. Dynamic operation of an active magnetic regenerator (amr): Numerical optimization of a packed-bed amr. v. 6, p. 1507–1517, 2011.

TUŠEK, J.; ZUPAN, S.; SARLAH, A.; PREBIL, I.; POREDOS, A. Development of rotary magnetic refrigerator. *International Journal of Refrigeration*, v. 33, p. 294–300, 2010.

UNITED NATIONS. *Handbook for the Montreal protocol on substances that deplete the ozone layer*. 14. ed. [S.l.]: United Nations Environment Programme, 2020.

VIEIRA, B. P.; BEZ, H. N.; KUEPFERLING, M.; ROSA, M. A.; SCHAFER, D.; CID, C. C. P.; VIEYRA, H. A.; BASSO, V.; LOZANO, J. A.; BARBOSA JR., J. R. Magnetocaloric properties of spheroidal $La(Fe,Mn,Si)_{13}H_y$ granules and their performance in epoxy-bonded active magnetic regenerators. *Applied Thermal Engineering*, v. 183, 2021.

WAKAO, N.; KAGUEI, S. *Heat and mass transfer in packed beds*. [S.l.]: New York: Gordon and Breach Science, 1982.

WEBB, R. I.; KIM, N. H. *Principles of Enhanced Heat Transfer*. 2. ed. [S.l.]: Taylor Francis, 2005.

YAN, Z.; CHEN, J. The effect of field-dependent heat capacity on the characteristics of the ferromagnetic ericsson refrigeration cycle. *Journal of Appiled Physics*, v. 72, p. 1–5, 1992.

YU, B.; LIU, M.; EGOLF, P. W.; KITANOVSKI, A. A review of magnetic refrigerator and heat pump prototypes built before the year 2010. *International Journal of Refrigeration*, v. 33, p. 1029–1066, 2010.

YU, B.; ZHANG, Y.; GAO, Q.; YANG, D. Research on performance of regenerative room temperature magnetic refrigeration cycle. *International Journal of Refrigeration*, v. 29, p. 1348–1357, 2006.

ZHANG, L.; SHERIF, S. A.; DEGREGORIA, A. J.; ZIMM, C. B.; VEZIROGLU, T. N. Design and optimization of a 0.1 ton/day active magnetic regenerative hydrogen liquefier. *Cryogenics*, v. 40, p. 269–278, 2000.

ZHANG, L.; SHERIF, S. A.; VEZIROGLU, T. N.; SHEFFIELD, J. W. Second law analysis of active magnetic regenerative hydrogen liquefier. *Cryogenics*, v. 33, p. 667–674, 1993.

ZHANG, M.; ABDELAZIZ, O.; MOMEN, A. M.; ABU-HEIBA, A. A numerical analysis of a magnetocaloric refrigerator with a 16-layer regenerator. *Sci Rep 7:13962*, 2017.

ZHUKOV, A. *Novel Functional Magnetic Materials*. [S.l.]: Springer, 2016.

Appendices

A Epoxy Closure Relationships

A.1 Epoxy Layer Length

Considering the system of a MCM sphere covered with epoxy shown in Figure 132, simple geometry gives:

$$V_{\text{MCM}} = (1 - \varepsilon)V_{\text{pm}} = \frac{\pi d_{\text{P}}^3}{6} \tag{A.1}$$

and:

$$V_{\text{ep}} = (\varepsilon - \varepsilon_{\text{f}})V_{\text{pm}} = \frac{\pi[(d_{\text{P}} + 2L_{\text{ep}})^3 - d_{\text{P}}^3]}{6} \tag{A.2}$$

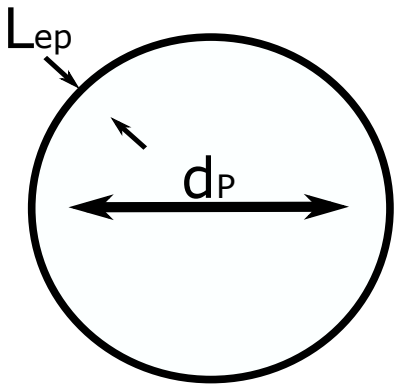

Figure 132 – Representation of a sphere of MCM covered by epoxy.

Dividing Equation A.2 by Equation A.1 gives:

$$\frac{\varepsilon - \varepsilon_{\text{f}}}{1 - \varepsilon} = \frac{(d_{\text{P}} + 2L_{\text{ep}})^3}{d_{\text{P}}^3} - 1 \tag{A.3}$$

and isolating L_{ep}:

$$L_{\text{ep}} = \frac{d_{\text{P}}}{2}\left[\left(\frac{\varepsilon - \varepsilon_{\text{f}}}{1 - \varepsilon} + 1\right)^{\frac{1}{3}} - 1\right] \tag{A.4}$$

A.2 Equivalent Thermophysical Properties

For heat exchange purposes, the solid phase is treated as a composite material in order to consider both the MCM and epoxy phases. As discussed in Section 3.6.3

the characteristic length of the material is given by $L_c = d_P/6 + L_{ep}$ and the equivalent thermal resistance is given by Equation 3.36:

$$k_{eq} = \left(\frac{d_P}{6} + L_{ep}\right)\left(\frac{d_P}{6k_s} + \frac{L_{ep}}{k_{ep}}\right)^{-1} \tag{A.5}$$

which allows the Biot number to be calculated as:

$$Bi = \frac{hL_c}{k_{eq}} \tag{A.6}$$

The Fourier number requires an equivalent specific heat capacity and equivalent density. The equivalent density is given by:

$$\frac{1}{\rho_{eq}} = \frac{m_{MCM}/m}{\rho_{MCM}} + \frac{m_{ep}/m}{\rho_{ep}} \tag{A.7}$$

where m is the total mass of the sphere. The equivalent specific heat capacity is similarly given by:

$$c_{eq} = \frac{m_{MCM}}{m}c_H + \frac{m_{ep}}{m}c_{ep} \tag{A.8}$$

With these equivalent properties, the Fourier number is given by:

$$Fo = \frac{k_{eq}}{\rho_{eq}c_{eq}}\frac{\tau}{L_c^2} \tag{A.9}$$

B Numerical Model Validation Results

The considerations regarding the validation of the numerical model can be found in Sections 5.1 and 5.7. The results shown in this appendix aim to further complement the discussions shown in these sections by increasing the number of experimental and numerical points that were evaluated. All conclusions and propositions made in the validation sections considered and can be extended to these results.

B.1 Regenerator-1 - Active Tests

This section contains the results related to section 5.1.1.2 which were not presented in the main body of the text. These are the temperature profiles at the ends of the regenerator during the active tests for temperature spans of 0, 6 and 12 K. Following what was discussed in the main text, the results show a good agreement between themselves, especially on the hot side.

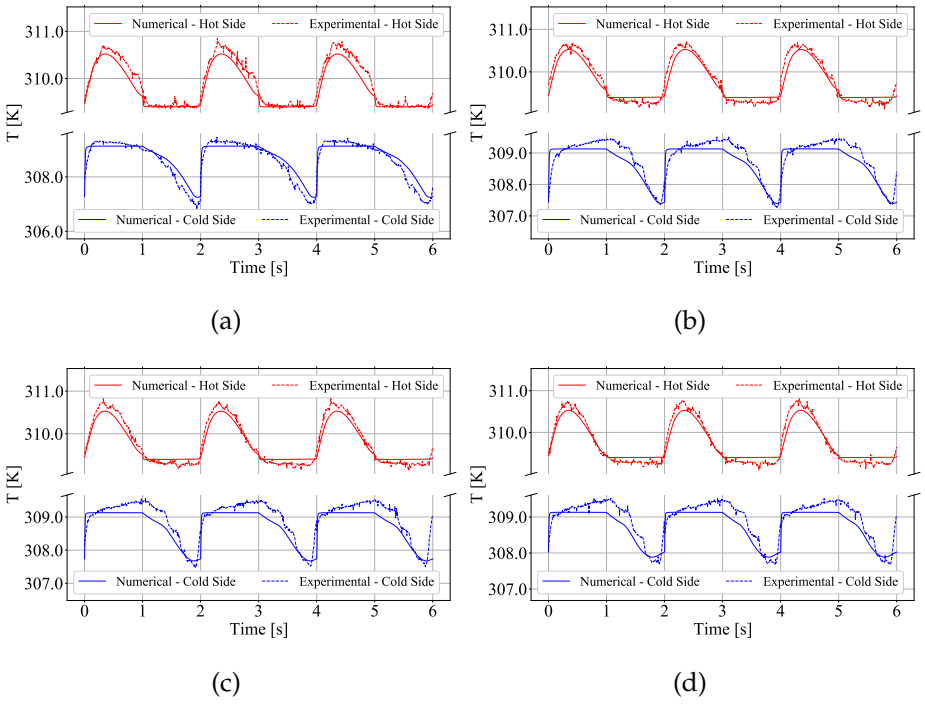

Figure 133 – Comparison between the numerical and experimental temperature profiles at the hot and cold ends of Regenerator-1 during three cycles. The cycle frequency is 0.5 Hz, the temperature span is 0 K and the mass flow rate is (a) 30, (b) 40, (c) 50 and (d) 60 kg/h.

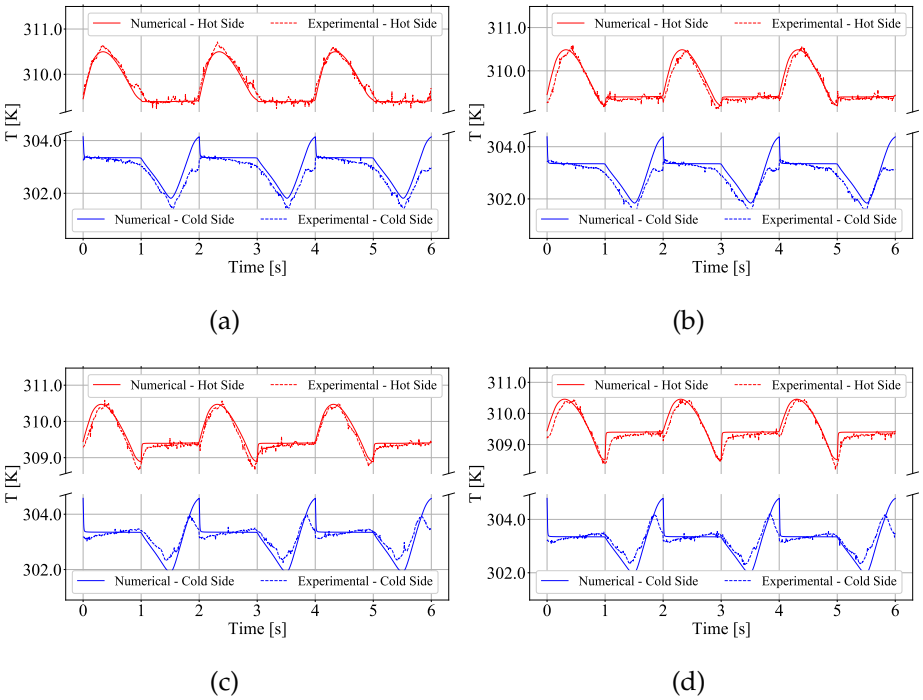

Figure 134 – Comparison between the numerical and experimental temperature profiles at the hot and cold ends of Regenerator-1 during three cycles. The cycle frequency is 0.5 Hz, the temperature span is 6 K and the mass flow rate is (a) 30, (b) 40, (c) 50 and (d) 60 kg/h.

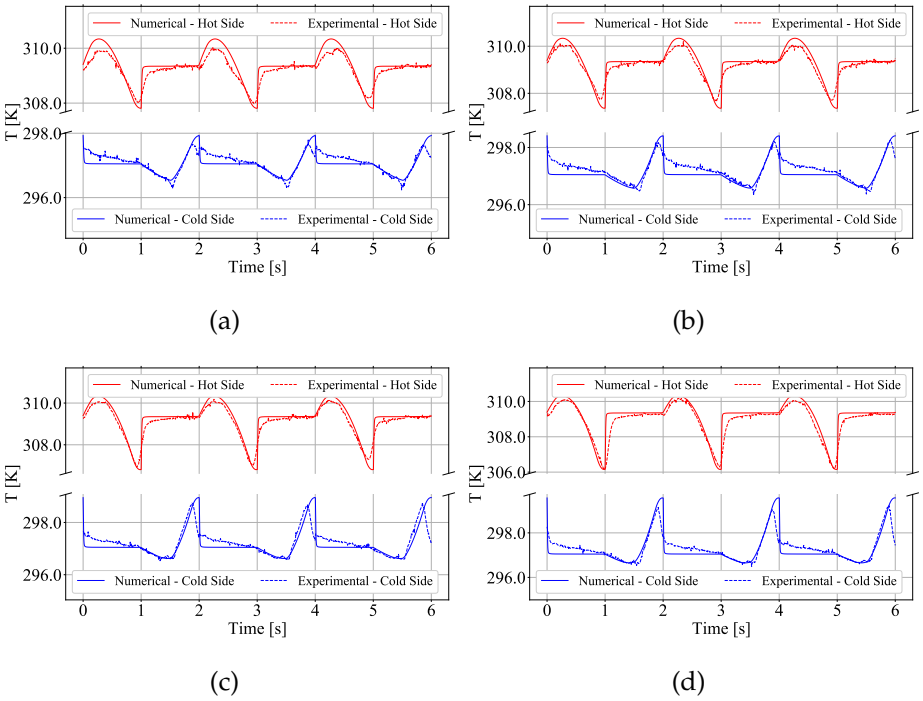

Figure 135 – Comparison between the numerical and experimental temperature profiles at the hot and cold ends of Regenerator-1 during three cycles. The cycle frequency is 0.5 Hz, the temperature span is 12 K and the mass flow rate is (a) 30, (b) 40, (c) 50 and (d) 60 kg/h.

B.2 Regenerator-2 - Passive Tests

This section contains the results related to section 5.1.2.1 which were not presented in the main body of the text. These include the effectiveness results for the tests with a blow fraction of 25% and frequency of 0.5 Hz and a blow fraction of 50% and frequency of 0.75 Hz. It also includes the temperature profiles at the ends of the regenerators for the conditions not shown in the main body of the text.

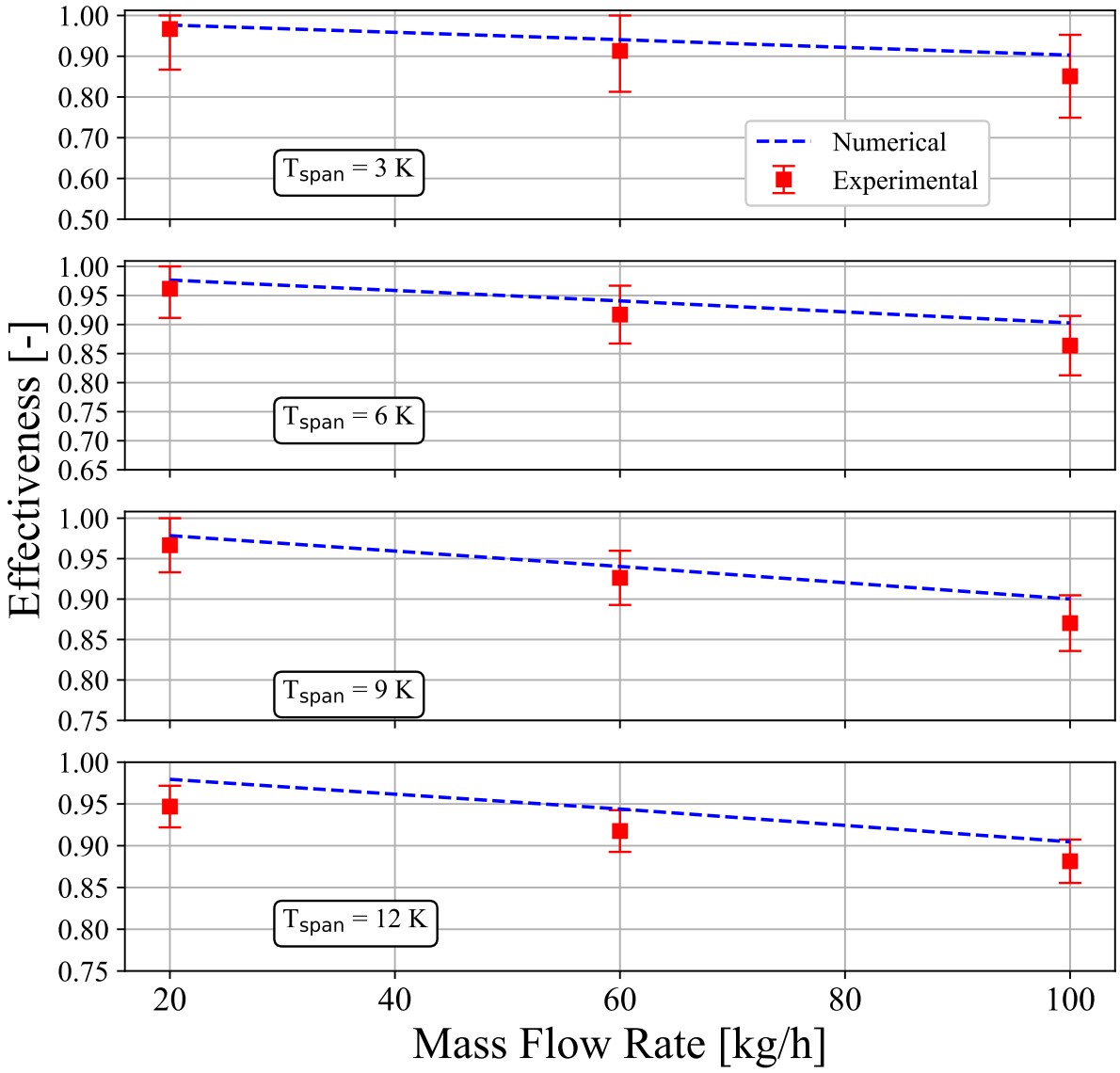

Figure 136 – Effectiveness results for the cold blow of Regenerator-2 for a frequency of 0.5 Hz and blow fraction of 25%. The model used the correlation proposed by Pallares & Grau (2010).

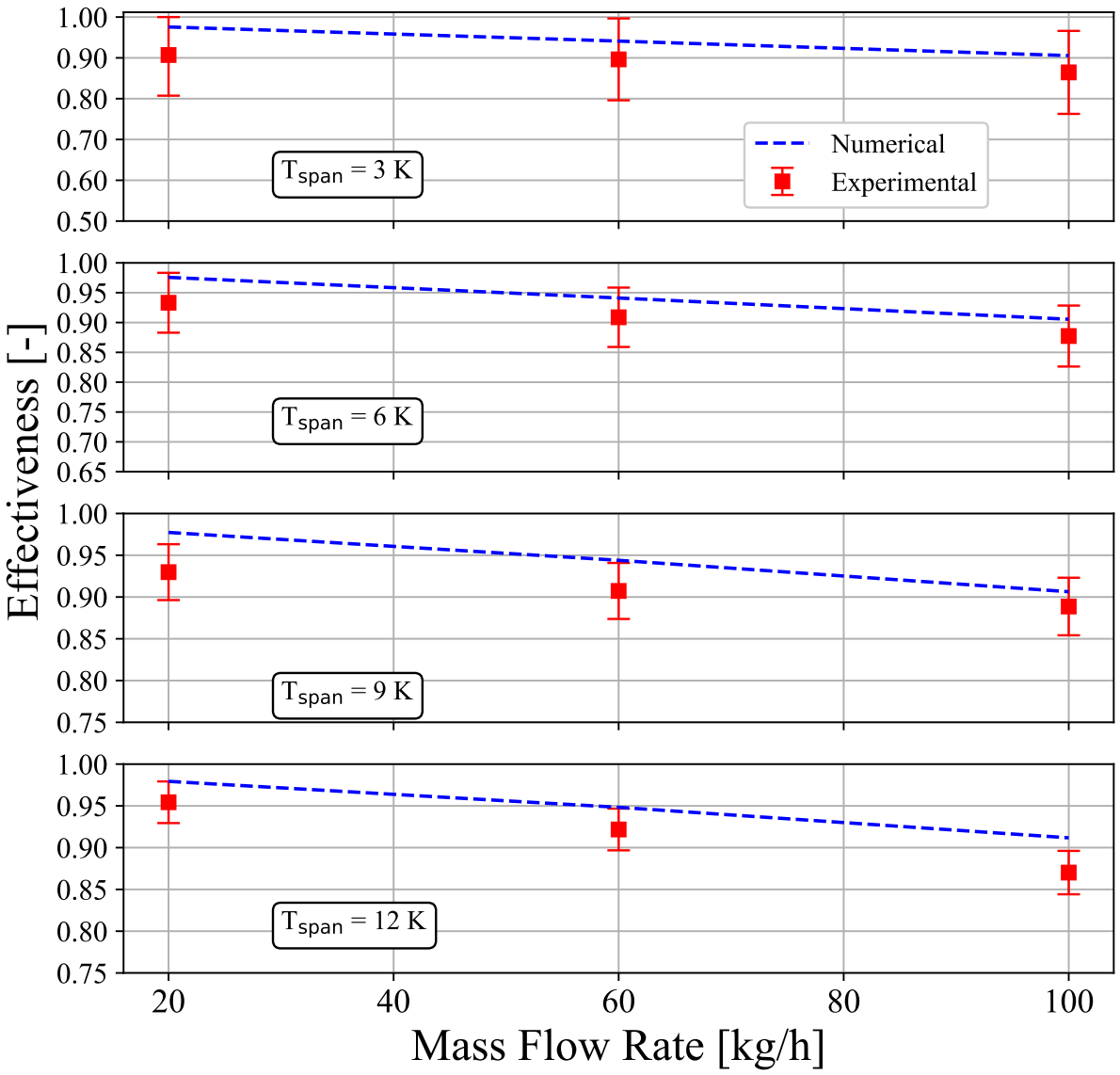

Figure 137 – Effectiveness results for the hot blow of Regenerator-2 for a frequency of 0.5 Hz and blow fraction of 25%. The model used the correlation proposed by Pallares & Grau (2010).

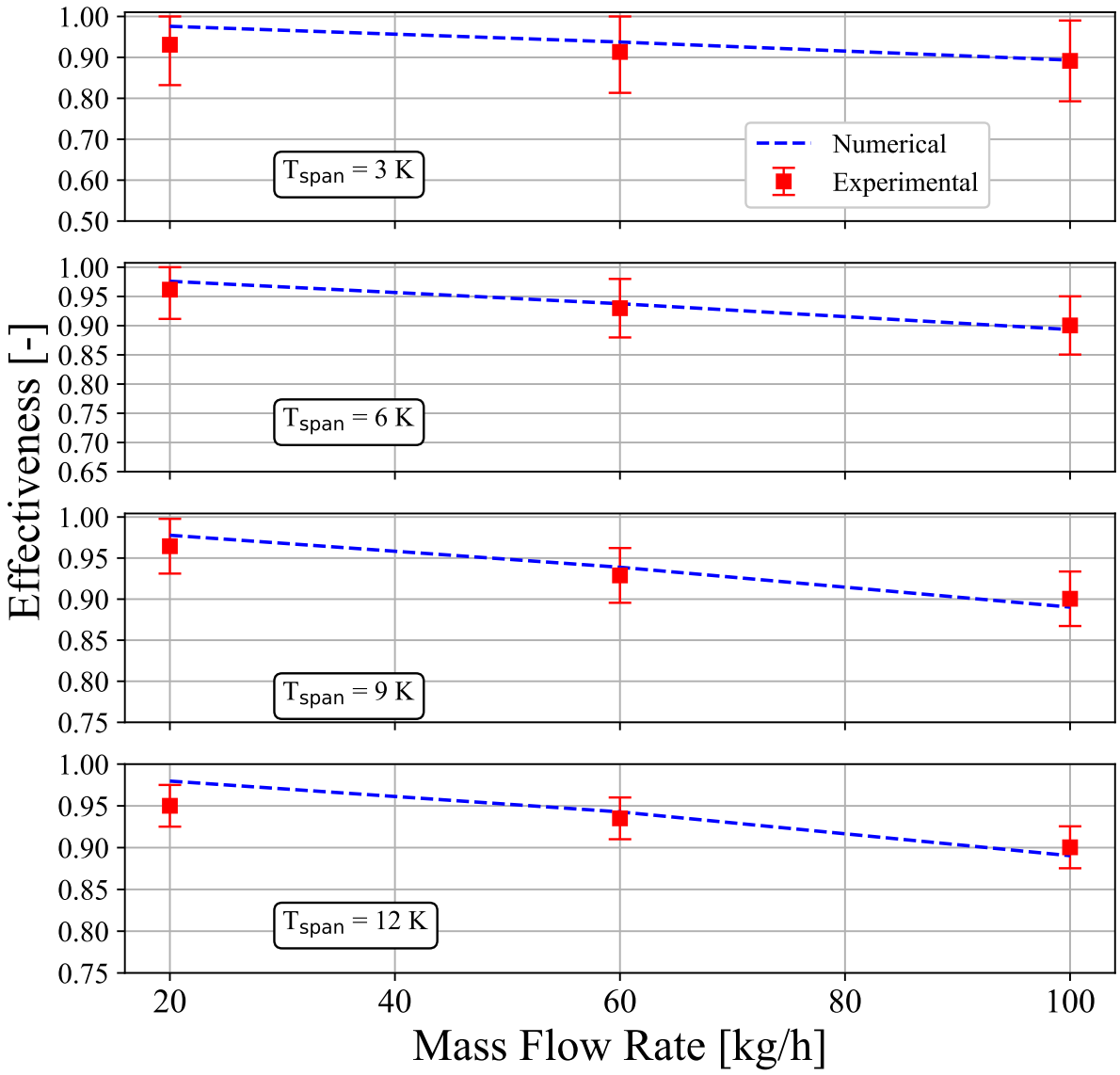

Figure 138 – Effectiveness results for the cold blow of Regenerator-2 for a frequency of 0.75 Hz and blow fraction of 50%. The model used the correlation proposed by Pallares & Grau (2010).

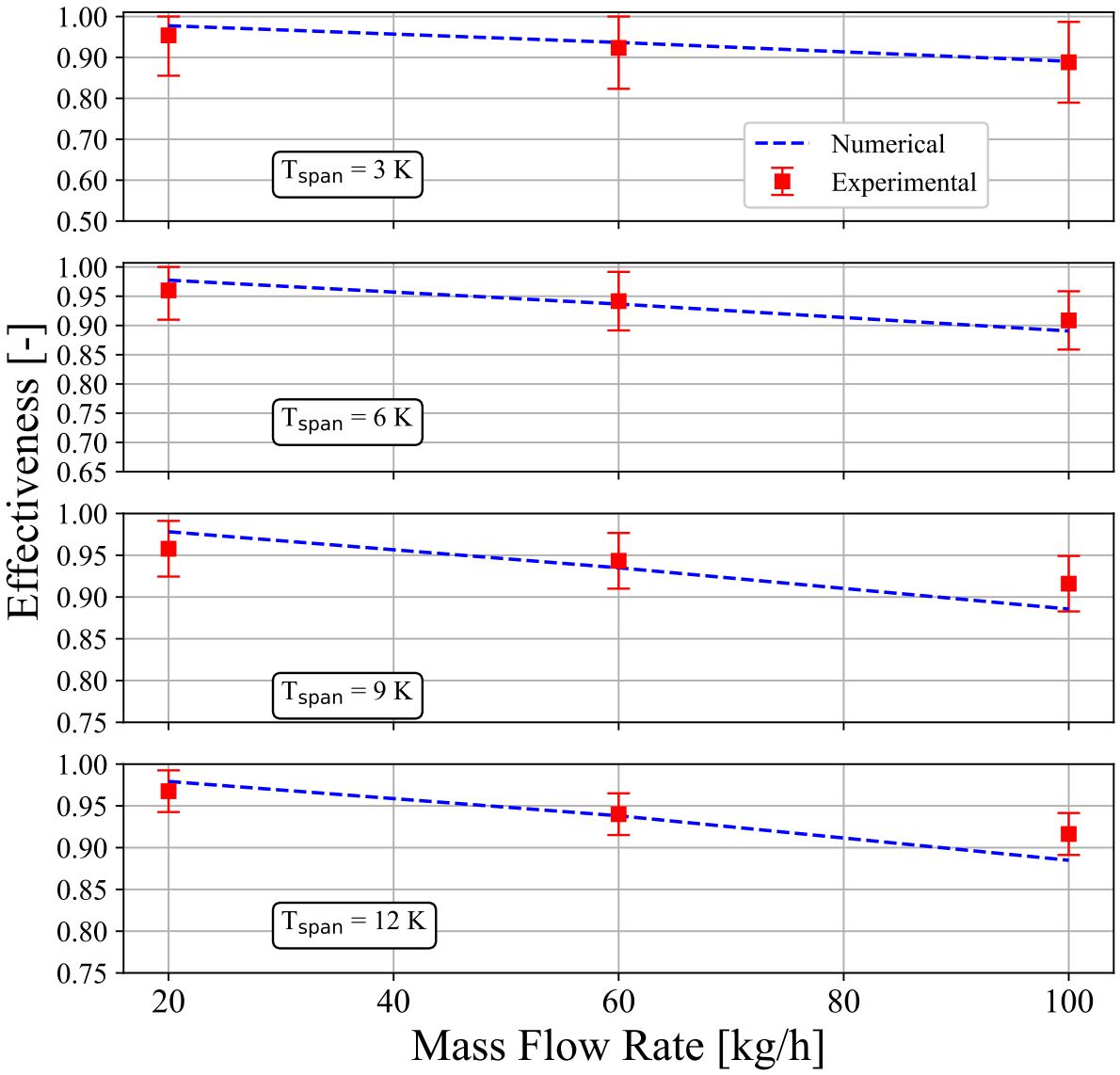

Figure 139 – Effectiveness results for the hot blow of Regenerator-2 for a frequency of 0.75 Hz and blow fraction of 50%. The model used the correlation proposed by Pallares & Grau (2010).

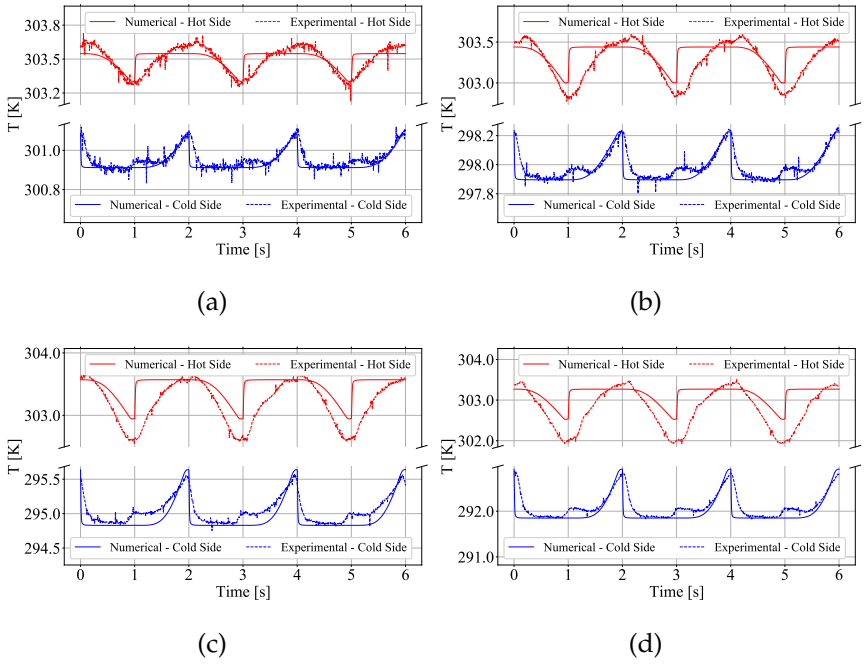

Figure 140 – Comparison between the numerical and experimental temperature profiles at the hot and cold ends of Regenerator-2 during three cycles of the passive tests. The cycle frequency is 0.5 Hz, the blow fraction is 50%, the mass flow rate is 20 kg/h and the temperature span is (a) 3, (b) 6, (c) 9 and (d) 12 K.

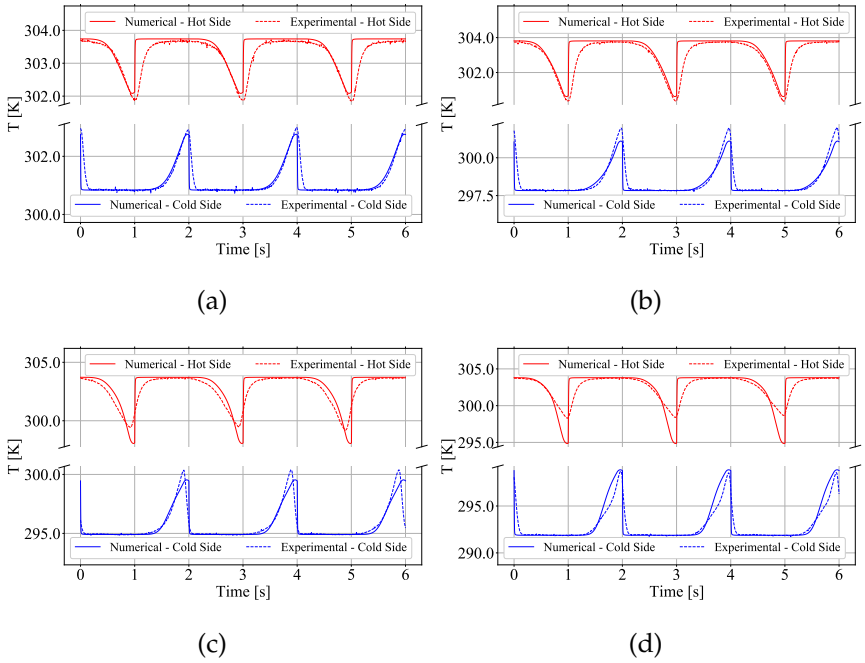

Figure 141 – Comparison between the numerical and experimental temperature profiles at the hot and cold ends of Regenerator-2 during three cycles of the passive tests. The cycle frequency is 0.5 Hz, the blow fraction is 50%, the mass flow rate is 100 kg/h and the temperature span is (a) 3, (b) 6, (c) 9 and (d) 12 K.

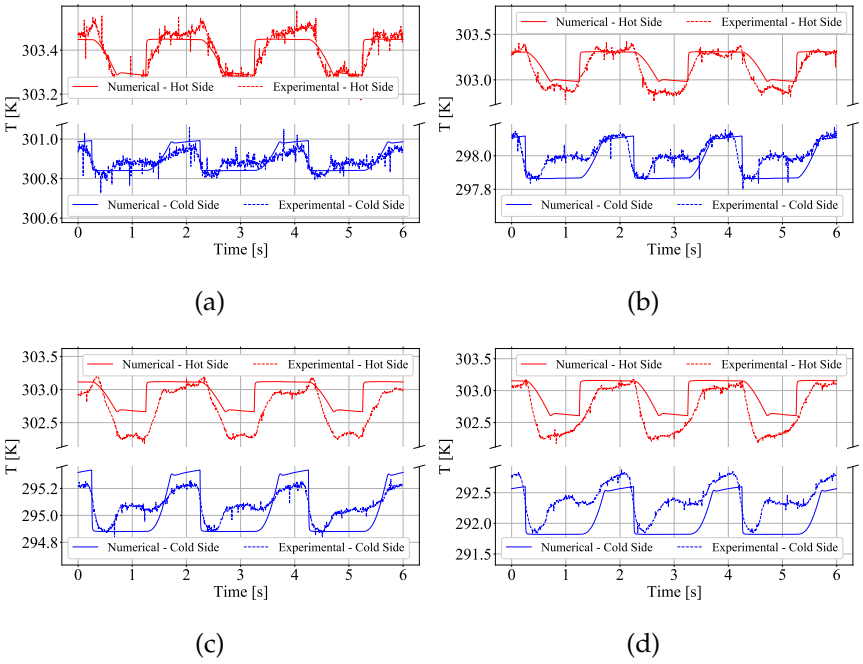

Figure 142 – Comparison between the numerical and experimental temperature profiles at the hot and cold ends of Regenerator-2 during three cycles of the passive tests. The cycle frequency is 0.5 Hz, the blow fraction is 25%, the mass flow rate is 20 kg/h and the temperature span is (a) 3, (b) 6, (c) 9 and (d) 12 K.

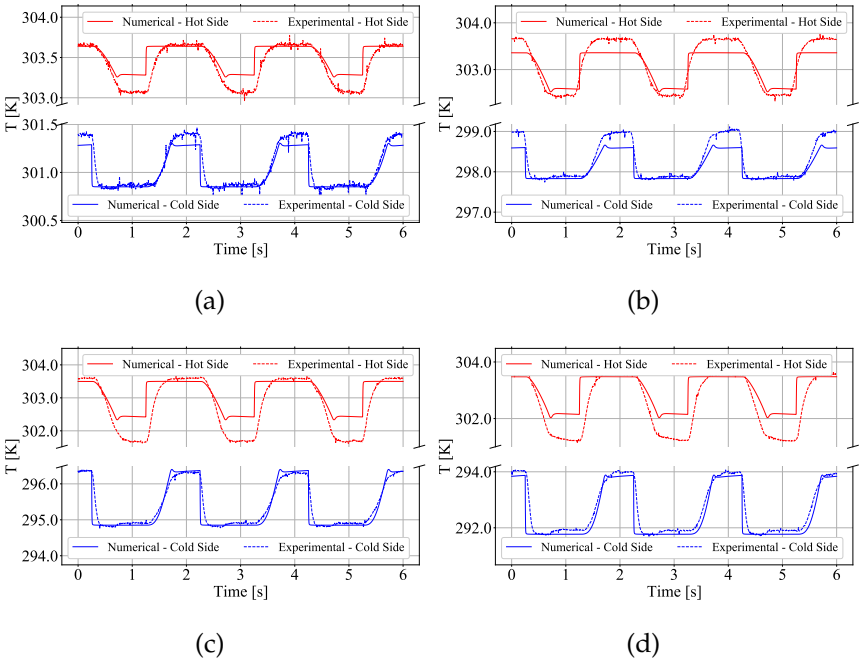

Figure 143 – Comparison between the numerical and experimental temperature profiles at the hot and cold ends of Regenerator-2 during three cycles of the passive tests. The cycle frequency is 0.5 Hz, the blow fraction is 25%, the mass flow rate is 60 kg/h and the temperature span is (a) 3, (b) 6, (c) 9 and (d) 12 K.

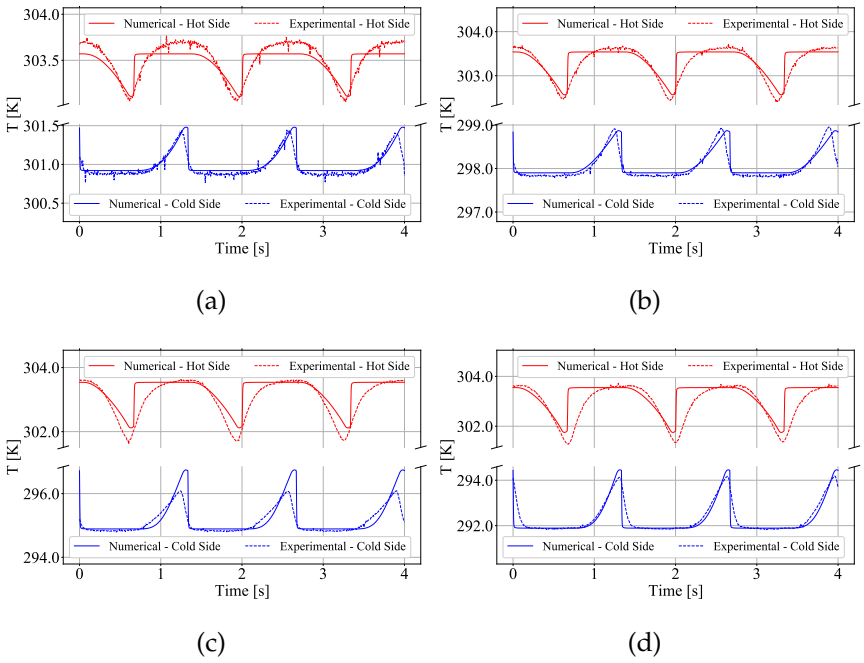

Figure 144 – Comparison between the numerical and experimental temperature profiles at the hot and cold ends of Regenerator-2 during three cycles of the passive tests. The cycle frequency is 0.75 Hz, the blow fraction is 50%, the mass flow rate is 60 kg/h and the temperature span is (a) 3, (b) 6, (c) 9 and (d) 12 K.

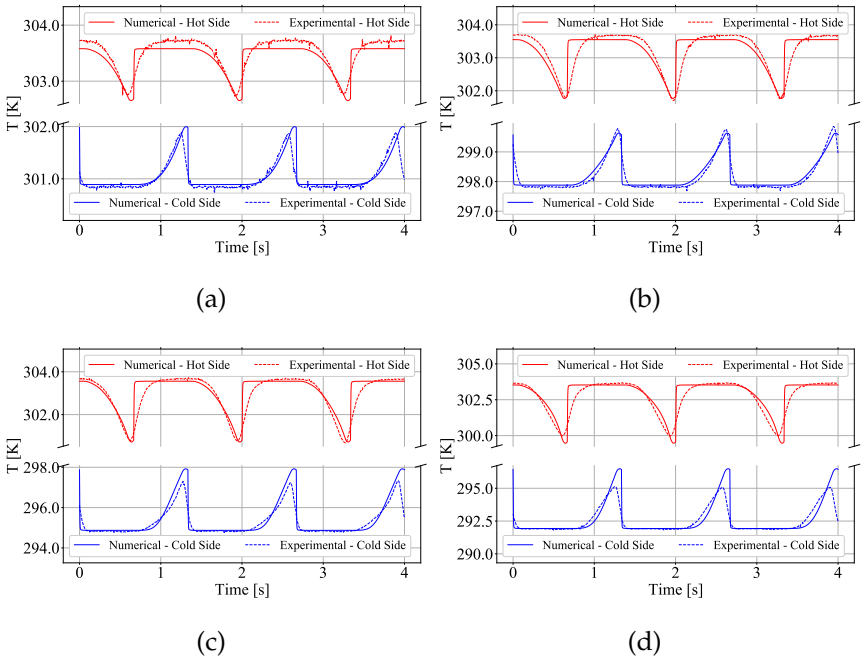

Figure 145 – Comparison between the numerical and experimental temperature profiles at the hot and cold ends of Regenerator-2 during three cycles of the passive tests. The cycle frequency is 0.75 Hz, the blow fraction is 50%, the mass flow rate is 100 kg/h and the temperature span is (a) 3, (b) 6, (c) 9 and (d) 12 K.

B.3 Regenerator-3 - Passive Tests

This section contains the results related to section 5.7.2 which were not presented in the main body of the text. These are the temperature profiles for the tests operating at 0.75 Hz that were not shown and all results obtained at 0.5 Hz.

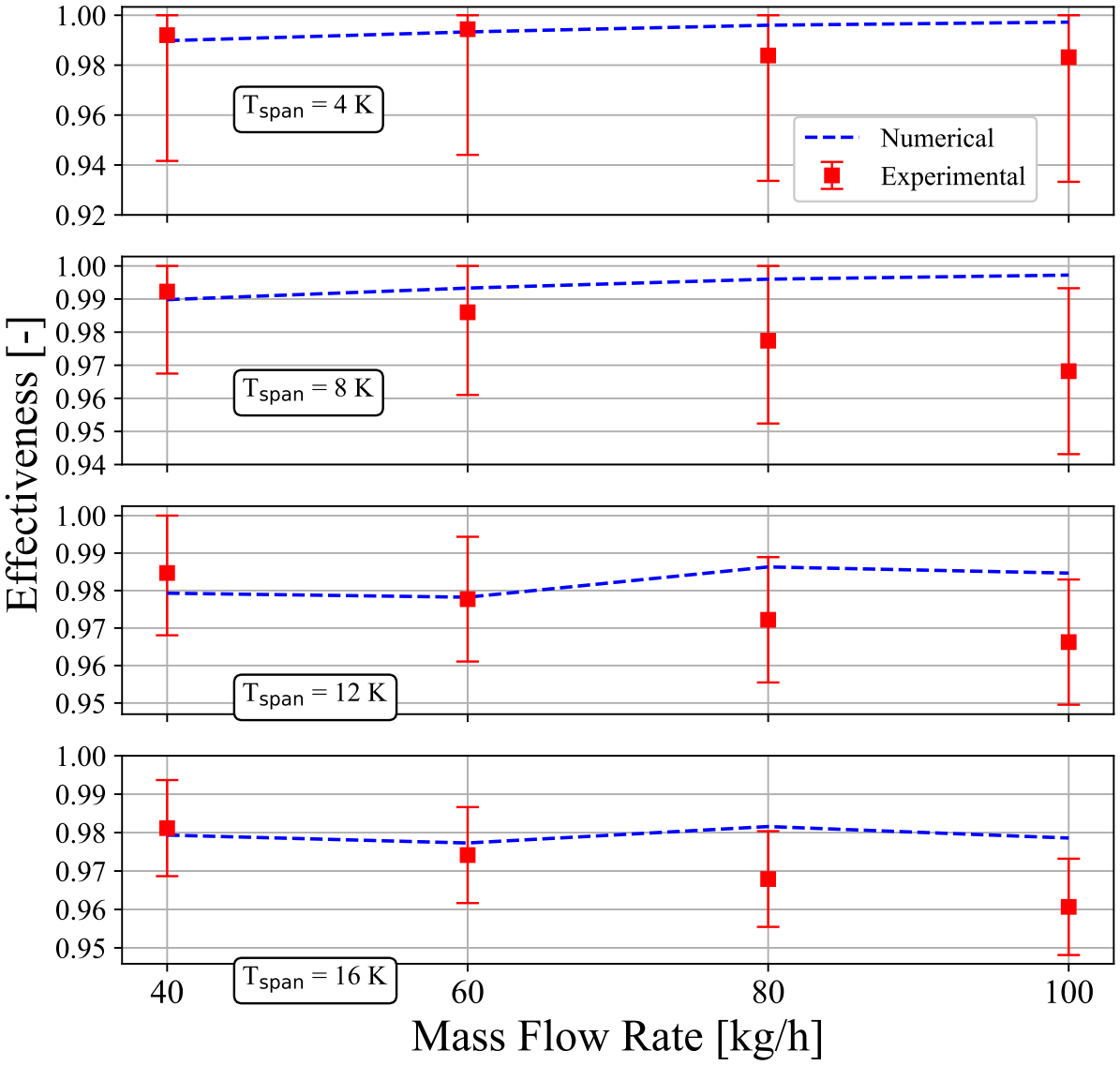

Figure 146 – Comparison between experimental and numerical results of effectiveness for Regenerator-3 during the cold blow operating at 0.5 Hz.

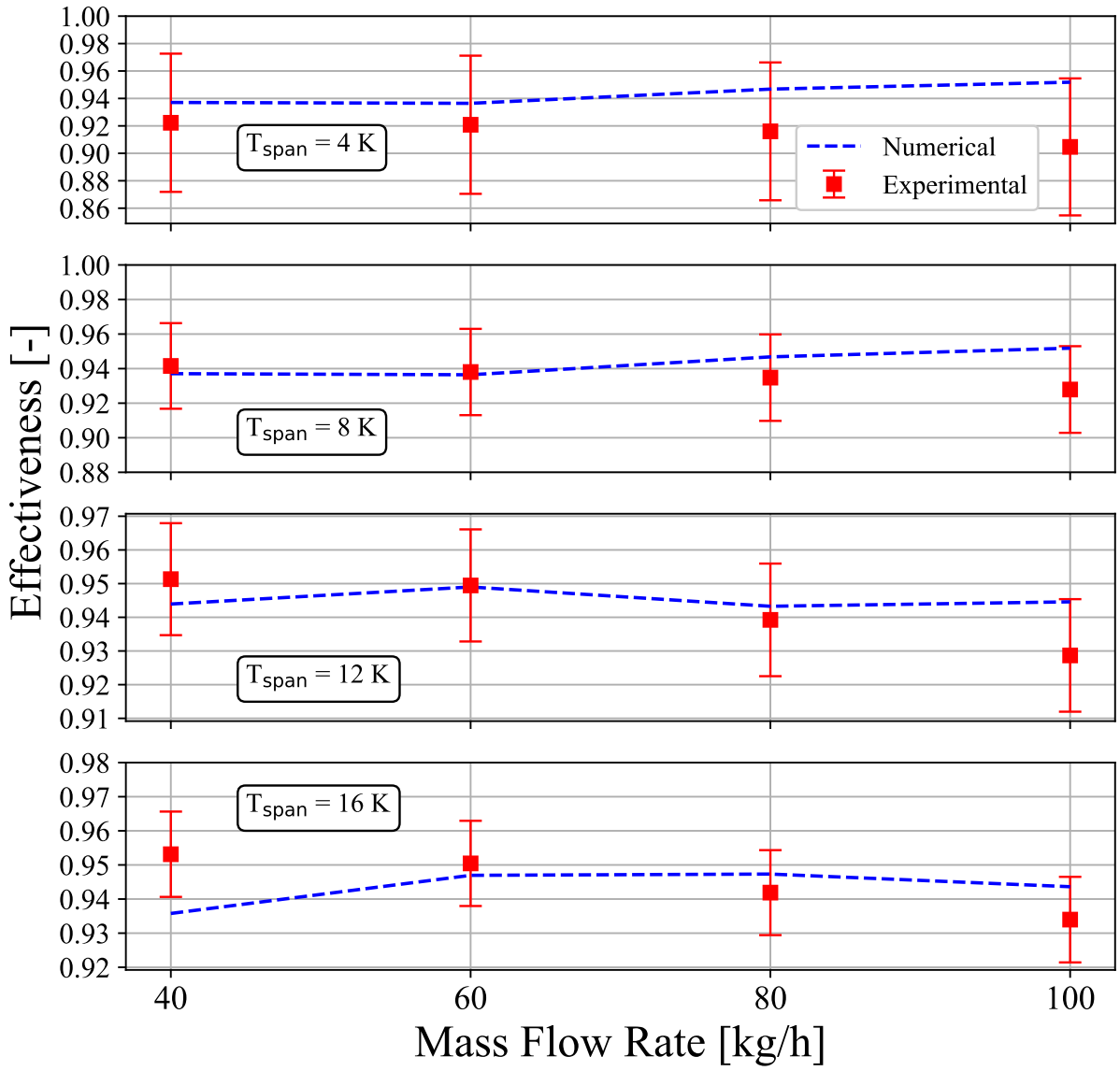

Figure 147 – Comparison between experimental and numerical results of effectiveness for Regenerator-3 during the hot blow operating at 0.5 Hz.

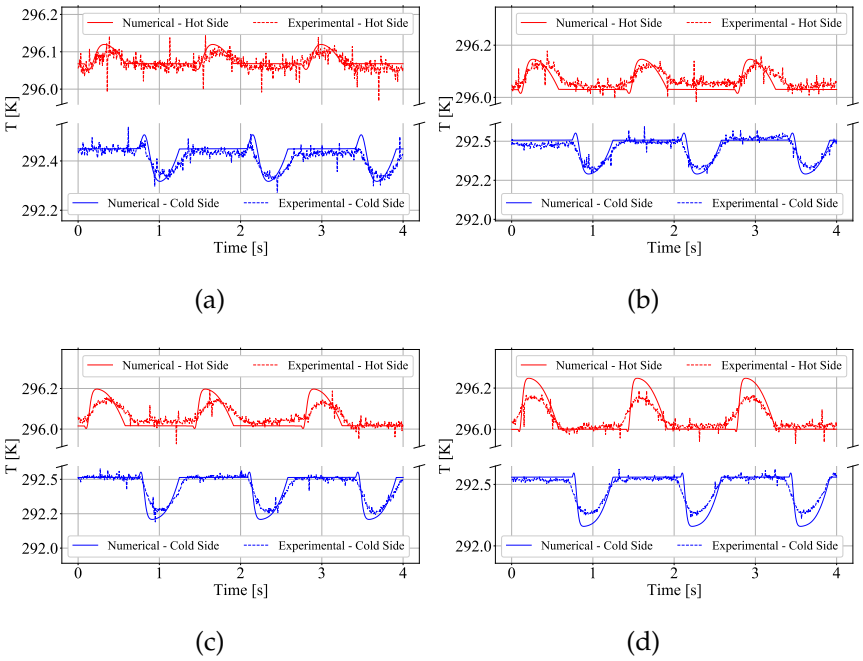

Figure 148 – Comparison between the numerical and experimental temperature profiles at approximately 110 mm from the hot and cold ends of Regenerator-3 during three cycles. The cycle frequency is 0.75 Hz, the temperature span is 4 K and the mass flow rate is (a) 40, (b) 60, (c) 80 and (d) 100 kg h^{-1}.

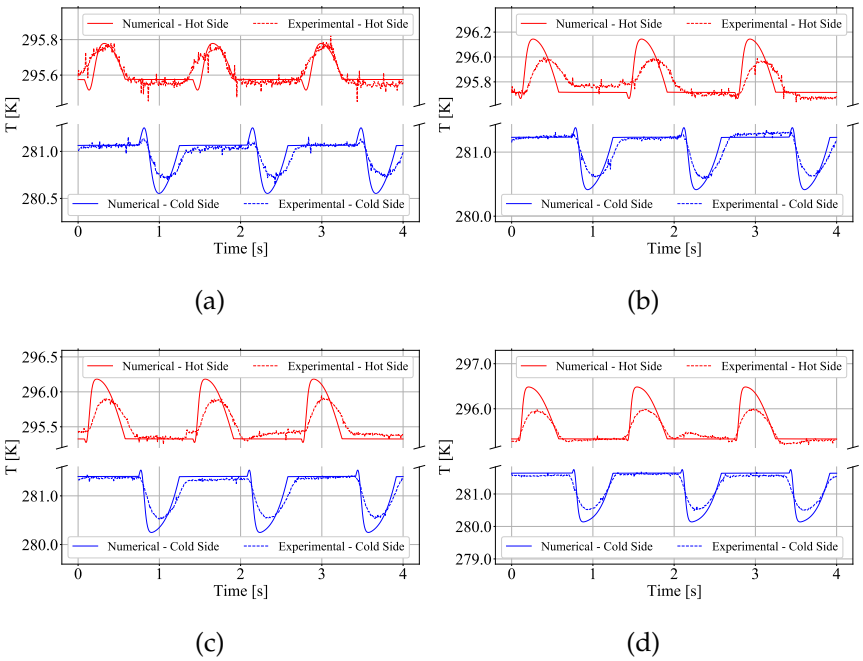

Figure 149 – Comparison between the numerical and experimental temperature profiles at approximately 110 mm from the hot and cold ends of Regenerator-3 during three cycles. The cycle frequency is 0.75 Hz, the temperature span is 16 K and the mass flow rate is (a) 40, (b) 60, (c) 80 and (d) 100 kg h^{-1}.

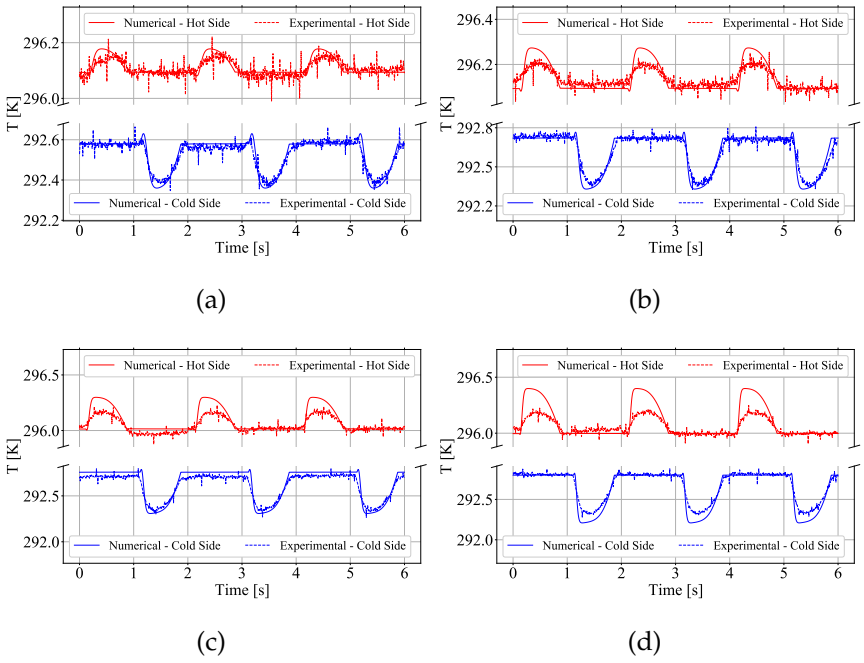

Figure 150 – Comparison between the numerical and experimental temperature profiles at approximately 110 mm from the hot and cold ends of Regenerator-3 during three cycles. The cycle frequency is 0.5 Hz, the temperature span is 4 K and the mass flow rate is (a) 40, (b) 60, (c) 80 and (d) 100 kg h^{-1}.

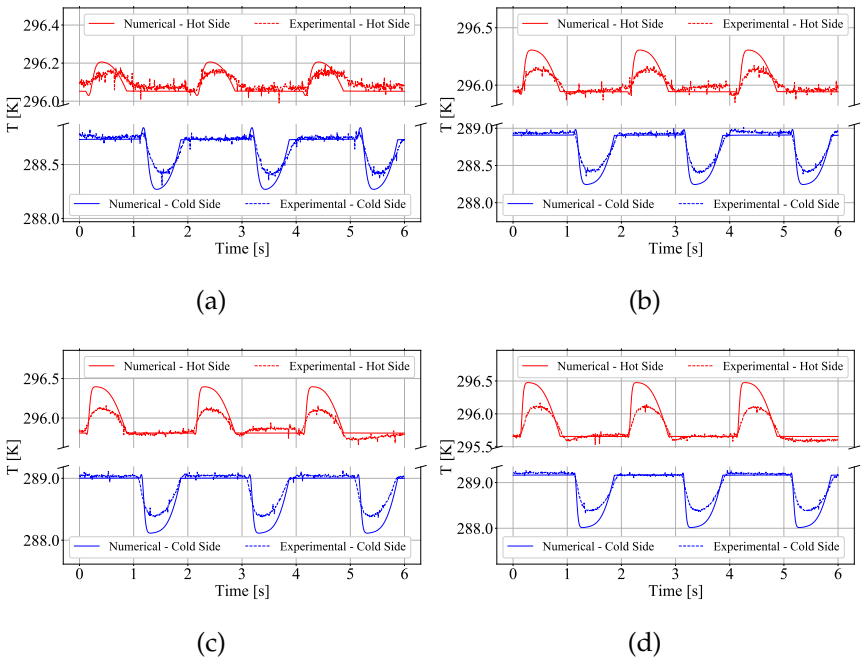

Figure 151 – Comparison between the numerical and experimental temperature profiles at approximately 110 mm from the hot and cold ends of Regenerator-3 during three cycles. The cycle frequency is 0.5 Hz, the temperature span is 8 K and the mass flow rate is (a) 40, (b) 60, (c) 80 and (d) 100 kg h^{-1}.

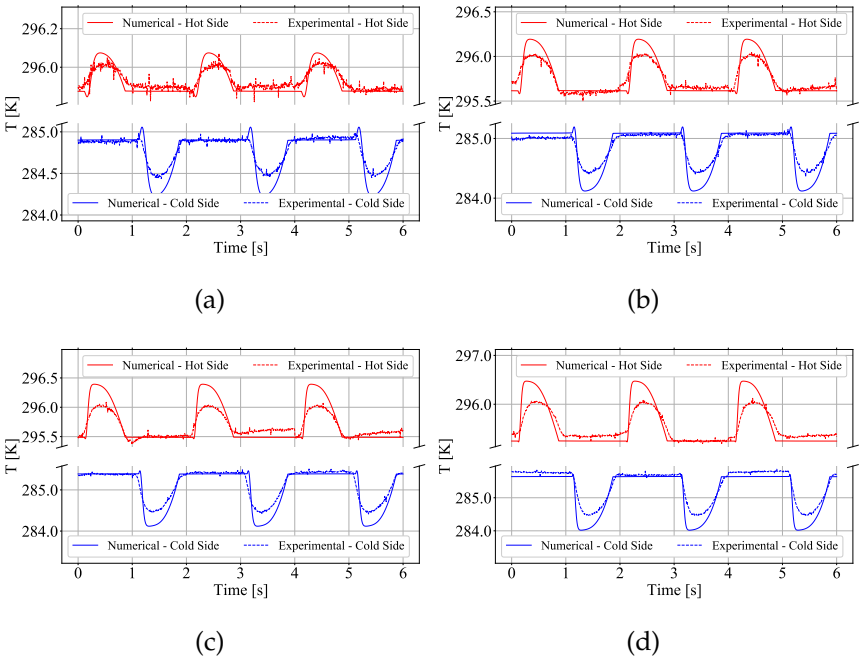

Figure 152 – Comparison between the numerical and experimental temperature profiles at approximately 110 mm from the hot and cold ends of Regenerator-3 during three cycles. The cycle frequency is 0.5 Hz, the temperature span is 12 K and the mass flow rate is (a) 40, (b) 60, (c) 80 and (d) 100 kg h^{-1}.

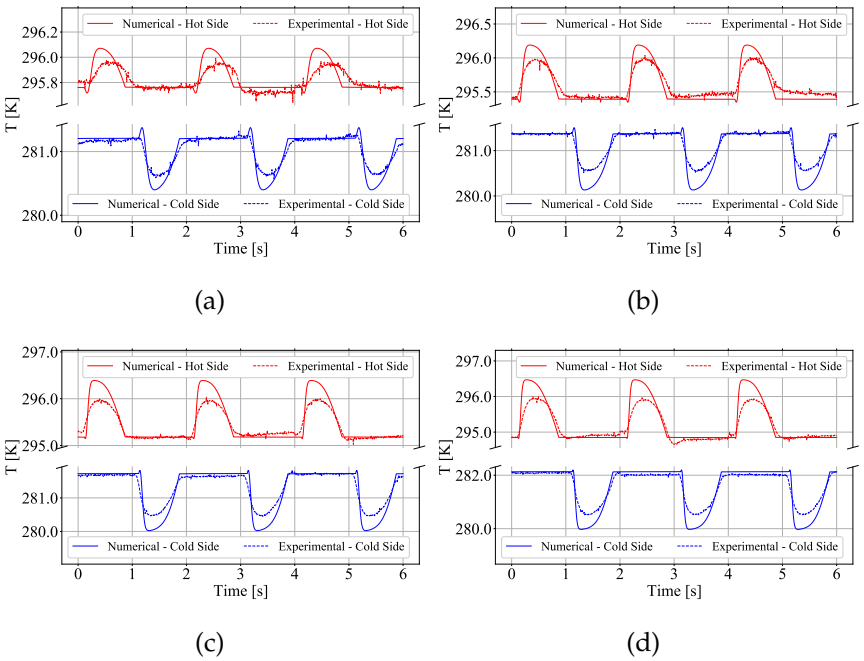

Figure 153 – Comparison between the numerical and experimental temperature profiles at approximately 110 mm from the hot and cold ends of Regenerator-3 during three cycles. The cycle frequency is 0.5 Hz, the temperature span is 16 K and the mass flow rate is (a) 40, (b) 60, (c) 80 and (d) 100 kg h^{-1}.

C Layer Length Optimization

The layer length optimization is used to minimize the negative effects of manufacturing deviations on the Curie temperatures of the regenerator materials. The procedure used in the optimization is simple, and the necessary input parameters are the operating conditions of the regenerator, the available Curie temperatures and the variation of the MCE peak temperature with the applied magnetic field ($\frac{\partial T_{\text{peak}}}{\partial H}$). The first step is to run the simulation assuming equal layer lengths, using the available Curie temperatures as if there were no deviations in their values. This step returns an initial estimate of the temperature profile of the solid phase over time at each of the control volumes in the regenerator. Then, the temperature at each instant is corrected to account for the deviation of the peak of the MCE using the following expression:

$$T_{\text{s}}^{*}(x,t) = T_{\text{s}}(x,t) - \frac{\partial T_{\text{peak}}}{\partial H} H_{\text{eff}}(x,t) \tag{C.1}$$

Finally, the average value of the corrected temperature considering all the instants with an existing MCE ($H_{\text{eff}}(t) \neq H_{\text{eff}}\ (t + \Delta t)$) is calculated in each control volume, and the Curie temperature closest to that value is applied to it, forming the layers. The resulting regenerator is then simulated once again, resulting in new solid phase temperature profiles. The process is then repeated until convergence and is shown in Figure 154. The convergence criteria (ε) is based on the cooling capacity and is usually around 5% of $Q_{c,i}$, but may vary from case to case. Most of the time, however, only one iteration is required.

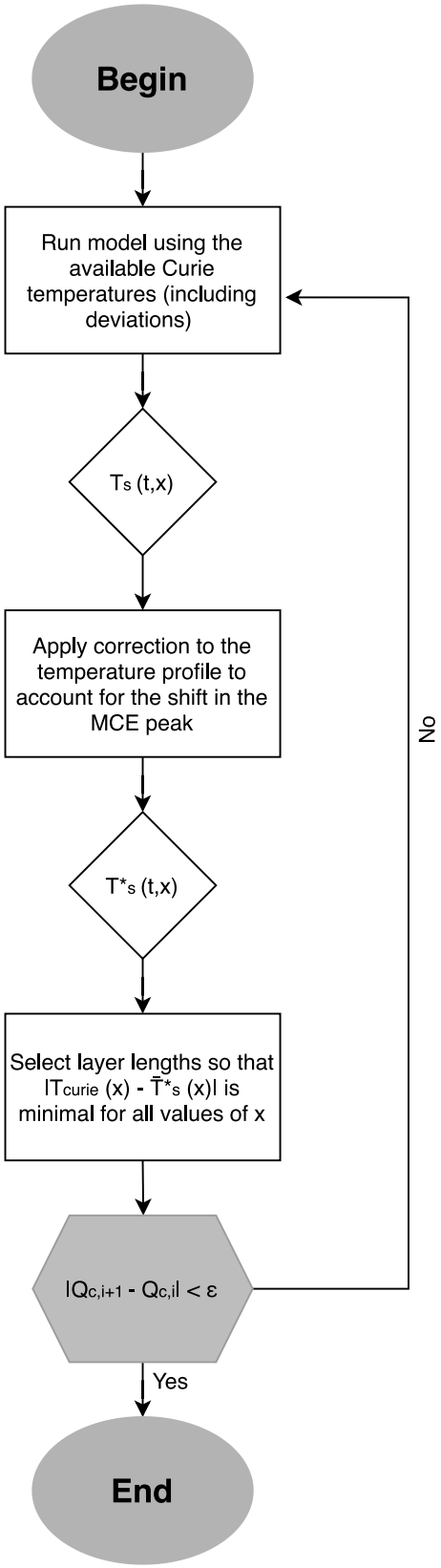

Figure 154 – Layer length optimization routine.

D Physical Properties of the Magnetocaloric Materials

Three different magnetocaloric materials were analysed in this work: CV-H, CV-HS and CV-HS-2. In order to determine their thermodynamical properties samples of these materials supplied by VACUUMSCHMELZE GmbH — VAC were sent to the Istituto Nazionale di Ricerca Metrologica (INRiM) where their properties were measured using the method described in Basso, Sasso & Küpferling (2010). This process yields two results: the specific heat capacity at a constant field as a function of temperature for magnetic flux densities of 0.0, 0.5, 1.0 and 1.5 T, and the specific entropy as a function of temperature for the same applied fields. Because these measurements are done both during heating and cooling to account for hysteresis, a total of 16 profiles are obtained, 8 for specific heat and 8 for entropy. Figures 155 and 156 show the results obtained for one of the samples of CV-HS that was submitted to these tests. It is important to note that the hysteresis of the material is very small, with the heating and cooling profiles being almost identical, and that the results prior to any treatment already closely resemble the expected profile, with only a few points showing noticeable deviations. Because of the low hysteresis, an average profile between heating and cooling is used during fitting. Another important detail is that the entropy is determined though the specific heat capacity, according to Equation 2.8. However, this equation only works at a constant field and thus cannot be used to determine the entropy variation with the magnetic flux density. This variation is determined through isothermal testing at different fields, which is also done by INRiM, in which the entropy at the smallest temperature and 0 T is assumed to be 0 J kg $^{-1}$ K $^{-1}$. A more detailed explanation of this process can be found in Basso et al. (2015).

The fitting process is based on the following expression for the specific heat capacity (BEZ, 2016):

$$c_{\mathrm{H}}(T,H) = a_1(T - T_{\mathrm{peak}}) + \begin{cases} (Y - b_{11})\left(\frac{d_{11}^2}{d_{11}^2 + (T - T_{\mathrm{peak}})^2}\right) + b_{11}, & \text{if } T < T_{\mathrm{peak}} \\ (Y - b_{21})\left(\frac{d_{21}^2}{d_{21}^2 + (T - T_{\mathrm{peak}})^2}\right) + b_{21}, & \text{if } T \geq T_{\mathrm{peak}} \end{cases} \tag{D.1}$$

where Y is the peak value of the heat capacity, b is the background heat capacity level, d is the full width at half maximum and a_1 is the slope of the heat capacity for $T < (T_{\mathrm{peak}} - 10)$. The fitting process then determines the optimal values for these coefficients for each of the four specific heat capacity profiles, resulting in the curves shown in Figure 157.

Lastly, it is necessary to determine the value of the specific heat capacity at the

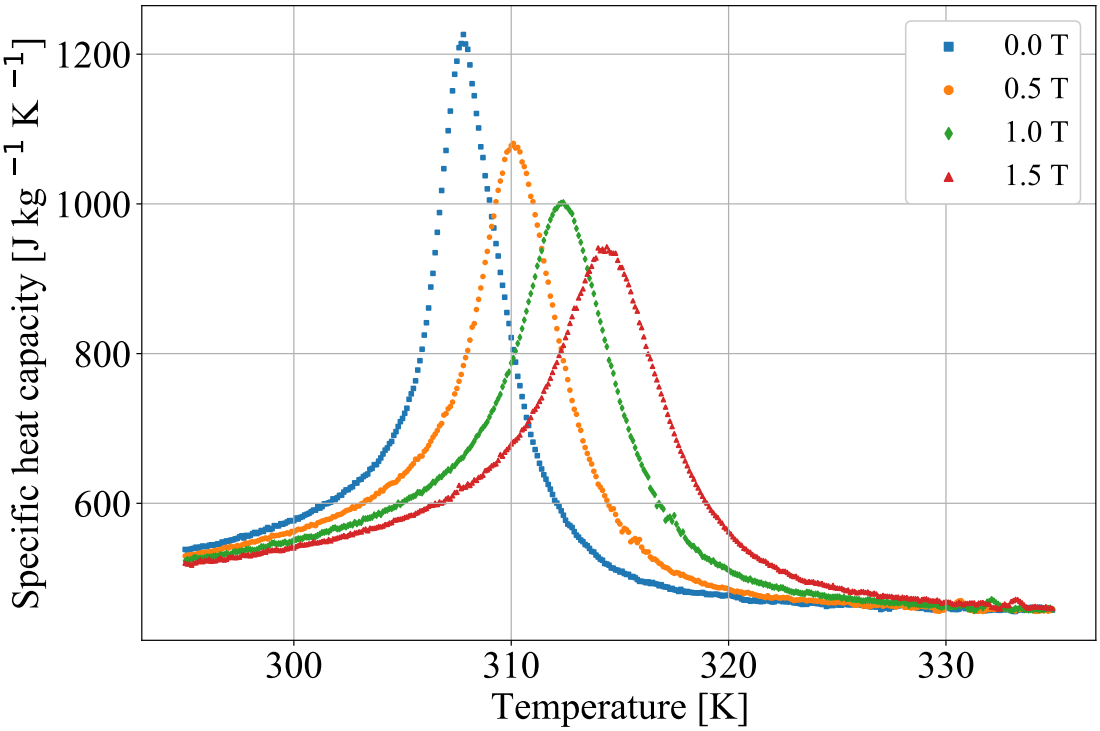

(a)

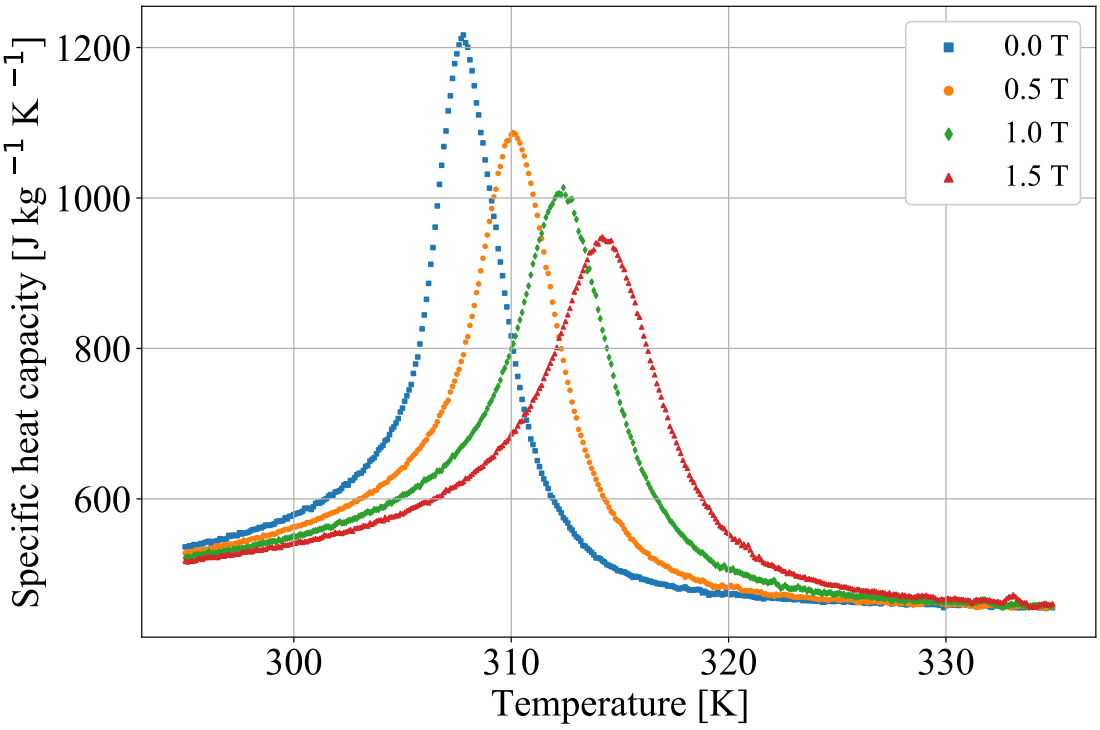

(b)

Figure 155 – Specific heat capacity measurements during (a) heating and (b) cooling obtained by INRiM for one of the CV-HS samples.

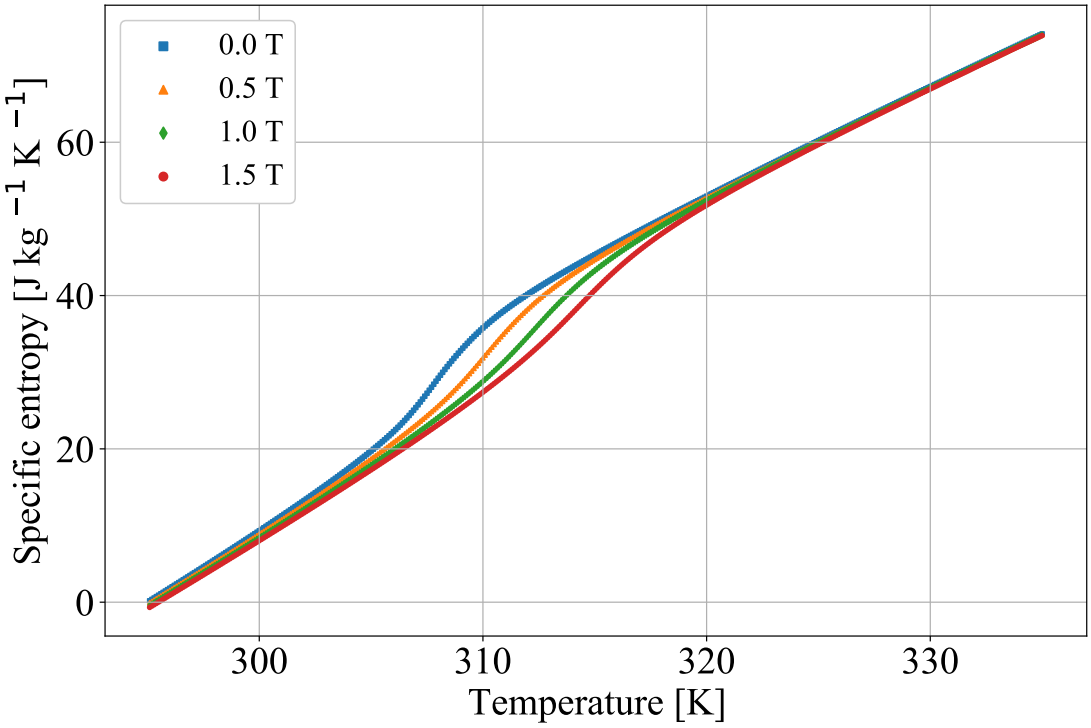

(a)

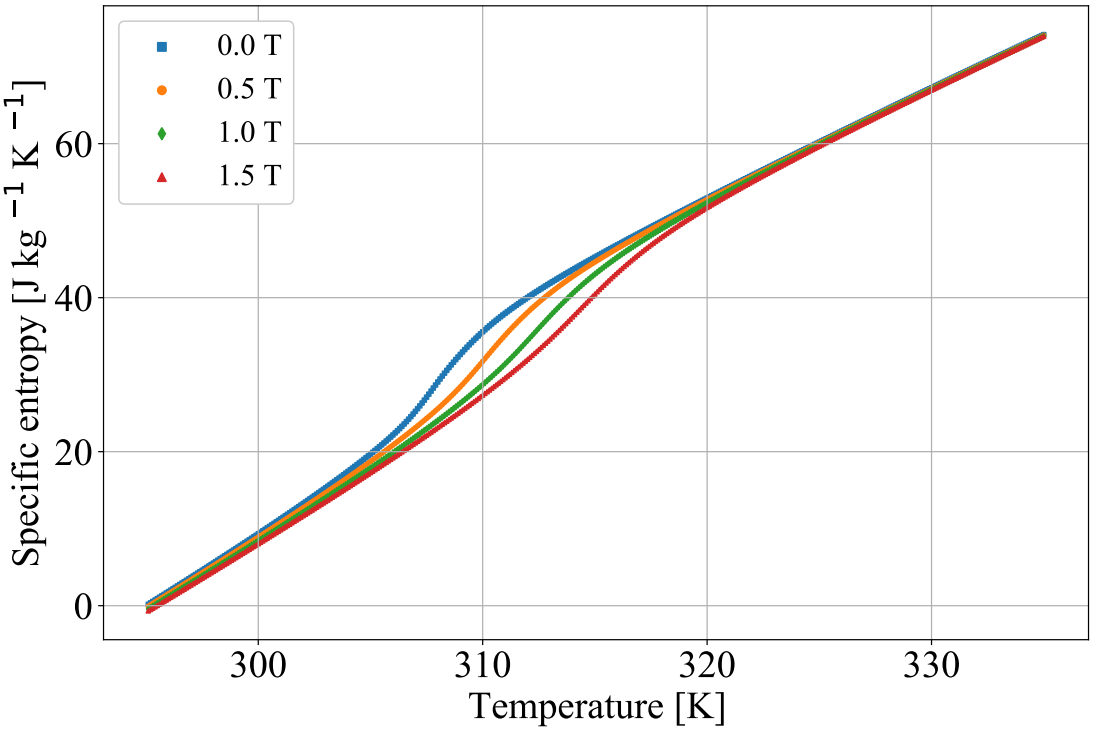

(b)

Figure 156 – Specific entropy derived from the measurements of specific heat capacity during (a) heating and (b) cooling obtained by INRiM for one of the CV-HS samples.

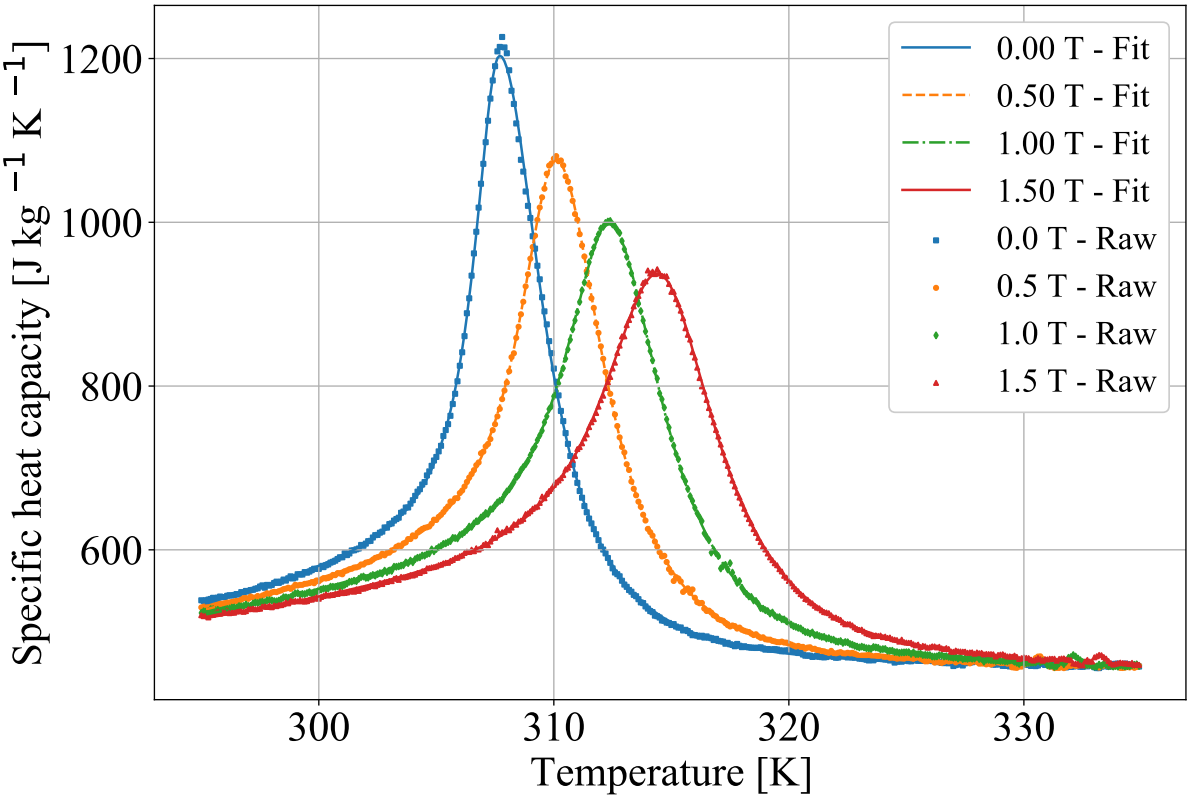

Figure 157 – Specific heat capacity raw data (heating) and fitting for the CV-HS sample.

magnetic flux densities between the four that are already known. To achieve this, all coefficients of Equation D.1 are interpolated using a scipy (python) library which determines the best interpolation function when given the data. The interpolated coefficients can then be used to determine the specific heat capacity profiles for any given magnetic flux density between 0.0 and 1.5 T. Figure 158 shows the specific heat capacity profiles obtained through this method. It can be seen that the interpolated profiles have the expected shape and values of a profile that would be located in-between the measured profiles. To determine the entropy profiles, the entropy value at the lowest temperature is interpolated in the desired field and is then used as the starting point for the integration of the corresponding specific heat capacity profile, according to Equation 2.8.

The exception to this process were the samples of CV-HS-2, which were not able to be fitted using Equation D.1. Because of that, a new correlation which did not require two separate expressions to represent the behaviour of the specific heat capacity was proposed:

$$c_{\mathrm{H}}(T,H) = 2(T-a_1)\left(\frac{b_1}{e^{-c_1(T-a_1-a_2)}}+h\right)+\frac{b_1c_1(T-a_1)^2e^{-c_1(T-a_1-a_2)}}{(e^{-c_1(T-a_1-a_2)}+1)^2}+ \\ \frac{d_1}{e^{-c_2(T-a_1-a_3)}+1}+\frac{d_1c_2(T-a_1)e^{-c_2(T-a_1-a_3)}}{(e^{-c_2(T-a_1-a_3)}+1)^2}+\frac{c_2f_1e^{-c_2(T-a_1-a_3)}}{(e^{-c_2(T-a_1-a_3)}+1)^2}+g \tag{D.2}$$

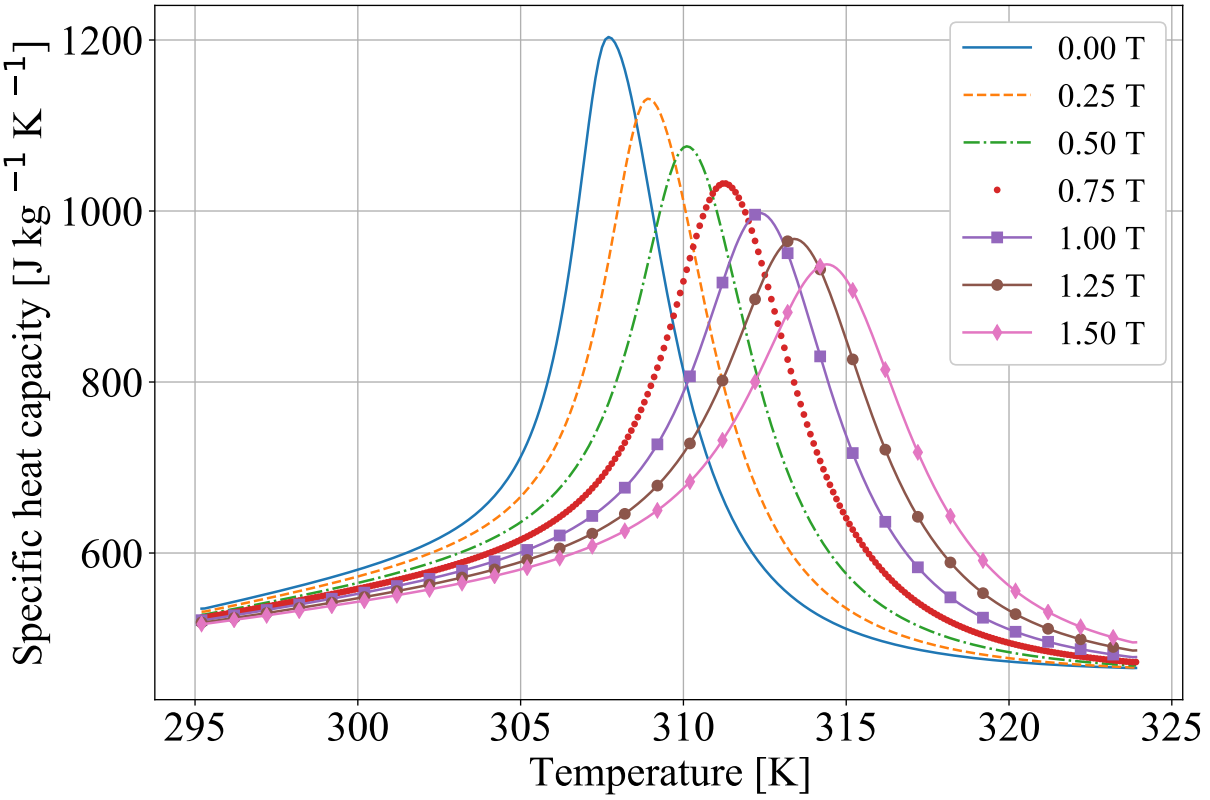

Figure 158 – Specific heat capacity of the CV-HS sample for different applied fields, including the original four and three that were obtained using the coefficient interpolation.

which comes from taking the derivative of an equation proposed for the specific entropy:

$$s(T,H) = \left(\frac{b_1}{1+e^{-c_1(T-a_1-a_2)}} + h\right)(T-a_1)^2 + \left(\frac{d_1}{1+e^{-c_2(T-a_1-a_3)}} + g\right)(T-a_1) + \frac{f_1}{1+e^{-c_2(T-a_1-a_3)}} + k \tag{D.3}$$

where the first term is used to adjust the derivative of the entropy at points which are further away from the Curie temperature, the second term gives the inclination of the entropy far from the Curie temperature before the adjustments made by the first term, the third therm controls the behaviour of the entropy near the Curie temperature and the last term adjusts the initial value of the entropy. After the fit of Equation D.2, the procedure is exactly the same, with the coefficients being interpolated to determine the property profiles for all desired fields between 0.0 and 1.5 T.

After this is done, the two properties required by the mathematical model, the specific heat and the derivative of the entropy with the applied field ($\frac{\partial s}{\partial H}$) were properly determined according to Section 3.4.2 and implemented in the model. Figures 159 to 161 show the resulting profiles in selected applied fields for the CV-H, CV-HS and CV-HS-2 samples that were used in this work.

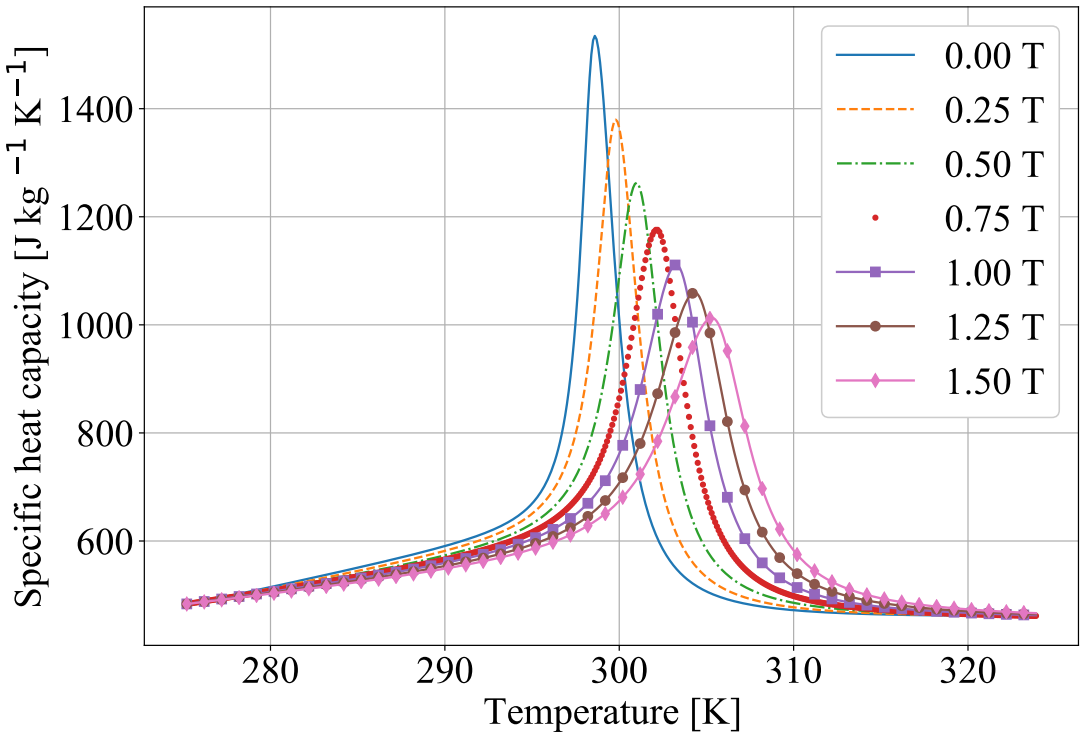

(a)

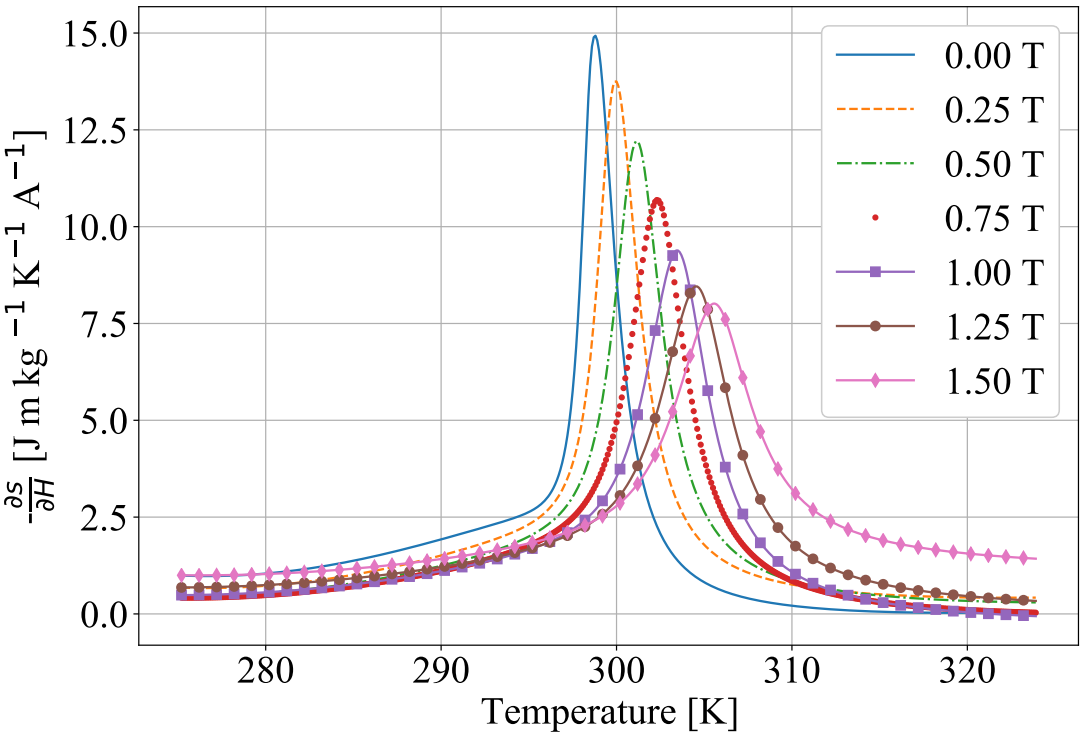

(b)

Figure 159 – (a) Specific heat capacity and (b) $\frac{\partial s}{\partial H}$ profiles of the CV-H sample used in the model.

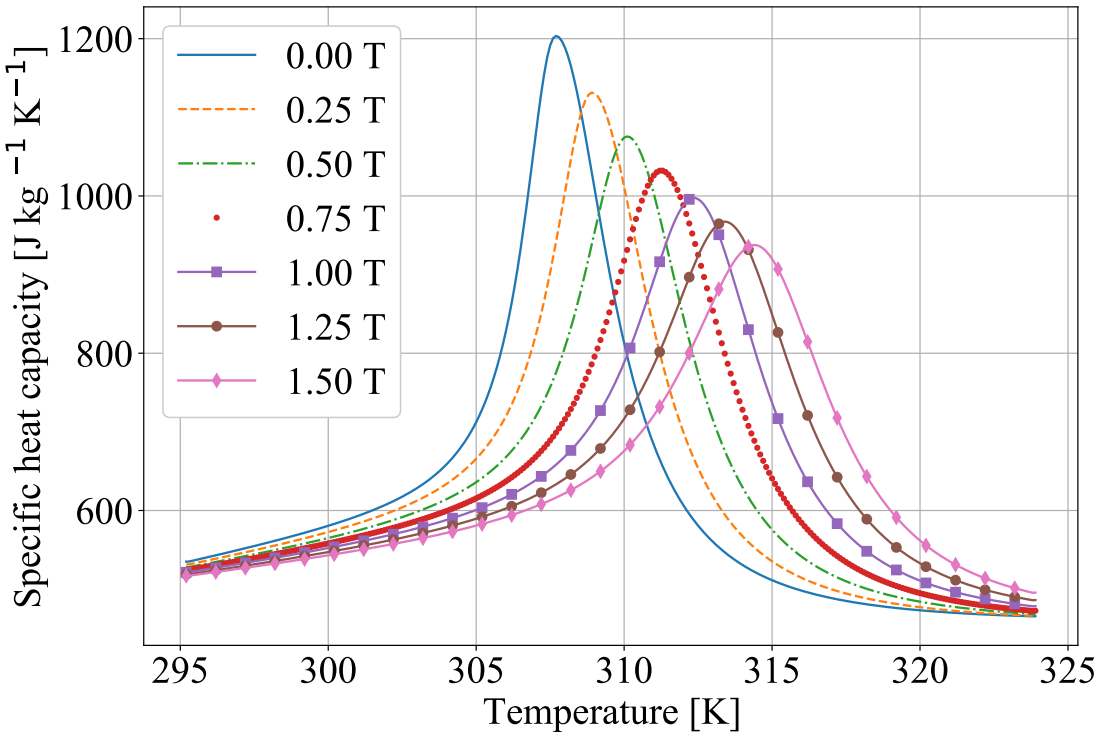

(a)

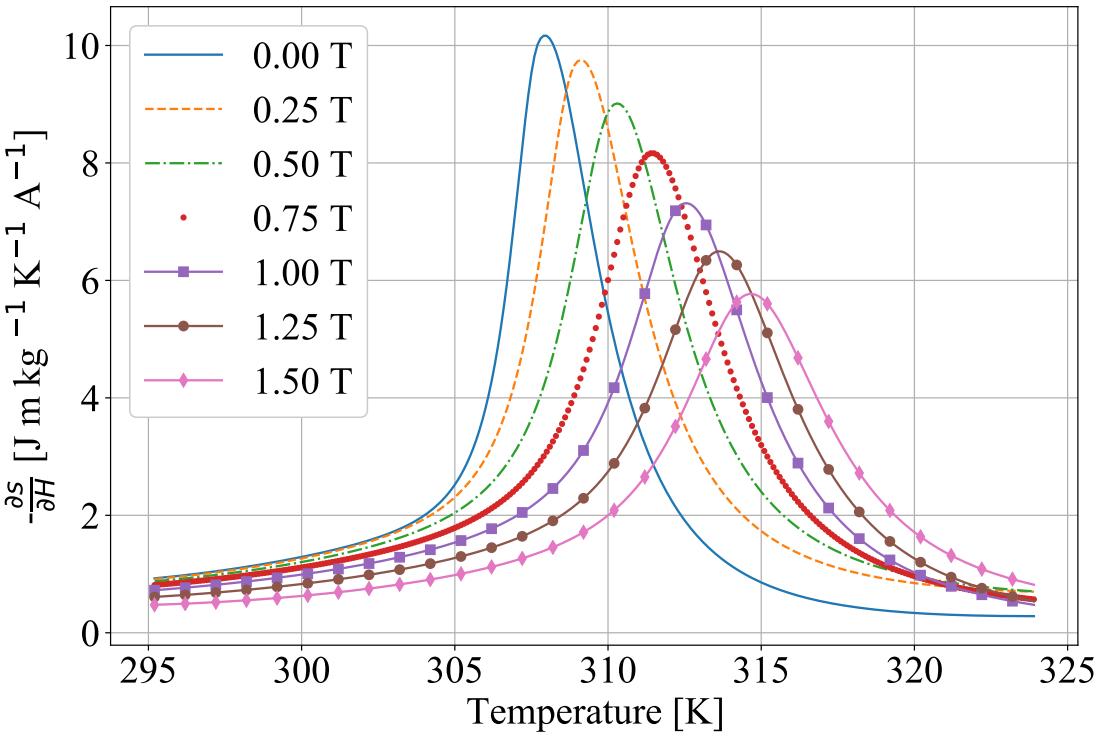

(b)

Figure 160 – (a) Specific heat capacity and (b) $\frac{\partial s}{\partial H}$ profiles of the CV-HS sample used in the model.

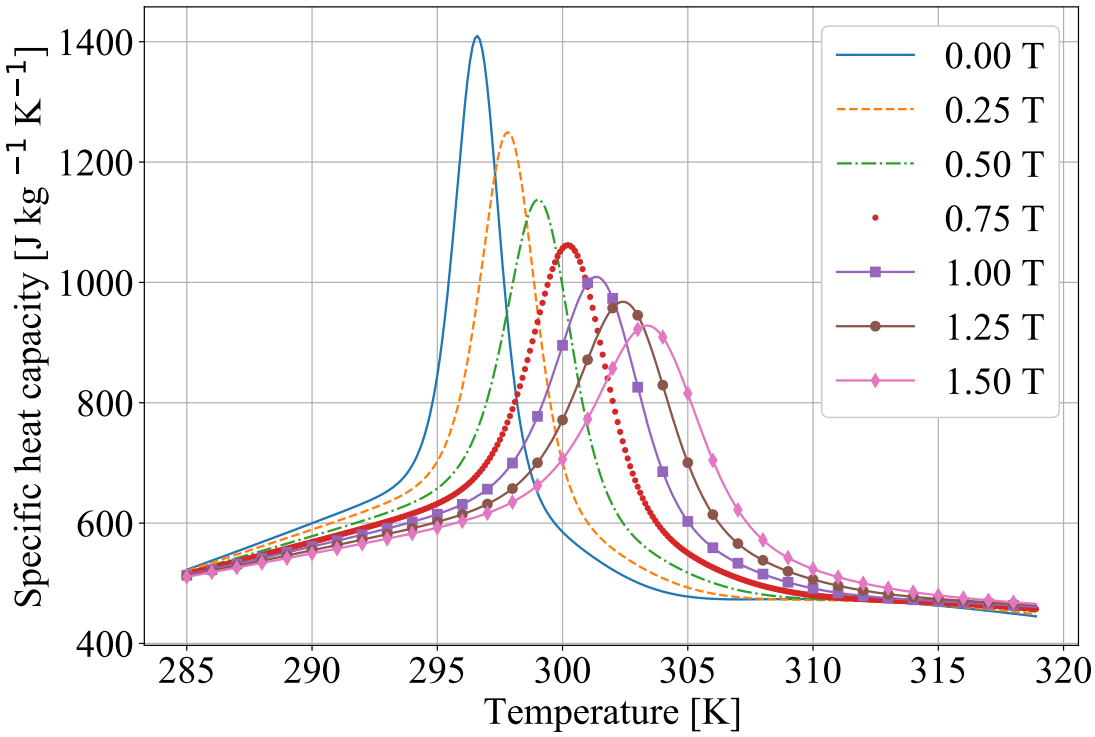

(a)

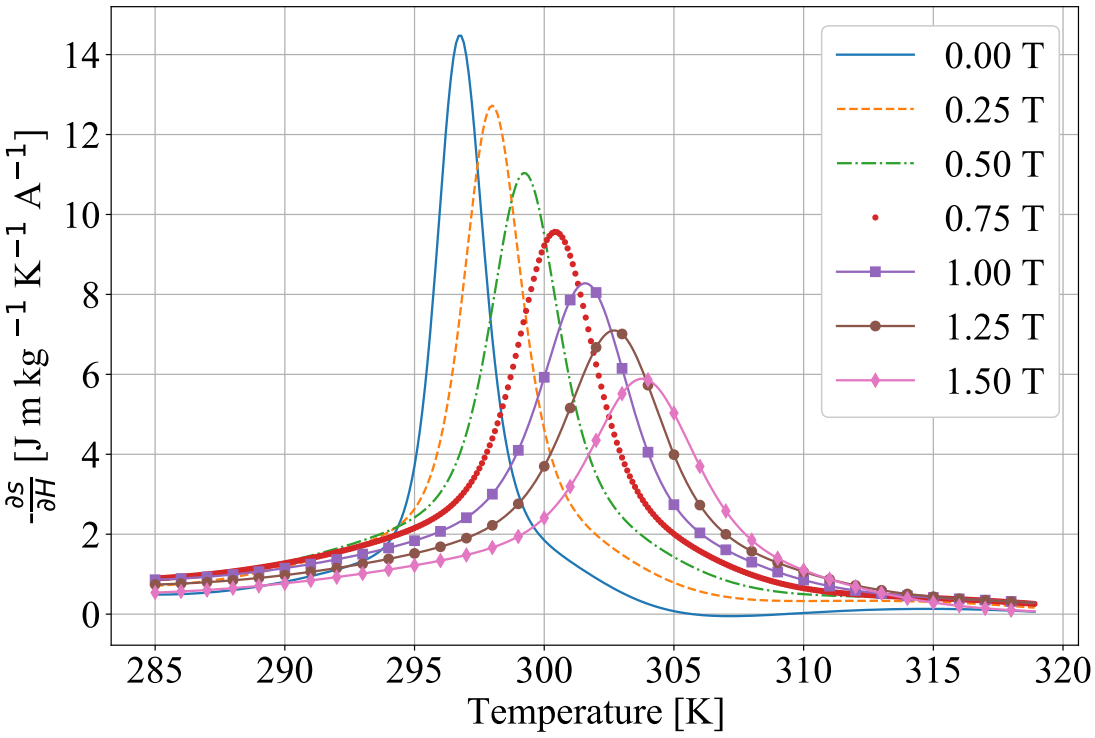

(b)

Figure 161 – (a) Specific heat capacity and (b) $\frac{\partial s}{\partial H}$ profiles of the CV-HS-2 sample used in the model.